High-Redshift Star-Forming Galaxies

Manuel Behrendt

München 2019

High-Redshift Star-Forming Galaxies

Manuel Behrendt

Dissertation
an der Fakultät für Physik
der Ludwig–Maximilians–Universität
München

vorgelegt von
Manuel Behrendt
aus Illertissen/Neu-Ulm

München, den 01.08.2019

Erstgutachter: Prof. Dr. Andreas Burkert
Zweitgutachter: Prof. Dr. Eric Emsellem
Tag der mündlichen Prüfung: 16.09.2019

Contents

List of Figures

List of Tables

Zusammenfassung

Vor zehn Milliarden Jahren war das Universum viel aktiver als heute. Irreguläre, gasreiche und turbulente Scheibengalaxien dominierten die Geschichte der kosmischen Sternentstehung mit 10-100-mal höheren Sternentstehungsraten als heute. Diese Galaxien enthalten oft riesige, kpc-große Klumpen, von denen kraftvolle Ausflüsse entstammen, die durch Sternfeedback verursacht werden. Es wird angenommen, dass diese massiven Objekte eine wichtige Rolle bei der Entstehung von Bulge-Komponenten spielen, die sich häufig im Zentrum einer Galaxie befinden. Die Entstehung der Riesenklumpen lässt sich durch die Gravitations-Scheiben-Instabilität erklären, die durch viele Simulationen und Beobachtungen gestützt wird. Die beobachteten hohen Gasanteile, Dichten und hohen Geschwindigkeitsdispersionen dieser Galaxien implizieren gravitationsbedingt instabile oder marginal stabile Scheiben über kosmische Zeiträume. Diese Bedingungen lassen große Störungen (Toomre-Länge) anwachsen, die zu massiven, durch die Schwerkraft gebundenen Klumpen führen können. Wir untersuchen die Erscheinungsform dieser riesigen Klumpen genauer, indem wir die lineare Störungstheorie für die Dicke-Scheiben-Approximation überarbeiten und verwenden hydrodynamische Simulationen mit sehr hoher und niedriger Auflösung (~ 3-100 pc) mit dem Adaptiven-Mesh Code RAMSES. Wir stellen fest, dass die Toomre-Länge bei einer Gasscheibe mit vertikalem Profil (dicke Scheibe) etwa doppelt so groß ist wie bei der Näherung der dünnen Scheibe, die normalerweise zur Abschätzung der Klumpen Eigenschaften verwendet wird. Zum ersten Mal bestätigen wir durch Simulationen das Anwachsen der vorhergesagten Störungen, die sich als Toomre-Ringe ausbilden. Klumpen bilden sich nicht direkt auf der vorhergesagten Toomre-Skala, das im Allgemeinen angenommen wird. Stattdessen kollabieren die anfänglich wachsenden Strukturen (Ringe) weiter und Klumpen können nach Erreichen höherer Dichten auf der Sub-Toomre-Skala (2. Phase) fragmentieren. Diese Bedingungen führen zur Bildung vieler und viel kleinerer Klumpen als durch Fragmentierung auf der Toomre-Skala vorhergesagt. Um eine fehlerhafte Fragmentierung bei maximaler Auflösung zu vermeiden, verwenden Simulationen normalerweise einen künstlichen Druck (APF), der eine minimale 'Jeans' Länge gewährleistet, die durch einige Auflösungselemente repräsentiert wird. Wir zeigen, dass in Simulationen mit niedrigerer Auflösung (wie in kosmologischen Zoom-In-Simulationen) dieser APF bereits bei geringen Dichten wirkt, die Kollaps Phase verhindert und zu massiven und aufgeblähten Klumpen führt, die ungefähr – aber zufällig – auf der ursprünglichen Toomre-Skala liegen. Diese Ergebnisse widerlegen die verbreiteten Hypothesen, dass sich Riesenklumpen direkt auf der Toomre-Skala bilden müssen und dann zu einer gravitationsgebundenen Substruktur Subfragmentieren (Top-Down-Szenario), wenn die Auflösung hoch genug ist. In den hochauflösenden Simulationen stellen wir stattdessen fest, dass sich die vielen kleineren Klumpen zu Klumpen Clustern (CCs) gruppieren, die als riesige und massive Objekte erscheinen (Bottom-up-Szenario), wenn wir die Auflösungsgrenze der Beobachtungen bei $z \sim 2$ berücksichtigen. Sie spiegeln die Massen, Größen und inneren kinematischen Eigenschaften von Riesenklumpen in hoch rotverschobenen Beobachtungen wider. In Genzel et al. (2011) folgerten sie aus der abgeleiteten Kinematik, dass ihre Klumpen entweder durch hohe Geschwindigkeitsdispersion druck gestützt sind oder aufgrund der geringen Geschwindigkeitsgradienten immer noch kolla-

bieren. In unseren Simulationen wird der Gradient durch einen Klumpen Cluster erklärt, der sich auf kpc-Skalen um seinen Massenschwerpunkt dreht. Darüber hinaus sagen die CCs eine Hierarchie von Eigenschaften auf mehreren Skalen voraus, die von der Beobachtungsauflösung abhängt. Dies kann mit zukünftigen Teleskopen getestet werden. Für eine hohe Beobachtungsauflösung sind gravitativ gebundene Cluster (geschlossene Cluster) sichtbar und mit abnehmender Auflösung können weniger Objekte identifiziert werden, was zu massiven und größeren Klumpen führt, die durch offene Cluster repräsentiert sind. Die hergeleitete Toomre-Länge für die Approximation der dicken Scheiben, die Entdeckung der Klumpen Cluster und das Bottom-up-Szenario öffnen die Tür für ein neues Verständnis der Natur der beobachteten Riesenklumpen. Das CC-Szenario könnte starke Auswirkungen auf die interne Evolution, die Lebensdauer und die Migrationszeitskalen der beobachteten Riesenklumpen, das Wachstum der Bulge-Komponente und auf die AGN-Aktivität, die Sternfeedback und die chemische Anreicherungsgeschichte von galaktischen Scheiben haben.

Abstract

Ten billion years ago, the Universe was much more active than today. Irregular gas-rich and turbulent disc galaxies dominated the cosmic star formation history with star formation rates 10-100 times higher than found today. These galaxies often contain giant, kpc-sized clumps that are the launching sites of powerful outflows caused by stellar feedback. These massive objects are thought to play an important role in the bulge formation process, often found in the centre of a galaxy. The origin of the giant clumps can be explained by gravitational disc instability, which is supported by many simulations and observations. The observed high gas fractions, densities and high-velocity dispersions of these galaxies imply gravitationally unstable or marginally stable discs over cosmic time. These conditions allow large perturbations (Toomre-length) to grow that can lead to massive gravitationally bound clumps. We investigate the nature of these giant clumps in more detail by revisiting the linear perturbation theory for the thick disc approximation and employ very high- and low-resolution hydrodynamic simulations (~3-100 pc) with the adaptive mesh refinement code RAMSES. We find that the Toomre-length is around two times larger for a gas disc with a vertical profile (thick disc) than for the thin disc approximation, which is typically used to estimate clump properties. For the first time, we confirm that simulations show the growth of the predicted perturbations that establish as Toomre-rings. Clumps do not form directly on the predicted Toomre scale, which is commonly assumed. Instead, the initial growing structures (rings) collapse further, and clumps can fragment after reaching higher densities on a sub-Toomre-scale (2nd phase). These conditions lead to the formation of many and much smaller clumps than predicted by fragmentation on the Toomre scale. To avoid spurious fragmentation at maximum resolution, simulations typically use an artificial pressure floor (APF) that ensures a minimum Jeans-length, resolved by a few resolution elements. We show that in lower resolution simulations (like cosmological zoom-in simulations) this APF acts already at low densities, preventing the collapse phase and leading to massive and inflated clumps that are roughly — but by chance — on the initial Toomre scale. These results disprove the common hypotheses that giant clumps need to form directly on the Toomre scale and sub-fragment to a gravitationally bound substructure (top-down scenario) if the resolution is high enough. In the high-resolution simulations instead, we find that the many smaller clumps group to clump clusters (CCs) that appear as a giant and massive objects (bottom-up scenario) if we consider the resolution limit of observations at $z \sim 2$. They reflect the masses, sizes and internal kinematic properties of giant clumps in high-redshift observations. In Genzel et al. (2011) they concluded from the inferred kinematics that their clumps are either pressure supported by high-velocity dispersion or are still undergoing collapse because of the small velocity gradients. In our simulations, the gradient is explained by a clump cluster rotating on kpc-scales around their centre of mass. Furthermore, the CCs predict a hierarchy of properties on several scales, which is dependent on the observational resolution. This can be tested by future telescopes. For high observational resolution, gravitationally bound clusters (closed clusters) are visible, and with a decreasing resolution, fewer objects can be identified, leading to massive and larger clumps that are represented by open clusters.

The derived Toomre-length for the thick disc approximation, the finding of the clump clusters and the bottom-up scenario open the door for a new understanding of the nature of the observed giant clumps. The CC scenario could have strong implications for the internal evolution, lifetimes and the migration timescales of the observed giant clumps, bulge growth and AGN activity, stellar feedback and the chemical enrichment history of galactic discs.

Chapter 1

Introduction

Not a long time ago humankind realised that we live in a giant galactic system called the Milky Way. It contains hundreds of billion stars spanned over $\sim 200,000$ light-years (ly) shaped like a disc which is rotating around its centre of mass. Galaxies are little islands in the Universe that turn gas into luminous stars and produce chemical elements by nuclear reactions. Massive stars enrich their environment with heavy elements at the end of their life-time via supernova explosions. Planetary systems are typically associated with a star, which

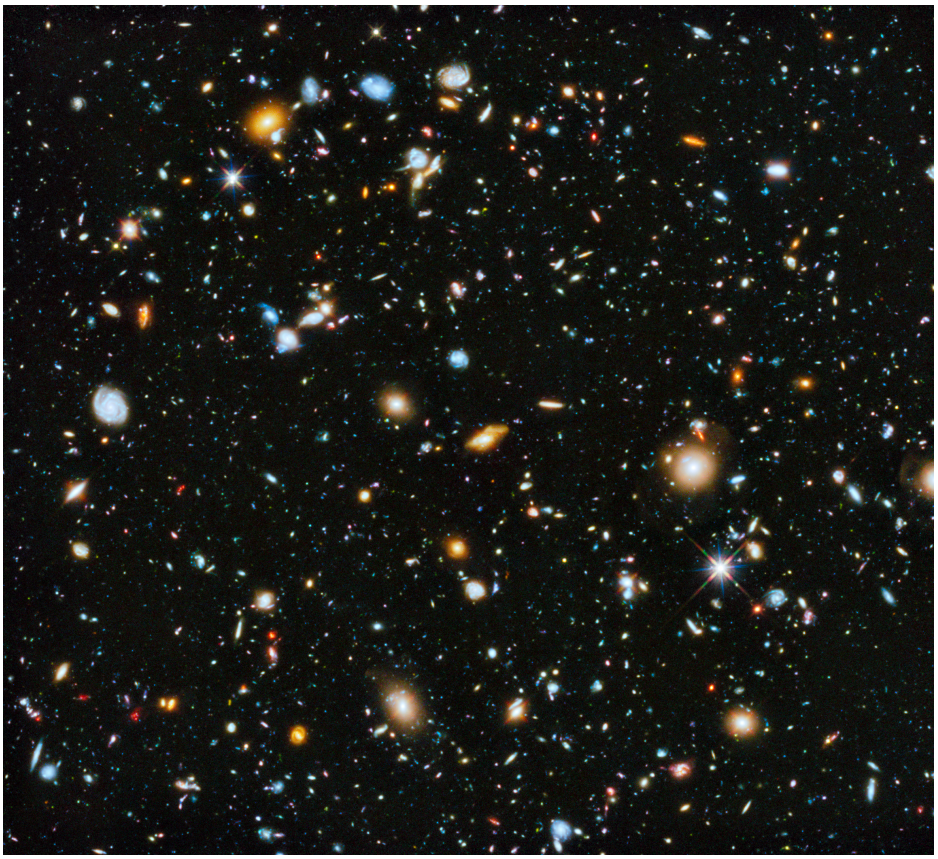

Figure 1.1: The Hubble eXtreme Deep Field image shows about 5,500 galaxies observed in the range from ultraviolet to near-infrared light and is smaller than a 1 mm x 1 mm square of paper held at 1 meter distance. The red galaxies are the remnants of major collisions during their elderly times. Many of the smaller galaxies are very young and include some of the most distant galaxies that existed shortly after the Big Bang. (Credit: www.nasa.gov)

maybe give the basis to emerge and harbour all kinds of life forms. A galaxy is a gravitationally bound system of stars, gas, dust, a black hole and mostly consists of dark matter, which we indirectly infer by the pull of its gravity. We can find a whole zoo of galaxies (Figure 1.1) in the Universe ranging from dwarfs with a few hundred million stars to large systems containing one hundred trillion stars. The light properties of its components tell us the story of each galaxy's past life and reveal the history and structure of the Universe. With modern telescopes, observers find that ancient galaxies were already around when the infant Universe was just a few hundred million years old.

In the following Section 1.1, we give a general summary of our current knowledge about the origin and formation of galaxies within the cosmological context. In Section 1.2 we overview present studies of galaxy classes, their evolution and global properties over cosmic time. Section 1.3 discusses the origin of the galaxy's internal structure formation supported by observed spatially and spectrally resolved properties and by theoretical work. We focus on the irregular and clumpy galaxies which have particular relevance in the early and more active phases of the Universe. Finally, we point out the limitation of current observations and theoretical work which we address within this PhD thesis (Section 1.4). In the subsequent chapters, we give the basis of the numerical methods (Chapter 2) that we apply in three published papers (Chapters 3, 4, 5), each containing its specific introduction. In Chapter 6, we summarize the key findings and discuss them in Chapter 7, where we give an outlook into current and future work.

1.1 The standard model of cosmology

The sections in this chapter are based on the following literature and references therein: Frieman, Turner & Huterer (2008); Mo, van den Bosch & White (2010); Spergel (2015); Silk & Mamon (2012); Bromm (2013); Schneider (2015); Naab & Ostriker (2017); Planck Collaboration et al. (2018a,b,c)

1.1.1 The evolution of the Universe

The Universe started to expand from a singularity 13.8 billion years ago. Its history is currently best described by the ΛCDM (Lambda Cold Dark Matter) model in cosmology. It is the most straightforward concept that can explain the following properties of the Universe:
- The abundance of hydrogen, helium, lithium of the primordial gas in the early Universe.
- The accelerating expansion of the Universe.
- The large scale structure in the distribution of galaxies.
- The existence and structure of the cosmic microwave background.

All the terms and phrases of this model are described in the following text.

In the standard model, the early Universe was a dense and very hot plasma where photons are strongly coupled with free electrons via Thompson scattering. The photons had a very short mean free path, and therefore, the Universe was opaque. With its expansion, it cooled to 2700 Kelvin after 380,000 years from the Big Bang (14 billion years ago), and electrons were able to combine with protons to form hydrogen atoms. At this time the photons can decouple from the matter, and the Universe became transparent. Since the perturbations no longer propagate, the existing density pattern becomes "frozen" (Figure 1.4, #2). The afterglow of

this light pattern is called the cosmic microwave background (CMB, Figure 1.2) from which the current energy densities of our Universe can be derived: 4% baryonic matter, 23% dark matter, 73% dark energy. It is the furthest in time we can explore using electromagnetic waves. Over several billion years, the Universe expanded further as demonstrated by observations performed since the late 1920s. The expansion of the space caused a growth of the wavelength of the travelling photons to roughly 1 millimetre today. This effect is called the cosmological redshift (see Figure 1.3). The effective temperature of the cosmic microwave background decreased to 2.7 Kelvin up to today, and therefore, its radiation can be detected by far-infrared and radio telescopes. It appears in all directions on the sky as an almost uniform background, in agreement with the cosmological principle where the standard model is based on. It assumes that on large scales, the Universe is very similar at every point (homogeneous) and has no preferential directions in space (isotropic). Very tiny fluctuations in the temperature

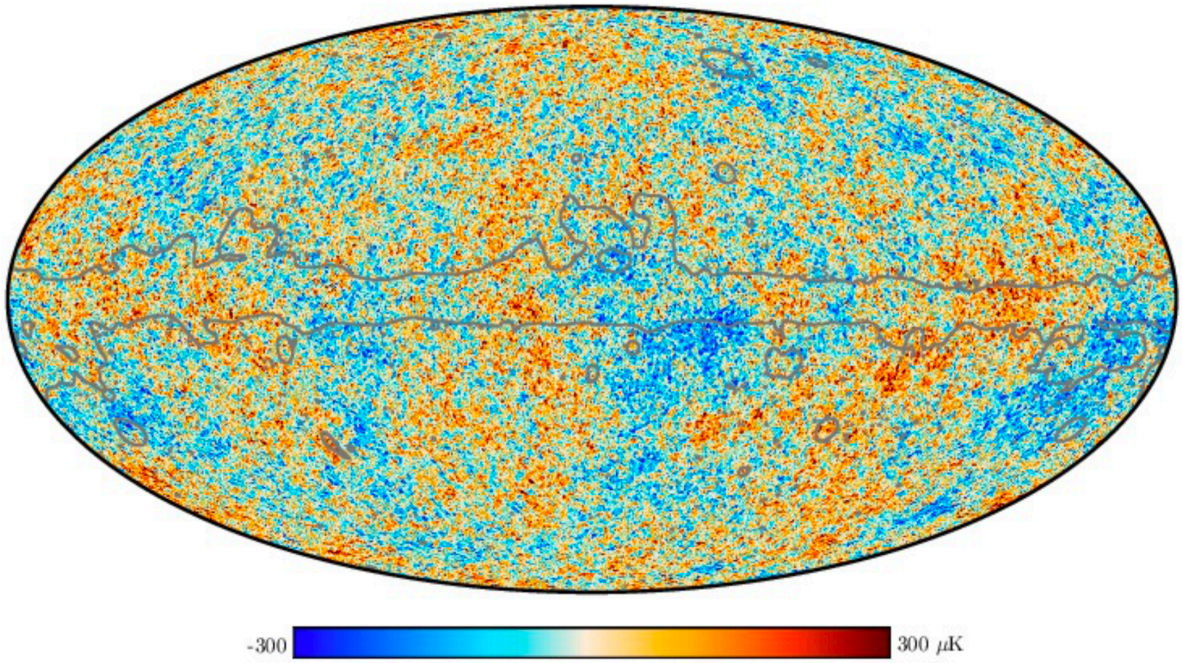

Figure 1.2: The anisotropies of the cosmic microwave background (CMB), as observed by ESA's Planck mission. It shows the 2018 temperature map. The grey line indicates the plane of the Milky Way disc. (Credit: Planck Collaboration et al. (2018b), Figure 6)

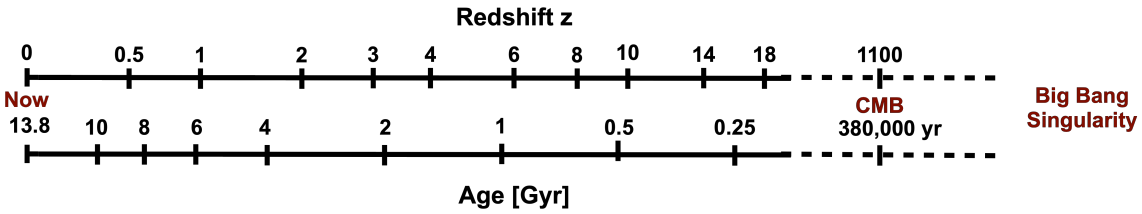

Figure 1.3: A simplified relation between the cosmological redshift and the age of the Universe for the standard cosmological model based on parameters from the Planck mission

of the CMB (anisotropies) appear on all scales. These density fluctuations in the primordial plasma are thought to be seeded initially by quantum fluctuations during the cosmic inflation (Figure 1.4, #1), a period of a rapid expansion that took place immediately after the hot Big Bang singularity. For the following era, the "Dark Ages", the mostly neutral Universe is not observable throughout the electromagnetic spectrum (Figure 1.4, #3). During this time the cold dark matter begins to collapse in overdense regions gravitationally. The baryonic matter follows the CDM and collapses into so-called CDM halos. The first stars begin to form, and the radiation reionises the intergalactic medium (Figure 1.4, #4) after ~ 380.000 years. The structure continues to grow, merges under the influence of gravity and form the so-called cosmic web (Figure 1.4, #5). By observations of many galaxies, the underlying dark matter density of the cosmic web can be indirectly traced. On the largest scales, these galaxies are bound to clusters. The organisation of the galaxies still retains the anisotropies and the imprint of the baryon acoustic oscillations (BAO) correlation length, established in the hot plasma at early times (Planck Collaboration et al., 2018a). Huge cosmological simulations based on the ΛCDM model have successfully reproduced the cosmic web (Figure 1.5, 1.21). Over time the mysterious dark energy increasingly started to dominate over the gravity, and the expansion of the Universe accelerates (Figure 1.4, #6). The Hubble constant for this model is 71 km/s/Mpc, and the density of the Universe is very close to the critical value for re-collapse. The concept of dark energy is closely associated with the cosmological constant Λ that arises in Albert Einstein's field equations of general relativity. It describes the energy density of space (or vacuum energy).

1.1.2 Galaxy formation

1.1.2.1 The first stars and first galaxies

During the dark ages (z~ 1100 to z~ 20) the inter-galactic-medium (IGM) was neutral with no existing light sources. At $z \sim 30$, the first structures arise through the growth of density fluctuations from the early Universe. When local dark matter perturbations reach a critical density, they can decouple from the expansion of the Universe via gravitational instability. They collapse to mini-halos with Jeans masses of $M_{halo} \sim 10^5 - 10^6$ $M_\odot$ until they are virialised because of their non-interactive and non-dissipative nature ($z \sim 20$, $t_{Universe} \sim 200$ Myr). The gaseous (baryonic) component is following the dark matter but can collapse further within these halos. The potential energy of the gas is transformed into heat through friction and settles down in the inner part of the halo until pressure balances the gravitational force. The infalling gas of the outer part of the halo is shock heated with the inner part. According to the virial theorem, half of its potential energy is transformed into kinetic energy, which in turn is converted into heat to its virial temperature of a few $T_{vir} \sim 1000$K. The primordial gas was only able to cool radiatively via molecular hydrogen H_2 and could fragment gravitationally into denser structures, high enough to form the first stars (population III). The halos grow to larger structures mainly through merging with other halos or are fed by filaments (gas+dark matter) of the large-scale density field. At around $z \sim 10$ (500 Myr) they reach $M_{halo} \sim 10^7 - 10^8 M_\odot$, have gravitational potential wells and are massive enough to prevent expulsion of the gas from the first stars. The characteristic temperature of the gas is of $T_{vir} \geq 10^4$K and cooling was only possible via atomic hydrogen HI. These bound structures are called the first galaxies containing very massive and short-lived stars which are creating expanding ionised bubbles of 10^4K via UV radiation. The population III stars explode in

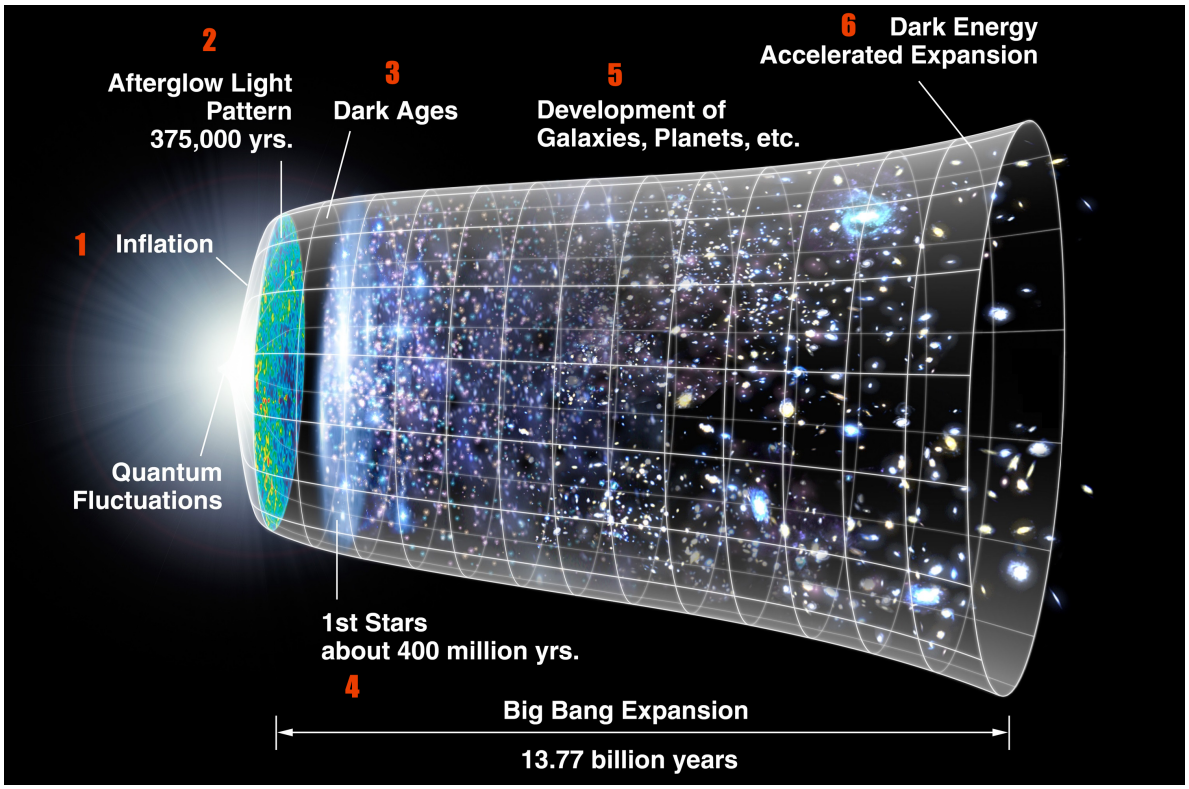

Figure 1.4: Evolutionary stages of the Universe from the Big Bang to the present. The size is depicted by the vertical extent of the grid in this graphic. (Credit: Adaption of the original image from NASA WMAP Science Team)

supernovae at the end of their lifetime and enrich their environment with metals (elements heavier than hydrogen or helium), making cooling more efficient. Furthermore, the stellar feedback prevents the gas from turning into stars on a very short time-scale. The second generation of stars can form with much less masses ≤ 1 $M_\odot$ and luminosity and very long lifetimes. These stars can still be found in globular clusters in the stellar halo or the bulge component of our Galaxy with ages of 10-13 Gyr. E.g. the metal-rich stars (population I) are in the disc component of the Galaxy having ages of 0-10 Gyr with the youngest ones in the spiral arms.

1.1.2.2 The formation of discs

Non-spherical dark matter overdensities in the early fluctuation can attain angular momentum due to a torque caused by the neighbouring perturbations tidal gravitational field. The dark matter halo cannot arbitrarily collapse due to its non-dissipative nature, but the gas can infall further towards the centre due to cooling. The gas rotation speeds up by preserving angular momentum, and frictional forces drive the gas onto circular orbits (angular momentum barrier) to form a flat disc. In this form, denser structures can develop and cool easier to create stars than in an almost spherical distribution.More matter is infalling mainly along filaments, which are connected to the halo and streams can reach even the central regions

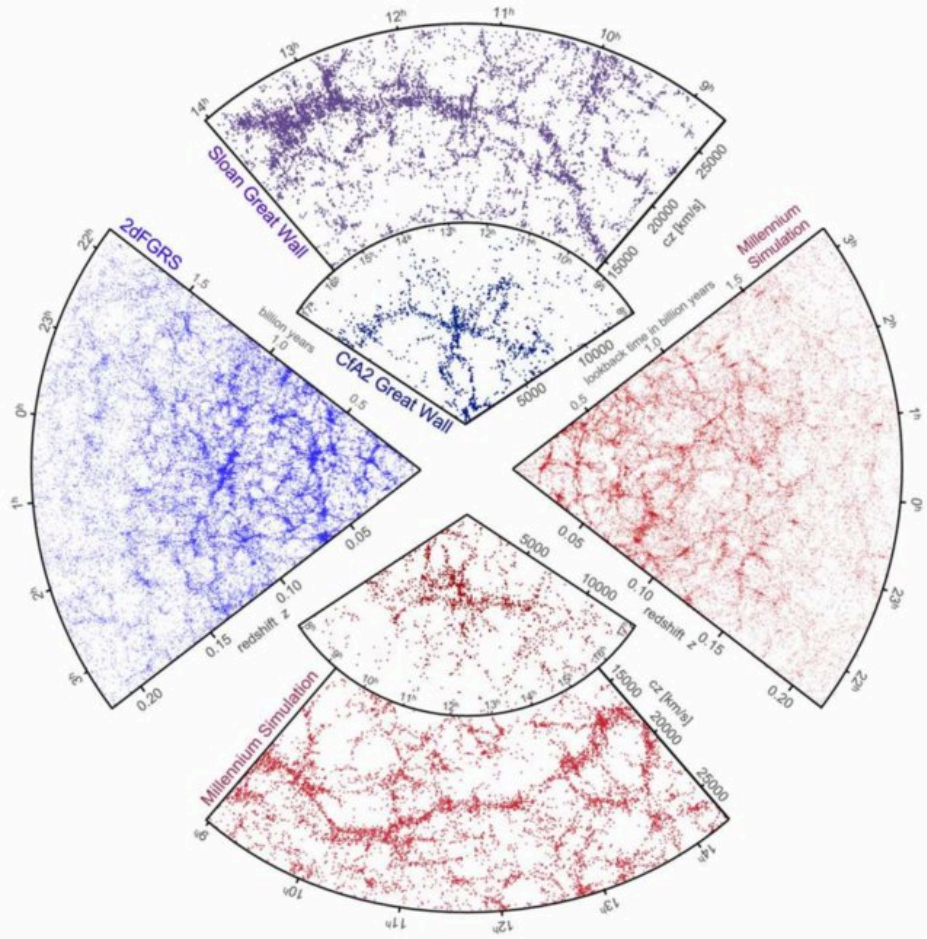

Figure 1.5: Simulated and observed galaxy distribution mocks constructed from the cosmological Millenium simulations (Springel et al., 2005, dark matter only) to mimick the 2 dF Galaxy Redshift Survey (http://www.2dfgrs.net/) and a portion of the Sloan Digital Sky Survey (https://www.sdss.org/). (Credit: Volker Springel)

without being strongly heated.

1.1.2.3 The formation of ellipticals

Elliptical galaxies are primarily found in galaxy groups and clusters, where they formed by merging with other galaxies. Lower-mass ellipticals (not dwarfs) form through major mergers of gas-rich discs (wet mergers) at high-redshifts. Thereby the stellar disc obtains a high-velocity dispersion and can transform into a spheroidal shape, and the perturbed gas can trigger massive starbursts. The merging of two ellipticals (dry mergers, where gas plays a small role) leads to massive ellipticals.

1.1.2.4 Galaxy growth and the mass function

Additionally, to the previous characterisation of the initial mini-halos, the abundance of the halos can be predicted. The Press-Schechter formalism allows for deriving the number den-

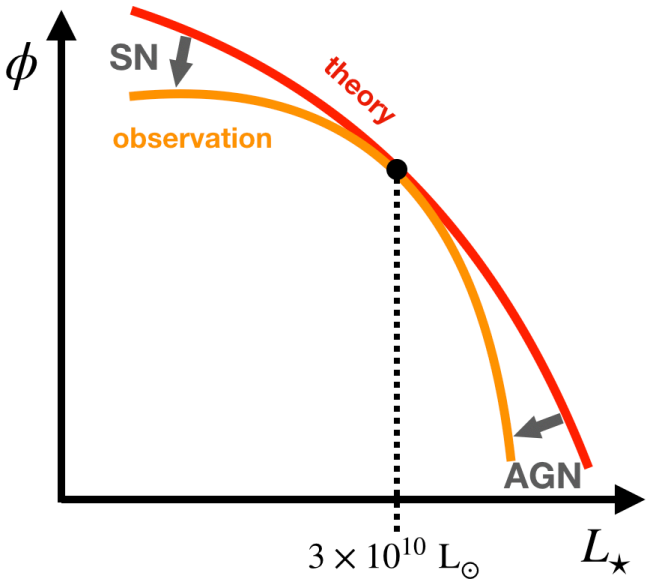

Figure 1.6: Schematical view of the observed (orange line) and theoretically expected (red line) galaxy luminosity function. The discrepencies between the low- and high-mass ends may be solved due to SN and AGN feedback, respectively.

sity of dark matter halos as a function of mass at any redshift. The model assumes a Gaussian random field of density perturbations, a linear gravitational growth, and a spherical collapse (Press & Schechter, 1974). Compared to simulations, the Press-Schechter mass function works reasonably well but predicts too many low-mass halos and too few high-mass halos. Alternatively, simple fit functions have been used that describe the dark matter halo abundance from numerical simulations very well. Since the density profile of dark matter is not directly observable, the comparison with theoretical profiles is not straight forward.

With the help of semi-analytic models[1], one can predict the baryonic component on top of a DM only simulation and by assuming a certain mass-to-light ratio a galaxy luminosity function (a distribution that represents the number of galaxies per luminosity interval) that can be observed (Figure 1.6). However, the stellar mass does not necessarily follow the halo mass, and therefore, their shapes are different. Too many galaxies are predicted at the low and high mass (or luminosity) end. In simulations, these problems can be solved by feedback mechanisms that lower the star formation efficiency on various scales. In massive galaxies, the so-called overcooling problem affects the high mass end of the simulated galaxy population and is addressed by heating the cold gas from AGN (Active Galactic Nuclei) feedback. The suppression of star formation in low mass galaxies is mainly driven by SNe (Supernovae) explosions, which has an only small impact on the formation of massive galaxies. The success of reproducing the observed galaxy luminosity function is the result of improved stellar and AGN feedback algorithms. The outcomes should be interpreted with caution since the feedback processes are complex and not well understood, and the galaxy formation simulations rely on calibrated “subgrid” models.

[1]Semi-analytical models are a statistical approach to predict galaxy properties by considering cosmological hierarchical clustering and physical processes like gas cooling, star formation, feedback, etc...

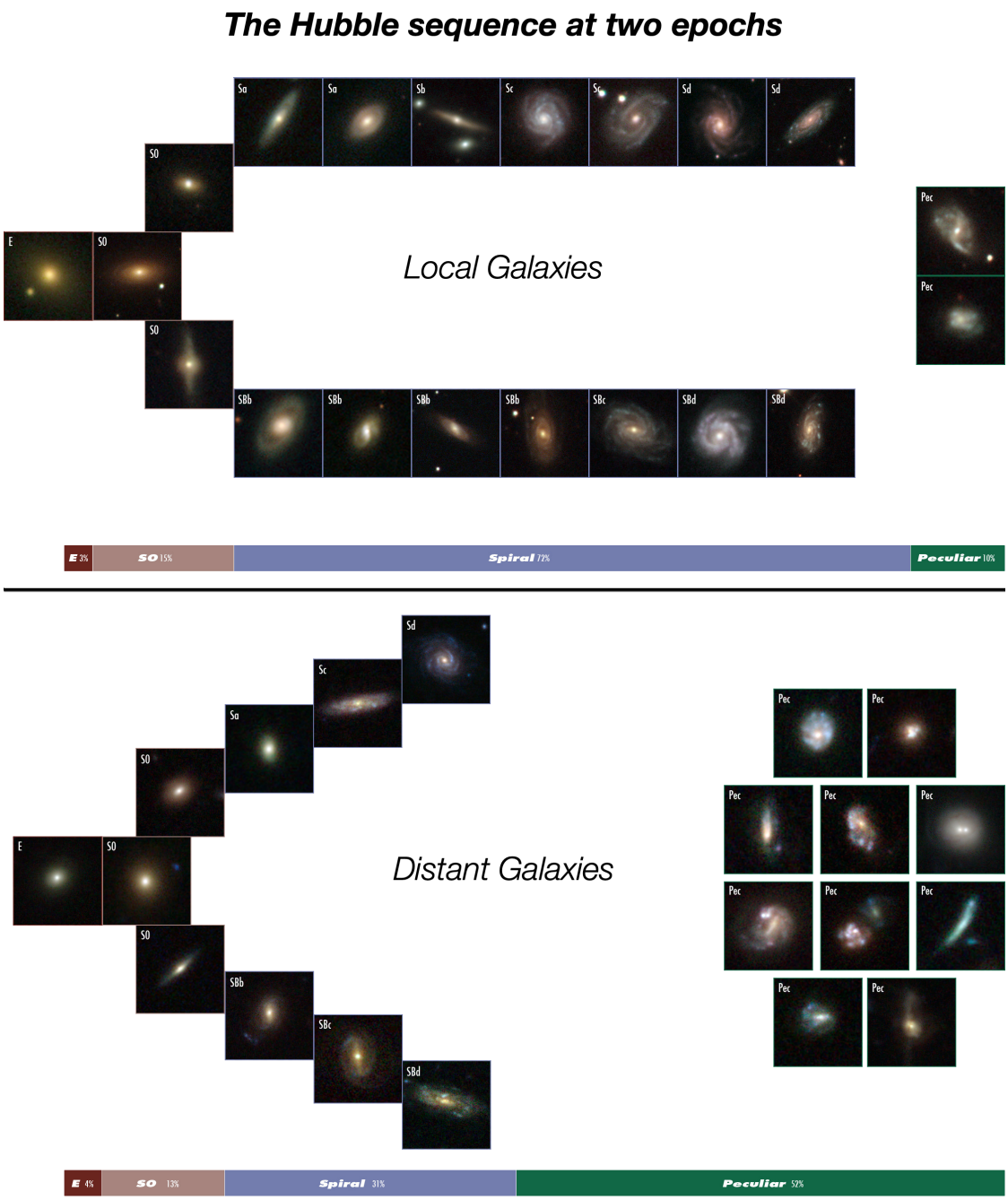

Figure 1.7: The image demonstrates that the Hubble sequence six billion years ago was very different from the one which can be seen today. The two sections show how many more peculiar shaped galaxies (marked Pec) are seen among distant galaxies, as opposed to among local galaxies. The data organisation follows the Hubble tuning-fork classification scheme invented in 1926 by Edwin Hubble.
(Credit: NASA, ESA, Sloan Digital Sky Survey, R. Delgado-Serrano and F. Hammer (Observatoire de Paris), 2010)

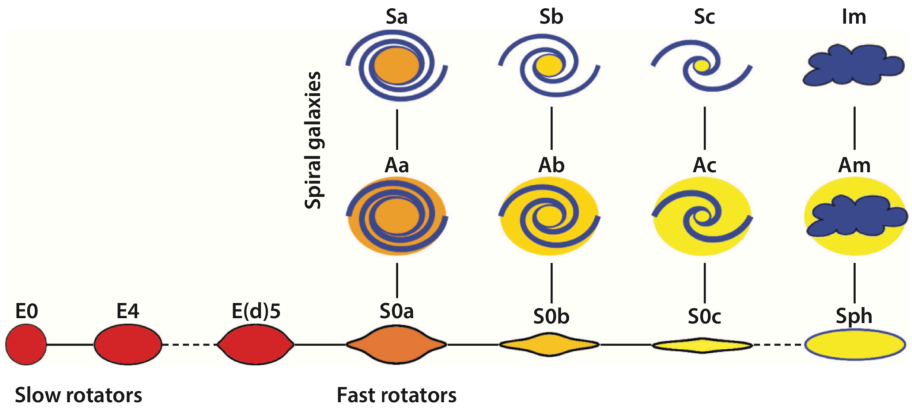

Figure 1.8: Schematic representation of intrinsic galaxy properties, introduced by Emsellem et al. (2007); Cappellari et al. (2011); Cappellari (2016). The early-type galaxies are visualized edge-on. The fast-rotator early-type galaxies (S0s) are flatter and form a parallel sequence to spiral galaxies and span the same full range of shapes. The slow rotators are rounder and have central cores in their surface brightness. The right side of the diagram includes spheroidal (Sph) galaxies which are bulgeless dwarf galaxies, but they are significantly rounder than S0c discs. The diagram includes the class of anemic spirals (Aa–Ac) by van den Bergh (1976). These represent transition objects between the genuine spirals, with obvious large-scale spiral arms and the fast rotators. The black solid lines connecting the galaxy images indicate an empirical continuity, and the dashed lines emphasize a dichotomy between the types. (Credit: Cappellari (2016), Figure 24)

1.2 General galaxy properties over cosmic time

1.2.1 Galaxy types

The galaxy morphology reflects their formation history, tells about their interactions with the environment, about the influence by internal perturbations, AGN activity, their dark matter component. The most commonly used classification system for galaxies is the Hubble sequence (Edwin Hubble in 1926), which divides regular galaxies into three general classes according to their morphological appearance. It is often referred to as the Hubble tuning fork diagram because of its shape. The top image in Figure 1.7 represents the local Universe corresponding to Delgado-Serrano et al. (2010): 3 percent ellipticals (E), 15 percent lenticulars (S0) and 72 percent spirals (S) and the fourth class contains 10 percent irregular or peculiar (Irr/Pec) shaped galaxies. The spirals are subdivided into branches according to their prominence of the disc/arms (Sa to Sd) and the bulge (SBb to SBd). It is intriguing that the "tuning fork" was already present when the Universe was very young. The major difference is that the peculiar shaped galaxies dominate the appearance of the morphology at earlier times and galaxies are in general smaller (see Section 1.2.2). The bottom image in Figure 1.7 represents the fractions of the galaxy types six billion years ago: It is found that 4 percent of distant galaxies were elliptical, 13 percent lenticular, 31 percent spiral and 52 percent peculiar. The abundance of the different galaxy types over cosmic time is more quantitatively described in Section 1.2.2.

The Hubble "tuning-fork" has its limitations, e.g. the arrangement gives the impression

that the S0 galaxies all have large bulge fractions as a transition between the spirals and ellipticals. To distinguish them quantitatively, Emsellem et al. (2007) introduced a new kinematic parameter λ_R, the specific angular momentum of the central stellar component which compares the luminosity-weighted averages of the stellar rotation (ordered motion) with the velocity dispersion (random motion). This parameter divides the early-type galaxies (ETGs = Es-S0s) into slow and fast rotators. In their sample, most are fast rotators that correspond to the elliptical and lenticular types, only a small fraction of the slow rotators are classified ellipticals. With a larger sample of ETGs, the ATLAS^{3D} project (Cappellari et al., 2011) explored the λ_R parameter further. They introduced a revised comb-shaped scheme (Figure 1.8) to illustrate the morphology of nearby ETGs that are composed of two classes with an apparent dichotomy in stellar mass (Cappellari, 2016). Slow rotators, are elliptical-like objects with intrinsic ellipticity $\epsilon \leq 0.4$ that dominate $M_{\rm crit} > 2 \times 10^{11} M_\odot$. Fast rotators are generally flatter than $\epsilon \geq 0.4$ and have masses below $M_{\rm crit} < 2 \times 10^{11} M_\odot$. They have morphologies similar to the spirals (with dust removed). They span the same range of bulge sizes of the spirals. Integral field spectroscopy (IFS) and redshift evolution studies consistently and independently indicate two evolutionary paths. The fast-rotator ETGs begin as star-forming discs and evolve through gas-accretion, bulge growth and quenching. Whereas the slow-rotators assemble near the centers of massive halos via high star formation at high-z and remain as such and evolve via gas poor mergers (dry-merger) (Schulze et al., 2018).

Future surveys will be extended to cover the whole sky and the high-redshift Universe with better spatial resolution, to study the morphology of much more galaxies and enhance the understanding of galaxy evolution.

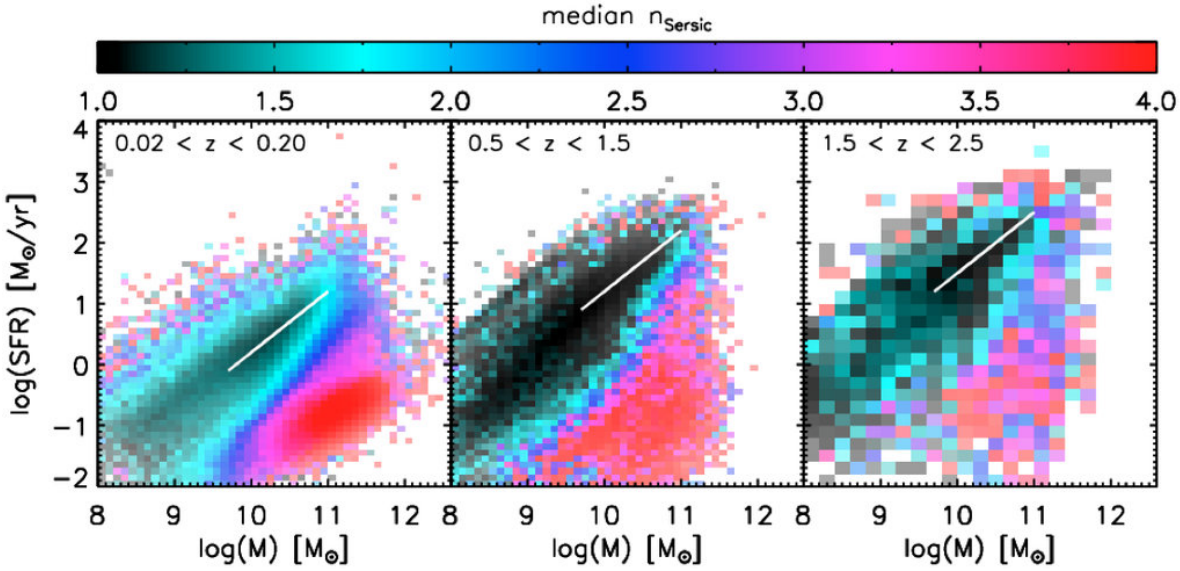

Figure 1.9: Surface brightness profile shape as described by the Sèrsic index in the SFR-mass plane in three different redshift bins. SFGs make most of the galaxies and are characterised by exponential discs, quiescent galaxies at all epochs are better described by de Vaucouleurs profiles. The active galaxies are well approximated by a constant slope of 1 (main sequence) and the SFR increases at a given stellar mass with lookback time (white line). (Credit: Wuyts et al. (2011), Figure 1)

1.2.2 Galaxy activity and growth

By relating the general two galaxy morphologies with their stellar content and star formation activity, a more global bimodality of the Hubble sequence becomes apparent. Exponential disc like galaxies (spirals and irregulars) are active and star-forming (blue on the color-magnitude diagram), while elliptical galaxies are referred to as passive galaxies (red on the color-magnitude diagram). This is clearly evident in the study of (Wuyts et al., 2011), see Figure 1.9 where the morphology is characterized by the Sèrsic index of the surface brightness profiles (n=1 for exponential profiles, n=4 for ellipcticals with the De-Vaucouleurs-profile). The histograms in three redshift bins illustrate that most of the galaxies are SFGs and follow a linear relationship in the Log(SFR) – Log($M_\star$) plane, called the "Main Sequence of Star-Forming Galaxies" with increasing activity going towards the distant Universe. More recent studies e.g. Lee et al. (2015) (see Figure 1.10) illustrate that the power law between SFR – $M_\star$ has a similar slope at all z and is only apparent for lower stellar masses. The relationship begins to flatten for higher masses $M_\star > 10^{10}$ $M_\odot$, while the details of the "bending" are still debated (Popesso et al., 2019).

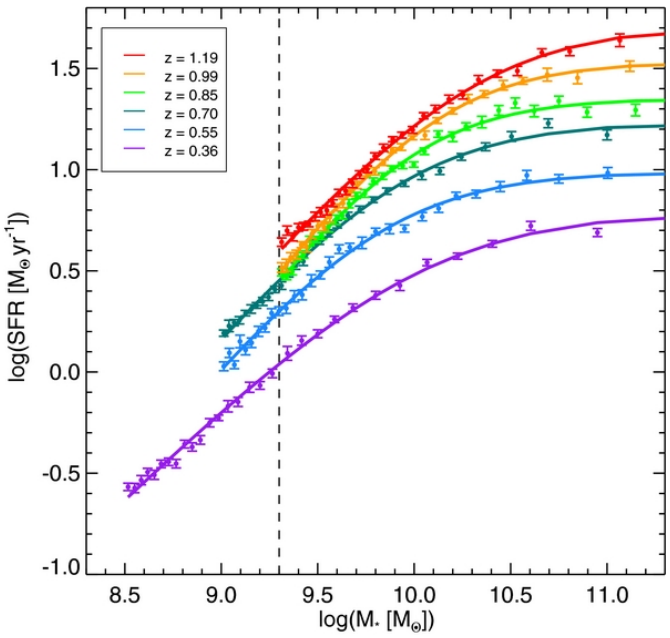

Figure 1.10: Median SFR in six equally populated redshift bins that have been split into 30 equally populated stellar mass bins. The Solid lines represent the best-fit curve. (Credit: Lee et al. (2015), Figure 5)

The growth of the SFGs and and the continuous star formation through cosmic times is sustained by the supply of gas from the cosmic web and by minor mergers that maintain large gas reservoirs for star formation (e.g. Kereš et al., 2005; Dekel et al., 2009), see also Section 1.2.3. The SFGs and quiescent galaxies follow very different size-mass (effective radius) relations over redshift. In van der Wel et al. (2014), 30,958 galaxies are separated into early- and late-type galaxies based on their star formation activity. ETGs are found to be on average smaller than LTGs at all redshift. High-z galaxies are substantially smaller than equally massive, present day counterparts. LTGs are smaller by a factor of two at z=2 and

massive ETGs by a factor of 4. One interpretation of the different growth rate is that the SFGs build-up their stellar component at all radii, whereas quiescent galaxies grow inside-out through accretion (e.g. van Dokkum et al., 2015).

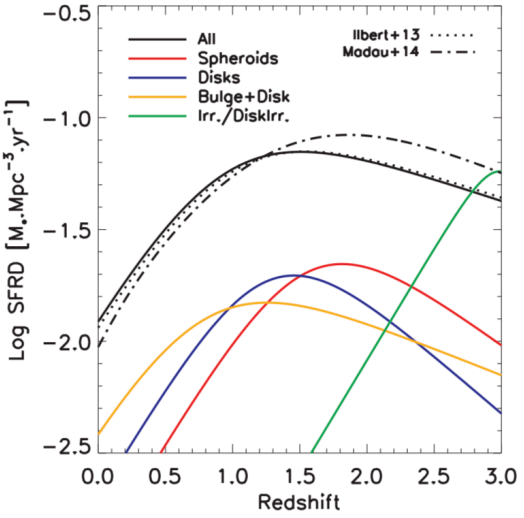

(a)

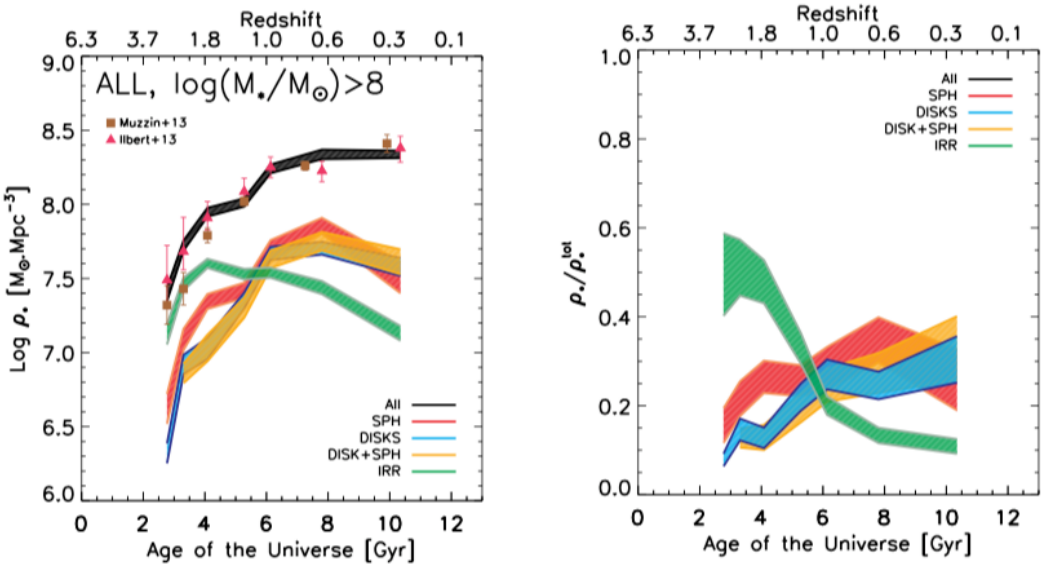

(b)

Figure 1.11: (a) The history of cosmic star formation (SFH). The black solid line shows the global sample and the different colours the SFHs of different morphologies (Credit: Huertas-Company et al. (2016), Figure 8). The black dash–dotted line corresponds to FUV+IR rest-frame measurements by Madau & Dickinson (2014). (b) Evolution of the stellar mass density for galaxies with $\log(M_\star/M_\odot > 10^8)$ $M_\odot$ (left plot). Full sample of 50,000 star-forming and quiescent galaxies. The colors correspond to different morphologies as labelled. The right plot are fractions. The pink triangles and brown squares are measurements from different studies (Credit: Huertas-Company et al. (2016), Figure 5 (left panel)).

A very fundamental observable is the cosmic star formation rate density (SFRD) (Madau & Dickinson, 2014) which peaked ~ 3.5 Gyr after the Big Bang ($z \sim 2$) and declined exponentially at z < 1 (see Figure 1.11a, dash-dotted line). The Universe was much more active in the past, where stars formed with a ~ 9 times higher rate than observed today. From z=2 to present day, most of the stars formed in galaxies along the main-sequence, suggesting the evolution is determined by a balance between gas accretion from the cosmic web and feedback processes which are related to the galaxy mass. Merger-driven starbursts play only a minor role. The contribution from the different galaxy types to the stellar mass density (SMD) and the SFRD (Figure 1.11a) over cosmic time is more quantitatively studied in (Huertas-Company et al., 2016), where they used a sample of 50,000 galaxies. They distinguish between compact spheroids, spiral discs, discs with a bulge component and irregular or disturbed galaxies (Figure, 1.11b). At z > 2 more than 70% of the stellar mass density (SMD) are in irregular galaxies and make up 80% of the star-forming galaxies. Their amount decreases dramatically over time and by $z \sim 0.5$ the irregular objects only dominate for $M_\star < 10^9\ M_\odot$. Regular discs emerge between z=1-2 and begin to dominate by $z \sim 1$, which implies the hypothesis that the star-forming galaxies undergo a gradual transformation from disturbed to spiral galaxies. At z > 2, 30% of the SMD is in compact spheroids and at z < 1 the SMD is equally distributed among discs, spheroids and mixed systems.

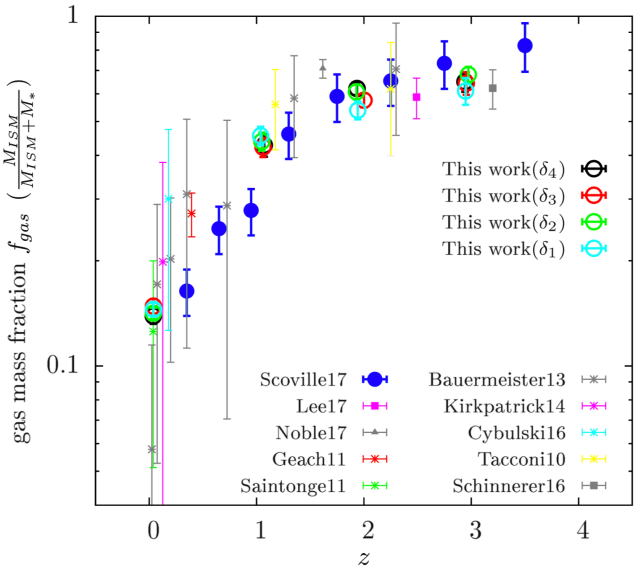

Figure 1.12: Redshift evolution of the gas mass fraction $f_{\rm gas}$ in different environmental density quantiles (empty circles), along with cluster and field quantities in the literature (shown for reference). $f_{\rm gas}$ in different environmental density bins show an independence of the environment. The gas mass fraction decreases with decreasing redshift and the data points nearly follow the overall decline in $f_{\rm gas}$ with cosmic time. (Credit: Darvish et al. (2018), Figure 3)

1.2.3 Gas fractions and star formation

The observed evolution of the gas fraction and its associated depletion time in main-sequence (MS) galaxies provides insights on how star formation proceeds over cosmic time. The star formation correlates strongly with cold (T = 10-30 K) molecular gas (n(H2) = 10^2 – 10^5 cm^{-3}) and only little with neutral atomic hydrogen (Kennicutt, 1989; Kennicutt et al., 2007; Bigiel et al., 2008, 2011; Leroy et al., 2008, 2013; Schruba et al., 2011). The molecular gas content probed by the CO proxy suggests a higher gas mass fraction in main-sequence SFGs at high-z (e.g. Tacconi et al., 2018). However, it is difficult to get a large sample size, since CO observations are very time-consuming (hours long exposure). The CO measurements are robustly converted into molecular gas estimates (Genzel et al., 2015, Tacconi et al. 2018), but see also Carilli & Walter (2013). An alternative and faster way (minute long exposures) is to use the long-wavelength Rayleigh-Jeans dust continuum emission, which is nearly always optically thin, providing a direct probe of the total dust and hence the dust-to-gas abundance ratio can be constrained (Scoville et al., 2014). This method is applied to a large sample in Darvish et al. (2018) and Figure 1.12 shows the resulting redshift evolution of the gas fraction which decreases with decreasing redshift, independent of the environment.
The star formation rates derived from observations imply that the gas content should be consumed on relatively short time scales. In the local Universe the gas depletion is longer and less than a few Gyrs (Kennicutt & Evans, 2012; Leroy et al., 2013; Bigiel et al., 2011; Schiminovich et al., 2010), whereas at high redshift (z > 2) it is shorter and less than a Gyr (e.g. Genzel et al., 2010; Daddi et al., 2010; Tacconi et al., 2013). Since SFGs reside on the MS of galaxies with a much longer period, the need for ongoing gas accretion is evident. The molecular gas to stellar mass ratios and the sSFRs (specific star formation rates) as a function of redshift track each other closely, which implies a higher rate of accretion at early times and may be a key in regulating a galaxy's SFR rather than changes in the galaxy scale star formation efficiency (Santini et al., 2014; Genzel et al., 2015; Scoville et al., 2016).

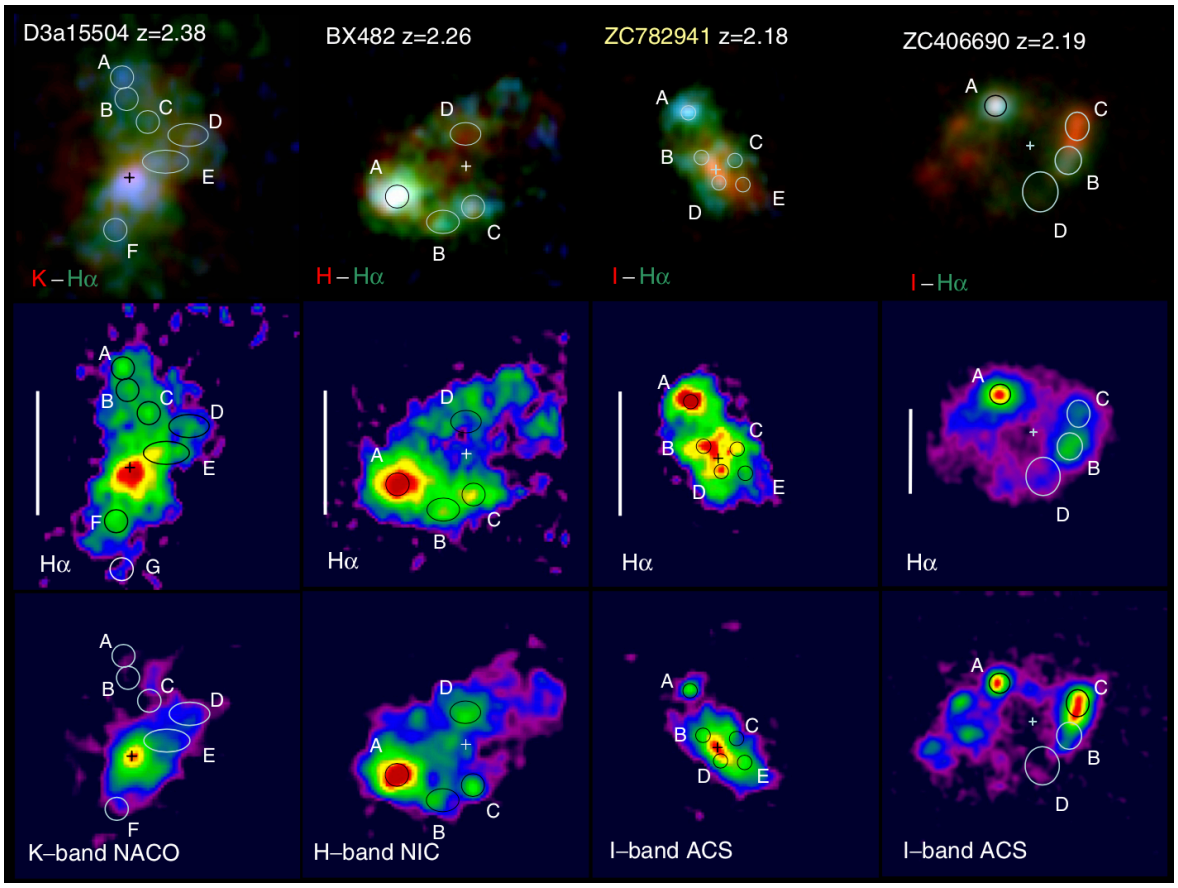

Figure 1.13: Hα and rest-frame UV/optical continuum images of four massive star-forming galaxies at z≃2. The most prominent identfied clumps are labeld by A, B, C, D. Top row: three-color composites of integrated Hα line emission (red), and continuum (blue–green) images. Middle: integrated Hα emission. The vertical bar marks ~8.4 kpc spatial scale. Bottom: *HST* NIC *H*-band, ACS *I*-band, or NACO-VLT AO K_s-band images of the program galaxies, at about the same resolution as the Hα maps. The color scale is linear and autoscaled. (Credit: Genzel et al. (2011), Figure 2)

1.3 Structure formation and internal galaxy properties at high-redshift

A key feature of observed irregular star-forming galaxies is that they contain kpc-sized clumps (one to several) with masses of $10^8 - 10^9$ $M_\odot$. In the Cosmic Assembly Near-IR Deep Extragalactic Legacy Survey (CANDELS; Grogin et al., 2011; Koekemoer et al., 2011) over 250,000 distant galaxies from z = 8 to 1.5 are documented, where more than half of the star-forming galaxies are clumpy (Bournaud, 2016, and references therein). Giant clumps are identified in Hα, which traces hydrogen that is ionised by massive young stars (Genzel et al., 2008, 2011) and therefore, probe star-forming regions (Figure 1.13). The clumps also appear in CO-line observations from which the molecular gas is inferred (Tacconi et al., 2013). Furthermore, giant clumps are found in the restframe-UV stellar light (Guo et al., 2015), see Figure

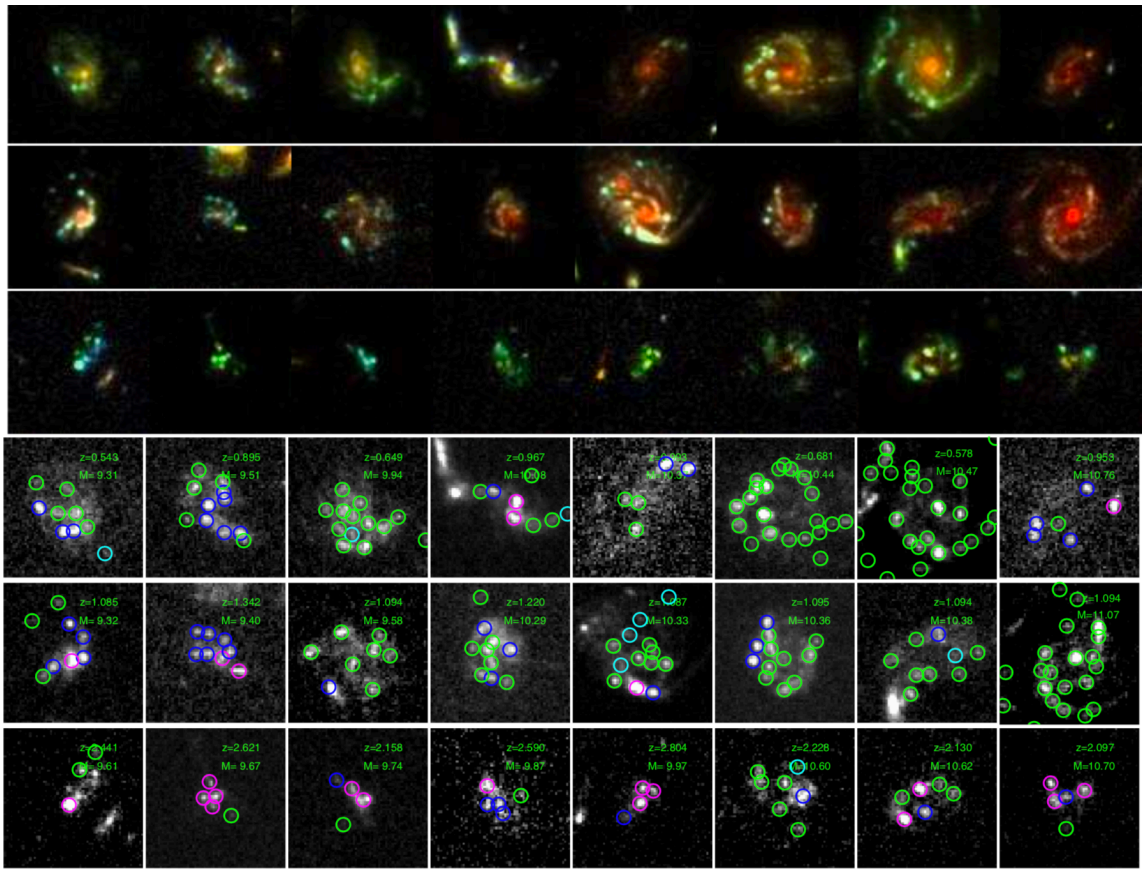

Figure 1.14: Examples of clumpy galaxies and identified blobs of *HST*/ACS and WFC3 images in the CANDELS/GOODS-S and UDS fields. The first three rows show the composite RGB images made by the F435W, F606W, and F850LP images of the galaxies. The last three rows show the same galaxies in the images used to detect blobs (circles). The redshift and stellar masses $M_\star$ of each galaxy are labeled. For each row, the $M_\star$ increases from the left to the right, while the redshift increases from the top to the bottom row. Note that the image scales of the first three rows are different from those of the last three rows. (Credit: Guo et al. (2015), Figure 4)

1.14, which is emitted by hot, young stars in their early or late evolutionary stages. In the restframe-optical wavelengths, they are relatively inconspicuous (Elmegreen et al., 2007) and nearly absent in the stellar mass distribution (Wuyts et al., 2012). From the estimated stellar ages, the deduced clump ages are between 10 to several 100 Myr (Förster Schreiber et al., 2011b; Wuyts et al., 2013; Zanella et al., 2015; Guo et al., 2018; Zanella et al., 2019). This indicates longer life-times of clumps that can persist stellar feedback and therefore, have enough time to migrate to the centre via dynamical friction and gravity torques caused by structures within the disc (Immeli et al., 2004a,b; Bournaud, Elmegreen & Elmegreen, 2007; Bournaud et al., 2014; Ceverino, Dekel & Bournaud, 2010; Mandelker et al., 2014). Clumps appear gravitationally bound, inferred from their masses and velocity dispersions e.g., (Elmegreen & Elmegreen, 2005; Genzel et al., 2008). Furthermore, a strong trend is found between ionised gas outflow rate an the star formation rate surface density. The mass outflow rates inferred

for the discs above this threshold are comparable to the star formation rates (and up to several times higher for bright clumps), implying that the outflows can efficiently drive large amounts of gas outside of the galaxies.

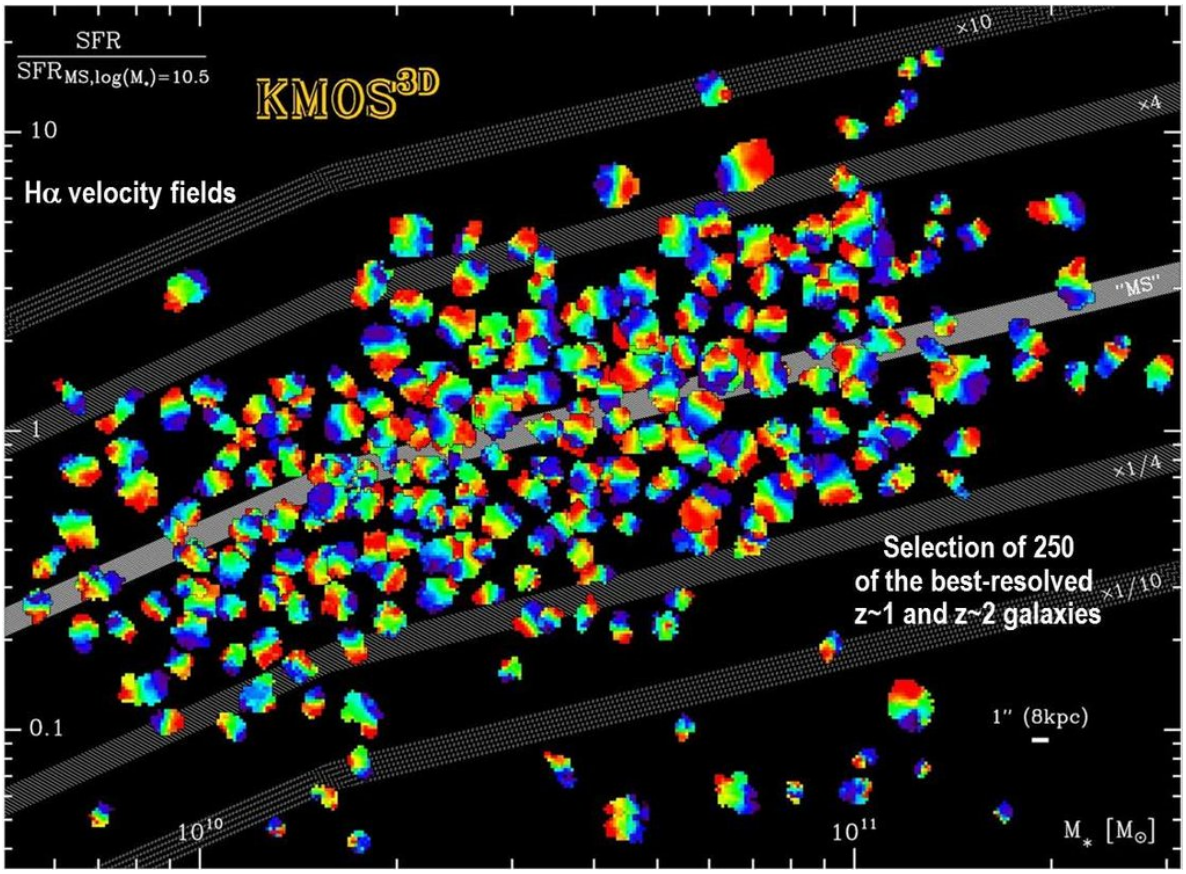

Figure 1.15: KMOS Hα velocity fields of the resolved KMOS^{3D} galaxies at their approximate locations in the SFR – $M_\star$ plane for the z ~ 1 and z ~ 2 samples. The solid line shows the canonical main sequence ("MS") at z ~ 1 and z ~ 2, respectively. The dashed and dotted lines show this main sequence scaled up or down by factors of ×4 and ×10, respectively. All sources are shown on the same angular scale, as denoted by the 1" scale bar at the bottom right of the plots. (Credit: Combined image from Wisnioski et al. (2015), Figure 5)

1.3.1 The origin of giant clumps

In observations most of the giant clumps in high-redshift galaxies appear typically younger than expected from small external galaxy companions (Förster Schreiber et al., 2011b; Wuyts et al., 2012; Elmegreen et al., 2009). In Zanella et al. (2019) they investigated the contribution of clumps and satellites to the galaxy mass assembly in 53 star-forming galaxies at z ~ 1 – 3. 30% of the identified objects are likely accreting satellites that make up to ~ 80% of the stellar mass of the host galaxy. The identified satellites are found on average at larger distances from the galaxy barycenter and are typically larger, more massive and older than the objects, recognised as in-situ clumps. The detected objects, identified as giant clumps

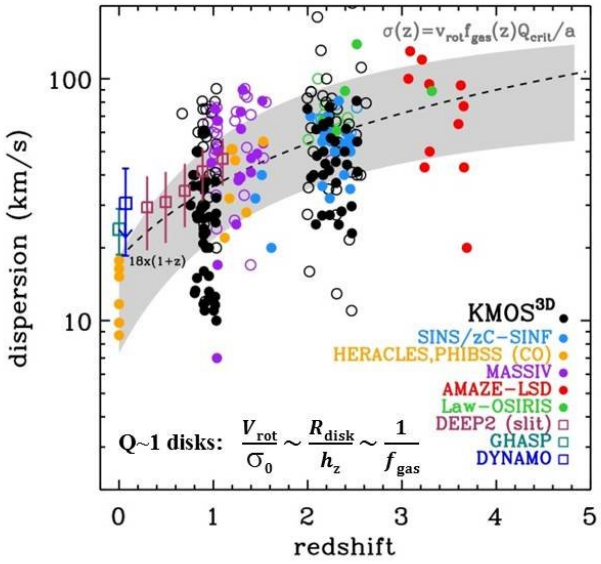

Figure 1.16: Galaxy velocity dispersion measurements from the literature at z = 0–4 from molecular and ionized gas emission (including IFS and long-slit). KMOS^{3D} measurements at z ~ 1 and z ~ 2 are shown by black circles. Filled circles represent disc galaxies or "rotators," open circles represent all other kinematic categories. Open squares are averages of surveys at z ≤ 1. Sources for the literature data are given in Section 5. The dashed line shows a simple (1 + z) evolution scaled by a factor of ×18 to overlap with the data. The gray band is described by $\sigma_0 = v_{rot}\ Q_{crit}\ f_{gas}(z)/a$ where $f_{gas}(z)$ is the gas fraction as a function of redshift (see Wisnioski et al. (2015)), $Q_{crit} = 1$ and $a = \sqrt{2}$ for a $\log(M_\star) = 10.5$ disc with constant rotational velocity. The upper and lower boundaries of the curves are defined by $v_{obs} = 250$ and 100km s^1 , respectively. (Credit: Combined image from Figure 8 + 10 in Wisnioski et al. (2015))

appear typically younger than the underlying disc but with a similar metallicity, implying an in-situ origin (~ 20% of the galaxy's stellar mass). Indeed, in the cosmological zoom-in simulations (Mandelker et al., 2014), only a limited fraction of the clumps are resulting from the accretion of small companions or external gas clumps.

In fact, the peculiar high gas fractions and kinematic features can explain the in-situ fragmentation via gravitational disc instability, expressed by the Toomre Q-parameter (Toomre, 1964). In the KMOS^{3D} survey a majority of the star-forming galaxies (Wisnioski et al., 2015) show smooth rotation velocity in Hα (Figure 1.15), indicating a disc with no dynamical evidence of having had a recent major merger. Furthermore, the velocity dispersion of the ionised and molecular gas (Wisnioski et al., 2015; Übler et al., 2019) is increasing significantly at higher redshift ($\propto 1 + z$), see also 1.16. The observed high gas densities and high random motions can lead to kpc-sized growing perturbations and the discs fragment into massive star-forming clumps if the Q-parameter is below a critical value $Q < Q_{crit}$ (Genzel et al., 2008; Dekel, Sari & Ceverino, 2009a). Indeed, observations indicate an average Q-parameter around marginal stability over cosmic time (Wisnioski et al., 2015), or lie below the critical value (Tadaki et al., 2018). Locally, substantial deviations are expected for Q,

with smaller values inside giant clumps and larger values in the intermediate regions (Genzel et al., 2011). Theoretical models have been very successful in explaining or simulating many observed properties via gravitational disc instability by using isolated discs or in a cosmological context with higher resolution (e.g. Noguchi, 1999; Immeli et al., 2004a; Bournaud, Elmegreen & Elmegreen, 2007; Bournaud et al., 2014; Ceverino et al., 2012), see also Section 1.4.

1.3.2 Rotationally supported clumps?

In the $z \sim 2$ observations of massive galaxies in Genzel et al. (2011) the clumps leave a modest imprint on the gas kinematics. Velocity gradients are found in the residual maps across the clumps with 10-40 km s^{-1} kpc^{-1} (Figure 1.17). When considering the beam-smearing effects and clump sizes these gradients may be consistent with significant rotational support, or in extreme cases they are pressure supported by high-velocity dispersion or they are still undergoing collapse because of the small velocity gradients. In the simulations of Ceverino et al. (2012), the rotationally supported clumps formed via gravitational disc instability. An analytical model explains the rotation, where a proto-clump is originating from a rotating disc and collapses to equilibrium while preserving angular momentum. In their cosmolog-

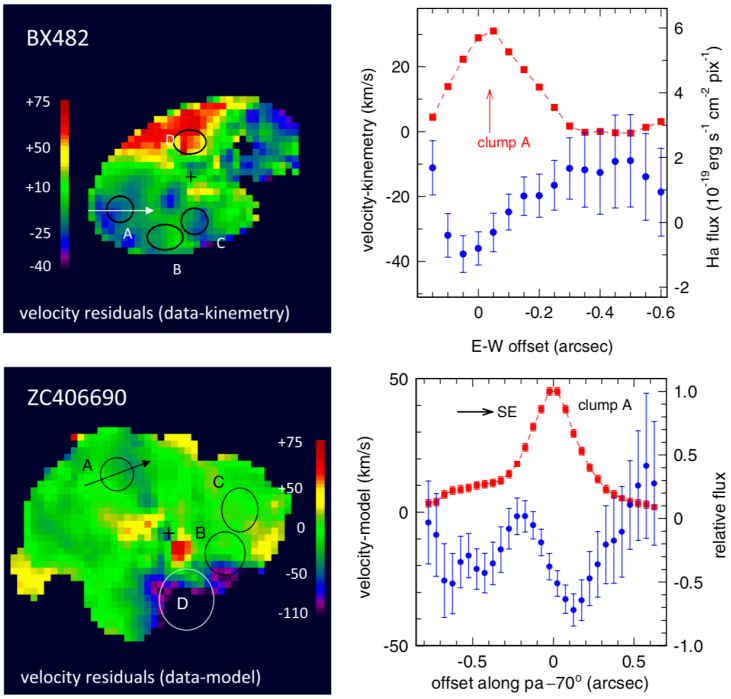

Figure 1.17: From Genzel et al. (2011), Figure 11: Velocity residual maps and position–velocity residual cuts across the brightest clump A in BX482 (top) and ZC406690 (bottom). The left panels are the residual maps (velocity (data) minus velocity (model or kinemetry)), the right panels give position–velocity residual cross-cuts across the brightest clumps in each galaxy, along the direction of the galaxy's maximum velocity gradient (line of nodes). The red points and dashed curve denote the Hα flux (right vertical axis) and the blue points and continuous curve denote the residual velocity (left vertical axis).

ical simulations, a clump rotation velocity is typically more than twice the disc dispersion ($V_{rot} \sim 100$ km s^{-1}). By adapting the limitations of high-z observational resolutions (applying beam smearing), the rotation signal is reduced to a small gradient of ≤ 30 km s^{-1} kpc^{-1} across the clump. Unfortunately, only a beam of FWHM = 0.8 kpc was applied, that is around two times better than the resolution in the observations of Genzel et al. (2011), implying that with a larger beam smearing, the clumps will increase its size significantly and the velocity gradient will disappear.

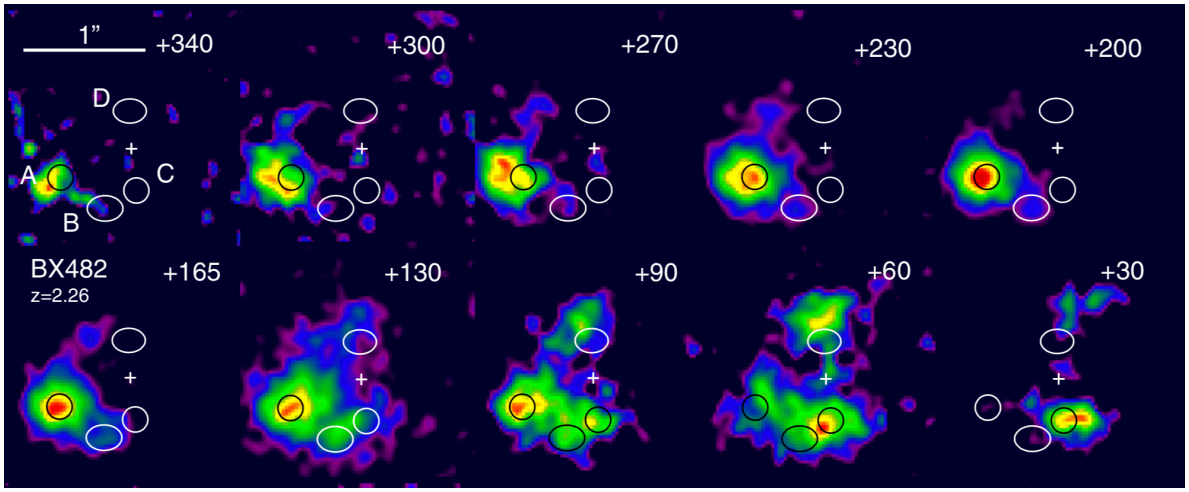

Figure 1.18: Adapted from Genzel et al. (2011), Figure 1: Maps of individual velocity “channels” of width ~ 34 km s^{-1} in the Hα line of the high-z galaxy BX482. Velocities relative to the systemic redshift indicated are given in km s^{-1}. Circles/ovals and symbols denote the clumps identified in these galaxies. Crosses denote the kinematic centers of the galaxy rotation. The color scale is linear and autoscaled to the brightest emission in each channel. An indication for a substructure can be identified for the clump A from the different maps.

1.3.3 Evidences for a giant clump substructure

Currently, for observations at z ~ 2 the spatial resolution is limited to ~ 1-2 kpc. One hint for a possible substructure on sub-kpc scales of a bright clump has been found in the seminal work of Genzel et al. (2011), by studying the clump gas kinematics of Hα and comparing the individual velocity channel maps (see Figure 1.18). The effect on clump properties due to different observational resolution is evident in the recent study of a strong gravitationally lensed massive galaxy ($M_\star \sim 4 \times 10^{10}$ $M_\odot$) “the cosmic snake” (Cava et al., 2018) and the comparison to its counter image (see Figure 1.19). With the SFR ~ 30 M$_\odot$ yr^{-1} it is comparable to galaxies on the main sequence at z ~ 1 - 2. Furthermore, the identified clump masses and sizes tend to correlate with the different magnifications of the images, giving 10^7 M$_\odot$ at high magnification (~ 30 pc resolution) and several 10^8 M$_\odot$ at low magnification (~ 300 pc resolution). Another possibility to study how the sub-structure clumps cluster to giant objects are the extremely rare local clumpy galaxies (see Figure 1.20) whose properties are similar to those of high-redshift discs (Fisher et al., 2017), found in a sub-sample of the DYNAMO-HST survey with massive galaxies of $M_\star \sim 1 - 5 \times 10^{10}$ M$_\star$, which correspond to galaxies that dominated the cosmic SFR at z ~ 1 - 3. In their degraded high-redshift maps

(taking blurring, surface brightness dimming, and a sensitivity cut similar to high-z observations with adaptive optics into account) the number of clumps is significantly reduced to 1-4 clumps per galaxy comparable to the amount of clumps detected in high-z surveys (Genzel et al., 2011; Swinbank et al., 2012; Wisnioski et al., 2012). DYNAMO clumps have diameters spanning the range ~ 100–800 pc. The limited sensitivity may also restrict the observations to more massive clumps within a galaxy as was shown in Tamburello et al. (2017) by Hα mocks created by radiative transfer postprocessing of a clumpy galaxy simulation.

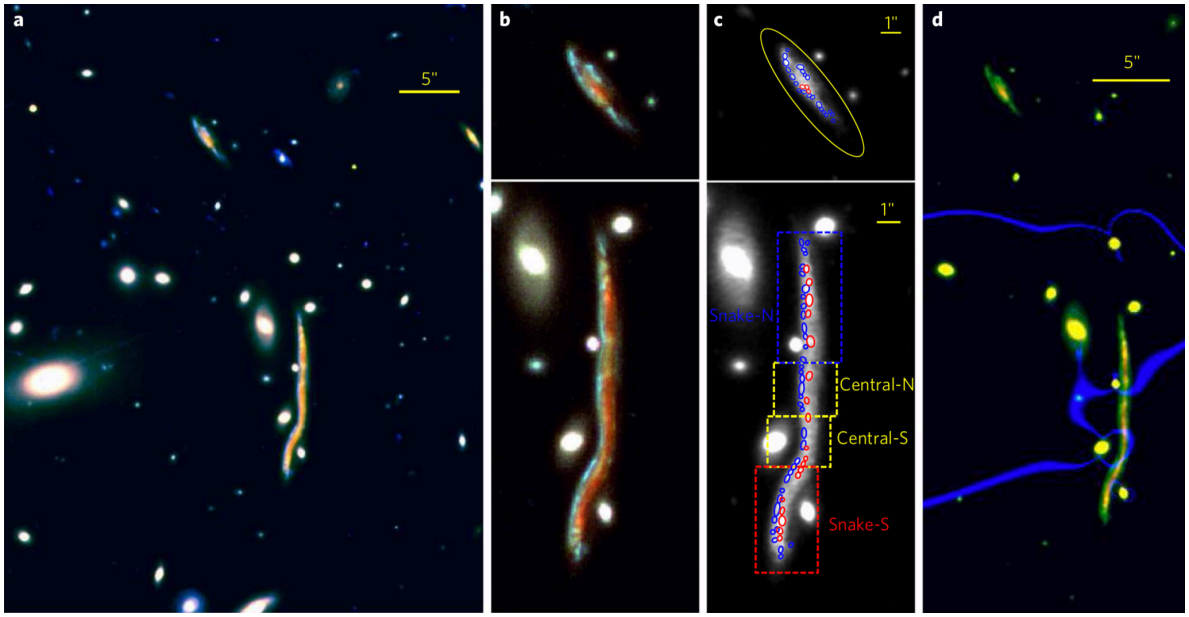

Figure 1.19: Overview of the cosmic snake and the counterimage: (a) A portion of the Hubble Space Telescope field of view showing an RGB colour composite image (R = F160W, G = F110W and B = F606W) of the galaxy cluster MACSJ1206.2-0847 including the giant arc (dubbed the cosmic snake) and its counterimage. (b) A magnified view of the cosmic snake (bottom) and the counterimage (top). (c) An image of the cosmic snake (bottom) and its counterimage (top) with regions defined as clumps (blue regions for blue clumps, red regions for red clumps, and yellow for the whole galaxy). Rectangular areas define the four portions of the cosmic snake (corresponding to multiple images); see main text for full definitions and explanations. (d) RGB composite image including: R = F160W, G = F110W, B = amplification map. For the fiducial lensing model, blue shaded areas indicate amplification above 100, close to the critical lines. Representative scale bars are provided in each panel (same scale for b,c). (Credit: Cava et al. (2018), Figure 1)

A rich sub-structure is currently only found in isolated disc simulations that fragment due to gravitational disc instability under very high resolution < 10 pc (Ceverino et al., 2012; Bournaud et al., 2014; Bournaud, 2016; Behrendt, Burkert & Schartmann, 2015, 2016; Behrendt, Schartmann & Burkert, 2019). Furthermore, recent simulations show a few small clumps forming due to non-axisymmetric instabilities, that can appear as a giant and more massive object by accounting for a limited observational resolution (Tamburello et al., 2017; Benincasa et al., 2019).

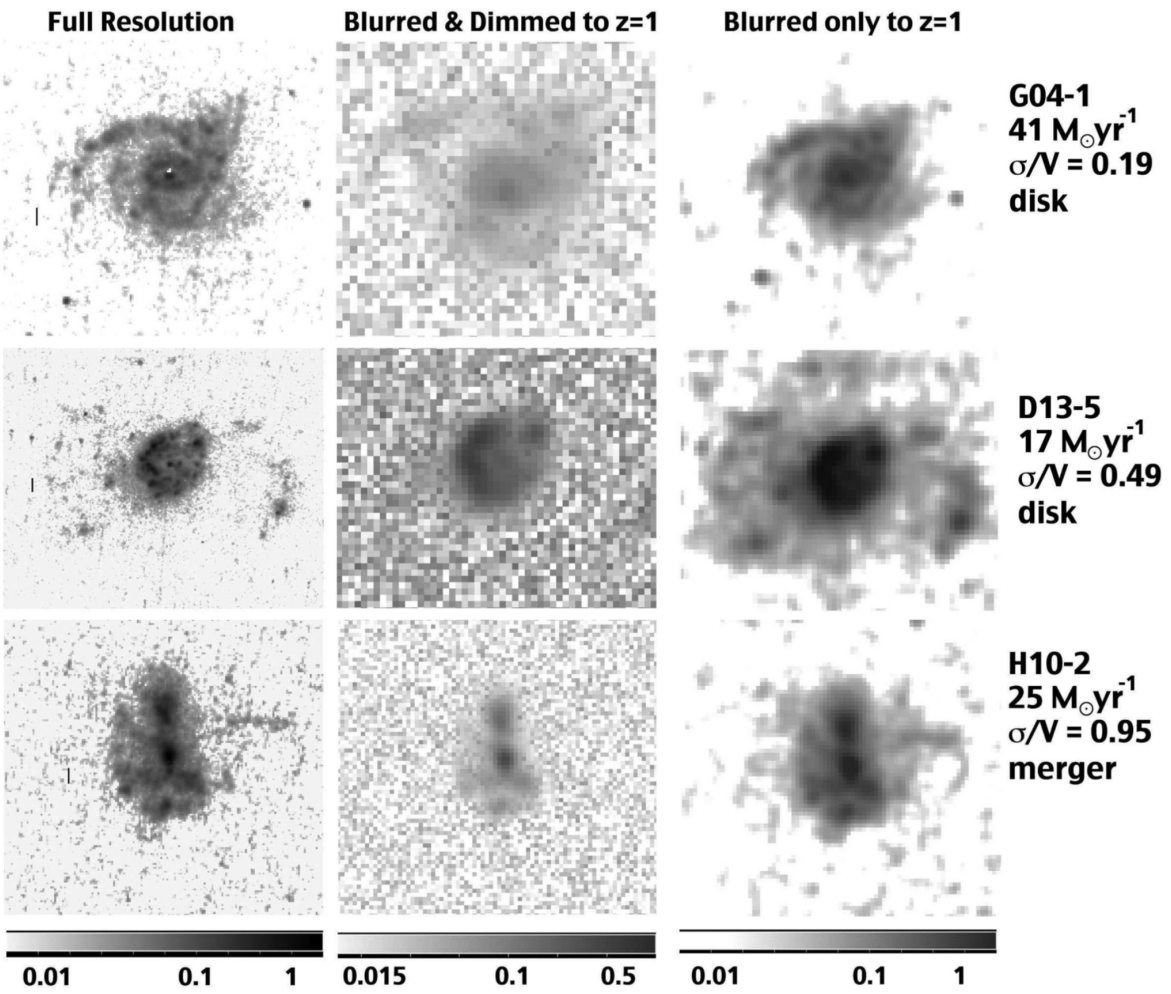

Figure 1.20: Adapted from Fisher et al. (2017), Figure 3: The continuum subtracted Hα+[NII] maps for the DYNAMO sample galaxies are shown. Left-hand column shows full resolution maps. The middle column shows maps that have been degraded to simulate z ~ 1 observations with blurring, surface brightness dimming, and a sensitivity cut similar to high-z adaptive optics observations. The right-hand column shows only the effect of blurring maps to match z ~ 1 resolution. The FWHM of the blurring corresponds to 1.6 kpc and pixel size 0.8 kpc. The colour bar shows the units of flux in 10^{-18} erg s^{-1} A^{-1} cm^{-1}. Also the galaxy name, total star formation rate (SFR), σ/V, and optical morphological classification is listed on the far right. A black line is plotted in each panel indicating 1 kpc. The DYNAMO sample shows clumpy structures on the scale of a few hundred parsecs.

1.4 The current work

In galaxy formation simulations, an extreme dynamic range is involved (Faucher-Giguère, 2018). Different approaches are used to focus on different parts of the involved processes. In cosmological simulations, large volumes on Mpc scales and low spatial resolution provide statistics based on samples of many galaxies. They follow the coupled dynamics of dark matter and baryons starting from the ΛCDM initial conditions. The newest generation of

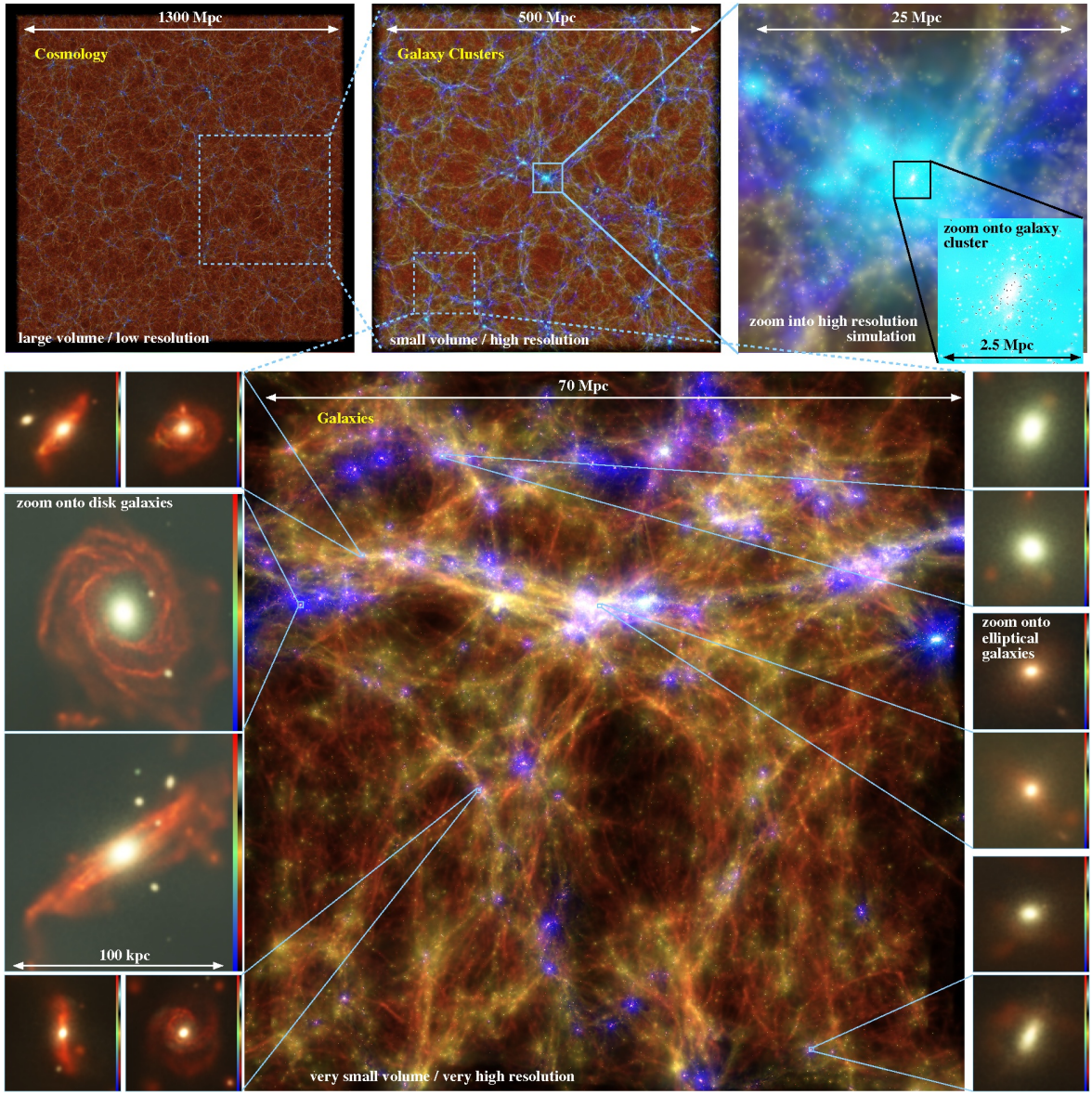

Figure 1.21: The different boxes of Magenticum Pathfinder as overview. Zooming from the largest scales (GPc scales) into galaxy clusters (Mpc scales) and even further down onto individual galaxies (tens of kpc scales). (Credit: Dolag et al. (2015); Teklu et al. (2015); Magneticum (2019). Simulation code: Gadget-3, Vizualisation code: Splotch)

cosmological simulations are starting to resolve the internal structure of disc galaxies, like spiral arms (see Figure 1.21). However, only zoom-in simulations and high-resolution simulations of isolated disc galaxies are currently able to resolve the clumpy structure that is found in high-redshift observations. In the following chapters, we make a small step towards understanding the nature behind the observed giant clumps and its possible sub-substructure by using isolated disc galaxy simulations with very high resolution. We study the gravitational disc instability in greater detail that can develop in gas-rich galaxies and lead to the creation of clumps and the peculiar properties. The well-defined conditions of the disc-setup reduce

the complexity that is involved in cosmological simulations. Our approach allows for capturing the effects of self-gravity and hydrodynamics of the structure formation robustly. In Chapter 3, we revisit the linear perturbation theory and study in detail how the perturbations grow in a simulation over time and finally collapse. Chapter 4 compares the simulated substructure with observations in great detail. Chapter 5 addresses the clump properties in high and low-resolution simulations and their relation to the artificial pressure floor. Furthermore, we investigate hierarchical scales that can emerge under different observational resolution.

Chapter 2

Numerical methods

Numerical modeling plays an important role in astrophysics. It allows us to solve difficult and complex systems that are intractable with the help of analytical techniques. Computer simulations enable us to realize virtual experiments under well defined conditions to understand and predict physical processes and their nonlinear evolution. The rapid increase of computer performance and new numerical methods enhances calculation time, memory usage and resolution. Furthermore, it gives the opportunity to tackle the manifold of physical processes that are involved in astrophysical systems. The following gives an overview of the main concepts of hydrodynamic simulations, applied with the help of the hybrid code `RAMSES` (Teyssier, 2002) within this thesis.

2.1 The continuum approximation

Hydrodynamic simulations of compressible flows are used in a wide range of scientific fields, like theoretical astrophysics, climate research, weather modeling or aerodynamics. These research areas operate on very different spatial scales, but are based on the same concept to model these systems. Molecules, atoms, ions or electrons are separated by relatively large regions of empty space and can be approximated by a compressible fluid. By using this approach, the individual motions of the particles are not followed anymore but are described as a continuum on much larger scales. It requires that the mean free path λ of the particle system is orders of magnitudes smaller than the typical scale of interest L. This condition is fulfilled for the galaxy simulations in this thesis and can be quantified by the Knudsen number $\mathrm{K_n}$:

$$\mathrm{K_n} = \frac{\lambda}{L} \ll 1 \tag{2.1}$$

2.2 Hydrodynamic equations

The gas flows in astrophysics are often of very low density, making internal friction negligible. Therefore, most simulations assume ideal gas dynamics as described by the Euler equations. When formulated in the Lagrangian form (convective form), the equations follow an individual fluid element as it moves through space and time. This approach is used in the particle-based technique SPH (smoothed particle hydrodynamics) method. Grid-based techniques use the Euler equations in Eulerian form (conservative form) where a specific location in space is considered through which the fluid flows. Then the equations describe the conservation of mass

$$\frac{\partial \rho}{\partial t} + \mathbf{u} \cdot \nabla \rho + \rho \nabla \cdot \mathbf{u} = 0, \tag{2.2}$$

the conservation of linear momentum

$$\frac{\partial \mathbf{u}}{\partial t} + \mathbf{u} \cdot \nabla \mathbf{u} + \frac{1}{\rho} \nabla P = 0, \tag{2.3}$$

and the conservation of total energy

$$\frac{\partial P}{\partial t} + \mathbf{u} \cdot \nabla P + \gamma P \nabla \cdot \mathbf{u} = 0, \tag{2.4}$$

where ρ is the gas density and $\mathbf{u}$ the velocity vector. To complete the equations the pressure P is related to thermodynamic variables with the equation of state (EOS) for an ideal gas

$$P = (\gamma - 1)\rho\epsilon \tag{2.5}$$

where γ is the adiabatic index (5/3 for a monoatomic gas) and ϵ the internal energy.

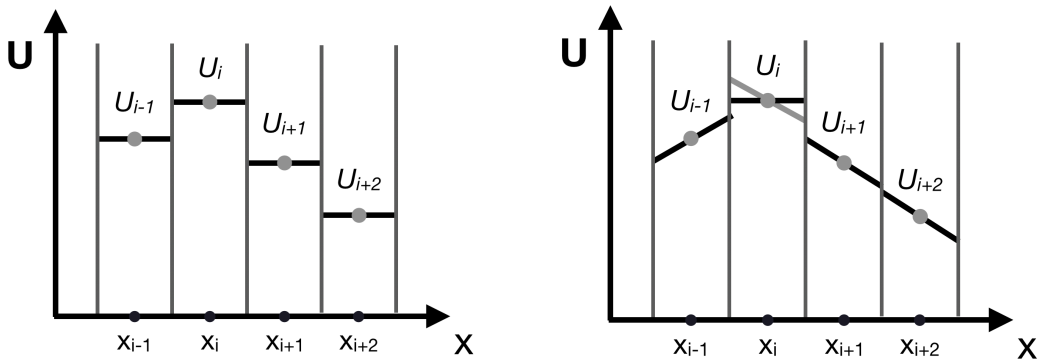

(a) Piecewise constant (b) Piecewise linear

Figure 2.1: (a) Piecewise constant reconstruction scheme for a fluid state U on a regular grid x. (b) Piecewise linear reconstruction scheme for a fluid state U on a regular grid x.

2.3 Solving the Euler equations

Two main types of structured grids are used in astrophysics to divide the computational domain into a set of finite cells. For a finite-difference discretisation the data is associated with a specific point in space. For a finite-volume discretisation, the data is represented by averaged values. The Euler equations (Equations 2.2-2.4) can be expressed as (Teyssier, 2015)

$$\frac{\partial \mathbf{U}}{\partial t} + \nabla \cdot \mathbf{F}(\mathbf{U}) = 0. \tag{2.6}$$

The state of the gas is represented by the vector $\mathbf{U}(\mathbf{x}, t) = (\rho, \rho\mathbf{v}, E)$, where E is the fluid total energy per unit volume and $\mathbf{F}$(x,t) the variable fluxes at the cell interfaces. Accordingly, the left side of the Equation 2.6 can be discretized to a finite time and space in one dimension by

$$\frac{U_i^{n+1} - U_i^n}{\Delta t} + \frac{F_{i+1/2}^{n+1/2} - F_{i-1/2}^{n+1/2}}{\Delta x} = S_i^{n+1/2} \tag{2.7}$$

while U_i^n is the approximation to the cell-averaged values at time t^n and for a cell center i. $F^{n+1/2}$ corresponds to the time centered fluxes at the cell interfaces $i-1/2$ and $i+1/2$. Δt is the timestep and Δx the one dimensional size of a cell. With the time centered source term $S_i^{n+1/2}$ several astrophysical applications can be included. For example, gravity is added to the equations (see Section 2.5) by modifying the source term of the momentum (Equation 2.3) and energy equation (Equation 2.4). The depletion of local gas for star formation can be modeled with a source term for the mass conservation (Equation 2.2) and cooling/heating by modifying the energy conservation (Equation 2.4). The fluxes at the interfaces are calculated by solving the *Riemann* problem (contact discontinuity) since it gives an exact solution to the nonlinear Euler equations (in the finite volume discretisation).

Two different methods are used to compute the fluxes at the cell interfaces. The traditional Godunov (Godunov, 1959) method at first-order spatial accuracy considers a numerical solution which is piecewise constant in each cell (Figure 2.1a). Second-order schemes are based on a linear interpolation between the cell interfaces (Figure 2.1b), the first of its kind being introduced by the MUSCL scheme (van Leer, 1976). The exact Riemann solution is computationally expensive and therefore, various approximate Riemann solvers are being used. The Lax-Friedrich solver (LeVeque, 2013) is a first-order Godunov scheme in time and space and avoids solving the Riemann problem at each cell interfaces by adding an artificial viscosity. This method is particularly diffusive and does not represent shocks well. The HLL (Harten–Lax–von Leer) Riemann approximation is of second-order in time and space and considers the integral form of the conservation equations and the largest and smallest signal velocities at the cell interface. The linear extrapolations of the cell states to the cell interfaces can introduce new extrema, which leads to large spurious oscillations in the fluid. Therefore, slope limiters are required to keep the scheme stable and the solution smooth (Hubbard, 1999). Furthermore, to ensure convergence when solving the advection of the flow, the CFL (Courant, Friedrichs & Lewy, 1967) condition is necessary. In the one-dimensional case the timestep Δt has to be small enough that the Courant number C is smaller than unity for the considered cell size Δx and the propagating maximum wave speed v:

$$C = \frac{v \cdot \Delta t}{\Delta x} < 1. \tag{2.8}$$

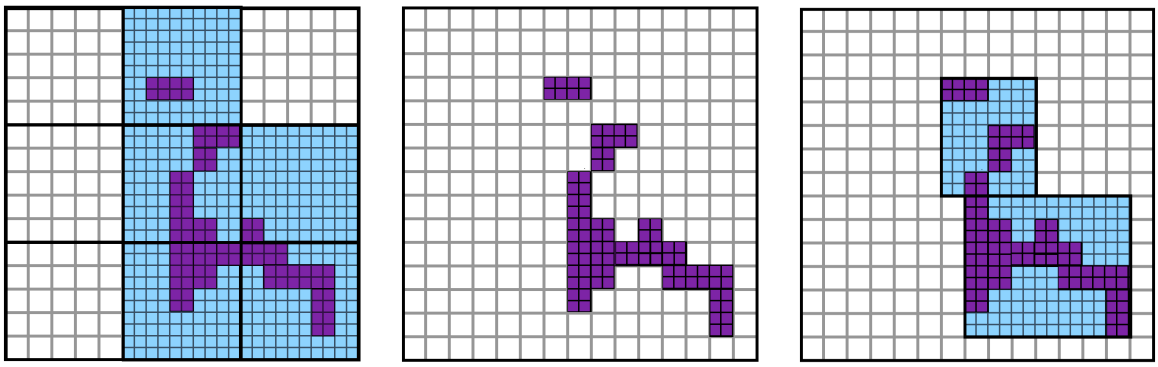

(a) Block-based (b) Cell-based (c) Patch-based

Figure 2.2: Three AMR approaches compared for a 2 level refinement example. The white cells are the coarse grid and blue corresponds to the refined regions. The purple cells represent the simulated gas that has been locally refined by the cell-based method.

2.4 Adaptive mesh refinement and timestepping

Astrophysical flows in the context of galaxy formation have to deal with a huge dynamical range in density, temperature and scale, which makes it impossible to follow them accurately on a uniform grid. Examples are large-scale structures like the cosmic web, the diffuse and hot halo gas, and on smaller scales the shear flows in galaxies, filaments and molecular clouds with star forming regions and discontinuities in shocks induced by supernova feedback. With the adaptive mesh refinement (AMR) technique, the numeric precision is adjusted to the physical problem of interest. In general, we distinguish three different approaches (Figure 2.2):

- The block-based method divides the simulation volume into fixed regions. If any cell reaches a specific condition that needs to be resolved better, the whole corresponding region is being refined. The data structure is relatively simple to process but can lead to a vast number of refined cells that have to be processed and to be stored.

- With the cell-based strategy, only the individual cells of interest are refined. Fewer cells have to be processed and to be stored. The bookkeeping of the data structure is complex, but the computational cost can be reduced dramatically compared to the other methods.

- With the patch-based approach, the cells of interest are grouped into rectangular regions with a better resolution. The technique unifies the advantages of the block-based and cell-based AMR. The mesh is more structured and simpler to process and has less refined cells involved than in the block-based approach.

Several conditions for the gas variables can be defined to increase the spatial resolution. Refinement strategies can be based, e.g. on a threshold or a gradient. In the thesis, we apply the Jeans length criterion on a cell-based AMR where the Jeans length is represented by at least 4 cells at each refinement level. High-density regions with relatively small Jeans lengths are represented by smaller sizes and accordingly low-density regions with relatively large Jeans

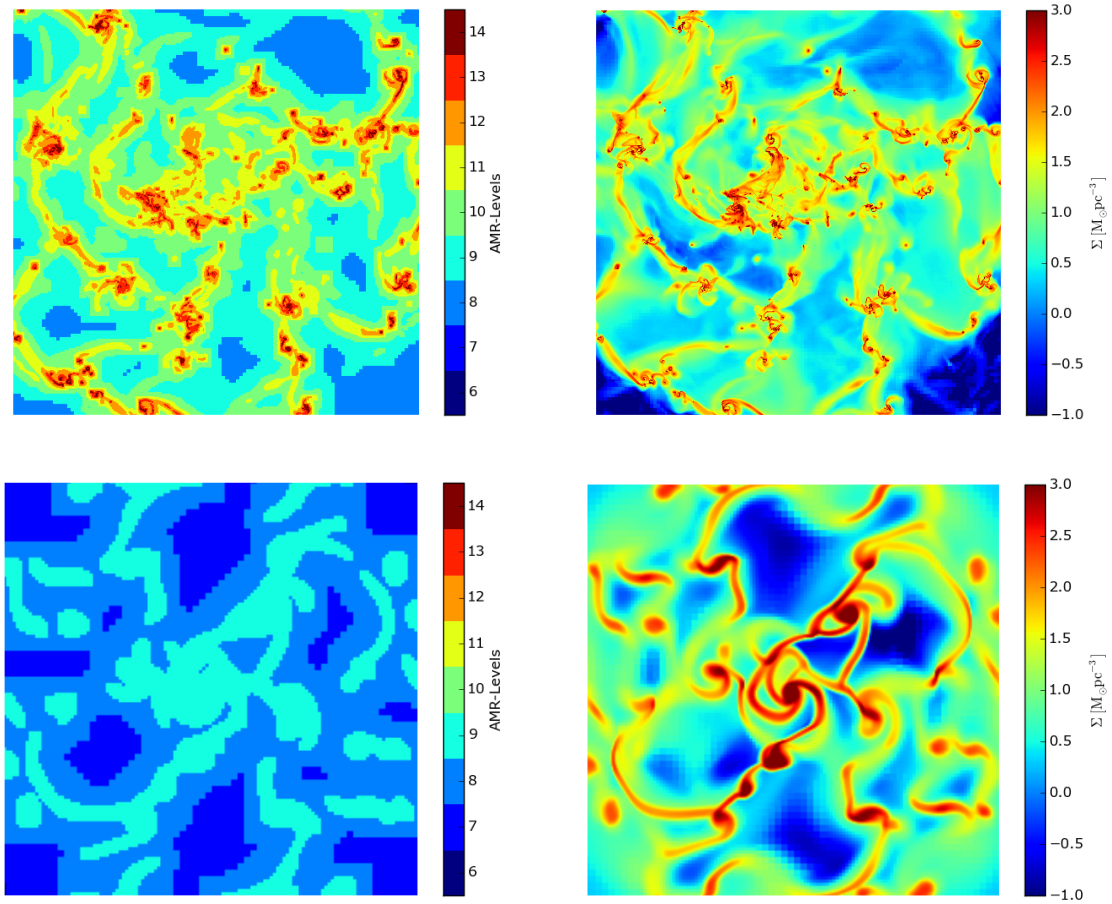

Figure 2.3: The left panel shows maps of the AMR levels of the mid-plane from two galaxy simulations in Chapter 5 and their corresponding surface density projections of the gas on the right panel. The maximum resolution level (L9) in the low-resolution run ULR is used for the clump regions (bottom-row), but in the high-resolution run MS it is applied to the interstellar gas (top-row). ULR represents the Jeans length with $N_{\rm J}$ = $N_{\rm p}$ = 4 cells on all levels and MS with $N_{\rm J}$ = 19 for the levels 6 to 13. For MS, the Jeans length is represented by ten cells at the maximum level $N_{\rm p}$ = 4. The levels correspond to the following physical sizes: L6 ≡ 750pc, L7 ≡ 375pc, L8 ≡ 187.5pc, L9 ≡ 93.8pc, L10 ≡ 48.9pc, L11 ≡ 23.4pc, L12 ≡ 11.7pc, L13 ≡ 5.9pc, L14 ≡ 2.9pc.

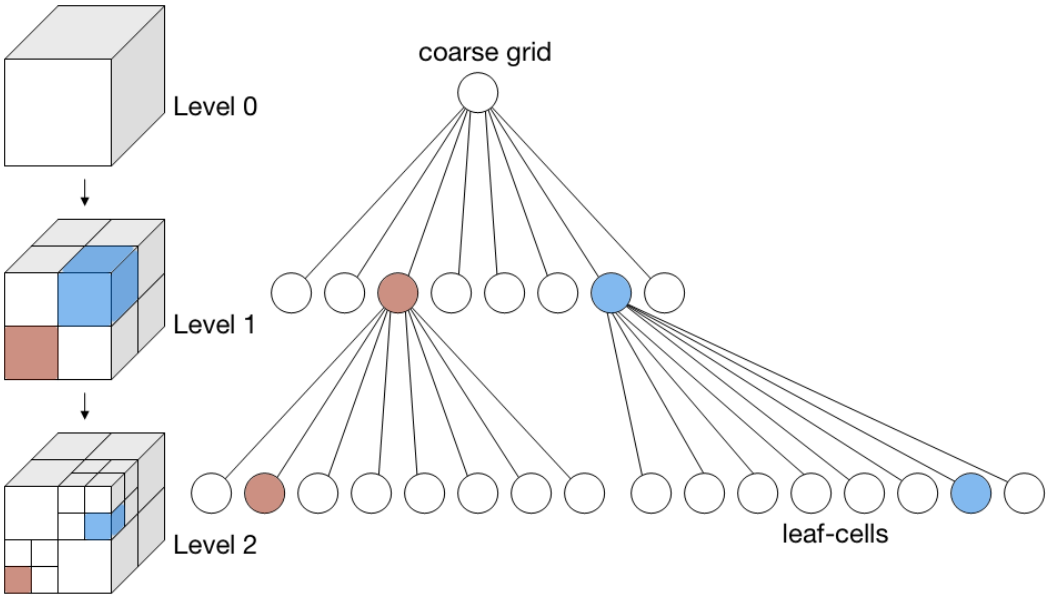

Figure 2.4: Left: Recursive subdivision of a cube into octants. Right: The corresponding octree. Credit: modified illustration from Nü (2006)

lengths are represented by larger cells (see Section 5.3.2). Figure 2.3 shows two simulations with different maximum resolution and different Jeans length refinement. This local dynamic technique ensures that all spatial scales are properly resolved by saving memory/storage and computational time, since the number of cells can be reduced significantly. In three dimensions, `RAMSES` uses an octtree, where the mesh starts with a base coarse grid for the minimum level. Cells are split into eight smaller sub-grids for regions that require more resolution. Deeper sub-grids are added recursively until it reaches a defined maximum level (Figure 2.4). Since the CFL condition is dependent on the spatial resolution, smaller cells can dictate the whole simulation to a small timestep, despite only using a small fraction of the simulation domain. Therefore, level sub-cycling is used to update the grid of each AMR level according to its own timestep. The coarser levels are synchronized with the finer levels.

2.5 Self gravity and external potential

Gravity is one of the most important fundamental forces in astrophysics. The gravitational force $\mathbf{F}_{\text{grav}}$ is given by the gradient of the gravitational potential ϕ and is related to the gas density by the Poisson equation:

$$\mathbf{F}_{\text{grav}} = -\rho_{\text{tot}} \nabla\phi \quad \text{with} \quad \Delta\phi = 4\pi G \rho_{\text{tot}}. \tag{2.9}$$

Gravity is added as a source term to the momentum equation (Equation 2.3) with $\mathbf{F}_{\text{grav}}$ and as work of the gravitational force $\mathbf{F}_{\text{grav}} \cdot \mathbf{u}$ to the energy equation (Equation 2.4). The self-gravity is calculated by using the density of the gas ρ_{gas} and an external potential can be included in form of a density distribution $\rho_{\text{tot}} = \rho_{\text{gas}} + \rho_{\text{pot}}$. In RAMSES, the Poisson equation is solved with two different iterative schemes of second order accuracy. On coarser levels, the multigrid method (MG) has been proven to be efficient and for the finer levels

the conjugate gradient method (CG). The MG method uses a hierarchy of discretizations with different spatial resolution. The solution on the finest grid is obtained by iteratively subtracting corrections from the solutions of the coarser grids.

2.6 Parallelisation

The adaptive mesh and the sub-cycling of the timesteps are important techniques to make simulations more efficient. Furthermore, the computation can be significantly accelerated by dividing the simulation box into sub-domains (distributed memory) that are calculated in parallel by many processors using MPI (Message Passing Interface). The three-dimensional domain is decomposed by applying the one-dimensional Peano-Hilbert space-filling curve (Peano, 1890; Hilbert, 1891). This strategy distributes the sub-domains to computational tasks to achieve well-balanced processes. An example for a two-dimensional domain decomposition is given in Figure 2.5. Each sub-domain has its own boundary represented by ghost cells. These ghost cells contain copies of the neighboring sub-domains or use the physical boundary conditions of the full domain, depending on their position. After each timestep the new informations in the boundaries have to be exchanged between the processes.

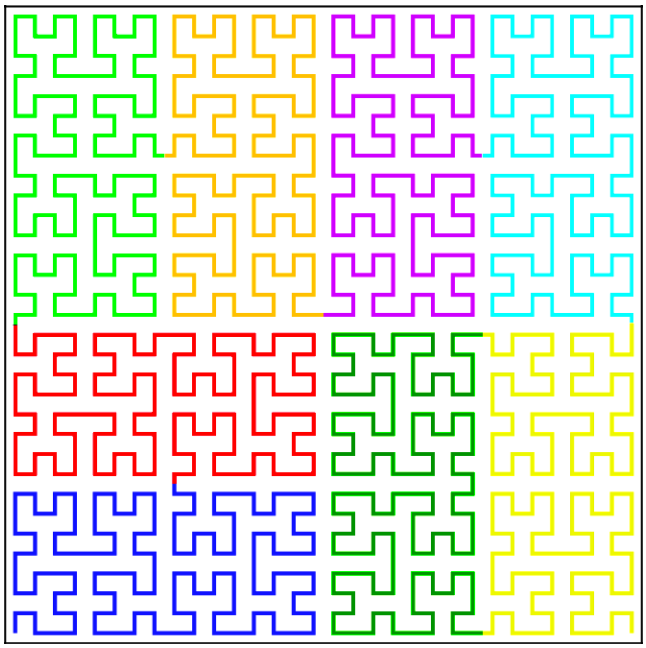

Figure 2.5: Example of a Peano-Hilbert space-filling curve domain decomposition. The one-dimensional line is filling up the two-dimensional space of a 32 x 32 grid. It provides an optimally partitioning of the grid for 8 processors (color coded).

Chapter 3

Structure formation in gas-rich galactic discs with finite thickness: from discs to rings

Published in: Monthly Notices of the Royal Astronomical Society
Behrendt, Burkert & Schartmann (2015)

3.1 Abstract

Gravitational instabilities play an important role in structure formation of gas-rich high-redshift disc galaxies. In this paper, we revisit the axisymmetric perturbation theory and the resulting growth of structure by taking the realistic thickness of the disc into account. In the unstable regime, which corresponds for thick discs to a Toomre parameter below the critical value $Q_{0,\mathrm{crit}} = 0.696$, we find a fastest growing perturbation wavelength that is always a factor 1.93 times larger than in the classical razor-thin disc approximation. This result is independent of the adopted disc scaleheight and by this independent of temperature and surface density. In order to test the analytical theory, we compare it with a high-resolution hydrodynamical simulation of an isothermal gravitationally unstable gas disc with the typical vertical sech^2 density profile and study its break up into rings that subsequently fragment into dense clumps. In the first phase, rings form, that organize themselves discretely, with distances corresponding to the local fastest growing perturbation wavelength. We find that the disc scaleheight has to be resolved initially with five or more grid cells in order to guarantee proper growth of the ring structures, which follow the analytical prediction. These rings later on contract to a thin and dense line, while at the same time accreting more gas from the inter-ring region. It is these dense, circular filaments, that subsequently fragment into a large number of clumps. Contrary to what is typically assumed, the clump sizes are therefore not directly determined by the fastest growing wavelength.

3.2 Introduction

Observations of massive galaxies at high redshift have revealed rotating discs (Förster Schreiber et al., 2009) with large gas fractions (Daddi et al., 2010) and high velocity dispersion. Their morphology is irregular and often dominated by a few kpc-sized clumps (Genzel et al., 2011), seen in the optical (Elmegreen et al., 2007), and also in ionized (Genzel et al., 2008) and molecular gas (Tacconi et al., 2013). In the Cosmic Assembly Near-IR Deep Extragalactic Legacy Survey (CANDELS; Grogin et al., 2011; Koekemoer et al., 2011) over 250 000 distant

galaxies from $z = 8$ to 1.5 are documented, where more than half of the star-forming galaxies are clumpy (Bournaud et al., 2014, and references therein). The main origin of bound clumps is expected to be a result of in situ gravitational disc fragmentation, as demonstrated by a large number of numerical simulations of self-gravitating gas-rich discs, either in a cosmological context (Agertz, Teyssier & Moore, 2009; Dekel, Sari & Ceverino, 2009b; Ceverino, Dekel & Bournaud, 2010; Ceverino et al., 2012) or in an isolated box (Immeli et al., 2004a,b; Bournaud, Elmegreen & Elmegreen, 2007; Ceverino et al., 2012). In general, local gravity has to overcome the stabilizing effects of thermal or turbulent pressure and differential rotation. This is quantified by the parameter Q_0 of Toomre (1964). Below a critical value ($Q_0 < 1$), axisymmetric instabilities (rings in an axisymmetric disc) can form, contract and finally break up into several clumps (Dekel, Sari & Ceverino, 2009b), faster than spiral patterns (non-axisymmetric modes) can form. Furthermore, to finally form strongly bound clumps that later on collapse to stars, sufficient cooling is required to ensure contraction to higher densities within short enough time-scales (Gammie, 2001; Dekel, Sari & Ceverino, 2009b).
A more detailed insight can be achieved from linear perturbation theory (Lin & Shu, 1964). It can describe the properties of structure formation, with respect to their sizes, masses and time-scales. Understanding these processes in detail is important in order to get a better view of the previous history and subsequent evolution of a disc. However, in these considerations, a razor-thin disc was assumed, characterized by its surface density Σ. Already Toomre (1964) pointed out that a disc with finite thickness leads to a reduction of the gravitational force in the mid-plane, where structure formation takes place. Therefore, the disc remains stable even below a Q_0-value of one and a revised critical value has to be determined with $Q_0 < Q_{\rm crit} < 1$, describing the unstable regime.

A self-gravitating gas disc with its isothermal vertical structure in hydrostatic equilibrium is given by the sech^2 density profile (Spitzer, 1942). Since there is no analytical solution for the reduction factor of the potential in the mid-plane for this profile, a good approximation is achieved by using an exponential function instead (e.g. Elmegreen, 1987), for which the reduction factor deviates from the one of the sech^2 profile with a maximum error of 14% (Kim, Ostriker & Stone, 2002; Kim, Kim & Ostriker, 2006; Kim & Ostriker, 2007). The critical value for the instability parameter was thus determined to $Q_{\rm crit} \simeq 0.647$ for an exponential profile approximation by Kim & Ostriker (2007) and for the sech^2 profile to $Q_{\rm crit} \simeq 0.693$ in Wang et al. (2010). Moreover, the reduced self-gravity also affects the sizes of the growing structures. Griv & Gedalin (2012) estimated for an exponential vertical distribution a factor of ~ 2 larger wavelengths for the fastest growing perturbations. These implications on stability and structure properties demonstrate the importance of considering the thickness effects.

In this paper, we go beyond previous work by investigating in detail how axisymmetric instabilities grow in an idealized gas disc simulation. Section 3.3 introduces the linear stability analysis for thick discs. From this we deduce the properties of the growing ring structures with respect to their sizes, masses and formation time-scales. Finally, we employ an idealized hydrodynamical simulation (Section 3.4) and compare the initial structure formation with the linear stability analysis (Section 3.5).

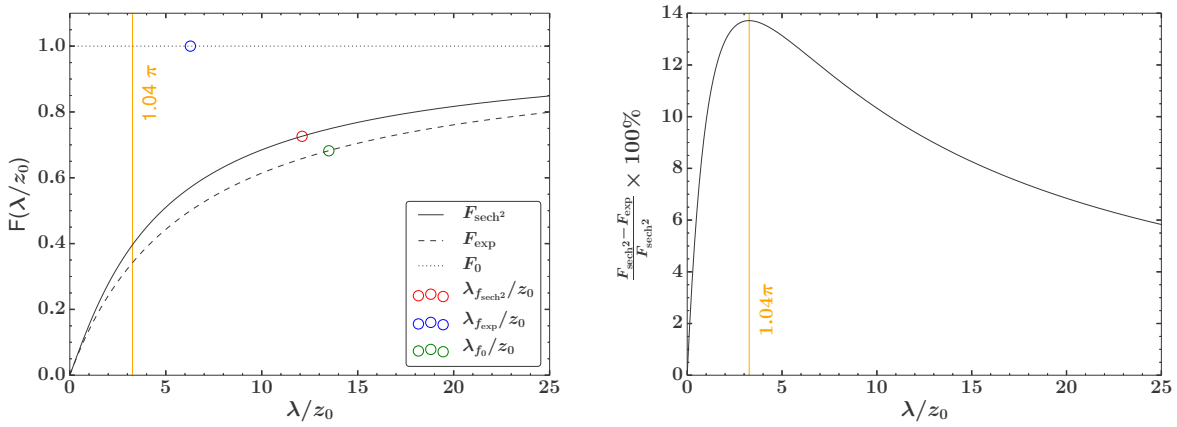

Figure 3.1: (a) General dependence of the reduction factor $F(\lambda/z_0)$. The numerical integration of F_{sech^2} is represented by the solid line (equation 3.6), the approximation F_{exp} by the dashed line (equation 3.7) and with no reduction for an infinitesimally thin disc by the dotted line. The coloured open circles mark the particular reduction for the constant relations between the scale-height and the fastest growing wavelength derived for the different vertical density distributions (Sections 3.3.3 and 3.3.4). (b) Per cent deviation between the reduction factor for the sech^2 profile and the approximation with the exponential profile, with the maximum of 13.7% at 1.04π.

3.3 Analytical model

We summarize the available literature on how perturbation theory has to be modified when moving from an infinitesimally thin disc to a more realistic disc with finite thickness. In general, this transition is expressed by a wavelength and scale-height dependent reduction factor of the perturbed potential. Based on the resulting modification of the dispersion relation, we explicitly present the analytical derivation of the fastest growing wavelength for a vertically exponential density distribution. The reduction factor is independent of the scale-height when the disc is in hydrostatic equilibrium. The fastest growing wavelength for the vertical sech^2 density profile is numerically approximated. At this wavelength, which is the dominant growing perturbation in a disc, the reduction factor is a constant and allows us to simplify the deduction of the physical properties of the growing ring structures and the local instability parameter.

3.3.1 Reduction factor

In classical linear perturbation theory, matter is assumed to be concentrated in a razor-thin layer with a surface density Σ. This overestimates the potential as in real discs matter is vertically arranged with the density having its maximum in the mid-plane where the initial structures form first. This softens the potential and requires a correction factor F in addition to modify the classical theory.
Density perturbations correlate with variations in the gravitational field and are usually specified by the perturbed local gravitational potential Φ_0 of an infinitesimal thin disc, which is

given by the solution of the Poisson equation in the stationary form (see Appendix 3.8.1). The total potential at the mid-plane, $z = 0$, of a disc with finite thickness can then be expressed by

$$\Phi_{\rm tot}(\lambda, x, z=0) = \Phi_0(\lambda, x, z=0)\; F(\lambda, z=0), \tag{3.1}$$

with the wavelength $\lambda \geq 0$ and $x = R - R_0$ the position near a given radius R_0. The reduction factor $F(\lambda)$ is generally between two limits: $\lim_{\lambda\to\infty} F(\lambda) = 1$ and $\lim_{\lambda\to 0} F(\lambda) = 0$. Therefore, for longer wavelengths λ, $\Phi_{\rm tot}$ (equation 3.1) behaves like the potential of a razor-thin disc and for shorter λ the potential is reduced (Fig. 3.1a), e.g. Kim, Ostriker & Stone (2002); Wang et al. (2010). The transition between the regimes depends on the vertical density distribution. The vertical structure of a self-gravitating and isothermal sheet in hydrostatic equilibrium is described by a $\mathrm{sech}^2(z/z_0)$ profile (Spitzer, 1942), with the sound speed $c_{\rm s}$ and the scale-height

$$z_0 = \frac{c_{\rm s}^2}{\pi G \Sigma}. \tag{3.2}$$

The reduction factor is then given by (see Appendix 3.8.1)

$$F_{\rm sech^2}(\lambda, z_0) = \int_{-\infty}^{\infty} \mathrm{e}^{-\frac{2\pi}{\lambda}|h|}\; \frac{\mathrm{sech}^2\,(h/z_0)}{2z_0}\; dh. \tag{3.3}$$

This is basically the summation over all contributions to the total potential at the mid-plane, generated from infinitesimally thin layers at all vertical distances h. Equation (3.3) can be integrated numerically. Alternatively, an analytical solution can be achieved by replacing the vertical sech^2 distribution by an exponential profile, which is a good approximation (Elmegreen & Elmegreen, 1983; Elmegreen, 1987; Kim, Ostriker & Stone, 2002; Wang et al., 2010; Elmegreen, 2011). The reduction factor is then

$$F_{\rm exp}(\lambda, z_0) = \int_{-\infty}^{\infty} \mathrm{e}^{-\frac{2\pi}{\lambda}|h|}\; \frac{\mathrm{e}^{-|h|/z_0}}{2z_0}\; dh, \tag{3.4}$$

and the solution

$$F_{\rm exp}(\lambda, z_0) = \left(1 + \frac{2\pi}{\lambda}\, z_0\right)^{-1}. \tag{3.5}$$

If we substitute $x = h/z_0$ in equations (3.3) and (3.4), and use the symmetry in vertical direction, the integral can be written as

$$F_{\rm sech^2}(\lambda, z_0) = \int_{0}^{\infty} \mathrm{e}^{-\frac{2\pi}{\lambda} z_0 x}\; \mathrm{sech}^2\,(x)\; dx, \tag{3.6}$$

and

$$F_{\rm exp}(\lambda, z_0) = \int_{0}^{\infty} \mathrm{e}^{-\frac{2\pi}{\lambda} z_0 x}\; \exp\,(-x)\; dx, \tag{3.7}$$

respectively. Both equations (equations 3.6 and 3.7) show a similar dependence on λ and z_0, the comparison is illustrated in Fig. 3.1a. In principle, for a given z_0, a smaller wavelength λ leads to smaller F. Much larger wavelengths λ on the other hand are required to reach the upper range of $F \approx 1$. The reduction factor $F_{\rm exp}$ underestimates the numerical solution of $F_{\rm sech^2}$, with a maximum error of 13.7% (Fig. 3.1b), in agreement with the result found by e.g. Kim, Ostriker & Stone (2002); Kim, Kim & Ostriker (2006) and Kim & Ostriker (2007). This maximum error is reached however at $\lambda/z_0 \simeq 1.04\pi$, which differs by roughly a factor of 2 from their result.

3.3.2 Modified dispersion relation

In this section, we introduce the modified local dispersion relation of Lin & Shu (1964) for geometrically thick gas discs, since it is important for our further calculations. It gives a relation between the angular frequency ω and density perturbations with wavelength λ in radial direction. Here, it indicates the possibility for growing axisymmetric perturbations, depending on the local conditions.
In general, to get the dispersion relation, linear perturbation theory is employed on the hydrodynamical equations and the Poisson equation (Section 3.3.1) for a self-gravitating and rotating gas disc in the razor-thin limit (Binney & Tremaine, 2008a). In our case, the reduction factor appears in addition and we find in the mid-plane for $\lambda > 0$ (e.g. Wang et al., 2010)

$$\omega^2 = \kappa^2 - 2\pi G\Sigma \left(\frac{2\pi}{\lambda}\right) F(\lambda, z_0) + c_s^2 \left(\frac{2\pi}{\lambda}\right)^2, \tag{3.8}$$

with the epicyclic frequency κ and the unperturbed surface density Σ. For $\omega^2 > 0$ the disc is stable against axisymmetric instabilities. If $\omega^2 < 0$, a certain range of perturbations can grow exponentially in rings. The more negative the values, the faster they grow. All parameters in equation (3.8) can change with radius for the case of an exponential surface density profile, which leads to a complex interplay between the three terms. However, in general we can say: the effect of self-gravity is destabilising, whereas the differential rotation, represented by $\kappa^2 > 0$, and the thermal pressure, with c_s^2, stabilize the disc. The dispersion relation (equation 3.8) inherits the properties of the reduction factor F (see Section 3.3.1). For larger perturbation wavelengths, F approaches unity which gives the solution of ω for a razor-thin layer. At smaller wavelengths, the thickness of the vertical density structure plays a stronger role and self-gravity is reduced in the mid-plane (e.g. Kim, Ostriker & Stone, 2002). With the reduction factor $F_{\rm exp}$, the relation leads, with all its dependences to the form (e.g. Shetty & Ostriker, 2006; Wang et al., 2010),

$$\omega_{\rm exp}^2 = \kappa^2 - \frac{4\pi^2 G\Sigma}{\lambda + 2\pi z_0} + c_s^2 \left(\frac{2\pi}{\lambda}\right)^2. \tag{3.9}$$

Since there is no wavelength dependence for κ, we can derive a rotation-independent form for the fastest growing perturbations in the next section.

3.3.3 The fastest growing perturbation wavelength for the exponential profile

The extremum of the dispersion relation as function of wavelength (equation 3.9) is determined by

$$\frac{\partial \omega_{\rm exp}^2}{\partial \lambda} = 4\pi^2 \left(\frac{G\,\Sigma}{(\lambda + 2\pi z_0)^2} - \frac{2c_s^2}{\lambda^3}\right) = 0. \tag{3.10}$$

We solve equation (3.10) in Appendix 3.8.2 analytically and get the fastest growing wavelength $\lambda_{f_{\rm exp}}$. The minimum is ensured by $\frac{\partial^2 \omega_{\rm exp}^2(\lambda_{f_{\rm exp}})}{\partial^2 \lambda} > 0$. It marks the maximum growth rate for an unstable disc. For a disc in hydrostatic equilibrium with given z_0 (equation 3.2) the solution simplifies and we can relate it to the classical solution in the razor-thin limit with

$$\lambda_{f_0} = \frac{2c_s^2}{G\Sigma}. \tag{3.11}$$

For the exponential profile approximation, we get

$$\lambda_{f_{\rm exp}} = A_{\rm exp}\, \lambda_{f_0}, \tag{3.12}$$

with the constant factor $A_{\rm exp} \simeq 2.148$ and no additional dependences. Since the form of equation (3.11) is similar to that of the scaleheight in equation (3.2), we can write

$$\lambda_{f_{\rm exp}} = A_{\rm exp}\, 2\pi z_0 \simeq 13.496\, z_0, \tag{3.13}$$

which is similar to the approximation found by Griv & Gedalin (2012) and Romeo & Agertz (2014) with $\sim 4\pi z_0$.
The reduction factor equation (3.5) then simplifies for $\lambda_{f_{\rm exp}}$ (equation 3.13) to a constant value

$$F_{\rm exp}(\lambda_{f_{\rm exp}}) = \left(1 + \frac{1}{A_{\rm exp}}\right)^{-1} \simeq 0.682, \tag{3.14}$$

independent of the scaleheight (Fig. 3.1a). According to the solution in equation (3.14), the potential in the mid-plane of a razor-thin disc is therefore overestimated by 46.628% (see equation 3.1).

3.3.4 Fastest growing perturbation wavelength for the sech^2-profile

We follow the steps described in Section 3.3.3 and determine the minimum of the dispersion relation for the sech^2 -profile by using the reduction factor $F_{\mathrm{sech}^2}(\lambda, z_0)$ with

$$\frac{\partial \omega^2_{\mathrm{sech}^2}}{\partial \lambda} = 4\pi^2 \left[\frac{G\,\Sigma}{\lambda} \left(\frac{F_{\mathrm{sech}^2}}{\lambda} - \frac{\partial F_{\mathrm{sech}^2}}{\partial \lambda} \right) - \frac{2c_{\rm s}^2}{\lambda^3} \right] = 0. \tag{3.15}$$

The wavelength λ is varied iteratively for several fixed scaleheights z_0 until equation (3.15) reaches zero. The integral F_{sech^2} of equation (3.3) and its differentiation in equation (3.15) is solved numerically. We find a relation for the fastest growing perturbation wavelength that is similar to the exponential case (equation 3.12)

$$\lambda_{f_{\mathrm{sech}^2}} = A_{\mathrm{sech}^2}\, \lambda_{f_0}, \tag{3.16}$$

with $A_{\mathrm{sech}^2} \simeq 1.926$. Expressed by the scaleheight it is

$$\lambda_{f_{\mathrm{sech}^2}} = A_{\mathrm{sech}^2}\, 2\pi z_0 \simeq 12.103\, z_0. \tag{3.17}$$

The error for the exponential profile approximation (equation 3.12) is therefore 11.527% compared to the numerical solution (equation 3.16), and for the thin disc approximation 48.079% (equation 3.11).
Again, we get a constant reduction factor for $\lambda_{f_{\mathrm{sech}^2}}$ for all z_0 with (Fig. 3.1a)

$$F_{\mathrm{sech}^2}(\lambda_{f_{\mathrm{sech}^2}}) \simeq 0.726, \tag{3.18}$$

with an error of 6.061% for $F_{\rm exp}(\lambda_{f_{\rm exp}})$ compared to the integral $F_{\mathrm{sech}^2}(\lambda_{f_{\mathrm{sech}^2}})$ and 37.741% for the thin disc approximation. Due to the steepness of the exponential profile in the innermost part, matter and self-gravity, respectively, is slightly underestimated in the mid-plane compared to the sech^2 distribution.

3.3.5 Ring properties

From the calculations above, we can derive properties of the possible growing structures if locally unstable. Due to axisymmetry, radial perturbations can grow within rings, with an overdense and an underdense part of the dominant growing wavelength. The initial radial thickness of the overdense region that will be investigated in detail in our disc simulation (see Section 3.5.4), is defined as

$$L_{\mathrm{sech}^2} = \frac{\lambda_{f_{\mathrm{sech}^2}}}{2}, \tag{3.19}$$

and related to the scale-height

$$L_{\mathrm{sech}^2} = A_{\mathrm{sech}^2}\, \pi z_0. \tag{3.20}$$

For the thin disc approximation, we have $L_0 = \lambda_{f_0}/2$ and get with equations (3.16) and (3.17) the relation

$$L_{\mathrm{sech}^2} = A_{\mathrm{sech}^2}\, L_0 = A_{\mathrm{sech}^2}\, \frac{c_\mathrm{s}^2}{G\Sigma}. \tag{3.21}$$

From this we can conclude that in thick discs, the initial radial ring widths are much larger than the scale-height and than in the razor-thin limit assumed.
The total mass of a ring can be estimated to first order as

$$M_{\mathrm{Ring}} = \pi\Sigma(R) \left[\left(R + \frac{\lambda_{f_{\mathrm{sech}^2}}}{2} \right)^2 - \left(R - \frac{\lambda_{f_{\mathrm{sech}^2}}}{2} \right)^2 \right], \tag{3.22}$$

which gives

$$M_{\mathrm{Ring}} = 2\pi\Sigma(R)\, R\, \lambda_{f_{\mathrm{sech}^2}}, \tag{3.23}$$

where R is the location of the maximum of the density perturbation.

3.3.6 Local disc instability parameter

Here we derive a local dimensionless stability parameter for a disc with finite thickness, following the example of Toomre (1964) for an infinitesimal-thin gas disc with

$$Q_0 = \frac{\kappa\, c_\mathrm{s}}{\pi G\Sigma}. \tag{3.24}$$

In contrast to other derivations we, apply the fastest growing wavelength on the dispersion relation to determine the parameter Q.
The disc is locally unstable for axisymmetric instabilities if $Q_0 < 1$. Q_0 can be obtained from the unmodified dispersion relation ω_0^2, for equation (3.8) with $z_0 = 0$. The global minimum of the dispersion relation determines the fastest growing λ_{f_0} (equation 3.11) and therefore is the 'last' possible wavelength which could grow if an unstable disc turns over to stability (from $\omega^2 < 0$ to $\omega^2 \geq 0$). The transition is given by $\omega_0^2(\lambda_{f_0}) = 0$ and by rearranging, it leads to the expression given in equation (3.24) with $Q_0 = 1$. In a similar way we proceed with the modified dispersion relation (equation 3.8) for the sech^2 density profile and with the fastest growing wavelength we have

$$\omega_{\mathrm{sech}^2}^2 = \kappa^2 - \frac{4\pi^2 G\Sigma}{\lambda_{f_{\mathrm{sech}^2}}} F_{\mathrm{sech}^2} + \frac{4\pi^2 c_\mathrm{s}^2}{\lambda_{f_{\mathrm{sech}^2}}^2} = 0. \tag{3.25}$$

We insert $\lambda_{f_{\mathrm{sech}^2}}$ (equation 3.16) to get

$$\omega^2_{\mathrm{sech}^2} = \kappa^2 - \frac{\pi^2 G^2 \Sigma^2}{c_\mathrm{s}^2}\left(\frac{2\,F_{\mathrm{sech}^2}}{A_{\mathrm{sech}^2}} - \frac{1}{A^2_{\mathrm{sech}^2}}\right) = 0. \tag{3.26}$$

Now, we substitute the classical parameter Q_0 (equation 3.24) and get

$$Q_{\mathrm{sech}^2} = Q_0 \times C_{\mathrm{sech}^2} = 1, \tag{3.27}$$

with the constant proportionality factor

$$C_{\mathrm{sech}^2} = \frac{A_{\mathrm{sech}^2}}{\sqrt{2\,F_{\mathrm{sech}^2}\,A_{\mathrm{sech}^2} - 1}} \simeq 1.437. \tag{3.28}$$

There is thus a simple linear relation between the thin disc approximation and a disc with finite thickness. The error of using $Q_0 = 1$ is 30.411%. The line of neutral stability, $Q_{\mathrm{sech}^2} = 1$, corresponds to $Q_{0,\mathrm{crit}} \simeq 0.696$, which is very similar to the approximation from Wang et al. (2010) with $Q_{0,\mathrm{crit}} \simeq 0.693$.
For the exponential profile approximation we have $C_{\mathrm{exp}} = 1.546$ and hence an error of 7.585% compared to C_{sech^2}. In this case, the critical value is $Q_{0,\mathrm{crit}} \simeq 0.647$, consistent with what is found by Kim, Ostriker & Stone (2002).

3.3.7 Time-scales

To get an estimation of the fragmentation time-scales, we calculate the time at which the amplitude of the fastest growing disturbance has increased by a factor of e. For negative ω^2, the growth rate p is $-p^2 = \omega^2$ and the amplitude of a perturbation grows with $\exp(p\,t)$ (Binney & Tremaine, 2008a). For an increase by a factor of e, the growth time-scale is $t = 1/p$. For the thin disc approximation,

$$t_0 = \left(\frac{\pi^2 G^2 \Sigma^2}{c_\mathrm{s}^2} - \kappa^2\right)^{-1/2}, \tag{3.29}$$

and expressed by the Q_0 parameter

$$t_0 = \kappa^{-1}\left(\frac{1}{Q_0^2} - 1\right)^{-1/2}. \tag{3.30}$$

By taking the thickness with the sech^2 profile into account, we get the general form

$$t_{\mathrm{sech}^2} = \left(\frac{4\pi^2 G\Sigma}{\lambda_{f_{\mathrm{sech}^2}}} F_{\mathrm{sech}^2} - \frac{4\pi^2 c_\mathrm{s}^2}{\lambda^2_{f_{\mathrm{sech}^2}}} - \kappa^2\right)^{-1/2}, \tag{3.31}$$

and by substituting $\lambda_{f_{\mathrm{sech}^2}}$ with equation (3.16) and inserting Q_0 it leads to

$$t_{\mathrm{sech}^2} = \kappa^{-1}\left(\frac{1}{Q_0^2\,C^2_{\mathrm{sech}^2}} - 1\right)^{-1/2}, \tag{3.32}$$

which goes to infinity for a marginally stable disc.

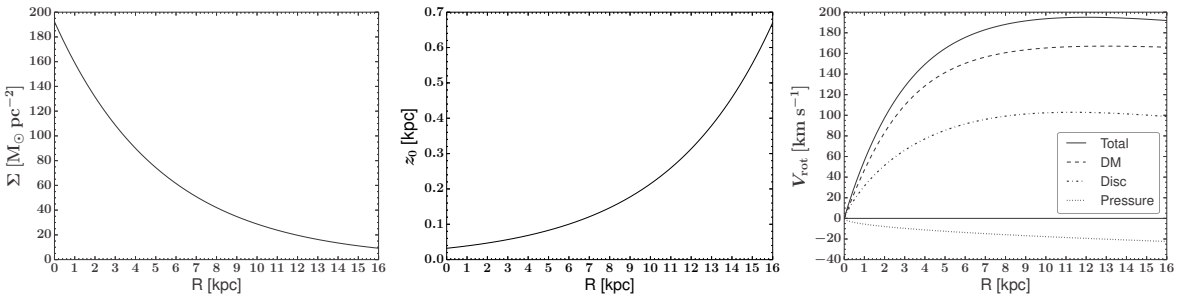

(a) (b) (c)

Figure 3.2: The radial setup properties of the gas disc with the (a) declining exponential surface density profile $\Sigma(R)$ (equation 3.47), (b) the increasing scale-height $z_0(R)$ (equation 3.51), (c) the total rotation curve $V_{\rm rot}(R)$ (see Section 3.4.2) and its decomposition into the contribution of the dominating dark matter halo, the gas disc and its correction due to the pressure gradient.

3.4 Numerical modelling

In order to test the predictions of the linear stability analysis, we employ simulations of an idealized gas disc. In the following, we describe the code and the disc model.

3.4.1 The simulation code

We use the hydrodynamical AMR (adaptive mesh refinement) code RAMSES (Teyssier, 2002) to perform simulations of a self-gravitating isolated gas disc with an isothermal equation of state (EoS), embedded in a dark matter halo. Since we are interested in the early phases without any strong discontinuities, here the Euler equations are being solved with the local Lax–Friedrichs scheme. The dark matter is handled as a static external density field added to the source term in the Poisson solver.
The mesh in the 48-kpc simulation box is structured by nested AMR grids from the coarsest level of 187.5 pc outside the disc to a maximum resolution of $\Delta x_{\rm min}$ = 5.86 pc inside, for the densest regions, employing an effective resolution of 2^8–2^{13} grid cells in all three direction. At each resolution level, we ensure that the Jeans length is resolved by at least 18 grid cells (see Section 3.4.3).

3.4.2 Disc model

We perform simulations of a massive gas disc $M_{\rm disc} = 2.7 \times 10^{10}$ M$_{\odot\odot}$ embedded in a spherical dark matter halo that within 16 kpc has a mass of $M_{\rm DM} = 1.03 \times 10^{11}$ M$_\odot$ following the Burkert (1995) density profile with a scalelength a_0 = 4 kpc. The gas temperature is 10^4 K and the disc has an exponential surface density profile with scalelength h = 5.26 kpc and truncation at $R_{\rm d}$ = 16 kpc (Fig. 3.2a). The central density is $\rho_\star = 3$ M$_\odot$ pc^{-3}. The parameters were chosen to resemble an initially unstable massive high-redshift disc galaxy (Genzel et al., 2011), with a relatively large scalelength, and a stable outer part with a relatively flat rotation curve.
The disc setup is initially in vertical hydrostatic equilibrium (see Appendix 3.8.3), which naturally leads, for an isothermal disc, to an increasing scaleheight with radius (Fig. 3.2b),

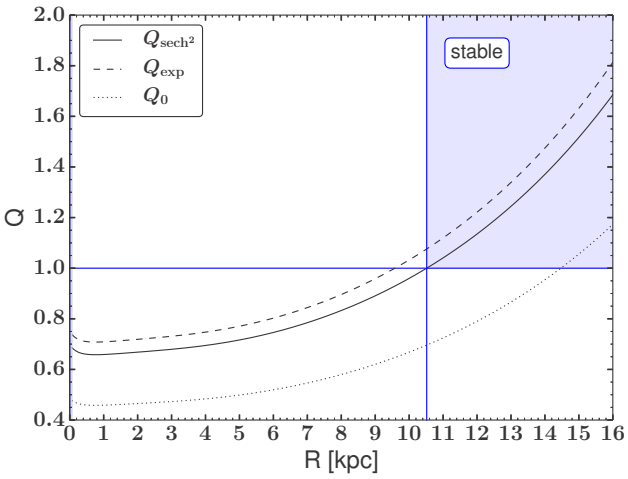

Figure 3.3: Local disc instability parameter: the solid line represents the numerical solution, according to the vertical sech^2 density profile (equation 3.27). The disc is unstable between radius $R = 0 - 10.517$ kpc and the stable part is illustrated by the blue shaded region. The exponential profile approximation (dashed line), gives a slightly more stable disc and therefore results in a smaller unstable region (see Section 3.3.6). The thin disc approximation, for $z_0 = 0$, with Toomre's Q_0 (dotted line) (equation 3.24), overestimates the instability dramatically, in intensity and with respect to the extent of the unstable region.

see also Wang et al. (2010). Hydrodynamical equilibrium is achieved by following the steps described in Wang et al. (2010), with the total rotation curve as shown in Fig. 3.2c, which consists of the contributions of the gas disc and the dark matter halo. For our sech^2-profile, the disc is unstable for axisymmetric perturbations between $R_{\mathrm{u}} = 0 - 10.517$ kpc (solid line in Fig. 3.3), becoming more stable for larger radii and totally stable for $R \geq 10.517$ kpc. The exponential profile approximation assumes a slightly more stable disc with a smaller unstable regime $R_{\mathrm{exp}} = 0 - 9.58$ kpc (dashed curve in Fig. 3.3). Using the classical Toomre Q_0, that is ignoring z_0, leads to a much more unstable disc between $R_0 = 0 - 14.47$ kpc (dotted curve in Fig. 3.3).
To form gravitationally bound clumps, an efficient cooling is needed (Gammie, 2001; Dekel, Sari & Ceverino, 2009b). This is ensured by the isothermal EoS, which keeps the temperature at 10^4 K at all densities.

3.4.3 Numerical considerations

To avoid artificial fragmentation in gravitationally collapsing gas, the Jeans length has to be resolved by at least four cells $N_{\mathrm{J}} = 4$ (Truelove et al., 1997). Ceverino, Dekel & Bournaud (2010) found convergence in their simulations in clump numbers and masses by resolving the Jeans length with at least seven elements, $N_{\mathrm{J}} = 7$, at each refinement level.
Furthermore, it is also crucial to resolve the mid-plane sufficiently, where the structures in the disc form first. Too low resolution cannot represent the higher densities there, which can lead to an unreasonable structure formation. Due to the Jeans length refinement and the density distribution of the disc, the initial AMR grid has a resolution gradient, with smaller cells in the galactic centre and larger ones at larger radius and height. The scaleheight is represented with at most two cells for $N_{\mathrm{J}} = 7$, and by increasing the number in test simulations, we

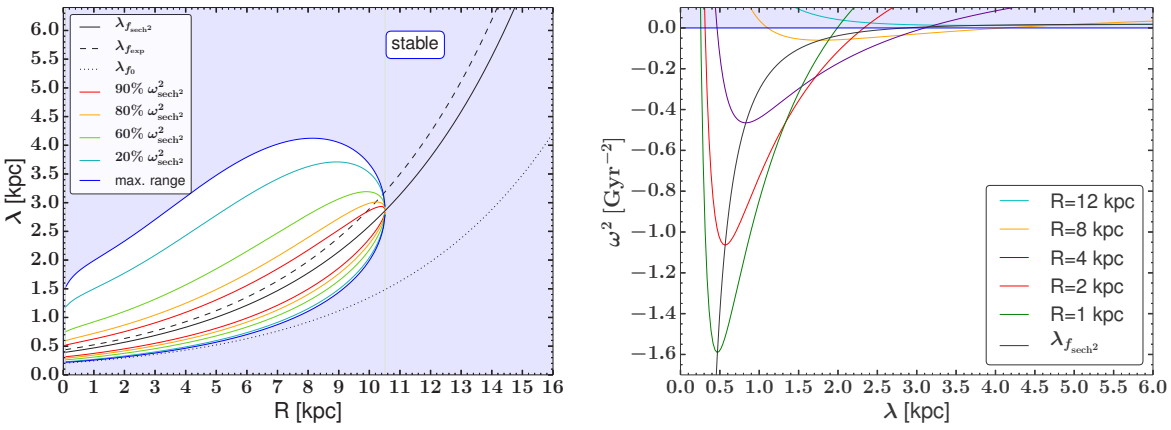

(a) (b)

Figure 3.4: (a) Possible growing wavelength at every disc radius. The black lines correspond to the fastest growing perturbation wavelength, of the sech^2 density profile (solid) (equation 3.16), the exponential density approximation (dashed) (equation 3.12) and the razor-thin disc treatment (dotted) (equation 3.11). The coloured solid lines represent unstable wavelengths with growth rates $p_{\mathrm{sech}^2} = \sqrt{-\omega^2_{\mathrm{sech}^2}}$ (Section 3.3.7) that are a fraction of the fastest growth rate and the white area is the complete region of possible growing perturbations. The transition to the stable regime (blue shaded region), with zero growth, is given by the blue solid lines. (b) The dispersion relation at different radii (coloured lines) gives the growth rate as a function of wavelength and represents slices of (a). The minimum of each R gives the fastest growing perturbation wavelength with $\lambda_{f_{\mathrm{sech}^2}}$ at that radius (black line).

found, that the ring-like structures emerge properly from the disc for $N_{\mathrm{J}} \geq 18$ grid cells per Jeans length, which corresponds to five cells per scaleheight at all radii. Too low resolution effectively raises the Q of the disc numerically and spiral-like features appear, as expected for values $Q \geq Q_{\mathrm{crit}}$, where axisymmetric modes are stable but nonaxisymmetric modes can still grow. The isothermal EoS keeps the disc scaleheight constant and therefore ensures, that it is sufficiently resolved until the structures begin to grow.
The disc is isothermal with 10^4 K. However to ensure the Jeans condition for higher densities also at maximum resolution, we add an artificial pressure floor (Bournaud et al., 2010a; Agertz, Teyssier & Moore, 2009)

$$T \geq \frac{G\, m_{\mathrm{H}}}{\pi\, k_{\mathrm{B}} \gamma} N^2 \Delta x^2_{\mathrm{min}}\, \rho, \tag{3.33}$$

where m_{H} is the atomic mass of hydrogen, k_{B} the Boltzmann constant, $\gamma = 1$ the adiabatic index, ρ the density and $N = 18$ the number of resolution elements per Jeans length for the smallest scales Δx_{min}. This does not affect the global ring formation but determines the thickness and pressure in the collapsed high-density ring structures and by this regulates their fragmentation into clumps. The effect of such a pressure floor on the clump numbers, final sizes and their interactions are beyond the scope of this study and will be investigated in a subsequent paper.

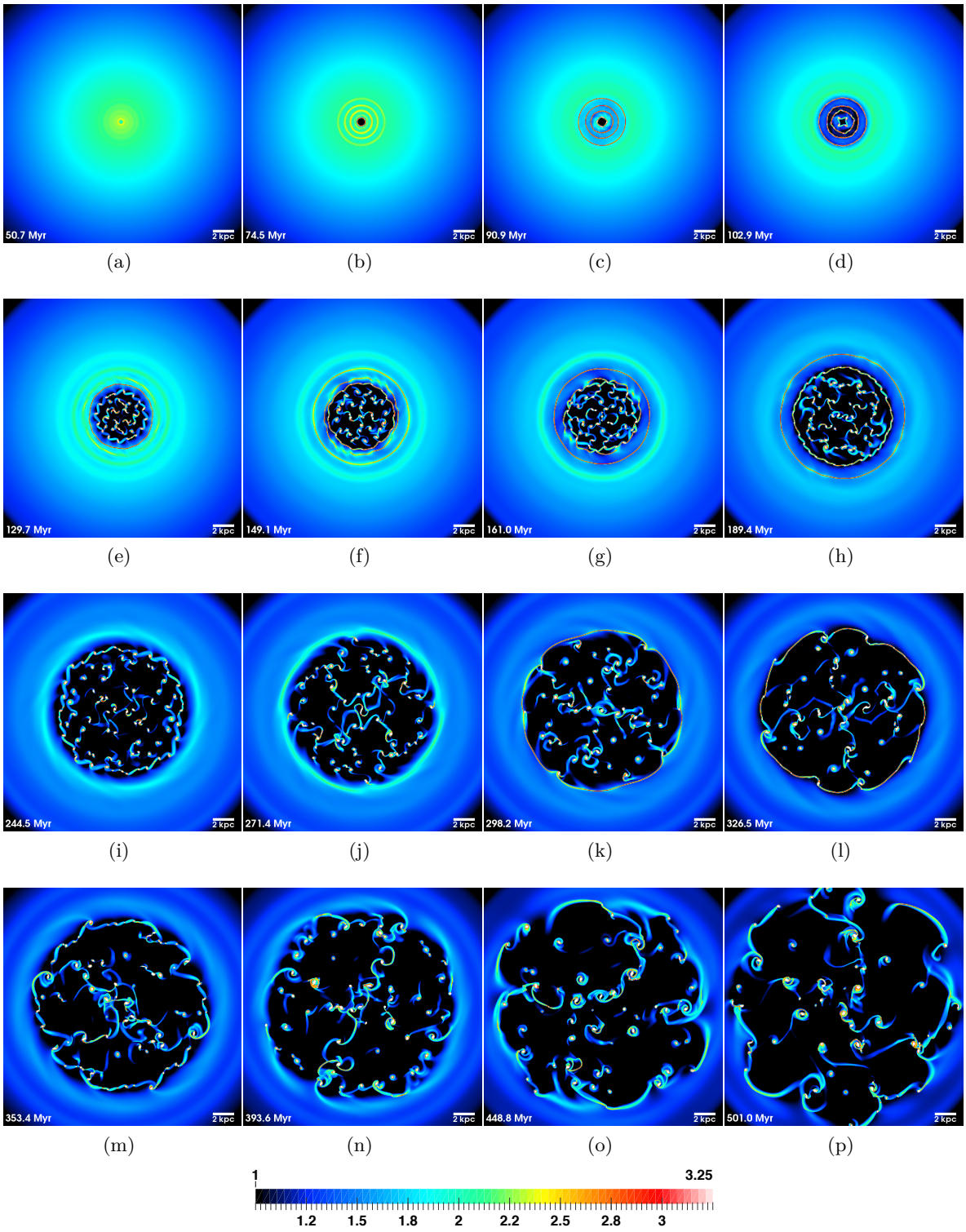

(a) (b) (c) (d)

(e) (f) (g) (h)

(i) (j) (k) (l)

(m) (n) (o) (p)

Figure 3.5: Surface density $\log_{10}(\Sigma\, M_\odot^{-1}\, pc^2)$ face-on view of the gas disc simulation at different timesteps. To illustrate the growing rings better, we limit the range of the visible densities. The upper limit is given by $1.8 \times 10^3\ M_\odot\ pc^{-2}$, while densities of $\sim 10^5\ M_\odot\ pc^{-2}$ are reached within some clumps.

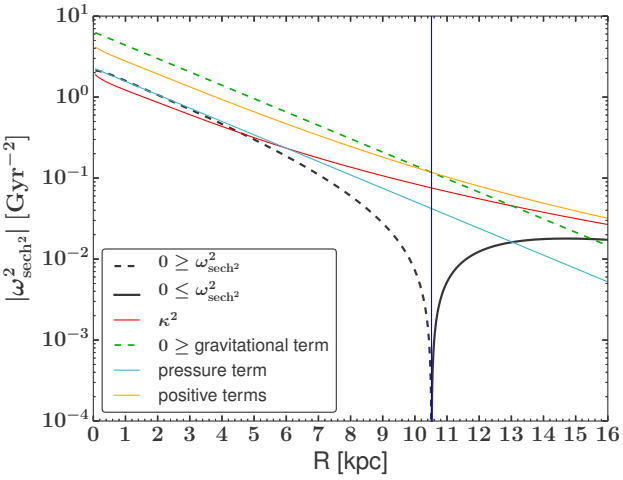

Figure 3.6: Minimum of the dispersion relation $\omega^2_{\mathrm{sech}^2} = \omega^2(\lambda_{f_{\mathrm{sech}^2}})$ (equation 3.8) in absolute values (black lines) and its decomposition (coloured lines) at every radius. The negative gravitational term (green) of equation (3.8) dominates the unstable regime (black dashed line), while the positive contributions become more important in the stable regime (black solid line). The stabilising terms (orange) consist of the epicyclic frequency term (red), with κ^2 and the pressure term (cyan), with $c_{\mathrm{s}}^2 \left(\frac{2\pi}{\lambda_{f_{\mathrm{sech}^2}}} \right)^2$. The effects of the epicyclic frequency and the pressure are comparable in the inner part of the disc, while κ^2 dominates for larger radii.

3.5 Results

3.5.1 Perturbation theory

From the modified dispersion relation (equation 3.8) for the sech^2 profile, we can derive the possible growing wavelengths for our disc model (Fig. 3.4a) in the unstable regime $R_{\mathrm{u}} = 0 - 10.517$ kpc. The fastest growing perturbation wavelength is different for every radius and increases outwards. For the sech^2 profile the range lies between $\lambda_{f_{\mathrm{sech}^2}} = [0.393, 2.862]$ kpc, while the exponential profile approximation would indicate $\lambda_{f_{\mathrm{exp}}} = [0.438, 3.191]$ kpc and in the razor-thin disc approximation we have $\lambda_{f_0} = [0.204, 1.486]$ kpc. For axisymmetric disturbances, the dispersion relation holds so long as $|kR| \gg 1$ (Binney & Tremaine, 2008a), which is $|2\pi R| \gg \lambda_{\mathrm{f}_{\mathrm{sech}^2}}$ and here fulfilled for $R \gg 63$ pc and $\lambda_{\mathrm{f}_{\mathrm{sech}^2}} \gg 392.7$. The growth rate is decreasing the larger the difference between λ and $\lambda_{f_{\mathrm{sech}^2}}$ (Fig. 3.4) and reaches zero at the maximum range. At every radius there are two wavelengths with the same growth rate $p_{\mathrm{sech}^2} = \sqrt{-\omega^2_{\mathrm{sech}^2}}$, a smaller and a larger one, relative to $\lambda_{f_{\mathrm{sech}^2}}$. With decreasing growth rate the asymmetry in the difference between λ and the corresponding fastest growing wavelength is increasing. In general, the smaller perturbation wavelengths in the disc centre can grow faster than the larger ones in the outer regime.
The dispersion relation ω^2 (Section 3.3.4) can be divided into a destabilizing term (negative), which is dominating the unstable regime R_{u}, and stabilizing terms (positive), taking over in the stable region, see Fig. 3.6. The stabilizing contribution in the disc centre is due to pressure (expressed by c_{s}) and differential rotation (expressed by κ^2), while going outwards,

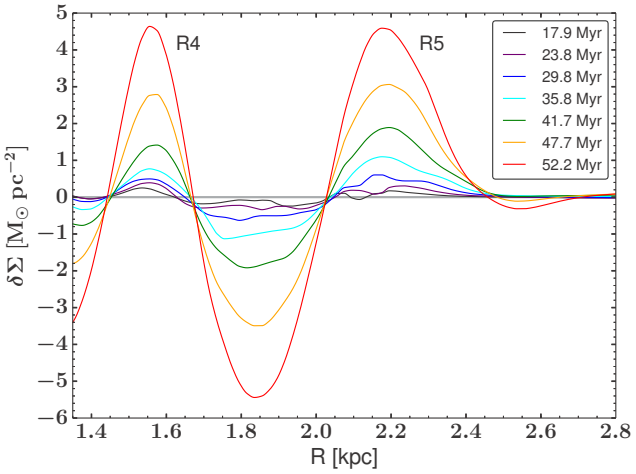

Figure 3.7: $\delta\Sigma$ profiles of rings $R4$ and $R5$ as function of time, to illustrate the clear growth of the ring structure and its wave shape character. At earlier times, superimposed fluctuations with different wavelengths and similar amplitudes appear, which makes it difficult to quantify the inflection points of the dominant wave (see Fig. 3.8). Later, one dominant wave establishes itself from the spectrum, which can be already identified at very early times.

the epicyclic frequency is more important than pressure.

3.5.2 General evolution of the surface density

Axisymmetric overdensities (rings) are forming inside–out (Fig. 3.5), as expected from our considerations in Section 3.5.1. They grow discretely at a certain radius, and their surface density increases, while they accrete mass from the inter-ring regions. At a certain point they begin to collapse to a thin circular line and finally break up into several bound clumps. A highly irregular and clumpy disc is developing within 500 Myr.
The first structures become visible in the surface density after 50 Myr (Figs 3.5 a and b) and evolve to distinct rings (Figs 3.5c-h). At later times, outer rings form with larger radial widths and on longer time-scale (Figs 3.5i-p). The last visible ring cannot fully evolve, since it is getting disturbed by the inner clumpy structure (Figs 3.5k-p).

3.5.3 Perturbation growth

The appearing rings are a result of growing perturbations of the dominant modes, from a very small density perturbation seed, caused by a superimposed wave spectrum, due to the initial AMR grid. To follow this process, we determine the relative changes of the surface density compared to the initial disc for several timesteps. Due to axisymmetry, we only consider one quadrant of the disc and average the surface density azimuthally within $\Delta R = 20$ pc bins. At each time step (~1.49 Myr), we subtract the initial surface density profile from the current one ($\delta\Sigma = \Sigma_t - \Sigma_0$). This method is only possible, because of the, initially, relatively well-balanced disc setup, and gives the quantities, which arise from the perturbation growth with a relatively clear measurable signal (see Fig. 3.7). We measure the initial seed overdensities with $\delta\Sigma(t = 0) \sim 10^{-3}$ M$_\odot$ pc^{-2}. They grow up to maximum values $\delta\Sigma(t) \sim 10^5$ M$_\odot$ pc^{-2} over time within the clumps. In Fig. 3.8, we limit the range to $\delta\Sigma = 10^{-2} - 8 \times 10^2$ M$_\odot$ pc^{-2}

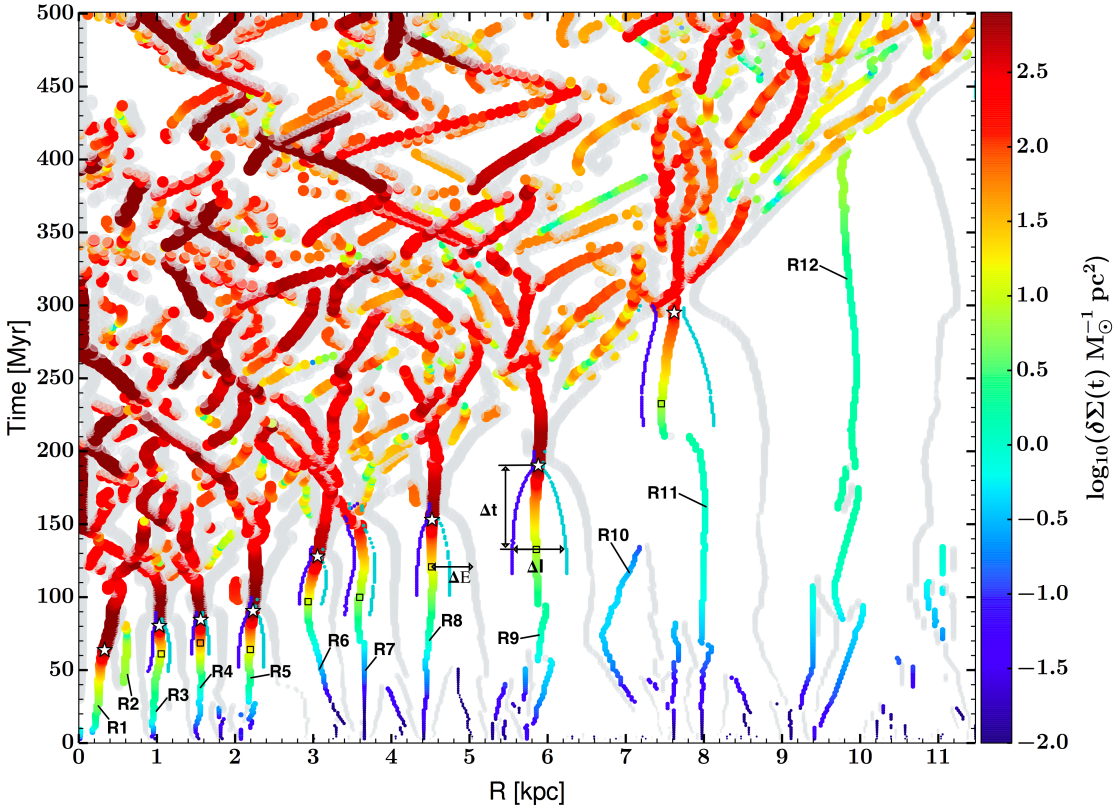

Figure 3.8: Growth of the overdensities $\delta\Sigma(t)$ (relative extrema) over time and radius (see Section 3.5.3). The colour and the size of the circles illustrate the amplitude of the relative maxima, whereas the grey circles represent the minima. To quantify the size of the fastest growing perturbation wavelength, we use the distance ΔI between the inflection points (dark-blue and cyan lines), corresponding to the overdense region of the ring L_{sech^2} (see Fig. 3.10). It is difficult to determine the growing perturbations in the initial fluctuation spectrum (see Fig. 3.7). We therefore specify the location of the inflection points when they have clearly formed (t_{g}), that is shortly before they begin to collapse (open squares). The star symbols mark the time $t_{\bigstar}$ when the density perturbations have gravitationally collapsed, shortly before they break up into clumps. The collapse time-scale Δt is the difference between t_{g} and $t_{\bigstar}$. ΔE is the distance between the maxima and their minima to the right at t_{g}. The clumpy disc is represented by the chaotic upper part of the plot.

to illustrate the amplitude of the ring overdensities. Most of the low-density disturbances disappear very early in the evolution. Only a few survive and lead to very high densities, form rings and finally fragment into a clumpy, disordered structure. The innermost ring, $R1$, is moving slightly outwards and comes very near to the second one, $R2$, while it is growing and finally begins to absorb $R2$ completely before it can break up into fragments. The rings $R3$, $R4$, $R5$, $R8$, $R9$ remain well isolated during their evolution. $R7$ is moving towards $R6$, while it is fragmenting (see also Fig. 3.5 (e)-(g)). $R10$ and $R12$ are not fully developing. While $R12$ is disrupted by the clumpy structure further in, before its fragmentation, $R10$ is moving outwards and is merging into a new maximum together with $R11$, which is causing the shift inwards of $R11$ at roughly $t = 200$ Myr. During the merging, $R10$ is not detectable

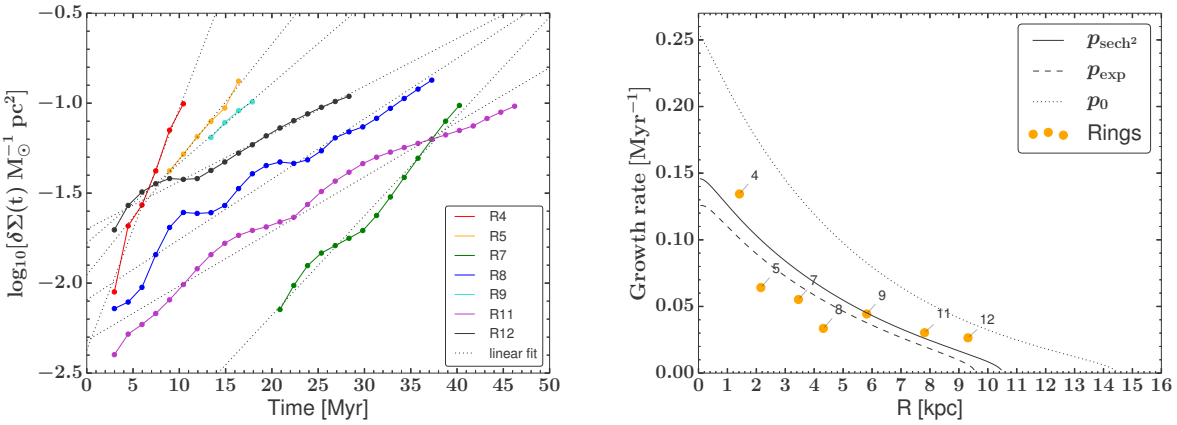

(a) (b)

Figure 3.9: (a) The logarithm of the ring overdensities over time (coloured lines) in the linear regime within the range of $\sim 10^{-2.5} - 10^{-1} M_\odot$ pc^{-2}. We make linear fits (dotted lines) to the logarithm of these amplitudes and consider only the fluctuations for which we have at least four snapshots. (b) The radius dependent growth rates $p = \sqrt{-\omega^2}$ (Section 3.3.7) correspond to the slopes of the linear fits in Fig. 3.9a (orange circles). The black lines represent the theoretically derived growth rates of the different vertical density profiles and the infinitesimally thin disc with p_0.

as a maximum because of its small amplitude.
In the beginning, the growth is exponential and therefore the rate is constant. This phase corresponds typically to overdensities of $\sim 10^{-2.5} - 10^{-1} M_\odot$ pc^{-2}, which we define as the linear domain. We make linear fits to the logarithm of these amplitudes over time and consider only the rings for which we have at least four snapshots (Fig. 3.9a). The measured slopes are in good agreement with the corresponding radius dependent theoretical growth rates (Section 3.3.7) $p_{\mathrm{sech}^2} = \sqrt{-\omega^2_{\mathrm{sech}^2}}$ and p_{exp} (Fig. 3.9b), while p_0 for an infinitesimally thin disc deviates strongly as expected.

3.5.4 Ring properties

To quantify the radial thickness of the rings, which is half of the fastest growing wavelength, we measure the distances between the inflection points ΔI of the perturbation (see Fig. 3.8). In the beginning, it is difficult to determine them from the low amplitude superimposed wavelength spectrum (e.g. Fig. 3.7). For the very low amplitudes the interactions of many initial perturbations, including those that do not grow, lead to several inflection points. With time the amplitudes of the growing wavelengths begin to dominate. At that point their inflection points can be measured properly. Therefore, we consider for the inflection points only the clearly evolved rings, a few timesteps before they begin to collapse due to self-gravity at time t_{g}. There we reach the time, when the rings' self-gravity is strong enough to begin the collapse. The minimum distance of the inflection points we define as the time $t_{\bigstar}$, just before the rings break up into clumps (marked with the symbol ★ in Fig. 3.8). Additionally, as a second constraint for the wavelength, we measure the distance ΔE between the relative maxima and minima (to the right, shown by the grey circles in Fig. 3.8) at time t_{g}. The radial

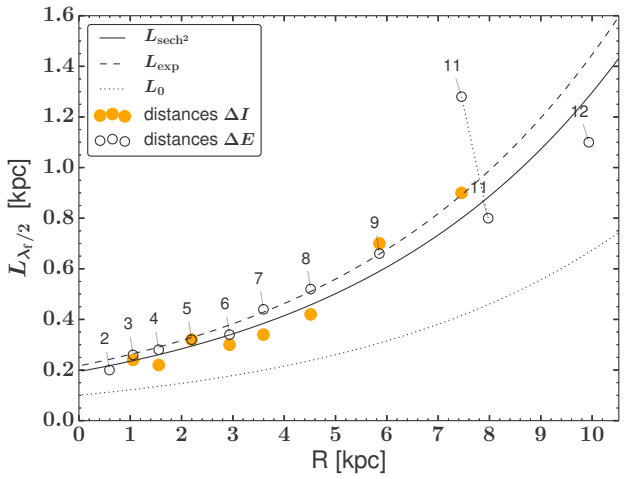

Figure 3.10: Theoretically derived radial thickness of the rings, which is half the fastest growing wavelength (see Section 3.3.5) at every radius (lines). L_{sech^2} and L_0 (equation 3.21) correspond to the vertical sech^2 density profile and to the thin disc approximation, respectively. For the vertical exponential profile approximation $L_{\mathrm{exp}} = \lambda_{\mathrm{f_{exp}}}/2$, we use equation 3.12. The data points are measured in the simulation at times t_{g}, when the rings begin to collapse. The orange circles correspond to the distances between the inflection points ΔI of the rings, the open circles give the distances between maxima and the minima ΔE, of the radial density distribution for one perturbation wavelength. For the rings $R2$ and $R12$, t_{g} is not well defined, hence we measure ΔE at $t = 50.7$ and 280.3 Myr, respectively. The density maximum of ring $R11$ is moving during its evolution (between $t \sim 200$ and 225 Myr) and the positions for both times are given by the open circles. Its minimum is not moving, which is causing the huge deviation from the expected value.

sizes ΔI and ΔE, measured at t_g (see Fig. 3.10), are in good agreement with the theoretical expectations for the sech^2 profile (see Section 3.3.5). The relative maximum of $R11$ is moving slightly inwards but not its already strongly evolved minimum, which causes the deviation from the expectation. The thin disc approximation assumes too small and the exponential density approximation slightly too large structures. At time t_g we can also determine the positions of eight rings within the disc (Fig. 3.11) and compare them to the theory in two ways. First, we take the positions of every measured ring and add radially to each the theoretical local perturbation wavelengths $\lambda_{f_{\mathrm{sech}^2}}$. This indeed gives us the opportunity to infer the distances to each of the next growing ring position, within small deviations. Most of the rings can be explained by this method, only Ring $R9$ has a larger deviation from the expectation. Furthermore, we also expect an additional ring $R10$, at $R \sim 7$ kpc, which is seen as an early phase in the evolution with its corresponding minima (see Fig. 3.8), but which merges with $R11$.

Alternatively, we start at a point near to the disc centre, take only the theoretically calculated local perturbation wavelength $\lambda_{f_{\mathrm{sech}^2}}$ and add it to infer the next position from where we repeat the process until the end of the unstable regime. All the following theoretical ring positions are dependent on the first ring. This is shown in Fig. 3.11. We choose the theoretical position of $R1$ in order to match most of the growing rings in the simulation. In our selection we are in quite good agreement with the measured rings, again an additional ring $R10$ is expected. If we repeat the same by using the perturbation wavelength $\lambda_{f_{\mathrm{exp}}}$ calculated in its unstable regime, we would expect a maximum of 10 rings and their predicted positions only partly agree with the simulation. With λ_{f_0}, we would expect 24 rings for the unstable regime of the thin disc approximation which is very different from the result of our simulation.

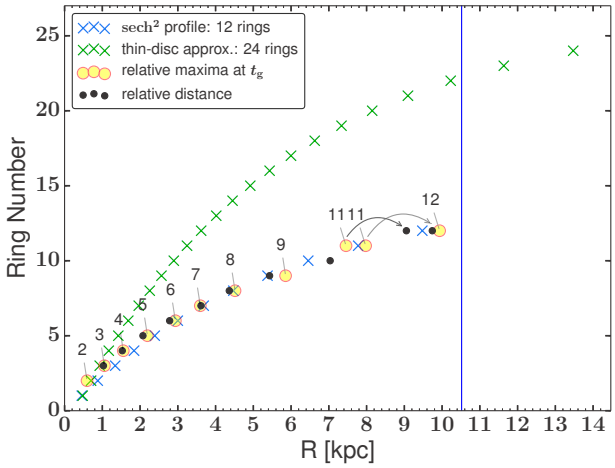

Figure 3.11: Comparison of the measured ring positions and numbers with the theoretical predictions within their unstable region. Here, we assume that the local fastest growing perturbation wavelength gives the distance to the next growing ring from inside–out. The blue crosses correspond to the sech^2 density profile and the green to the thin disc approximation. The orange data points show the measured positions of the relative density maximum at the time t_g (see also explanation in Fig. 3.10). For the black data points, we calculate the local perturbation wavelength relative for each orange data point to get every relative distance (sech^2 profile). The maxima of ring $R11$ is moving slightly inwards, therefore two data points are given.

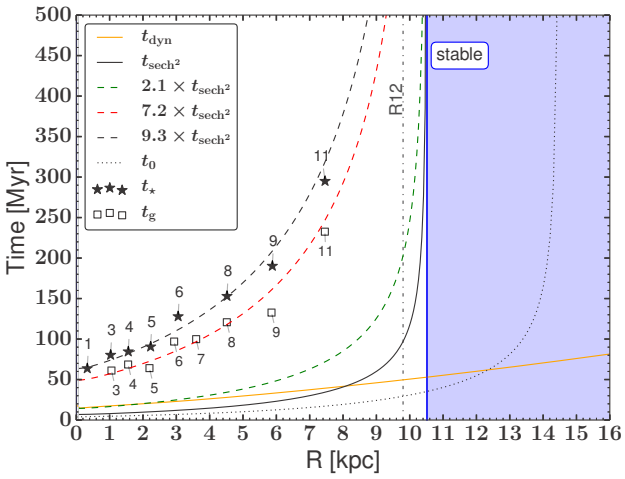

Figure 3.12: Demonstration of the different time-scales (see Section 3.3.7 and Fig. 3.8). The solid black line gives the theoretical time-scale t_{sech^2}, in which the perturbations can grow by a factor of e. The open squares give the time t_g when the ring-like structures begin to collapse, the star symbols the time $t_\bigstar$, when they reach the minimum thickness, shortly before breaking up into clumps. The t_g measurements follow $7.2 \times t_{\mathrm{sech}^2}$ (red dashed line) and the data for $t_\bigstar$ is close to $9.3 \times t_{\mathrm{sech}^2}$ (black ed line). The resulting collapsing time-scale Δt between these two time-scales is $2.1 \times t_{\mathrm{sech}^2}$ (green dashed line) and is very similar to the dynamical crossing time t_{dyn} in the inner region ($R \leq 3.5$ kpc). The dash–dotted line gives roughly the position of $R12$ and shows that the expected theoretical fragmentation is at very late times, compared to the ring structures that develop inside the disc. The thin disc approximation gives a far shorter time-scale (dotted line), and predicts fragmentation even in the already stable region according to linear analysis (blue shaded).

3.5.5 Time-scales

Here we compare our disc simulation to the time-scale t_{sech^2} (3.3.7), when the perturbation density Σ has increased by a factor of e (Fig. 3.12). The growth time remains rather short up to ~ 6 kpc and finally rises strongly and goes to infinity at $Q_{\mathrm{sech}^2} = 1$. If we rewrite equation (3.32) by inserting Q_0, we get

$$t_{\mathrm{sech}^2} = \left(D\,\Sigma^2 - \kappa^2\right)^{-1/2}, \tag{3.34}$$

with the constant factor $D = \left(\frac{\pi G}{C_{\mathrm{sech}^2}\, c_s}\right)^2$ and the only two radial dependent parameters Σ and κ. The surface density, which plays a destabilizing role, and the epicyclic frequency which stabilizes, decrease both with radius, but Σ decreases faster, especially for the last third of the unstable regime. The shape of the time-scale dependence on radius stays similar from the beginning of the growing structures up to the collapsed rings. This means that the growth time can roughly be expressed by a constant factor k times t_{sech^2} at every radius ($k \times t_{\mathrm{sech}^2}$). The rings begin to collapse at $t_g \approx 7.2 \times t_{\mathrm{sech}^2}$ (dashed red line), and reach maximum density at $t_\bigstar \approx 9.3 \times t_{\mathrm{sech}^2}$ (dashed black line), when the simulation attains the resolution limit (t_g and $t_\bigstar$ are the arithmetic mean of the corresponding data points). The collapsing time-scale Δt therefore is $2.1 \times t_{\mathrm{sech}^2}$, which is very similar to the dynamical crossing time $t_{\mathrm{dyn}} = \frac{R}{V_{\mathrm{rot}}}$ for

the inner $R = 3.5$ kpc, but is much larger with increasing radius. For the time-scale t_0 of the thin disc approximation we could not find a factor to describe the measured times t_g and $t_\bigstar$.

3.6 Discussion and Conclusions

We studied the structure formation due to gravitational instability in a self-gravitating gas disc in greater detail. The axisymmetric perturbation theory is revisited by taking its finite thickness with a typical vertical sech^2 density profile into account. To test the derived properties, we employed idealized simulations of an isothermal gas disc in hydrodynamical equilibrium, unstable to axisymmetric perturbations. From the linear stability analysis follows:

1. In the unstable regime, the fastest growing perturbation wavelength $\lambda_{f_{\mathrm{sech}^2}}$ of a vertical sech^2 density profile is always 1.926 times larger than in the classical razor-thin disc approximation $\lambda_{f_0} = \frac{2c_s^2}{G\Sigma}$ and differs therefore by 48.079%. The widely used approximation of an exponential profile leads to a wavelength $\lambda_{f_{\mathrm{exp}}}$ which is always 2.148 times larger than λ_{f_0} and gives an error of $\sim 11.527\%$ compared to $\lambda_{f_{\mathrm{sech}^2}}$. These ratios are independent of the disc scaleheight and therefore the temperature or surface density of the disc and lead to a simple correlation between $\lambda_{\mathrm{f}_{\mathrm{sech}^2}}$ and λ_{f_0} in hydrostatic equilibrium.

2. In contrast to other derivations we apply the fastest growing wavelength on the dispersion relation to determine the Toomre instability parameter and find for thick discs with a sech^2 profile the critical value $Q_{0,\mathrm{crit}} \simeq 0.696$ which is very similar to the value found by Wang et al. (2010) with $Q_{0,\mathrm{Wang}} \simeq 0.693$. For the exponential density approximation, we found the same value as in Kim, Ostriker & Stone (2002) with $Q_{0,\mathrm{KOS}} \simeq 0.647$. Also here, the relations to the razor-thin disc instability parameter are independent of the disc scaleheight. The classical Toomre Q parameter overestimates local self-gravity and leads to the assumption of a too large radial unstable regime, while the exponential approximation underestimates local self-gravity and infers a slightly too small unstable region in our disc model.

In order to test the analytical solution and to explore the transition into the highly non-linear regime, we compare it with our hydrodynamical simulations and can conclude.

1. In the first phase, rings form that organize themselves discretely, with distances corresponding to the local fastest growing perturbation wavelength $\lambda_{f_{\mathrm{sech}^2}}(R)$. The radial thickness of the measured overdensity is compatible to half of the wavelength $L_{\mathrm{sech}^2}(R) = \lambda_{f_{\mathrm{sech}^2}}(R)/2$. The total number of growing rings, calculated in their respective unstable regime, is for the exponential profile approximation underestimated by $\sim 17\%$ and their predicted positions only partly agree with the simulation. For the thin disc approach, the number is overestimated by a factor of 2.
   For an isothermal disc, both features, ring size (radial thickness) and distance, increase with radius where also the time-scales increase steeply when approaching the stable regime. While the perturbation wavelength is only dependent on sound speed and surface density (equation 3.16), the stability and growth time is additionally dependent on the differential rotation, as κ is proportional to the angular frequency Ω (equation 3.34). The initial perturbation spectrum is seeded by the AMR grid; however, the fastest growing modes agree with the linear analysis and later on dominate.

2. The individual rings grow in density, and later on contract to thin and dense circular lines, over the same time accreting more gas from the inter-ring regions. In the beginning, the growth is exponential and therefore the rate is constant up to overdensities of ~ 0.1 $M_\odot$ pc^{-2}, which we define as the linear domain, and which is in good agreement with the linear analysis. The ring growth rates are roughly self-similar, which is reflected in the growth by a constant factor k times t_{sech^2} at every radius ($\sim k \times t_{\mathrm{sech}^2}$), where t_{sech^2} is the theoretical time when the perturbation density Σ has increased by a factor of e. We determine the collapse time-scale Δt to be $2.1 \times t_{\mathrm{sech}^2}$, which is similar to the dynamical crossing time within the inner 3.5 kpc and strongly deviates for larger radii. We estimate the ring mass to be $M_{\mathrm{Ring}} = 2\pi\Sigma(R)\ R\ \lambda_{\mathrm{f}_{\mathrm{sech}^2}}$, where R is the location of the maximum of the density perturbation. In the thin disc approximation, the mass is underestimated by $\sim 48\%$ due to the linear proportionality of the mass to the fastest growing wavelength.

3. The dense and thin circular, ring-like filaments finally fragment into a large number of clumps. The clump sizes are not dependent on the initial radial ring widths anymore and cannot be directly predicted from the simple perturbation theory, as is usually assumed. They break up into individual clumps in an evolutionary phase where the rings have already developed strongly non-linear, perturbed regions. At this point, the role of axisymmetric perturbations, the resolution limit, the artificial pressure floor and other physical processes become important. We will investigate the emergence of clumps by ring instabilities in an upcoming publication. Furthermore, non-axisymmetric modes have to be studied in greater detail.

4. In order to guarantee proper growth of the initial ring structures, we find that simulations have to resolve the initial Jeans length in the disc mid-plane with more than 18 grid cells, which corresponds to about five cells per disc scaleheight.

3.7 Acknowledgements

We thank our referee Richard Durisen, for important comments that helped to clarify the paper. We are grateful to Alessandro Romeo and Bruce Elmegreen for comments and Alessandro Ballone for useful discussions. Computer resources for this project have been provided by the Leibniz Supercomputer Centre under grant: h0075. MS was supported by the Deutsche Forschungsgemeinschaft under the priority programme 1573 ('Physics of the Interstellar Medium').

3.8 Appendix

3.8.1 Derivation of the reduction factor of the potential due to the disc thickness

Density perturbations correlate with variations in the gravitational field and are specified by the local gravitational potential Φ_0, which is given by the solution of the Poisson equation in the stationary form with (e.g. Binney & Tremaine, 2008a; Wang et al., 2010)

$$\Phi_0(k,x,z) = -\frac{2\pi G\Sigma}{\mid k \mid} \, \mathrm{e}^{\mathrm{i}kx-|kz|}. \tag{3.35}$$

Here, Σ is the total surface density, k the wavenumber, and $x = R - R_0$ the position near a given location R_0, and G is the gravitational constant. Φ_0 approaches zero for low surface densities Σ and large distances z from the plane. We consider only $k \geq 0$ and replace the wavenumber by the wavelength $\lambda = 2\pi/k$, then

$$\Phi_0(\lambda,x,z) = -G\,\Sigma\,\lambda\,\mathrm{e}^{\frac{2\pi}{\lambda}(\mathrm{i}x-|z|)}. \tag{3.36}$$

For the total potential of an axisymmetric three-dimensional disc with a finite thickness, we sum-up all contributions, generated from infinitesimally thin layers at all vertical distances h (e.g. Wang et al. (2010))

$$\Phi_{\mathrm{tot}}(\lambda,x,z) = \int_{-\infty}^{\infty} \Phi_0(\lambda,x,z-h)\,t(h)\,dh. \tag{3.37}$$

Here, $t(h)$ represents the vertical distribution of the gas density and satisfies the normalization condition

$$\int_{-\infty}^{+\infty} t(h)\,dh = 1, \tag{3.38}$$

while $\Sigma t(h)\,dh$ is the surface density of an infinitesimally thin layer that is located at h above the mid-plane. Then

$$\Phi_{\mathrm{tot}}(\lambda,x,z) = -G\,\Sigma\,\lambda\,\mathrm{e}^{\frac{2\pi}{\lambda}\mathrm{i}x}\int_{-\infty}^{\infty}\mathrm{e}^{-\frac{2\pi}{\lambda}|z-h|}\,t(h)\,dh, \tag{3.39}$$

while the reduction factor is defined due to equation (3.1) as

$$F(\lambda) = \int_{-\infty}^{\infty}\mathrm{e}^{-\frac{2\pi}{\lambda}|h|}\,t(h)\,dh. \tag{3.40}$$

Hence with the normalization equation (3.38) $t(h) = \mathrm{sech}^2(h/z_0)/(2z_0)$ and equation (3.40) leads to equation (3.3) and for the exponential profile to equation (3.4).

3.8.2 Calculation of the fastest growing wavelength for the exponential profile approximation

Here, we calculate the analytical solution of the fastest growing perturbation wavelength $\lambda_{f_{\mathrm{exp}}} = \lambda_{f_{\mathrm{exp}}}(\Sigma, c_{\mathrm{s}}, z_0)$, the global minimum of the dispersion relation for the exponential thickness approximation equation (3.9) for $\lambda > 0$

$$\frac{\partial\omega^2_{\mathrm{exp}}}{\partial\lambda} = 4\pi^2\left(\frac{G\,\Sigma}{(\lambda+2\pi z_0)^2} - \frac{2c_{\mathrm{s}}^2}{\lambda^3}\right) = 0, \tag{3.41}$$

with $\frac{\partial^2 \omega^2_{\rm exp}}{\partial^2 \lambda} < 0$.
We only consider the real solution of three (two are imaginary), and is given by

$$\lambda_{f_{\rm exp}} = \frac{2c_{\rm s}^2}{3G\Sigma} + \frac{4c_{\rm s}^2}{9G^2\Sigma^2}\frac{(c_{\rm s}^2 + 6\pi G\,\Sigma\, z_0)}{T_A} + T_A, \tag{3.42}$$

with the substitution

$$T_{\rm A} = \left(\sqrt{\frac{16\pi^4 c_{\rm s}^4 z_0^4}{G^2\Sigma^2} + \frac{64\pi^3 c_{\rm s}^6 z_0^3}{27G^3\Sigma^3}} + \frac{8c_{\rm s}^6}{27G^3\Sigma^3} + \frac{8\pi c_{\rm s}^4 z_0}{3G^2\Sigma^2} + \frac{4\pi^2 c_{\rm s}^2 z_0^2}{G\Sigma}\right)^{1/3}. \tag{3.43}$$

With the scaleheight z_0 equation (3.2) and the fastest growing wavelength λ_{f_0} equation (3.11) of the thin disc approximation, which simplifies to $\lambda_{f_{\rm exp}}(\Sigma, c_{\rm s}, z_0) \rightarrow \lambda_{f_{\rm exp}}(\Sigma, c_{\rm s}) \rightarrow \lambda_{f_{\rm exp}}(\lambda_{f_0})$, and is

$$\lambda_{f_{\rm exp}} = \lambda_{f_0}\left(\frac{1}{3} + \frac{7}{9T_{\rm A}} + T_{\rm A}\right), \tag{3.44}$$

with

$$T_{\rm A} = \left(\sqrt{\frac{1}{4} + \frac{1}{27}} + \frac{1}{27} + \frac{1}{3} + \frac{1}{2}\right)^{1/3}, \tag{3.45}$$

leading finally to

$$\lambda_{f_{\rm exp}} \simeq 2.148\,\lambda_{f_0}, \tag{3.46}$$

where we call the constant factor $A_{\rm exp} \simeq 2.148$.

3.8.3 Hydrostatic equilibrium

In this section, we describe how to bring our isothermal disc in hydrostatic equilibrium. We proceed with two requirements.
1. The disc has to have an exponential surface density

$$\Sigma(R) = \Sigma_0\,\exp\left(-\frac{R}{h}\right), \tag{3.47}$$

with the central surface density Σ_0 and the scalelength h.
2. A self-gravitating gas disc with its isothermal vertical structure in hydrostatic equilibrium is given by the sech^2 density profile (Spitzer, 1942)

$$\rho_{\rm gas}(R,z) = \rho(R,0)\,\mathrm{sech}^2\left(\frac{z}{z_0(R)}\right), \tag{3.48}$$

where we keep the mid-plane density distribution $\rho(R,0)$ unknown and the scaleheight $z_0(R)$ a radial dependent quantity (Wang et al., 2010).
The surface density is the integral over the vertical gas distribution (equation 3.48) and gives

$$\Sigma(R) = \int_{-\infty}^{\infty} \rho_{\rm gas}(R,z)\,{\rm dz} = 2\,\rho(R,0)\,z_0(R), \tag{3.49}$$

and is therefore with our first requirement (equation 3.47)

$$\Sigma(R) = 2\,\rho(R,0)\,z_0(R) = \Sigma_0\,\exp\left(-\frac{R}{h}\right), \tag{3.50}$$

where the scaleheight for the constant c_s is (Wang et al., 2010; Binney & Tremaine, 2008a)

$$z_0(R) = \frac{c_s}{\sqrt{2\pi G\,\rho(R,0)}}. \tag{3.51}$$

Equations 3.50 and 3.51 lead to

$$\rho_{gas}(R,z) = \rho_c \exp\left(-\frac{R}{h}\right)^2 \operatorname{sech}^2\left(\frac{z}{z_0(R)}\right), \tag{3.52}$$

with the constant central density

$$\rho_c = \frac{\Sigma_0^2 \pi G}{2c_s^2}. \tag{3.53}$$

The calculation does not take an external potential into account and, therefore, requires the vertical force of self-gravitating gas to dominate the external dark matter halo potential within the disc (see Wang et al. (2010)):

$$F_{z,gas} \gg F_{z,DM}, \tag{3.54}$$

which is fulfilled for our disc setup (see Fig. 3.13).

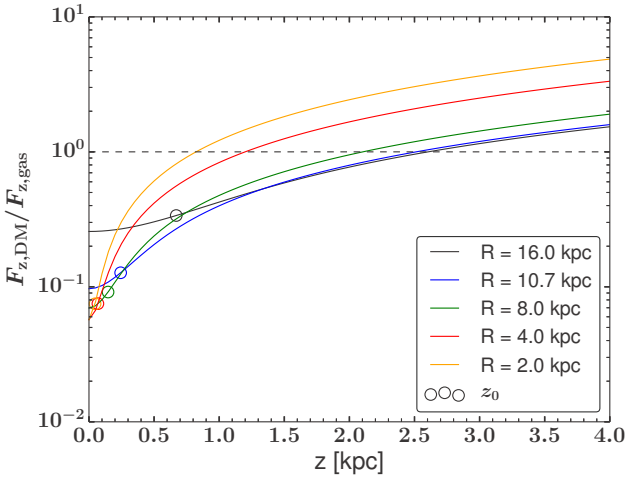

Figure 3.13: The ratio of the vertical forces corresponding to the gas disc and the dark matter halo for different disc radii. With distance from the mid-plane the dark matter plays an increasingly stronger role. The open circles mark the scaleheights z_0 at the corresponding radius R and lie clearly in the regime, where the self-gravity of the disc still strongly dominates.

Chapter 4

Clusters of small clumps can explain the peculiar properties of giant clumps in high-redshift galaxies

Published in: The Astrophysical Journal Letters
Behrendt, Burkert & Schartmann (2016)

4.1 Abstract

Giant clumps are a characteristic feature of observed high-redshift disk galaxies. We propose that these kpc-sized clumps have a complex substructure and are the result of many smaller clumps self-organizing themselves into clump clusters (CC). This bottom-up scenario is in contrast to the common top-down view that these giant clumps form first and then sub fragment. Using a high resolution hydrodynamical simulation of an isolated, fragmented massive gas disk and mimicking the observations from Genzel et al. (2011) at $z \sim 2$, we find remarkable agreement in many details. The CCs appear as single entities of sizes $R_{\mathrm{HWHM}} \simeq 0.9 - 1.4$ kpc and masses $\sim 1.5 - 3 \times 10^9$ $\mathrm{M}_\odot$ representative of high-z observations. They are organized in a ring around the center of the galaxy. The origin of the observed clumps' high intrinsic velocity dispersion $\sigma_{\mathrm{intrinsic}} \simeq 50 - 100$ km s^{-1} is fully explained by the internal irregular motions of their substructure in our simulation. No additional energy input, e.g. via stellar feedback, is necessary. Furthermore, in agreement with observations, we find a small velocity gradient $V_{\mathrm{grad}} \simeq 8 - 27$ km s^{-1} kpc^{-1} along the CCs in the beam smeared velocity residual maps which corresponds to net prograde and retrograde rotation with respect to the rotation of the galactic disk. The CC scenario could have strong implications for the internal evolution, lifetimes and the migration timescales of the observed giant clumps, bulge growth and AGN activity, stellar feedback and the chemical enrichment history of galactic disks.

4.2 Introduction

Typical characteristics of observed high redshift ($z \sim 1-3$) star-forming galaxies are their large baryonic cold gas fractions (Daddi et al., 2008, 2010; Tacconi et al., 2008, 2010, 2013) and high velocity dispersion, their irregular morphology and a few kpc-sized clumps containing baryonic masses of $\gtrsim 10^8 - 10^9$ $\mathrm{M}_\odot$ (Elmegreen, Elmegreen & Hirst, 2004; Elmegreen et al., 2005a, 2007; Förster Schreiber et al., 2009, 2011a,b; Genzel et al., 2011, 2014). The common understanding is that these higher gas fractions and densities lead to gravitationally unstable disks with a Toomre parameter $Q < 0.7$ (Toomre, 1964; Goldreich & Lynden-Bell, 1965;

Behrendt, Burkert & Schartmann, 2015) that fragment into a few kpc-sized objects (Bournaud, 2016, and references therein). This picture is supported by the detection of massive clumps in observations and from cosmological simulations. Linear perturbation theory indeed predicts a dominant growing wavelength of order of several 100 pc to kpc (e.g. Dekel, Sari & Ceverino, 2009b; Genzel et al., 2011). Behrendt, Burkert & Schartmann (2015) however showed recently that this wavelength determines the initial sizes of a few axisymmetric rings growing from inside-out instead of a few kpc-sized clumps if initially the densities in the mid-plane are sufficiently resolved (see also Bournaud et al. 2014 and Figure 6 in Bournaud 2016). These rings break up into many clumps after they collapsed onto pc-scales. The typical clump ensemble in a simulation of a massive disk with $\sim 3\times10^{10}$ $M_\odot$ is initially dominated by clumps with average masses of $\sim 2\times10^{7}$ $M_\odot$ and a typical radius $R \sim 35$ pc and later on most of the mass resides in a population of clumps with $\sim 2\times10^{8}$ $M_\odot$ and a radius of $R \sim 60$ pc (M. Behrendt et al., 2016, in preparation). Interestingly, a similar mass range has been found in the studies of Tamburello et al. (2015) where the clumps fragment from spiral features produced at $Q \sim Q_{\rm crit}$. Later on, the clumps in our simulation quickly form groups on several 100 pc to kpc-scales which we will call clump clusters [1] (CC).

In this letter we explore the question whether these CCs could resemble the properties of the giant clumps observed in redshift 2 galaxies. An important role plays the instrumental resolution which spatially smears-out the information on kpc-scales. Hints for substructure are however mainly given by local gas-rich disk galaxies which can be observed with much higher resolution. The DYNAMO survey identified local galaxies with very similar properties as found at $z \sim 2$ (Green et al., 2010; Fisher et al., 2014; Bassett et al., 2014) containing clumps with typical diameters $< d_{\rm clump} > \sim 0.6$ kpc (Fisher, 2015).

We use a higher resolution version of the simulation presented in Behrendt, Burkert & Schartmann (2015) and compare clump cluster properties with the giant clumps of the five luminous star-forming disk galaxies at $z \sim 2$ from Genzel et al. (2011). This pioneering work for the first time presented detailed line profiles of individual giant clumps. The following list summarizes the observationally motivated questions that can be explained by our CC scenario.

1. Do the giant clumps have substructure? Observationally, only one example of a very bright clump is found where a substructure is hinted in the velocity channel maps given the large beam smearing.

2. What is the origin of the high intrinsic velocity dispersion $\sigma_{\rm intrinsic} \simeq 50-100$ km s^{-1} of the clumps? Often this is attributed to stellar feedback, but in the analysis of the observations no significant correlation between local velocity dispersion and star formation rates could be found.

3. Are the giant clumps rotationally supported? Small velocity gradients are found along the clumps $V_{\rm grad} \simeq 10-30$ km s^{-1} kpc^{-1} in the velocity residual maps which corresponds to net prograde and retrograde rotation with respect to the rotation of the galaxy. When considering the beam-smearing effects on the kinematics Genzel et al. (2011) concluded that these clumps are either pressure supported by high velocity dispersion (see also Dekel & Krumholz, 2013) or they are still undergoing collapse because of the small velocity gradients.

[1] The term "clump clusters" was used in the literature previously to describe a conglomeration of kpc-sized structures seen at high redshifts. It was later on abandoned and replaced by the notation "clumpy galaxies" (see the explanation in Elmegreen & Elmegreen, 2005).

In Section 4.3 we describe the simulation code and the disk setup and how we mimick the observations. Section 4.4 gives an overview of the disk evolution and addresses the single issues listed above. Finally, in Section 4.5 we summarize the results and derive implications.

4.3 Simulation

4.3.1 Code and disk setup

We run the simulation with the hydrodynamical AMR code RAMSES (Teyssier, 2002) in a box of 48 kpc and with a maximum resolution Δx = 2.9 pc. The hydrodynamical equations describing the evolution of the self-gravitating gas disk with an isothermal equation of state are solved by the HLL Riemann solver and the MinMod slope limiter (Fromang, Hennebelle & Teyssier, 2006). A static dark matter halo is added as an external potential. To sufficiently resolve the mid-plane gas density distribution we represent the Jeans length by at least $N_{\rm J}$ = 19 grid cells at every resolution level and the refinement criterium stops at maximum resolution. To avoid artificial fragmentation also for higher densities at 2.9 pc resolution we add a pressure floor in order to assure $N_{\rm J}$ = 7 grid elements per Jeans length which leads to a lower limit for the clump radius of 10.3 pc (Truelove et al., 1997; Agertz, Teyssier & Moore, 2009; Bournaud et al., 2010b). The same disk model as in Behrendt, Burkert & Schartmann (2015) is used. We adopt an exponential gas disk with total mass $M_{\rm disk} = 2.7 \times 10^{10}$ M$_\odot$, scale length h = 5.26 kpc and outer radius $R_{\rm disk}$ = 16 kpc. The Toomre parameter is $Q < 0.7$ within 10.5 kpc and the disk is therefore unstable to axisymmetric modes in this radius regime. The dark matter halo has the density profile of Burkert (1995) with $M_{\rm DM} = 1.03 \times 10^{11}$ M$_\odot$ within 16 kpc. The isothermal temperature of 10^4 K represents the typical micro-turbulent pressure floor and keeps the initial vertical density distribution stable until the disk fragments.

4.3.2 Mimicking the observations

We compare the results with the clump properties of the Hα observations of five disk galaxies from Genzel et al. (2011) at $z \sim 2.2-2.4$. The instrumental angular resolutions of $0''.18-0''.25$ correspond to FWHM $\simeq 1.5-2.1$ kpc. We "observe" the simulated galaxy at an inclination $i = 60°$ which is the most likely value for a random orientation and construct line-of-sight (LOS) maps of the spatial and kinematic components. The resolution of the observational instrument is mimicked by convolving the LOS surface density with a 2D Gaussian of FWHM = 1.6 kpc (Section 3.2). The result can be interpreted as a map of the molecular gas surface density since the majority of the gas mass ($\sim 76\%$) resides in clumps with surface densities $\gg 100$ M$_\odot$ pc^{-2}. This corresponds to the observed Hα maps due to the usually adopted linear "Kennicutt-Schmidt" relation from Tacconi et al. (2013) (PHIBBS calibration), see also Genzel et al. (2014). For the kinematic analysis we take the mass-weighted LOS velocity information of the simulation. Tacconi et al. (2013) found that the ratio of rotational velocity to local velocity dispersion in CO agree to first order with ratios obtained from Hα of similar star forming galaxies. The LOS velocities of the clump regions in Section (3.3) are binned into "channels" of width 34 km s^{-1} and spatially convolved. To obtain the intrinsic clump velocities the beam-smeared LOS velocity of a rotating featureless exponential disk model is subtracted. We do not convolve with the instrumental spectral resolution of FWHM = 85 km s^{-1} since this contribution is already removed in the observational values we compare with.

4.4 Results

4.4.1 Overview of the disk evolution

The simulation evolves like in Behrendt, Burkert & Schartmann (2015). The main difference in the new simulation is its higher spatial resolution which in turn increases the resolution of the CCs that are the focus of this letter. In addition, we were able to reduce the pressure floor to a more realistical value. The unstable disk fragments into rings from inside-out in

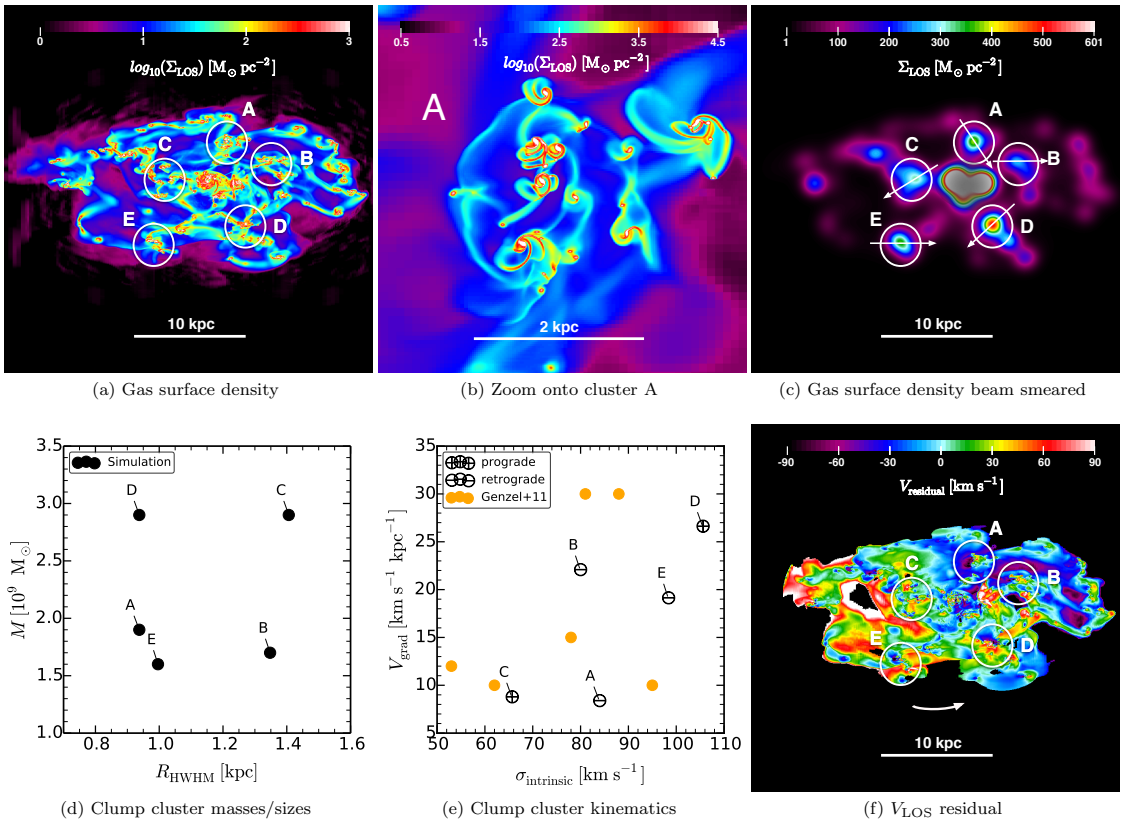

(a) Gas surface density (b) Zoom onto cluster A (c) Gas surface density beam smeared

(d) Clump cluster masses/sizes (e) Clump cluster kinematics (f) $V_{\rm LOS}$ residual

Figure 4.1: (a) The LOS surface density of the galaxy at an inclination $i = 60°$ (limited to a maximum of 10^3 $M_\odot$ pc^{-2}). The analyzed clusters are marked with circles and labeled (A, B, C, D, E). (b) The zoom-in face-on surface density map of cluster A limited to the maximum surface density $10^{4.5}$ $M_\odot$ pc^{-2}. (c) The beam smeared LOS surface density (FWHM = 1.6 kpc) of the galaxy at $i = 60°$. The arrows represent the measured cuts of the velocity gradients and point into the direction from blue to redshifted. $V_{\rm grad}$ is calculated within $R_{\rm HWHM}$ in Equation (4.1). The center is intentionally shaded for better visualisation of the clump structure in the disk region. (d) The masses of the simulated CCs and their radii $R_{\rm HWHM}$. (e) The velocity gradients along the clusters (arrows in Figure 1c) within $R_{\rm HWHM}$ and their intrinsic velocity dispersion are compared with the observations (Genzel et al., 2011). Their rotational direction is given by the plus symbol for prograde and the minus symbol for retrograde spin with respect to the rotation of the galaxy. (f) LOS velocity residual maps (limited velocity range) of the galaxy at $i = 60°$ for surface densities $\Sigma_{\rm LOS} > 4$ $M_\odot$ pc^{-2} and within the disk radius of 16 kpc.

excellent agreement with the local fastest growing wavelength. The rings subsequently break up into hundreds of clumps, identified with a clump finder (Bleuler & Teyssier, 2014) and considering gas densities $n_H \geq 100$ cm^{-3}. The clump statistic will be discussed in great details in a forthcoming paper (M. Behrendt et al., 2016, in preparation). The clumps initially have typical masses of several $\times 10^7$ M$_\odot$ and radii around 35 pc. They later on evolve by merging with other clumps and re-organize themselves into large clump clusters. The fragmented disk (at 655 Myr) can be seen in the LOS surface density map in Figure 1a. In this simulation we do not include stellar feedback. We however refer to the study and discussion in Bournaud et al. (2014) who have shown that mainly the clumps below a mass of a few 10^7 M$_\odot$ are short-lived and effected by stellar feedback processes while the more massive clumps can survive several hundreds of Myr which is long enough for clump clusters to form, as discussed in the next section. In future work we will include stellar feedback in order to investigate its effect on the evolution.

4.4.2 Clump clusters appear as kpc-sized clumps

The clumps organize themselves into clusters on several 100 pc to kpc scales. These clump clusters represent groups of individual clumps with diameters ~ 100 pc. As an example, a zoom-in onto the Cluster A in the evolved disk (655 Myr) is shown in Figure 1b. The region has a radius of ~ 1.25 kpc in the face-on view. When we convolve the LOS surface density map with a Gaussian filter of FWHM = 1.6 kpc the substructure of the CCs is completely smeared out (Figure 1c). They now appear as single entities, arranged into a ring with a radius of 4 - 7.7 kpc around the center of the galaxy. At t=655 Myr we also find that clump clusters merge in the center of the galaxy, leading to the formation of a bulge component. The details of bulge formation by CCs will be investigated in a forthcoming paper (M. Behrendt et al., 2016, in preparation). Here, we focus on the prominent CCs, labeled A,B,C,D,E in the galactic disk region. Since the disk is fragmenting from inside-out these clusters were build from clumps that formed after 300 Myr. The beam smeared CC's surface densities peak at $\Sigma_{\rm LOS}$ = 300 – 600 M$_\odot$ pc^{-2} and the more elongated clusters (B, C) have somewhat smaller surface densities in the convolved map compared to the clusters with more concentrated substructure (A, D, E). Their large radii of $R_{\rm HWHM}$ = 0.95 – 1.4 kpc (Figure 1d) are similar to the identified clumps in Genzel et al. (2011). The CC's total masses are $1.6 - 3 \times\ 10^9$ M$_\odot$. The typical clumps in Genzel et al. (2011) have masses a few times 10^9 M$_\odot$ and the most extreme clumps masses of ~ 10^{10} M$_\odot$. The difference to our result can by explained by the around three times larger total baryonic mass in their observed galaxies.

4.4.3 Origin of the intrinsic high velocity dispersion

The measured intrinsic velocity dispersion of the five CCs is shown in Figure 1e. Before we construct the integrated spectrum of the cluster regions we take the LOS velocity and bin it into "channel" maps of width 34 km s^{-1} which we spatially convolve with a Gaussian of FWHM = 1.6 kpc. Then we subtract the beam-smeared rotation of the smoothed galactic disk model to extract the velocity imprint of the clumps. The remaining integrated residual velocities of a cluster region are normalized to the maximum "intensity" (LOS surface density). As shown in Figure 1e our CCs have velocity dispersions of $\sigma_{\rm intrinsic} \simeq 65 - 105$ km s^{-1} in remarkable agreement with the observations. These high values are a result of the internal irregular motions of their substructures. The original (unsmeared) data gives almost the same

velocity dispersion with only $1-5$ km s^{-1} difference.

4.4.4 Spin of the kpc-sized clumps

In not enough resolved numerical simulations of gas-rich disks the kpc-sized clumps are fast rotating and supported by internal centrifugal forces (e.g. Immeli et al., 2004b,a; Dekel, Sari & Ceverino, 2009b; Aumer et al., 2010). This is in contradiction to the observations that indicate dispersion-dominated clumps, being stabilized by random motion rather than rotation (see also Dekel & Krumholz, 2013). The high resolution simulations presented in Ceverino et al. (2012) indeed show a rich spectrum of substructures (see also Bournaud, 2016), similar to our simulation. They argue that the internal supersonic turbulence dominates the kinematics of the giant clumps and induces the break-up into sub-units. We instead conclude that small clumps form first, organize themselves to giant clusters which build the substructure that regulates the cluster dynamics. Following Genzel et al. (2011) we measure velocity gradients along cuts of largest gradients

$$V_{\rm grad} = \frac{(v_{\rm max} - v_{\rm min})_{\rm residual}}{2\sin(i) R_{\rm HWHM}} \tag{4.1}$$

of the CCs of our beam smeared residual maps (inclination corrected) which we indicate with arrows in Figure 1c. The gradients range in between $V_{\rm grad} \simeq 8-27$ km s^{-1} kpc^{-1} (Figure 1e) which is again in surprisingly good agreement with the observations. The self-rotation of the individual clumps within a CC is completely washed out and only a gradient over the whole cluster region remains which has several reasons. For better understanding we show the un-smeared LOS residual velocities in Figure 1f where the clusters can be identified as "Rotating Islands" (A, B, D, E). They appear as large blue and red shifted areas with small substructures of high velocities representing the individual, spinning clumps. Cluster C shows only a modest imprint of a velocity gradient with ~ 8 km s^{-1} kpc^{-1} since its substructures are "coincidently" close together. The other clusters rotate either slowly or faster around their centers of mass and are continuously perturbed by encounters with other CCs. We could not find any correlation between the kinematics and their masses or radii. Clusters with a larger $V_{\rm grad}$ have a tendency to also have an increased $\sigma_{\rm intrinsic}$ in our snapshot, however, the statistics is too low to argue that it is significant. The observed clumps also show prograde and retrograde velocity gradients with respect to the rotation of the galaxy. A giant clump which formed due to gravitational instability in a sheared disk should however have an angular momentum vector pointing into the same direction as its host galaxy. This coordinated rotation is indeed seen in the clumps that formed initially by gravitational disk instabilities. The situation is however different for our CCs as they continuously interact or merge with clumps. The clusters A,B,E rotate retrograde while C and D rotate prograde (indicated by the direction of the arrow from blue to redshifted velocities in Figure 1c and by the symbols in Figure 1e).

4.5 Summary and Conclusions

We compared a high-resolution simulation of a clumpy massive gas disk with the $z \sim 2$ galaxies of Genzel et al. (2011). The Toomre unstable $Q < Q_{\rm crit}$ disk naturally evolves into a large number of clumps, initially with an average mass 2×10^7 M$_\odot$ ($R = 35$ pc) and later on most of

the mass in mergers of $\sim 2 \times 10^8$ $M_\odot$ with a radius of $R \sim 60$ pc (M. Behrendt et al., 2016, in preparation). They subsequently self-organize into several 100 pc to kpc-sized clump clusters (CCs) in a ring-like distribution. We analyze the fully fragmented disk at an inclination of $i = 60°$. By mimicking the observations we find the following results:

1. In the beam-smeared disk (FWHM = 1.6 kpc) the small-scale substructure disappears and only a few giant clumps are visible with $R_{\rm HWHM} \simeq 0.9 - 1.4$ kpc and masses of $\sim 1.5 - 3 \times 10^9$ $M_\odot$. They are organized in a ring with a radius of 4 - 7.7 kpc around the center of the galaxy. The giant clumps are actually clump clusters and show a rich substructure on pc scales. The model galaxy has around three times less baryonic mass than the observed galaxies in Genzel et al. (2011) which is reflected in 3 times less massive clump clusters.

2. The high intrinsic velocity dispersion $\sigma_{\rm intrinsic} \simeq 65 - 105$ km s^{-1} of the CCs is caused by their subclump's high irregular motions. This is in contrast to previous assumptions that attributed the dispersion to turbulence, generated by stellar feedback. We tested the effect of beam smearing on the inferred velocity dispersions and find no significant differences, indicating that these signatures can be used as realistic indicators of the CC kinematics. The observed high dispersion of massive clumps in gas-rich galaxies might therefore be indirect evidence for a cluster of weakly bound substructures and a characteristic property of CCs. This is also in agreement with the finding of Genzel et al. (2011) that there does not exist a correlation between their dispersion of $\sigma_{\rm intrinsic} \simeq 53 - 95$ km s^{-1} and the star formation rates.

3. The clump clusters show small velocity gradients $V_{\rm grad} \simeq 8 - 27$ km s^{-1} kpc^{-1} which corresponds to net prograde or retrograde rotation with respect to the galaxy. The larger values correspond to faster rotating CCs and the smaller either to slowly spinning clusters or the substructure is "coincidently" close together to appear as a giant clump when beam-smeared.

We demonstrated that clump clusters can explain many observed properties of giant clumps at high-redshift. If the observed unresolved massive clumps indeed are ensembles of dense subclumps, this has strong implications for any model that infers their evolution. Kpc sized clumps are expected to migrate to the disk center via dynamical friction and tidal torques on a few orbital timescales where they contribute to the formation of a bulge (Noguchi, 1999; Immeli et al., 2004b,a; Förster Schreiber et al., 2006; Genzel et al., 2006, 2008, 2011; Elmegreen, Bournaud & Elmegreen, 2008; Carollo et al., 2007; Bournaud, Elmegreen & Martig, 2009; Dekel, Sari & Ceverino, 2009b; Ceverino, Dekel & Bournaud, 2010; Bournaud, 2016). The CC scenario could have a strong effect on the estimated migration timescale of dense gas into centers of gas-rich galaxies which can have strong influence on the feeding of central black holes and AGN activity. Star formation and stellar feedback processes should also be strongly affected by the substructure (Dekel & Krumholz, 2013) and their chemical enrichment history. Here we focused on the structure of CCs and their observational properties. However, CCs also have an interesting and complex evolution. They for example are exchanging their substructure or even disperse and reform. This will be discussed in detail in a subsequent paper.

4.6 Acknowledgements

We thank the referee for constructive comments that improved the quality of the manuscript. We are grateful to Philipp Lang, Lucio Mayer, Go Ogiya, Michael Opitsch and Valentina Tamburello for fruitful discussions. We also thank Frédéric Bournaud and Avishai Dekel for valuable comments. The computer simulations were performed on the HPC system HYDRA at the Rechenzentrum Garching (RZG) of the Max Planck Gesellschaft.

Chapter 5

The possible hierarchical scales of observed clumps in high-redshift disc galaxies

Published in: Monthly Notices of the Royal Astronomical Society
Behrendt, Schartmann & Burkert (2019)

5.1 Abstract

Giant clumps on ~ kpc scales and with masses of $10^8 - 10^9$ $M_\odot$ are ubiquitous in observed high-redshift disc galaxies. Recent simulations and observations with high spatial resolution indicate the existence of substructure within these clumps. We perform high-resolution simulations of a massive galaxy to study the substructure formation within the framework of gravitational disc instability. We focus on an isolated and pure gas disk with an isothermal equation of state with $T = 10^4$ K that allows capturing the effects of self-gravity and hydrodynamics robustly. The main mass of the galaxy resides in rotationally supported clumps which grow by merging to a maximum clump mass of 10^8 $M_\odot$ with diameter ~ 120 pc for the dense gas. They group to clump clusters (CCs) within relatively short times ($\ll$ 50 Myr), which are present over the whole simulation time. We identify several mass and size scales on which the clusters appear as single objects at the corresponding observational resolution between ~ $10^8 - 10^9$ $M_\odot$. Most of the clusters emerge as dense groups and for larger beams they are more likely to be open structures represented by a single object. In the high resolution runs higher densities can be reached, and the initial structures can collapse further and fragment to many clumps smaller than the initial Toomre length. In our low resolution runs, the clumps directly form on larger scales 0.3 – 1 kpc with $10^8 - 10^9$ $M_\odot$. Here, the artificial pressure floor which is typically used to prevent spurious fragmentation strongly influences the initial formation of clumps and their properties at very low densities.

5.2 Introduction

The challenging observations of the distant Universe give us the outstanding opportunity to study the galaxy evolution at very early times. They reveal a diversity of galactic systems with physical properties that are different than in the local Universe. At redshift $z \sim 2$, gas-rich (Daddi et al., 2010; Tacconi et al., 2013) galaxies with an irregular morphology (Elmegreen et al., 2005b) and high random motions with an underlying coherent rotating disc (Förster Schreiber et al., 2009; Wisnioski et al., 2012) have been found. The star formation rates are

a factor of 10 to 100 times larger than in present-day Milky Way type galaxies (Elmegreen & Elmegreen, 2005; Genzel et al., 2011). A key feature are ~ kpc-sized, massive clumps of several ~ 10^8 – 10^9 $M_\odot$ with high star formation rate densities containing relatively young stars of 10 Myrs to several 100 Myrs (Förster Schreiber et al., 2011b; Wuyts et al., 2013; Zanella et al., 2015; Guo et al., 2018).

The origin of the giant clumps is well explained in the framework of the gravitational disc instability. The observed high gas densities and high random motions can lead to kpc-sized growing perturbations and the discs fragment into massive star-forming clumps if the Toomre Q parameter is below a critical value $Q < Q_{\rm crit}$ (Genzel et al., 2008; Dekel, Sari & Ceverino, 2009a). With this approach, theoretical models have been very successful in explaining or simulating many observed properties. In general, cosmological zoom-in simulations find typically a handful of giant clumps which directly form on the mass and size scales which are observed at kpc spatial resolution (Dekel, Sari & Ceverino, 2009a; Ceverino, Dekel & Bournaud, 2010; Ceverino et al., 2012). Here, the advantage is that the cosmological context can be taken into account, e.g. infalling gas from the cosmic web. A complementary approach is to simulate a galaxy in an isolated box. The advantages are the significant higher resolution that can be reached (initially and finally) and the well-defined conditions to reduce the complexity. At higher resolution a rich substructure is found within giant clumps (Ceverino et al., 2012; Bournaud et al., 2014; Bournaud, 2016; Behrendt, Burkert & Schartmann, 2016; Oklopčić et al., 2017). Overall, two possible scenarios may lead to the formation of giant clump sub-structure. In the so-called "top-down" scenario, giant gravitationally bound clumps may form directly and sub-fragment due to growing perturbations on the sub-clump scale enabled by higher resolution simulations. This picture may be supported by cosmological simulations, but at present has not been showcased in any study. In Oklopčić et al. (2017) they find sub-fragmentation caused by stellar feedback which leads to very short lived (~ 20 Myr) giant clumps. In the second scenario, many gravitationally bound clumps form on smaller scales than the estimated initial growing Toomre length (Benincasa et al., 2019). They later on conglomerate to clusters representing giant clumps with several smaller clumps ("sub-structure") (Behrendt, Burkert & Schartmann, 2015, 2016; Tamburello et al., 2017). These clusters would appear homogeneous if observed at a typical resolution of 1.6 kpc at $z \sim 2$. These clump clusters have been shown to have similar kinematic properties (Behrendt, Burkert & Schartmann, 2016) as observed for the giant star forming clumps in Genzel et al. (2011). Which of the two massive clump formation scenarios is reproduced in nature is still unclear. The effect on clump properties due to different observational resolution is evident in the recent study of a strong gravitationally lensed massive galaxy ($M_\star \approx 4 \times 10^{10}$ $M_\odot$) "the cosmic snake" (Cava et al., 2018) and the comparison to its counter image. With the SFR ~ 30 $M_\odot$ yr^{-1} it is comparable to galaxies on the main sequence at $z \sim 1$–2. Furthermore, the identified clump masses and sizes tend to correlate with the different magnifications of the images, giving 10^7 $M_\odot$ at high magnification (~ 30 pc resolution) and several 10^8 $M_\odot$ at low magnification (~ 300 pc resolution). Currently, for observations at $z \sim 2$ the spatial resolution is limited to ~ 1 – 2 kpc. One hint for a possible substructure on sub-kpc scales of a bright clump has been found in the seminal work of Genzel et al. (2011), by studying the clump gas kinematics of Hα and comparing the individual velocity channel maps. Those galaxies have very high gas fractions and much higher SFR ~ 120 – 290 $M_\odot$ yr^{-1} corresponding to the upper range of mass and bolometric luminosity of the $z \sim 2$ star forming galaxies on the main sequence (Förster Schreiber et al., 2009). Another possibility to study clump clustering are the extremely rare local clumpy galaxies whose properties are similar to those of high-redshift

discs (Fisher et al. 2017), found in a sub-sample of the DYNAMO-HST survey with massive galaxies of $M_\star \sim 1-5\times10^{10}M_\odot$, which correspond to galaxies that dominated the cosmic SFR at $z\sim1-3$. In their simulated high-redshift maps (taking blurring, surface brightness dimming, and a sensitivity cut similar to high-z observations with adaptive optics into account) the number of clumps is significantly reduced to 1-4 clumps per galaxy comparable to the amount of clumps detected in high-z surveys (Genzel et al., 2011; Swinbank et al., 2012; Wisnioski et al., 2012). The limited sensitivity may also restrict the observations to more massive clumps within a galaxy as was shown in Tamburello et al. (2017) by Hα mocks created by radiative transfer postprocessing of a clumpy galaxy simulation.
Besides the resolution effects on clump properties, an important numerical issue is the so-called artificial pressure floor (APF) in simulations. Typically, the Jeans length is resolved by several elements to avoid spurious fragmentation of a collapsing clump (Truelove et al., 1997). At the highest refinement level, this can be satisfied by using an artificially induced pressure which is commonly used in clumpy galaxy simulations (Robertson & Kravtsov, 2008; Dekel, Sari & Ceverino, 2009b; Agertz et al., 2009; Teyssier, Chapon & Bournaud, 2010; Ceverino et al., 2012; Bournaud et al., 2014; Kim et al., 2016; Hopkins et al., 2018). The effect on the number of clumps by varying the APF at the same resolution has been studied in Ceverino, Dekel & Bournaud (2010). They suggested to investigate its influence on clump properties also for simulations better than 10 pc maximum resolution.

To understand the two fragmentation scenarios from top-down and bottom-up and the clump clustering better we complement the previous studies in this article. Section 5.3 gives an overview of the used simulation methods and the different runs. Section 5.4 (i) analyses the fragmentation of a Toomre unstable gas disc and gives the detailed clump statistic over time by comparing between simulations of < 100 pc and < 10 pc maximum resolution. (ii) Furthermore, we investigate the effect of the artificial pressure floor on the clump properties. In the second part of the paper in Section 5.5 we investigate (iii) on which scales the clumps appear as clusters (iv) and how their properties are related to low and high beam smearing. In Section 5.6 we give the summary and discussion of the findings.

5.3 Simulation Methods

5.3.1 Disc model

For the disc model, we use the same setup as in Behrendt, Burkert & Schartmann (2015) which is initially in hydrostatic equilibrium in vertical direction and in centrifugal equilibrium in radial direction. The main parameters were chosen to resemble a massive high-redshift disc galaxy (Genzel et al., 2011). The gas disc has an exponential surface density profile with a total mass of $M_{\rm disc} = 2.7\times10^{10}$ M$_\odot$ with a maximum radius of $R_{\rm disc} = 16$ kpc and a scale-length $h = 5.26$ kpc and is Toomre unstable within the inner 10.5 kpc. The relatively large scale-length ensures the unstable regime and the relatively large disc radius gives a smoother transition of the low density part to the environment. The dark matter halo follows the Burkert (1995) density profile with a mass of $M_{\rm DM} = 1.03\times10^{11}$ M$_\odot$ within the disc radius and a scale length of $r_{\rm s} = 4$ kpc. Efficient cooling is needed to form gravitationally bound clumps, ensured by the isothermal equation of state (EoS), which keeps the temperature at 10^4 K (mean molecular weight $\mu = 1$) for the initial setup and for higher densities that are not affected by the artificial pressure floor (see Section 5.3.2.2). Here, it represents the typical

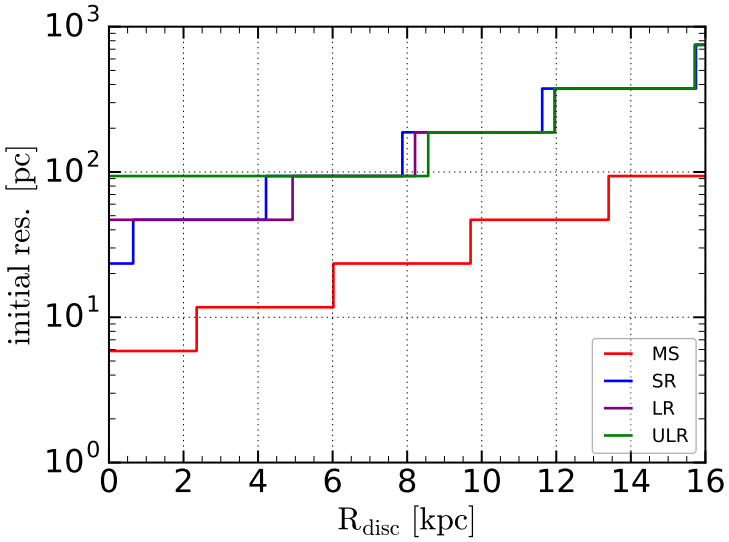

Figure 5.1: Radial dependence of the initial resolution in the mid-plane of the axisymmetric disc for the different runs.

micro-turbulent pressure floor of the interstellar medium (ISM) which cannot be resolved in our simulations and keeps the initial conditions of the vertical density distribution stable until the growing perturbations begin to transform the disc locally. For the low resolution simulations the temperature is deviating from 10^4K in the inner parts due to the artificial pressure floor, see Section 5.3.2.2. The model does not include a stellar disc or a bulge component (see Section 5.6).

5.3.2 Numerical setup

5.3.2.1 The high-resolution simulations

The simulations (Tab. 5.1) are performed with the hydrodynamical AMR (adaptive mesh refinement) code RAMSES (Teyssier, 2002). The gas is self-gravitating and the thermodynamics are regulated by an isothermal EoS. The hydrodynamical equations are being solved by using the HLL Riemann solver (Harten, Lax & van Leer, 1983) and making use of the MinMod slope limiter (Roe, 1986). The galaxy is centered in an isolated 48 kpc simulation box. The dark matter is added as a static external density field to the source term of the Poisson solver. To avoid artificial fragmentation in a gravitationally collapsing gas the Jeans length is typically required to be resolved by at least four cells $N_{\rm J} = 4$ (Truelove et al., 1997) for all refinement levels. This refinement strategy sets and limits the initial resolution which is decreasing with radius (Figure 5.1), due to the density gradient and the isothermal EoS of the galaxy. For the main simulation MS with $N_{\rm J} = 19$ we apply most of the analysis and compare it with runs using $N_{\rm J} = 4$ which are reaching a lower initial resolution (SR, LR, ULR). The sizes of the first forming structures (rings) can be characterised by the Toomre length (Behrendt, Burkert & Schartmann, 2015) and are therefore initially resolved in all runs (Table 5.1) with several resolution elements. In the fragmented discs the simulations reach in the densest regions (clumps) a maximum resolution of $\Delta x_{\rm min} = 2.9$ pc for the main simulation

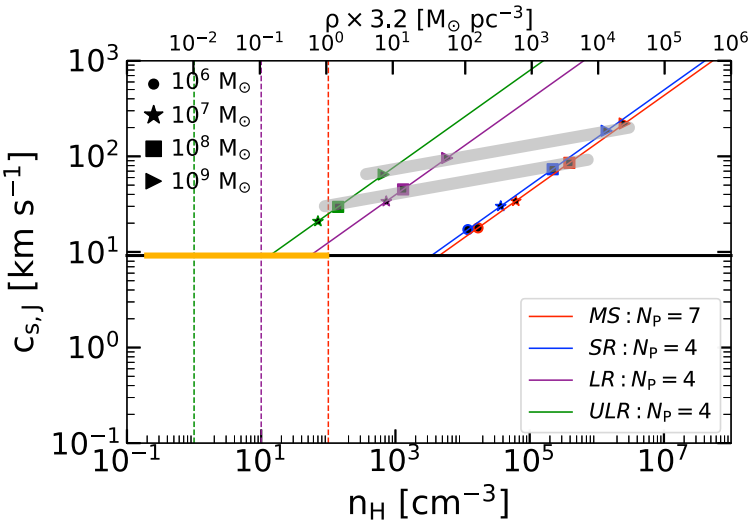

Figure 5.2: Density dependence of the induced artificial pressure floor (Section 5.3) expressed as the sound speed $c_{s,J}$ at the maximum resolution for the different simulations (Table 5.1). The minimum sound speed in the simulations corresponds to ~ 10 km s^{-1} and applies for the initial mid-plane densities between $0.2 - 93$ cm^{-3} (orange line). The vertical dashed lines correspond to the density thresholds used by the clump finder in the different simulations ($n_H = 1, 10, 100$ cm^{-3}). The different symbols correspond to the typical central densities of the selected clump-masses, defined in Section 5.4.2.2. We measure the maximum density in each mass bin and average over the simulation time. The grey shaded lines illustrate the relation between the clump densities per mass bin for 10^8 M$_\odot$ and 10^9 M$_\odot$, the resolution and accordingly the artificial pressure floor.

Table 5.1: The main differences of the simulations.

Simulation	Description	$\Delta x_{\rm min}$[a] [pc]	$N_{\rm J}$[b] [cells]	$N_{\rm P}$[c] [cells]	n_0[d] [cm^{-3}]	$L_{\rm MinJeans}$[e] [pc]	$N_{\rm Toomre}$[f] [cells]
MS	Main simulation	2.9	19	7	4.5×10^3	20.5	25-55
SR	Lower resolution	5.9	4	4	3.4×10^3	23.4	4-10
LR	Low resolution	46.9	4	4	53	187.5	4-10
ULR	Ultra low resolution	93.8	4	4	13	375	2-10

[a] The cell size at maximum resolution.
[b] The number of cells that resolve the Jeans length at all refinement levels except for the maximum resolution.
[c] The number of cells that represent the Jeans length at maximum resolution ensured by the artificial pressure floor.
[d] The critical density where the artificial pressure floor sets in.
[e] The smallest Jeans length that can be resolved.
[e] The number of cells that represent the initial Toomre length $L_{\rm Toomre}$.

(MS) (two times higher than in the previous work Behrendt, Burkert & Schartmann, 2015). For the run SR, we reach $\Delta x_{\rm min}$ = 5.9 pc. At the maximum refinement level higher densities could collapse further when resolved with less than 4 cells, as pressure gradients remain unresolved. This could lead to numerical fragmentation. It is common practice to ensure at least 4 cells (Truelove et al., 1997)

$$N_{\rm P} = \frac{\lambda_{\rm J}}{\Delta x_{\rm min}} \geq 4, \tag{5.1}$$

by introducing an artificial pressure floor (APF) which results in a constant minimum jeans length

$$\lambda_{\rm J} = \sqrt{\frac{\pi c_{\rm s,J}^2}{G\rho}} = \text{constant}, \tag{5.2}$$

that can be resolved in the simulations (see Section 5.2). The additional pressure can be expressed by the sound speed

$$c_{\rm s,J}^2 = \frac{G}{\pi} N_{\rm P}^2 \, \Delta x_{\rm min}^2 \, \rho, \quad \text{for } c_{\rm s,J} \gtrapprox 10 \text{ km s}^{-1}. \tag{5.3}$$

The equation is dependent on the number of cells per Jeans length $N_{\rm P}$, the simulation's maximum resolution $\Delta x_{\rm min}$, the density ρ in the computational cell and the gravitational constant G (see Figure 5.2). Therefore, we obtain with $N_{\rm P}$ = 7 in run MS the minimum resolved length of $L_{\rm MinJeans}$ = 20.5 pc. Typically, $N_{\rm P}$ = 4 is used in simulations, comparable with run SR that has $L_{\rm MinJeans}$ = 23.4 pc. We call the minimum resolved length in the simulations **the effective resolution**. The higher value for $N_{\rm P}$ in the main simulation ensures a very similar minimum resolved length as in run SR which is reached in the collapsed regions, inside the clumps. This allows us to identify possible resolution effects on the initial fragmentation due to their different Jeans number N_J.

5.3.2.2 The low-resolution simulations

The initial resolution in run LR and ULR are already reaching the maximum possible limit in the central part of the galaxies (Figure 5.1). To ensure a resolved Jeans length also there, the artificial pressure support is already in the beginning effecting the setup in run LR for radii R=0-0.25 kpc and more strongly in run ULR between R=0-5 kpc (see in Figure 5.2 the enhanced sound speed at the low densities for the setup). In the fragmented disc a maximum resolution of $\Delta x_{\rm min}$ = 46.9 pc for LR and for the run ULR only $\Delta x_{\rm min}$ = 93.8 pc can be reached. But, due to the APF, the minimum structures that can be resolved are in run LR limited to $L_{\rm MinJeans}$ = 187.5 pc and for run ULR to $L_{\rm MinJeans}$ = 375 pc.

5.3.3 Clump definitions

We use two possibilities to measure the clump properties. First, with the 3D density approach we compare the clump characteristics between the different simulations. Second, the surface density images of the galaxy allow to characterise the clump clustering and to compare the identified objects with observations.

5.3.3.1 3D density approach

The clumps are identified in the simulation on the fly (Bleuler & Teyssier, 2014; Bleuler et al., 2015) by considering gas densities above the threshold $n_{\rm H} \geq 100$ cm^{-3} for the runs MS and SR which are typical for molecular gas and also potential sites for star formation (at much higher densities). The clumps in the simulations with less resolution not only reach much lower maximum densities, but also experience in general a shift towards lower densities which makes a redefinition of the density threshold unavoidable (see Section 5.4.2.3). The clumps are well represented by densities $n_{\rm H} \geq 10$ cm^{-3} in run LR and for run ULR for densities $n_{\rm H} \geq 1$ cm^{-3} and lead to a similar total mass. Similarly, the density thresholds for the star formation are adapted in cosmological simulations in dependence on resolution. At first the clump finder algorithm divides the density field by a watershed segmentation into regions (sub-structure) associated to a certain density peak. Peaks with a low density contrast to the background are merged to a neighbour through their densest saddle point (noise removal). Finally, the left sub-structure is recursively merged to form larger associated objects based on a threshold. We define the clump radius in the xy-plane as

$$R_{\rm xy} = \sqrt{\frac{A_{\rm xy}}{\pi}} = \sqrt{\frac{\Delta x \Delta y}{4}}, \tag{5.4}$$

where $\Delta x/2$ and $\Delta y/2$ are the maximal semi-axes in the plane of the area

$$A_{\rm xy} = \frac{\pi\ \Delta x \Delta y}{4}. \tag{5.5}$$

For the vertical size definition we take the average of the maximal inferred radii in the xz- and yz-plane with

$$R_{\rm z} = \frac{R_{\rm xz} + R_{\rm yz}}{2} = \frac{1}{2}\left(\sqrt{\frac{A_{\rm xz}}{\pi}} + \sqrt{\frac{A_{\rm yz}}{\pi}}\right) = \frac{1}{4}\left(\sqrt{\Delta x \Delta z} + \sqrt{\Delta y \Delta z}\right). \tag{5.6}$$

5.3.3.2 2D images

2D images are created by observing the surface density line-of-sight and are spatially convolved by a Gaussian kernel of different full width at half maximum (FWHHM = 0.1-2kpc). For the identification of the clumps and clump clusters we apply the blob detection algorithm of the `scikit-image` library (van der Walt et al., 2014) with the Laplacian of Gaussian approach on the beam smeared images in linear scale (Section 5.5). It computes the Laplacian of Gaussian with successively increasing the standard deviation and stacks them up in a cube. The local maxima in the cube are the positions of the objects from where we estimate their FWHM sizes $D_{\rm FWHM}$ (geometrical mean) and masses $M_{\rm FWHM}$. After every calculation step of a CC, its region is cut out from the image to avoid double inspection of the mass which would be rarely occurring. We continuously change the detection threshold, for small convolutions we find a surface density of $\Sigma = 70$ M$_\odot$ pc^{-2} to avoid spurious detections and for the largest beam smearing (BS) $\Sigma = 25$ M$_\odot$ pc^{-2} to avoid under-detections due to a decreased and flatter surface density.

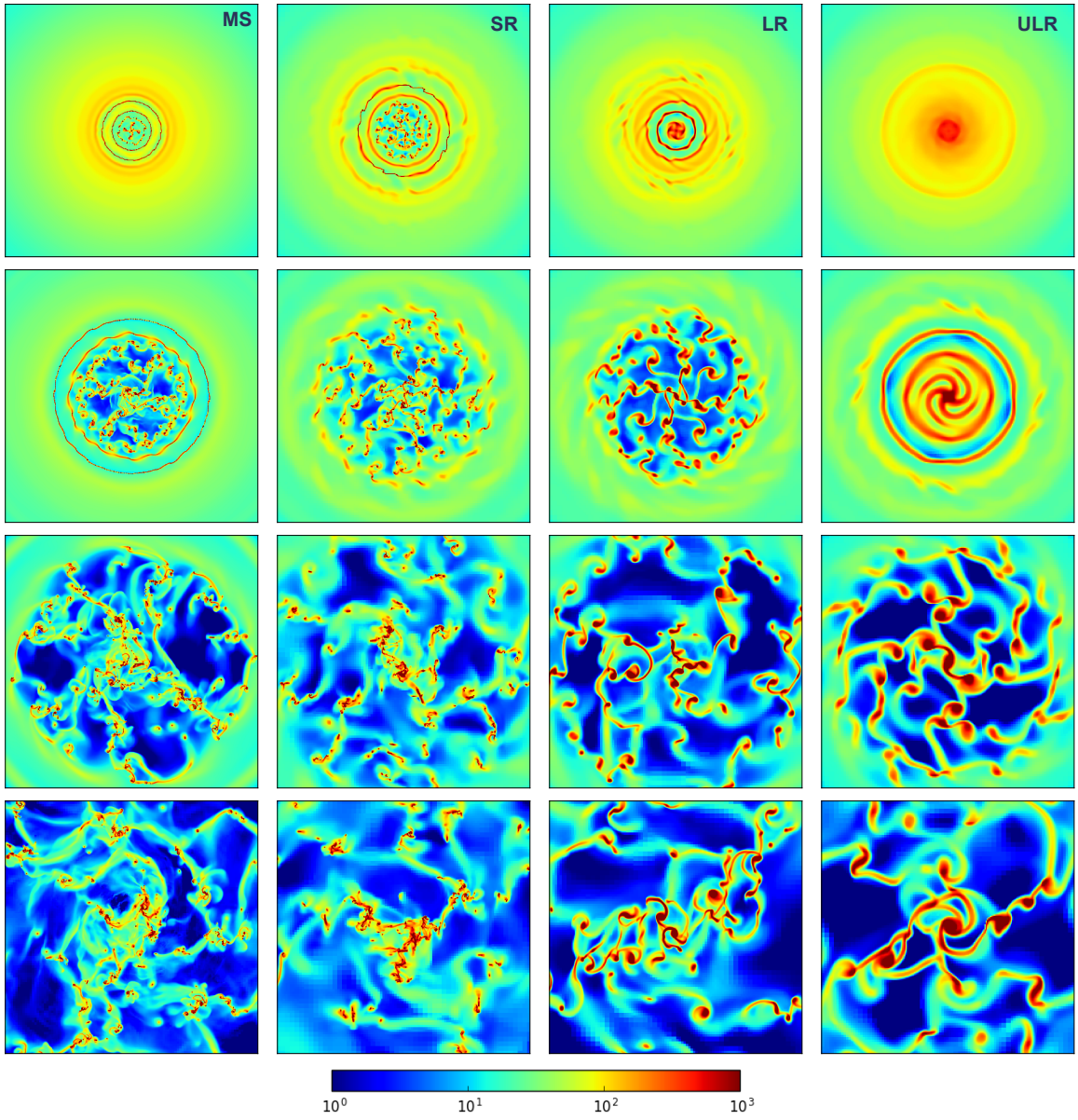

Figure 5.3: Surface density evolution of the discs of the different simulations. The images show the surface density log10(Σ) [$M_\odot$ pc^{-2}] face-on view of the gas disc at times $t = 100, 200, 400$ and 600 Myr for the four rows. Each panel shows a 20×20 kpc^2 map centered on the disc. The different columns represent the four different simulations. The colors are limited to the range $1-10^3$ $M_\odot$ pc^{-2} while densities of 10^6 $M_\odot$ pc^{-2} are reached in the centre of some clumps (MS). The snapshot at 655 Myr of MS can be seen in Figure 5.16.

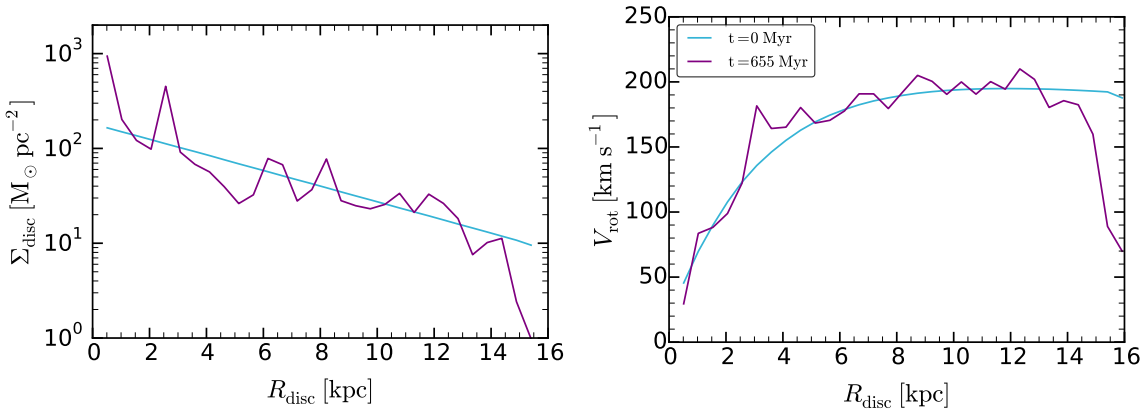

(a) (b)

Figure 5.4: Profiles of run MS (500 pc bins): (a) Average gas surface density profile of the initial disc (pale blue) and at t = 655 Myr (purple). (b) Mass-weighted average rotation velocity of the gas.

5.4 Simulation results

In the following (Section 5.4.1), we compare the general properties of the different simulations and characterize in particular the main simulation MS (Table 5.1). The detailed clump properties are analysed separately in Section 5.4.2.

5.4.1 General properties

5.4.1.1 Disc evolution

The gas disc in the main simulation MS (Figure 5.3, left column) fragments into rings (> 50 Myr) from inside-out in agreement with the local fastest growing wavelength, often referred to as Toomre length (see Behrendt, Burkert & Schartmann, 2015). Later on, the individual ring-like structures collapse under their self-gravity from kpc scales to dense circular filaments where they subsequently break-up into many bound clumps with diameters of around $d_{\rm clump}$ ~ 100 pc for higher densities (see Section 5.4.2). Several clumps begin to interact with each other or merge. The disc naturally develops a clumpy and irregular morphology and after ~ 550 Myr the total disc has been fragmented. The disc in the simulation with the lower initial resolution SR develops a similar clumpiness while not all the rings fully emerge compared to MS. In the low resolution simulations LR and ULR we find marginally developing rings which are not collapsing and the clumps are directly forming with larger sizes. The APF operates for run ULR already initially in the center of the galaxy and changes the initial setup after the first timestep. The consequence is a marginally stable condition which allows for non-axisymmetric instabilities, and spiral-arm like features grow (see also Wang et al., 2010). The runs MS and SR have a lot of clumps which are merging or grouping to clusters on several hundred pc to kpc scales (Behrendt, Burkert & Schartmann, 2015). The cluster properties and their evolution will be described in Section 5.5. After t = 655 Myr for MS, the surface density (Figure 5.4a) still reflects on average the initial exponential profile with local variations. Strong migration to the centre of the galaxy is not apparent, but local

Table 5.2: Definition of the surface density regimes.

Notation	Σ [$M_\odot$ pc^{-2}]	Regimes for the evolved disc
■ total	$1 - 10^6$	total considered density range
■ *H*	$> 10^3$	*higher* densities within the clumps
■ *C*	$> 10^2$	typical gas densities for the *clumps*
■ *A*	$10 - 10^2$	elongated, *arm*-like features
■ *L*	< 10	*low* density, inter-clump gas

accumulation of mass. Furthermore, the rotation curve (Figure 5.4b) keeps its initial shape on average (mass weighted).

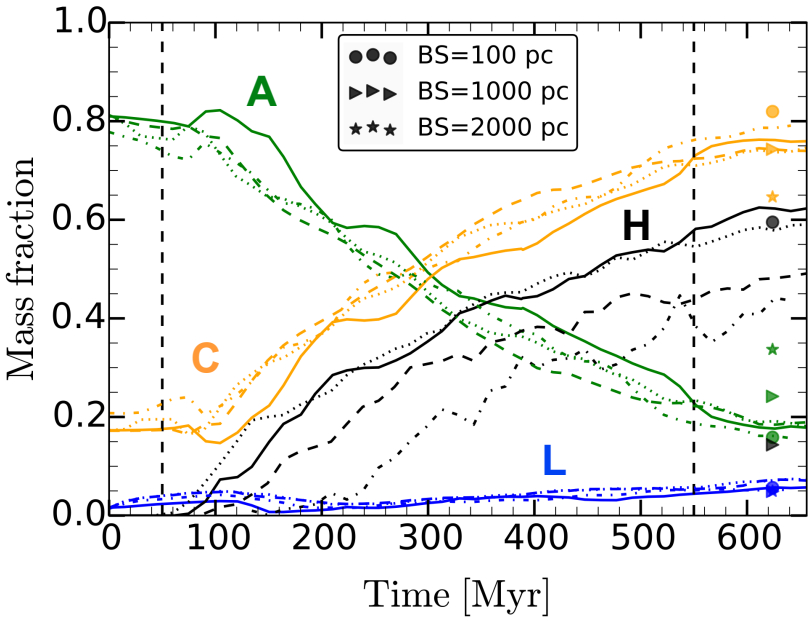

Figure 5.5: The evolution of the disc mass fractions for the different surface density regimes (for colors see Table 5.2) is very similar for the runs *MS* (solid lines) and *SR* (dotted lines), only the higher densities (black lines) are not reached by the runs *LR* and *ULR* (dashed and dashed-dotted black lines). All runs show a similar mass fraction for the clump areas (orange). The vertical dashed black lines indicate the beginning and the end of the fragmentation process in the disc. The symbols illustrate the effects of different beam-smearing at later times (see Section 5.5).

5.4.1.2 Mass redistribution

Despite the different evolution of the fragments at different resolution, we find similarities for the total mass fraction of the different structures in the galaxy. For the following analysis we distinguish between four surface density regimes within the disc (see Table 5.2). The initially limited surface density range is redistributed to values over several orders of magnitudes $\Sigma \sim 10^0 - 10^6$ $M_\odot$ pc^{-2} at $t = 655$ Myr. **Regime** *C* defines densities which roughly describe

the clump areas with $\Sigma > 10^2$ M$_\odot$ pc^{-2} and represents the majority of the mass (76% for MS) for the evolved disc (Figure 5.5) and in the beginning already for the central disc region. At first the disc consists of lower densities in the range $\Sigma = 8 \times 10^0 - 2 \times 10^2$ M$_\odot$ pc^{-2} which in the evolved disc characterises the gas surrounding the clumps in the elongated, *arm*-like features (**regime** A) with a mass fraction of 18%, since the main mass is with time transferred to higher densities. The *low* density gas (**regime** L) with $\Sigma < 10$ M$_\odot$ pc^{-2} represents the smallest fraction of the mass (2 – 6%) and does not change significantly over time. In the beginning it resides at the outer edge of the galaxy and in the evolved disc it is also found between the main gravitationally bound structures, distributed over the total disc, but less common in the central region of the galaxy. After the disc is fully fragmented (after ~ 550 Myr), the mass fractions of the different regimes are quasi-steady for the rest of the simulation (Figure 5.5). Within the resolution study, we find significantly lower mass fractions for the low resolution runs LR and ULR for the highest densities within the clumps $\Sigma > 10^3$ M$_\odot$ pc^{-2} (**Regime** H). All other regimes show similar mass fractions for the full resolution study.

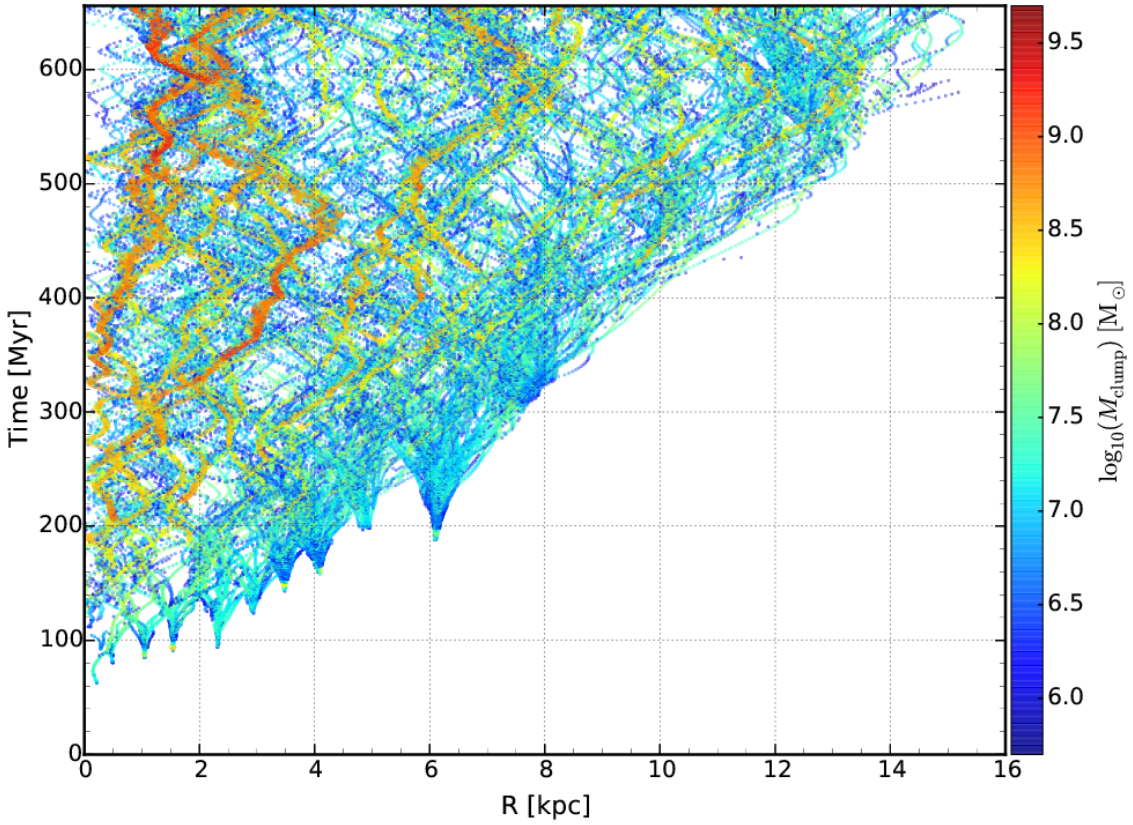

Figure 5.6: For run MS: Overview of the clump mass evolution (Δt ~ 1.5 Myr) and their radial positions within the face-on disc. The origin of the ~ 10^7 M$_\odot$ clumps in the ring-like structures as well as their fast merging to ~ 10^8 M$_\odot$ (within 50 Myr) is very well visible. Larger masses are more prominent at small radii. The mass range shown is limited to the minimum of 5×10^5 M$_\odot$. Clumps with masses above $> 10^8$ M$_\odot$ are indicated by larger symbol sizes.

5.4.2 Clump statistics

5.4.2.1 General clump evolution of MS

The overall clump evolution of MS is shown in Figure 5.6 with their radial positions in the disc and their individual masses for timesteps $\Delta t \sim 1.5$ Myr. A large number of clumps fragment in the dense circular filament-like structures (11 rings, the outermost at ~ 8 kpc). Their typical initial masses are between $\sim 10^6 - 5 \times 10^7$ $M_\odot$. Very early they gravitationally interact with structures formed further in and further out. They are locally attracted by their next neighbours which leads for half of the clumps within one ring to a movement towards the galaxy centre and the other half towards larger radii, by conserving the angular momentum. This oscillating behaviour continuous and the clumps move steadily inwards and outwards, which induces a strong mixing. Many merge with each other, to e.g. 10^8 $M_\odot$ within 50 Myr and only a few above 10^9 $M_\odot$ are visible on the map (mainly at small disc radii). When following the path of the most massive clumps over time, it can be seen that they are temporarily present and some are losing material when crossing the path of fast encounters (e.g. at $R_{\rm disc} \sim 4$ kpc, ~ 450 Myr) but then again accumulating mass.

5.4.2.2 Detailed clump properties of MS

For the following analysis we consider the mass bins:

$$\begin{aligned}
&\sim 10^6\ M_\odot \equiv\ ]5\times\ 10^5 : 5\times 10^6]\ M_\odot,\\
&\sim 10^7\ M_\odot \equiv\ ]5\times\ 10^6 : 5\times 10^7]\ M_\odot,\\
&\sim 10^8\ M_\odot \equiv\ ]5\times\ 10^7 : 5\times 10^8]\ M_\odot,\\
&\sim 10^9\ M_\odot \equiv\ ]5\times\ 10^8 : 5\times 10^9]\ M_\odot.
\end{aligned}$$

We recall (Figure 5.6) that the initial clumps which form within the rings have $\sim 10^6 - 10^7 M_\odot$. The relatively steady amount of clumps in the mass bin of 10^7 $M_\odot$ is in balance between newly forming $\sim 10^7$ $M_\odot$ clumps and merging to $\sim 10^8$ $M_\odot$ clumps. The more massive clumps form later since it needs, e.g. 100 clumps with 10^7 $M_\odot$ to merge to 10^9 $M_\odot$ but are more frequent in the central disc region due to a larger volume filling-factor. All mass bins stay quasi-steady after the disc is fully fragmented (> 550 Myr) and most of the mass resides in clumps of $\sim 10^8$ $M_\odot$ with a total of $\sim 10^{10}$ $M_\odot$ and are distributed over the whole disc (Figure 5.6). The clumps in the mass bin 10^6 $M_\odot$ play with a total mass $\sim 3 \times 10^8$ $M_\odot$ only a minor role compared to the total mass of clumps above $> 10^7$ $M_\odot$. The clump masses are related to different sizes, ranging between $R_{\rm xy} \simeq 20 - 60$ pc (Figure 5.7b). The clumps have a disc-like shape and lie initially in the xy-plane and are well represented by the radius definition in Section 5.3.3. Interactions between the clumps, especially in the central disc region, lead to tilting with respect to the equatorial plane which explains the slow decrease of the mean radius $R_{\rm xy}$ over time and the small increase of the measured mean vertical sizes $R_{\rm z}$ (Figure.5.7c). This is especially the case for the massive merger-products, e.g. the tilted 10^9 $M_\odot$ clumps, where the size definition does not work anymore (measured in xy-plane of the galaxy) and they appear with similar xy-sizes as the 10^8 $M_\odot$ clumps. The minimum thickness in the very center of the clumps is given by the artificial pressure floor with $R_{\rm z} \sim 10$ pc which is for the diameter equal to the given minimum Jeans length (see Section 5.3, 5.4.2.6). This can be especially seen in the beginning of the statistics for $R_{\rm z}$. The diameters of the clumps with 10^6 $M_\odot$ are close to the minimum Jeans length (factor ~ 1.7 difference), while the clumps

with 10^7 $M_\odot$ are larger by a factor of ~ 3 and the mergers with 10^8 $M_\odot$ are even ~ 5 times larger and therefore better resolved.

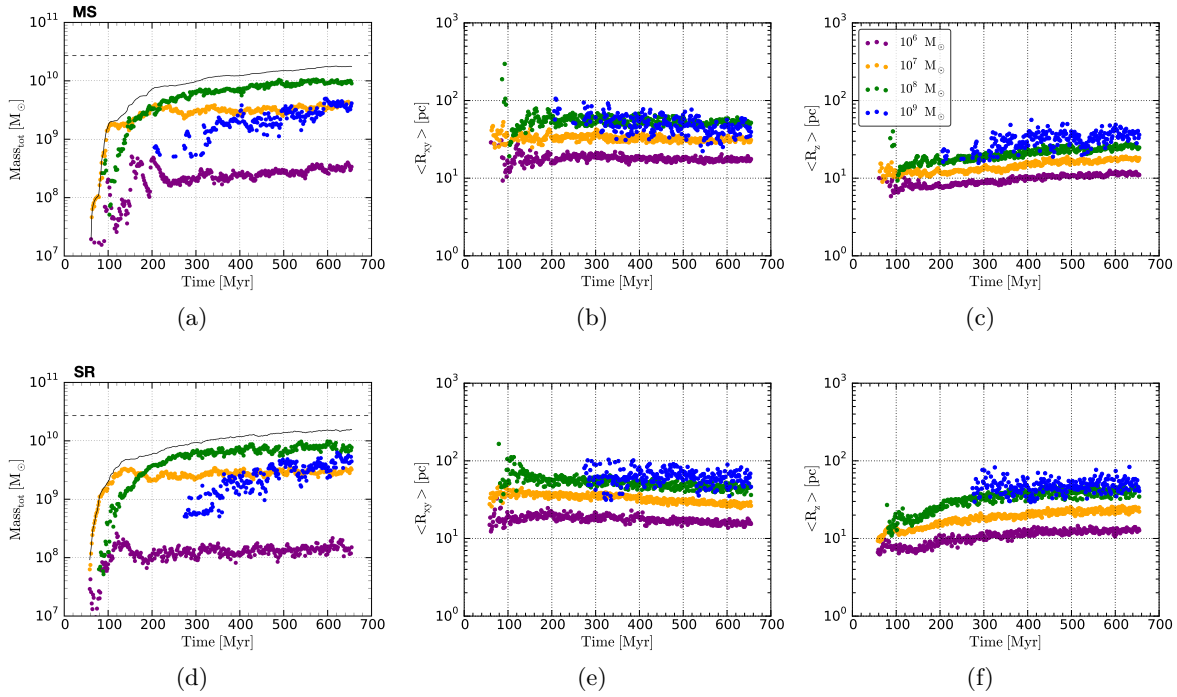

Figure 5.7: Evolution of the identified clumps and their properties over time (Δt ~ 1.5 Myr). The first row corresponds to the main simulation MS and the second row to the run SR. (a), (d): The total mass within all clumps in black and the colored symbols represent the total mass within each mass bin $]5\times10^{i-1}-5\times10^{i}]$ ($M_\odot$). The total disc mass is illustrated by the dashed black line. (b), (e): Evolution of the clump radii in the plane R_{xy} and for (c), (f) in vertical direction R_z.

5.4.2.3 Comparison between the different runs

In this Section we compare the evolutionary clump properties between the different runs and the main simulation (Table 5.1). In general, we find from high to low resolution a strong shift towards lower densities, higher masses and larger sizes (Figure 5.2, see clump-mass symbols). The clump properties change systematically with the associated artificial pressure floor. Firstly, this is reflected in the maximum densities that are reached on average in each clump. For example, the typical maximum density in the 10^8 $M_\odot$ clumps is for MS more than three orders of magnitude higher than for ULR. Secondly, the density threshold for the clump definition does not capture all clumps anymore for the lower resolution runs LR and ULR. Therefore, we chose the minimum density by visual inspection of the dense clump regions. With this definition the total mass of the clumps are in all runs very similar and only by 6-13 percent lower than in MS. This is in line with the mass estimation in Section 5.4.1.2, see Figure 5.5. Overall, the clump statistics in this section describe the "high density" part of the clump regions. They are closely surrounded by more gas with lower densities which is ~ 30 percent more in mass quantified by the surface density approach (see Figure 5.5). For the run

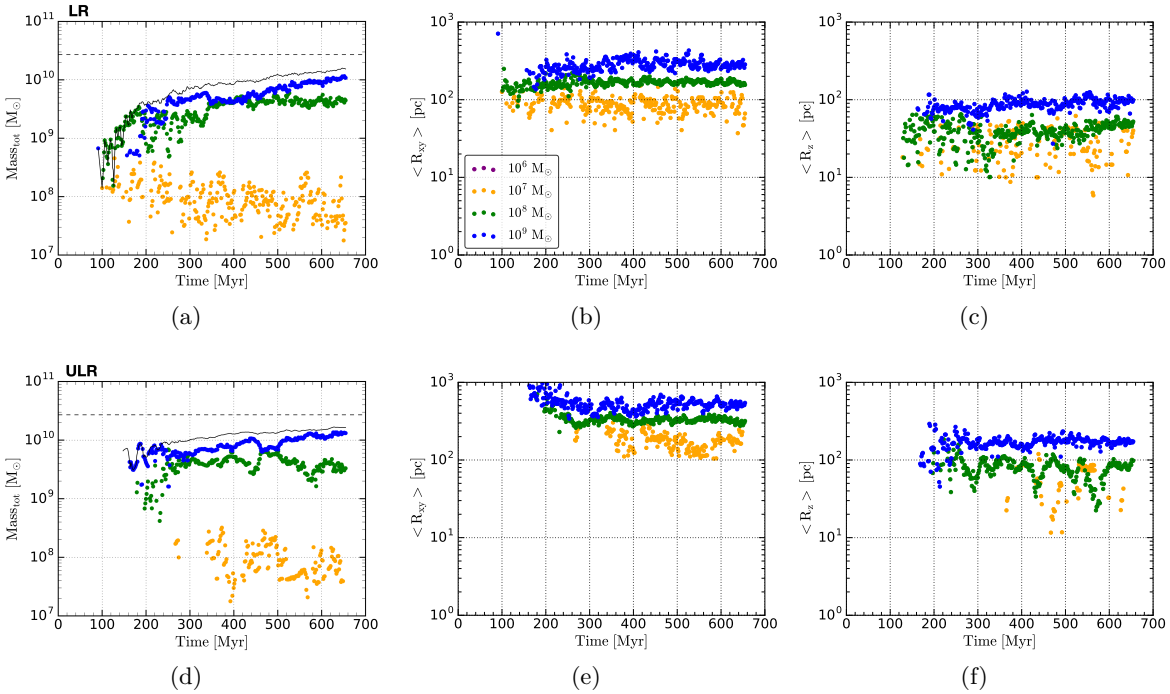

Figure 5.8: Evolution of the identified clumps and their properties over time ($\Delta t \sim 1.5$ Myr). The first row corresponds to the simulation LR and the second row to the run ULR. (a), (d): The total mass within all clumps in black and the colored symbols represent the total mass within each mass bin $]5\times10^{i-1} - 5\times10^{i}]$ ($M_\odot$). The total disc mass is illustrated by the dashed black line. (b), (e): Evolution of the clump radii in the plane R_{xy} and for (c), (f) in vertical direction R_z.

(a) (b) (c)

Figure 5.9: The clump properties of the different runs relative to the main simulation *MS* for each mass bin at t=655 Myr. Several trends from high to low resolution are present: (a) The mass is shifted towards more massive clumps and the low-mass clumps are suppressed more and more. (b) The clump size is dramatically increasing for most clump masses, (c) the vertical height is getting larger too.

SR (Figure 5.7, lower panel) we find in general a very similar clump-mass distribution from beginning on and similar sizes despite that lower densities are reached and the same density threshold for the clump-finder as in run *MS* is used. The measured maximum heights are similar too, as the minimum Jeans length due to the pressure floor is not deviating much. We find a very small trend towards higher values since the clumps tend to tilt on average more. The smaller the clump masses the more they are suppressed, while for the 10^9 $M_\odot$ mass bin a very small trend to more mass is apparent (see also Figure 5.9a). When lowering the resolution (*LR* and *ULR*, Figure 5.8) the amount of clumps below 10^9 $M_\odot$ are more and more suppressed and their mass contributes less (Figure 5.9a). A significant trend towards larger sizes and heights per mass bin is apparent (Figure 5.9b, 5.9c). The maximum heights are roughly increasing with the imposed minimum Jeans length (Figure 5.9c) and the clumps tend to be tilted less than in the higher resolution cases. Almost all clumps are larger than the minimum Jeans length imposed by the pressure floor. Only the 10^7 $M_\odot$ clumps for *LR* are smaller than the minimum Jeans length but are also almost not present anymore.
In summary we find that most of the mass resides in clumps of 10^8 $M_\odot$ (mergers) in the higher resolution runs and a shift towards 10^9 $M_\odot$ (no-mergers) for lower resolutions. The size (in the xy-plane) of the clumps with 10^8 $M_\odot$ increases up to ~ 6 times and for 10^9 $M_\odot$ by a factor of ~ 14 for lower resolution.

5.4.2.4 Mass-radius relation

The relations between the clump masses and their radii for all runs are shown in Figure 5.10 (average between 400 – 655 Myr). The kernel density estimation gives us the abundance of clumps with given mass-radius properties (Figure 5.10) within the time range. For the higher resolution simulations *MS* and *SR* we find the most abundant clumps at around 10^7 $M_\odot$ and we recall that most of the mass resides in clumps with around 10^8 $M_\odot$. Furthermore, mostly masses of 5×10^8 $M_\odot$ represent the 10^9 $M_\odot$ mass bin. The relation for simulation *SR* is slightly shifted towards smaller sizes at the same mass and a larger density threshold for the clump finder could compensate the effect. We recall that not as high densities are reached than in run *MS*. For the lower resolution runs *LR* and *ULR* the density shift is more visible and the clump finding has been adapted to a smaller density threshold. The smaller masses

are completely absent and the relation is for both runs shifted in parallel to each other. It is apparent that the 10^8 $M_\odot$ clumps are different when comparing the low and high resolution simulations. Clumps for run LR are 3 times larger (Figure 5.9b) than in MS and a factor 6 larger for ULR and are therefore correspondingly much less dense.

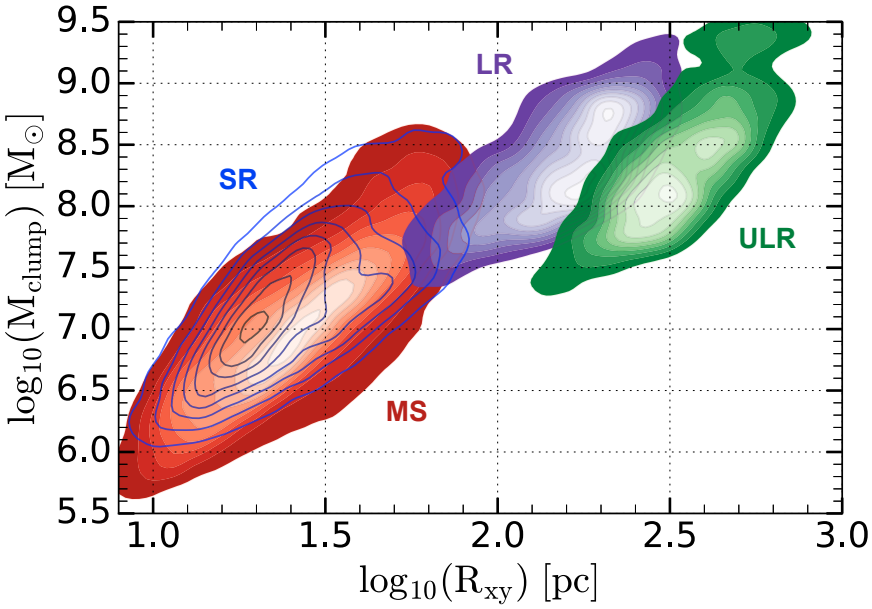

Figure 5.10: Clump mass-radius relation for the different runs averaged over the time 450-655 Myr. The data is represented by a Kernel density estimation and illustrates the abundance of clumps over the time range. The white color in each color-map corresponds to the most frequent clumps and the red shading to run MS, the purple to LR and the green to run ULR. Run SR is represented by blue closed contour lines while a smaller circumference corresponds to a higher abundance.

5.4.2.5 Clump's relation to the artificial pressure floor

In the previous sections we explored in general the influence of the resolution on the clump properties. Here we investigate the impact of the APF more directly on the clump mass and density. If the Jeans mass corresponding to the APF is similar to the clump's mass, we can speak of a clump with artificially given properties. In the simulation code the Jeans length (Equation 5.2) is applied on quadratic cells. Therefore, we define the Jeans mass as

$$M_\mathrm{J} = \lambda_\mathrm{J}^3 \ <\rho>, \tag{5.7}$$

which is 1.9 times larger than for the spherical case. Since the Jeans length is given as a constant at the highest resolution within the clump, we can write

$$M_\mathrm{J} = (N_\mathrm{P}\Delta x_\mathrm{min})^3 \ <\rho> . \tag{5.8}$$

The APF dominated clumps have then $M_\mathrm{clump} \approx M_\mathrm{J}$ for the average density $<\rho_\mathrm{clump}> \approx <\rho_\mathrm{J}>$, while $M_\mathrm{clump} < M_\mathrm{J}$ is suppressed. We take all identified clumps at every timestep between 400-655 Myr (well fragmented disc) and calculate their average density and total mass. The kernel

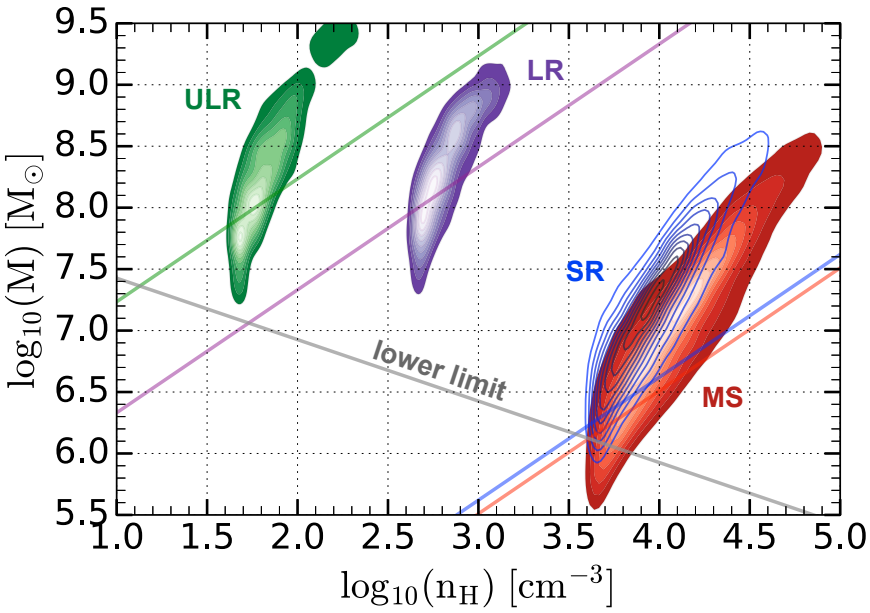

Figure 5.11: The average density and mass of the clumps between 450-655 Myr of the different runs are represented by a kernel density estimation (colored shadings and contour lines as in Figure 5.10. The Jeans mass and their corresponding average densities expected from the artificial pressure floor of the different simulations are represented by the colored lines. The areas above and on the left side of the individual lines are possible clump properties. The grey line gives the lower limit for Jeans masses given by the minimum sound speed $c_s \sim 10$ km s^{-1} and is only reached by the smallest clumps in run MS.

density estimation gives us the abundance of the clump's mass-density properties (Figure 5.11) within the time range. The bulk of the clumps (initial clumps in a ring) in simulation LR and ULR are well described by the minimum Jeans mass-density relation. The initial clumps in the main simulation MS and in run SR do clearly not lie on the APF induced relationship. Clumps above the lines are less influenced by the APF and with distance to the relation are more and more rotationally supported, which will be shown in the next Sections. Another way to present the effect of the APF is the face-on projection of the disc with the mass weighted sound speed (Figure 5.12). The clumps of the runs LR and ULR show extremely high sound speeds between $c_{s,J} \simeq 20 - 200$ km s^{-1}, and their areas are larger for ULR than for LR.

5.4.2.6 Intrinsic clump profiles of MS

To understand the nature of the clumps even better it is necessary to measure their intrinsic properties. We cut out a region around each clump, 25 percent larger than defined by the clump finder. The centre of mass defines the origin of the clumps coordinate system. The velocities in the clump rest frame are given by the local values in each cell subtracted by the mass weighted clumps linear velocity x,y,z components in the disc. For the radial profiles of different properties the values are mass weighted and averaged within 3 pc radial bins.
We selected three clumps as archetypes, corresponding to the masses of $\sim 2 \times 10^8$ M$_\odot$ (clump V1) which represent most of the mass in the galaxy, $\sim 2 \times 10^7$ M$_\odot$ (clump V2) which belongs

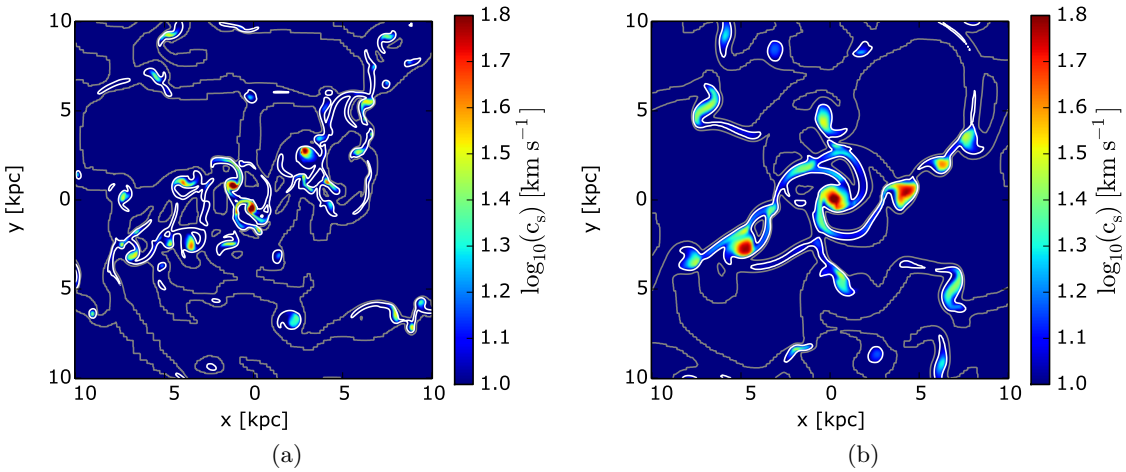

Figure 5.12: The average mass weighted sound speed of the face-on discs for the run *LR* (left) and the run *ULR* (right) at 600 Myr (see Figure 5.3 for the corresponding surface density plot). Very high sound speeds are present within the clump regimes, indicated by the white contours at 100 $M_\odot$ pc^{-2}. The grey contours correspond to 10 $M_\odot$ pc^{-2} and show the arm like features.

to the group with the most frequent clumps and of $\sim 4 \times 10^6$ $M_\odot$ (clump V3) which are mainly influenced by the APF. In Figure 5.13 we provide their intrinsic radial profiles. The volume densities show in general an exponential decline. The rotational velocities show a typical profile for a baryonic mass dominated rotationally supported exponential disc. The clumps maximum rotation is clearly related to the clump mass with $M_{\rm clump}$ [$M_\odot$] $\simeq 10^4 \times V^2_{\rm rot,max}$ [km s^{-1}] (Figure 5.14) with ranges between $V_{\rm max} \sim 10 - 200$ km s^{-1}. A similar relationship follows from the circular speed of the exponential disc at the radius for the peak velocity (see Equation 2.165 in (Binney & Tremaine, 2008b), substituted by the mass within $R_{\rm h}$ with $M_{\rm h} = 2\pi\Sigma_0 R^2_{\rm h}$ and the ratio $y = \frac{2.15R_{\rm h}}{2R_{\rm h}}$ with the peak radius $2.15 \times R_{\rm h}$). The different clumps along the mass-radius relation (Figure 5.10) are distributed over all the disc (Figure 5.14) and significant deviations from the relation (Figure 5.14) correspond to those clumps in the central region of the galaxy and are caused by tilts to the disc plane due to more frequent interactions as well as our definition of the clump radius, measured in the xy-plane. The sound speed peaks in the centre of the clump at highest density, induced by the artificial pressure floor, and declines with radius. The radial velocity dispersion is in general not larger than the sound speed. Both are calculated locally and then azimuthally averaged (mass-weighted).

5.4.2.7 Rotational supported clumps

In the following we clarify the contributions of the clumps' rotation, the minimum sound speed $c_{\rm s} \sim 10$ km s^{-1} and the artificial pressure floor to their internal dynamics by analysing properties at the time step 655 Myr. For the analysis we assume that the clumps are in dynamical equilibrium, since their radial velocities are negligible compared to their total rotational velocities (Figure 5.13 b, e, h). Then, the circular velocity can be expressed by the rotational velocity and the gradient of the thermal pressure (e.g. Binney & Tremaine

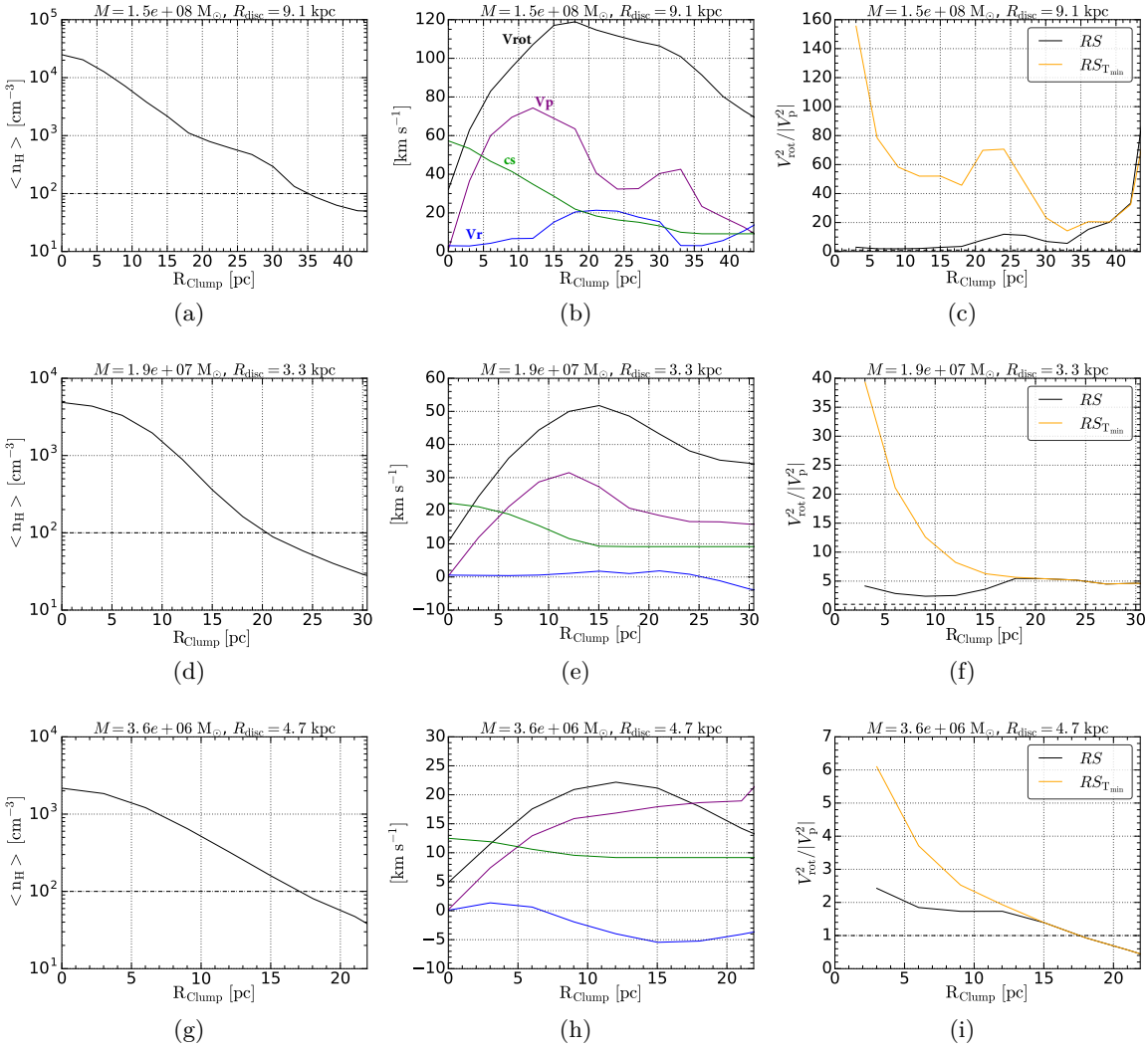

Figure 5.13: Examples of radial profiles of three typical clumps (t = 655 Myr) in the main simulation MS. The first row corresponds to the clump $V1$ with a mass of $\sim 2\times10^8$ M$_\odot$, the second row to $V2$ with $\sim 2\times10^7$ M$_\odot$ and the last row to clump $V3$ with $\sim 4\times10^6$ M$_\odot$. (a), (d), (g) show the density profile; (b), (e), (h) give the kinematic profiles of the rotational velocity $v_{\rm rot}$, the gradient of the thermal pressure $v_{\rm p}$ (Equation 5.9) , radial velocity $v_{\rm r}$ and the sound speed $c_{\rm s}$; (c), (f) (i) show the ratio between the measured rotation and the effective velocity dispersion (black line) and the orange line the ratio between the measured rotation and the minimum sound speed of $c_{\rm s} \sim 10$ km s^{-1}.

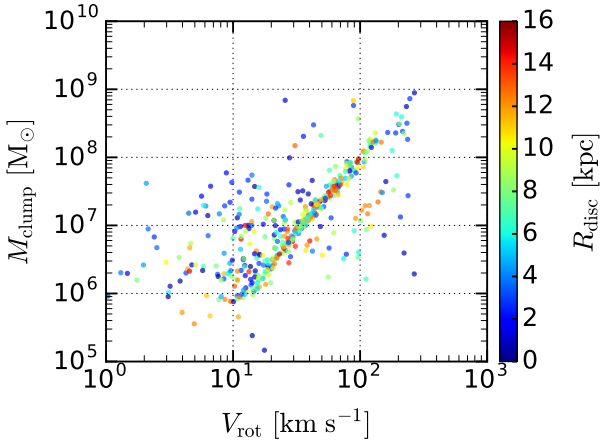

Figure 5.14: The comparison between the clump masses and their maximum rotation velocities at t=655 Myr. Their radial positions within the disc are indicated by the color.

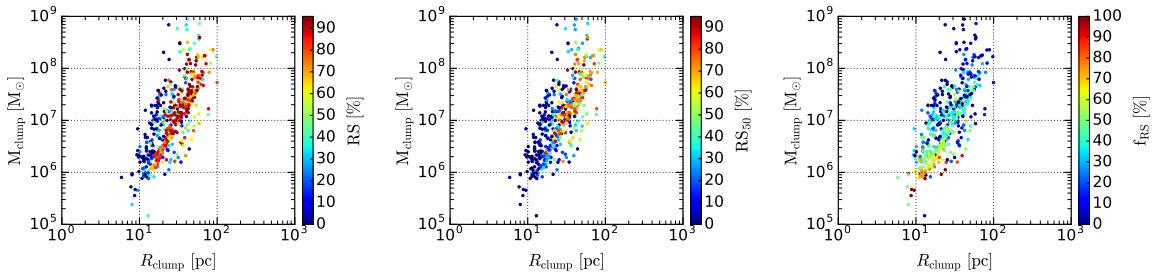

(a) (b) (c)

Figure 5.15: (a) Fraction of each clump that fulfills the rotational support criterium $RS > 1$ (Equation 5.10). (b) Fraction of each clump that is rotationally supported by at least 50 percent, defined by the criterium $RS_{50\%} > 2$ (Equation 5.11). (c) Shows how much of the clump is dominated by the artificial pressure support over the pressure coming from the minimum temperature of the simulation (Equation 5.12).

(2008b), Equations 4.229, 4.230)

$$V_{\rm circ}^2 = V_{\rm rot}^2 - \frac{r}{\rho}\,\frac{\partial(\rho\, c_{\rm s}^2)}{\partial r} = V_{\rm rot}^2 - V_{\rm p}^2. \tag{5.9}$$

The clump is locally rotationally supported if the first term of Equation 5.9 dominates the second term, which we refer to as $V_{\rm p}^2$, expressed by the ratio

$$RS = \frac{V_{\rm rot}^2}{V_{\rm p}^2} > 1, \tag{5.10}$$

while the pressure term is calculated numerically. For completeness, we plot the radial profiles of $V_{\rm p}$ in Figures 5.13b, 5.13e, 5.13h. The three examples (black line) in Figures 5.13c, 5.13f, 5.13i show the radial dependence of Equation 5.10. The clumps are mainly supported by rotation. This is also true for the rest of the clumps at this timestep (Figure 5.15a) where we measure intrinsically what fraction of the clump radius is dominated by the rotation term. For the clumps lying on the tight M-R relation, RS dominates by at least 70% in the inner region. While on the lower mass-end of the relation the pressure plays an important role which can also be seen in Figure 5.13h for clump V3. The left side of the relation lacks on rotational signal due to their tilts to our measurement in the xy-plane. With the above measurement we only identified if there is a rotational support. To understand better its importance we measure how much of the clump is rotationally supported by more than 50% (Equation 5.9), expressed by the ratio

$$RS_{50} = \frac{V_{\rm rot}^2}{|V_{\rm p}^2|} > 2. \tag{5.11}$$

Figure 5.15b clearly illustrates that rotation dominates the main clumps ($> 10^7$ M$_\odot$) by more than 70%. Now it is even more visible that for the smaller clump masses the pressure term plays a stronger role. Here, we have not distinguished between the contribution of the artificial pressure floor or the minimum temperature. To compare both contributions, we ignore the artificial pressure floor (Figures 5.13c, 5.13f, 5.13i) and calculate Equation 5.10 with only the contribution of the minimum sound speed $c_{\rm s} \sim 10$ km s^{-1} and call it $RS_{\rm T_{min}}$. The rotational support in the central part of the clump appears now much higher and is outside towards larger radii similar to the profile where the artificial pressure floor is taken into account. This means that the hotter inner part has a stronger contribution from the artificial pressure floor and outside only the minimum sound speed plays a role. To quantify the dominance of the artificial pressure floor over the pressure due to the minimum temperature of the simulation, we take the ratio between both of the RS parameter (Figure 5.15c)

$$f_{RS} = \frac{RS}{RS_{\rm T_{min}}} = \frac{|V_{\rm p,T_{min}}^2|}{|V_{\rm p}^2|} \geq 0.9 \tag{5.12}$$

The rotational term drops out and and only the two pressure terms are compared while we have $RS_{\rm T_{min}} \geq RS$ (see Figures 5.13c, 5.13f, 5.13i). This means that the artificial pressure is dominating whenever $f_{RS} < 1$ and for $f_{RS} = 1$ the minimum temperature is more important. We allow for a small deviation of 10 percent and whenever f_{RS} has values between $0.9 - 1$ the clump is locally supported by the pressure induced by the minimum temperature of the simulation. This is mainly the case for smaller clump masses (Figure 5.15c) below $< 10^7$ M$_\odot$. With increasing mass more and more of the clumps pressure gradient is dominated by the artificial pressure floor, but plays a smaller role than their rotational support (Figure 5.15b).

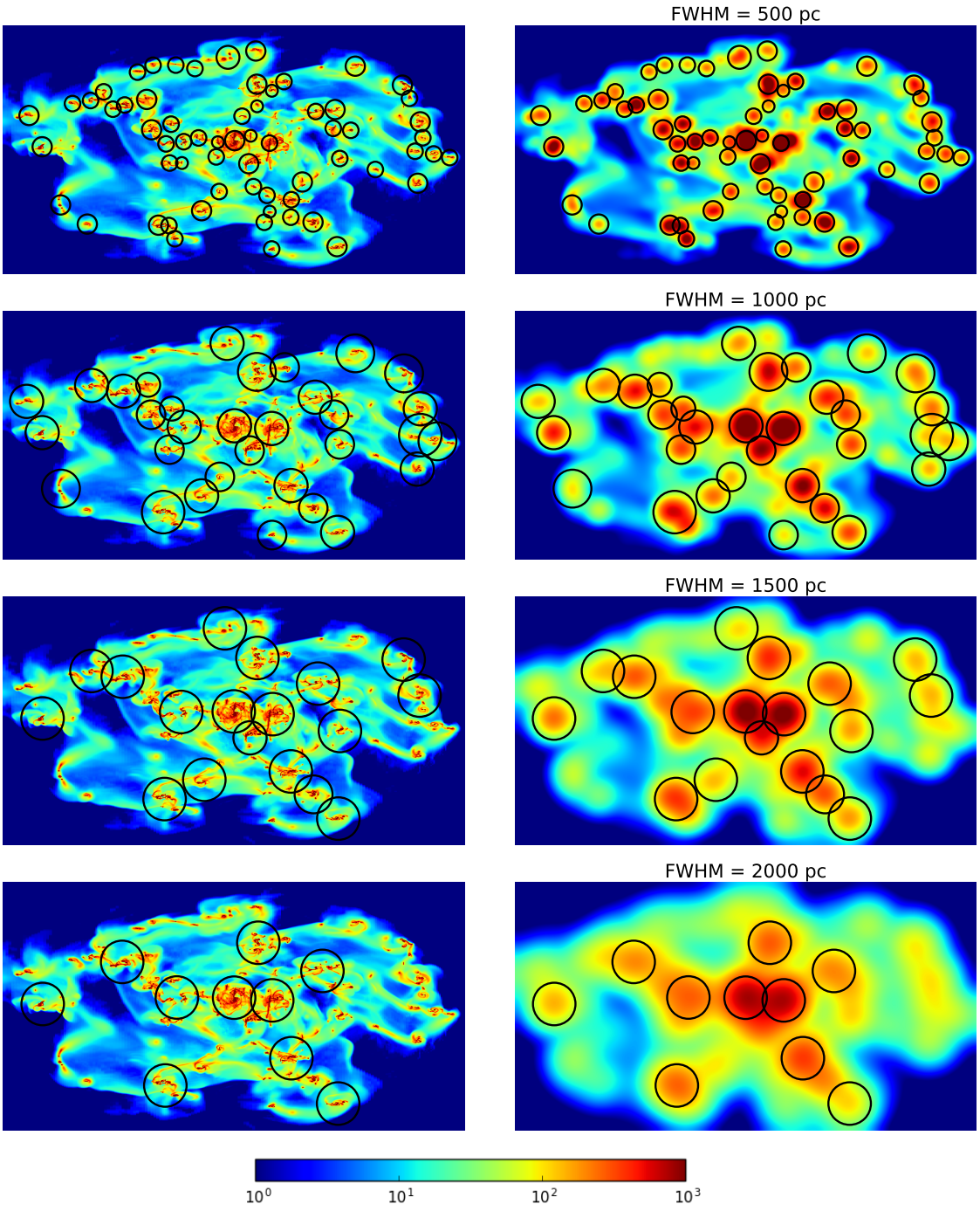

Figure 5.16: LOS observations of the surface density ($\log_{10}(\Sigma)$ [$M_\odot$ pc^{-2}]) of the inclined galaxy (60°) at timestep 655 Myr (same as in Behrendt, Burkert & Schartmann (2016)). Each panel shows a 22 x 12 kpc^2 map centered on the disc. The left column is the original image which can be compared with different beam smeared versions in the right column. The identified groups or CCs are marked with a circle of the found structure size (FWHM).

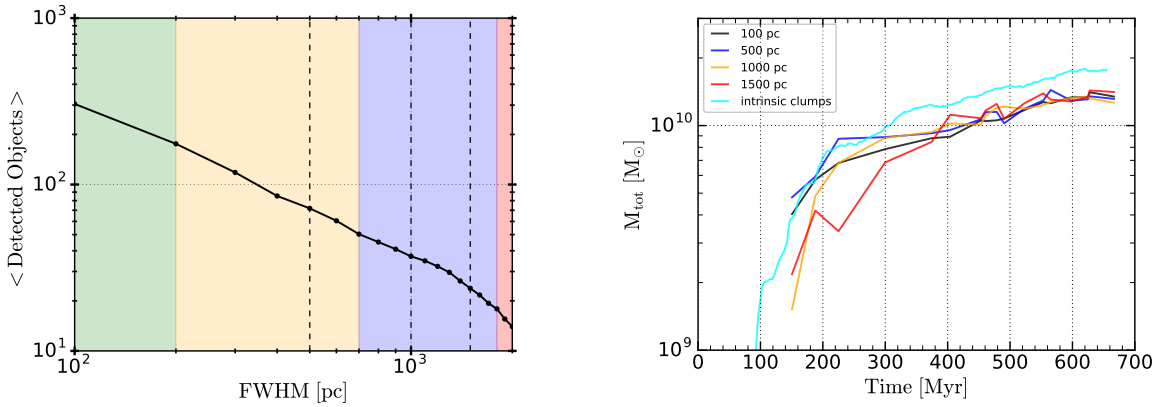

(a) (b)

Figure 5.17: (a) The number of objects found by the blob finder dramatically decreases with the FWHM of the beam smearing (time average between 450 - 655 Myr). The background colors correspond to the ranges of the identified clump cluster scales (see Table 5.3). (b) Total mass of the identified objects over time for different FWHM of the beam smearing, compared to the total mass of the intrinsic clumps of run *MS* (Section 5.4.2.2).

5.5 The hierarchical clustering of clumps

After the disc fragmentation to single clumps, they immediately group to clump clusters (CCs) on different spatial scales. In this section we identify these scales by using different beam-smearings (BS) and estimate the corresponding masses and sizes of the CCs. As in Behrendt, Burkert & Schartmann (2016), we interpolate the data on a uniform grid with pixel size 11.7 pc and incline the galaxy by 60 degrees. The surface density is observed along the line-of-sight and is spatially convolved by a Gaussian kernel of different full width at half maximum (FWHM = 100 pc - 2000 pc). Figure 5.16 shows the evolved disc (same snapshot as in Behrendt, Burkert & Schartmann (2016)) under different observed spatial resolutions, each compared to the highly resolved simulation picture. For every considered convolution we overplot the image with circles to indicate the positions and FWHM sizes of the detected structures (see Figure 5.16 and for the size definition: Section 5.3.3.2). With larger FWHM of the beam smearing kernel the amount of visible clumps or clump clusters dramatically decreases (see also Figure 5.17a) since they are represented by a few giant objects on larger scales. The smooth relationship between detected objects and BS is caused by several reasons. Firstly, the CCs are not isolated entities, but in the convolution are also neighboring clumps or CCs involved. Secondly, isolated objects can disappear with larger BS due to a flat density profile and do not contribute to the statistics. With BS the mass is distributed over larger scales, expressed by lower densities in the maps. This is visible in the shift of the mass-fractions (see Figure 5.5) of the density-regimes defined in the full resolution observation (Table 5.2). The highest density regime *H* disappears with higher BS and the mass-fraction for the defined clump region ($> 10^2$ $M_\odot$ pc^{-2}) is declining, while the mass-fraction for the defined intermediate gas density ($10^1 - 10^2$ $M_\odot$ pc^{-2}), the arm-like features is increasing.

The total mass of the identified objects is for the evolved disc ~ 30 percent of the total disc mass for all BS (Figure 5.17b). This is ~ 20 percent smaller than the clump mass obtained

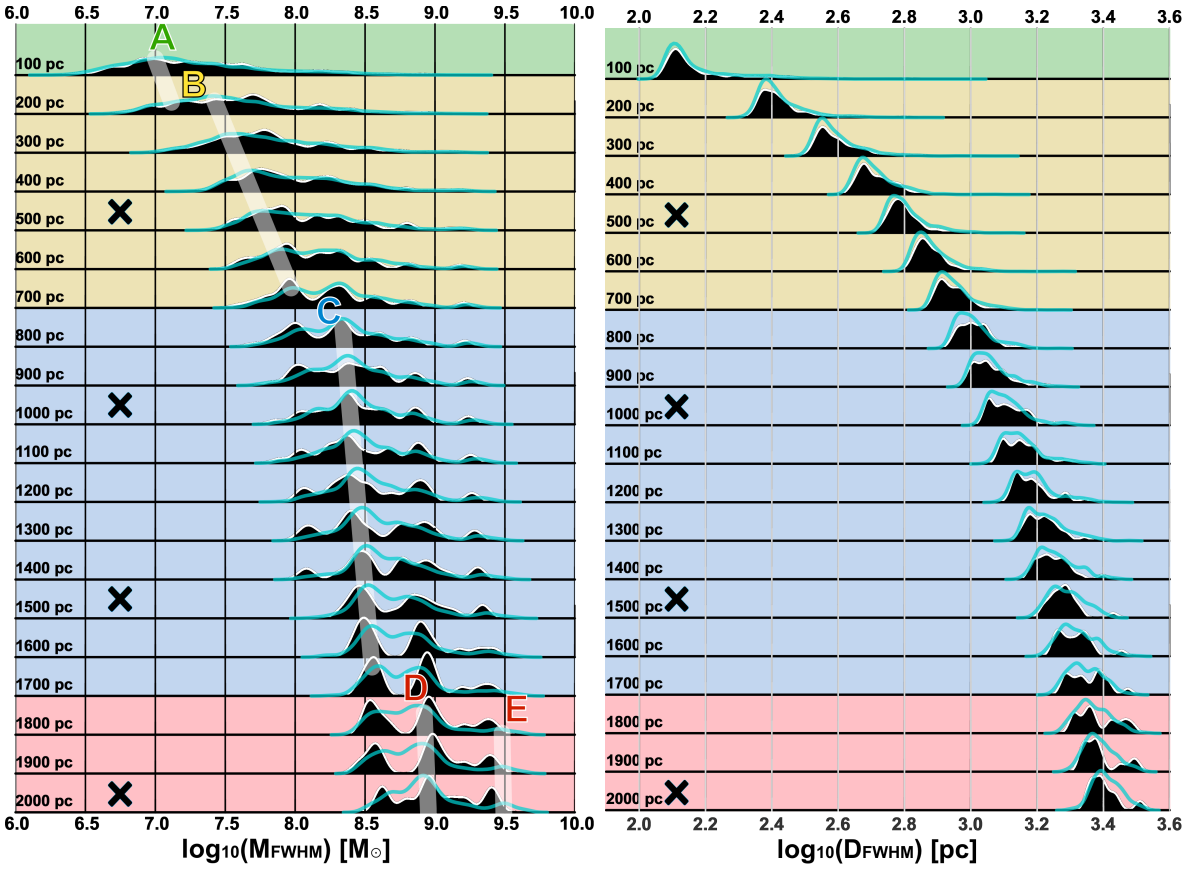

(a) (b)

Figure 5.18: The dependence of the mass (a) and size (b) number density distributions of the identified clumps and clump clusters on the beam smearing in lin-log representation (y-axis: FWHM of the beam smearing kernel). The black shaded histograms correspond to the single time step at 655 Myr and is overlayed with the average distributions between the time 450 - 655 Myr (cyan line). The dominant number of clumps or clusters of the average distributions are highlighted by the white guidelines (A,B,C,D,E) and their identified ranges with color in the background (see Table 5.3). The line-of-sight maps in Figure 5.16 are marked by the black crosses.

Table 5.3: Overview of the hierarchical properties of the identified clumps and clump cluster mass and size scales. Derived from data between 450 - 670 Myrs. For range A we give only the identified clump masses and sizes at FWHM=100pc. Within the BS-ranges B,C,D,E we take their average masses or sizes.

Name Ranges	Definition	Shading [color]	BS (FWHM) [pc]	M_{FWHM} [$M_\odot$]	D_{FWHM} [pc]	Detected Objects[a] [%]	Description
A	clumps	green	100-200	$\sim 10^7$	~ 125	60-100	intrinsic clumps
B	smallest clusters	yellow	200-700	$\sim 4.5 \times 10^7$	~ 450	23-60	dense groups
C	intermediate clusters	blue	700-1800	$\sim 3.2 \times 10^8$	~ 1500	5-23	mainly dense groups, partly open CCs
D	largest clusters	red	1800-2000	$\sim 9 \times 10^8$	~ 2000	5-6	dense groups and open CCs
E	central clusters	(red)	1800-2000	$\sim 3.2 \times 10^9$	~ 3200		dense grouping (sub-sample of D)

[a] The relative percentage of each range to the number of clumps detected for a beam smearing of FWHM=100pc.

from the RAMSES clump finder (3D density approach) in Section 5.4.2.2. If we increase the identified radius from the line-of-sight (LOS) clump detection by 50 percent we match the total mass of the intrinsic clumps. This means that the BS did not lead to fully Gaussian profiles since the FWHM should cover most of the clump mass within this area.

5.5.1 Identification of characteristic CC scales

For each beam smeared map (in FWHM=100 pc steps) we create mass and size histograms, compiled to the plots in Figure 5.18. Each distribution is represented by a kernel density estimation (KDE) in log scale (using the `Seaborn` library Waskom et al., 2017) to make them better readable. To adequately represent the finite data by the smoothing of the KDE we find for the D_{FWHM} distribution the Gaussian kernel 0.014 dex and for the M_{FWHM} distribution 0.0525 dex. The single timestep at 655 Myr (as shown in Figure 5.16) is compared with the time average for the evolved disc (between 450-655 Myr, sampled every 15 Myrs). In general, we find a continuous rise for the mass and radius with increasing BS. The time averaged radius distributions have small widths and are mainly single peaked for all measured BS. The same peaks are visible in the single time step example as well, but break up into multiple sub-peaks. The mass distributions are much broader (~ 1 dex) with different features (single, double, triple peaked) that identify the typical mass of a cluster. The peaks of the mass distributions for the single timestep example are mainly close to the time average distributions but much more prominent. Furthermore, for smaller BS of FWHM 100-300 pc we find a smoother distribution for the time average, due to stronger deviations of the identified objects between the timesteps, but are still represented by the dominant peak for the time average. The features of the mass profiles can be explained as the following. With increasing BS more and more clumps are sufficiently close together to appear as larger and single objects. These groups appear as a bump in the mass distribution which stays the same with stronger BS while the size still increases. For an isolated group of clumps this works very well, but in a galaxy the groups are surrounded by more structures which leads to a small increase in mass.

Therefore, we can identify a typical mass for CCs which stays quite similar in a certain range. These scales are dominating in different BS-ranges (colored background) which we highlight for the time-average data as guide lines in Figure 5.18 (summarized in Table 5.3). In the following we briefly describe each range and transition:

A: Intrinsic clumps
At the smallest BS we find mainly single clumps. The estimated clump properties at a BS of FWHM = 100 pc are close to the properties estimated from the intrinsic clump finder (Section 5.4.2.2) for the average mass. We find agreement for the most frequent clumps in the distribution with $< M_{FWHM} > \simeq 10^7$ $M_\odot$ and the size $< D_{FWHM} > \simeq 125$ pc. The first transition from single clumps to groups is within the BS of 100 pc - 200 pc. The dominant peak is replaced by a new one, indicated by the semi-transparent guidelines. The identified fraction of objects decreases dramatically to 60 percent within this small increase of BS (Figure 5.17a).

B: Smallest clusters (FWHM 200-700 pc)
The smallest clusters dominate the distribution in this range at an average mass of $< M_{FWHM} > \simeq 4.5 \times 10^7$ $M_\odot$ and an average size of $< D_{FWHM} > \simeq 450$ pc.The example with FWHM=500 pc in Figure 5.16 shows how several clumps appear as single objects in dense groups on these scales and some of the remaining single and isolated clumps disappear, because the BS reduces the peak density below the detection threshold of the blob finder. With larger BS another peak begins to form, representing the next larger scale of typical clusters described in range C. The number of identified objects decrease from 60 to 18 percent.

C: Intermediate clusters (FWHM 700-1800 pc)
These CCs are mainly present on average for $< M_{FWHM} > \simeq 3.2 \times 10^8$ $M_\odot$ on the average scale $< D_{FWHM} > \simeq 1500$ pc and are formed from groups of the previous range (compare in Figure 5.16 the example with FWHM=500 pc and FWHM=1000 pc). The smallest isolated clusters are smeared to larger radii and are disappearing within this range (flatter surface density), especially at the galaxy edge. Groups with close partners combine to become larger and more mass rich entities (compare in Figure 5.16 the example with FWHM=1000 pc and FWHM=1500 pc). Therefore, open clusters are also representing the giant BS objects. The dominant CCs of the following range D are already appearing (compare examples FWHM=1000 pc with FWHM=1500 pc in Figure 5.16) and in general represent the identified cluster scales in range C. A small fraction of 18-6 percent for the identified objects is left.

D: Largest clusters (FWHM 1800-2000 pc)
On these scales the dominant CCs have on average $< M_{FWHM} > \simeq 9 \times 10^8$ $M_\odot$ and an average size of $D_{FWHM} \simeq 2000$ pc. The clusters are the same and are represented on larger scales. This behaviour continuous with increasing BS (compare examples FWHM=1500 pc and FWHM=2000 pc in Figure 5.16). Some of the previous clusters cannot be identified because of their very low density contrast, again, mainly at larger disc radii. With 1.5 - 6 percent only a handful of objects can be identified.

E: Central clusters (FWHM 1800-2000 pc)
A peak at higher masses begins to evolve with $M_{\mathrm{FWHM}} \simeq 3.2 \times 10^9 \mathrm{M}_\odot$ in the center of the galaxy together with the peak described in range D, and typically consists of one or two distinguishable clusters. Since they are very dense groups, they are already present in the mass distributions from a BS of FWHM = 500 pc on, but increase in mass.

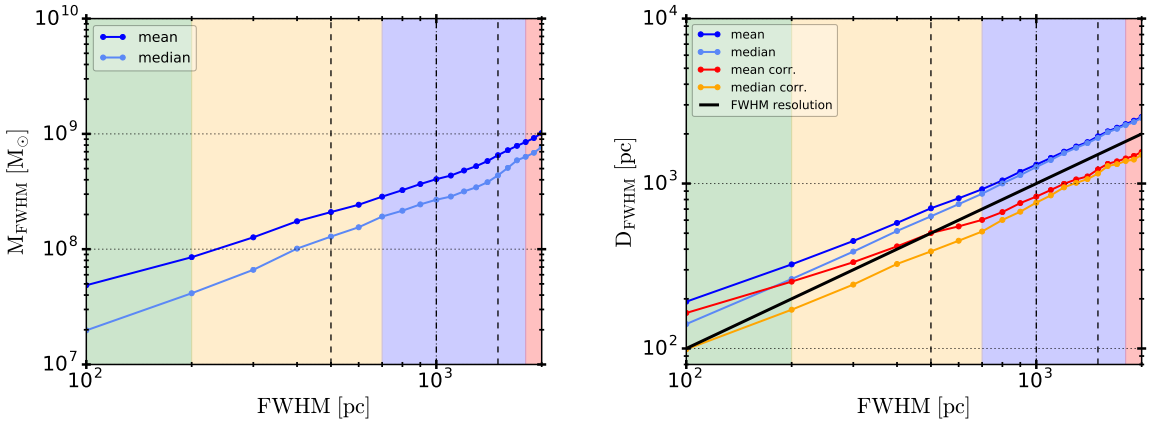

Figure 5.19: (a) The mean and the median of the mass of detected clumps and CCs is constantly rising with increasing FWHM of the beam smearing. (b) The linear relationship between the average and median size to the BS of detected clumps and CCs (blue and pale blue). The red and orange line result from quadratically subtracting the FWHM of the beam. The background colors refer to the identified cluster ranges (see Table 5.3). The vertical dashed black lines correspond to the line-of-sight maps in Figure 5.16.

5.5.2 Average CC properties correlation with beam smearing

The average mass and diameter profiles of the CCs are shown in Figure 5.19. Both have a strong relation to the beam smearing and the hierarchical grouping of the clumps is not visible. The positively skewed mass distributions are expressed by the smaller median and the higher mean values. We find

$$< \mathrm{M_{FWHM}} > \ (\mathrm{M}_\odot) \simeq (4 \times 10^5) \times \mathrm{FWHM\ (pc)}. \tag{5.13}$$

The CCs size $\mathrm{D_{FWHM}}$ distributions are very symmetrical, represented in the similar values for the mean and the median. We find for their relation to BS

$$< \mathrm{D_{FWHM}} > \ (\mathrm{pc}) \simeq (1.5 - 2) \times \mathrm{FWHM\ (pc)}. \tag{5.14}$$

Both relations together give the correlation between mass and sizes (see Figure 5.20)

$$< \mathrm{M_{FWHM}} > \ (\mathrm{M}_\odot) \simeq (2 - 2.67) \times 10^5 \times \mathrm{D_{FWHM}\ (pc)} \tag{5.15}$$

If we correct for BS (quadratically subtract the corresponding BS), the relation is

$$< \mathrm{D_{FWHM}} > \ (\mathrm{pc}) \simeq (0.8 - 1) \times \mathrm{FWHM\ (pc)}. \tag{5.16}$$

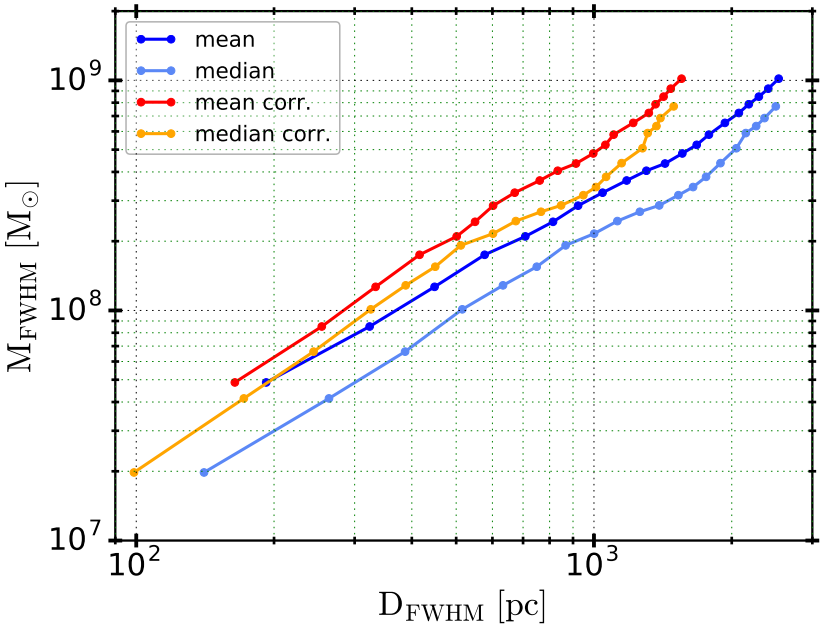

Figure 5.20: The relation between the mean and median mass and size of the detected clumps and CCs. The red and orange line result from quadratically subtracting the FWHM of the corresponding beam.

and leads to

$$< M_{FWHM} > \ (M_\odot) \simeq (4-5) \times 10^5 \times D_{FWHM} \ (pc). \tag{5.17}$$

We find strong deviations from the relationship below a BS of FWHM < 100 pc and above FWHM > 2 kpc.

5.6 Summary and Discussion

We simulated a massive gas disc with $\sim 3 \times 10^{10}$ $M_\odot$, Toomre unstable at different initial and maximum resolutions ($\sim 3 - 90$pc). All runs initially resolve the Toomre length by several resolution elements at all radii. Therefore, we can test the top-down hypothesis that giant clumps form directly on the Toomre scale and their sub-fragmentation on smaller scales within the clumps due to high resolution. Furthermore, we explore the relationship between the artificial pressure floor (APF) and the clump properties over time. Adding an APF is a numerical technique to prevent artificial fragmentation at maximum resolution. Finally, we investigate the clustering scales of the many clumps in the high resolution run and their properties related to the beam smearing between 0.1-2 kpc.

- **Indication for a bottom-up scenario:** The simulations reveal significant differences concerning the clump properties in the fragmented disc. The runs considered for various maximum resolutions demonstrate that the initial fragmentation process changes from a few giant clumps of $10^8 - 10^9$ $M_\odot$ with a diameter of 0.6- 1 kpc ($\sim$ comparable to the initial Toomre length) to many and much smaller and less massive clumps with $\sim 10^7$ $M_\odot$ with a diameter of ~ 100pc. A direct sub-fragmentation of the larger clumps with increasing resolution is absent. Instead, we see a transition from a direct formation of large clumps in the low resolution run to fully developing rings, which can further collapse until they fragment on much smaller scales than the initial Toomre length in the high resolution simulation. We find no strong relationship to the initial Toomre length in the evolved disc anymore. For this comparison study it is important to keep the minimum temperature the same at all times. It represents a minimum micro-turbulent pressure floor of the ISM which cannot be resolved in our simulations. Observations imply that the galaxies evolve with a Toomre parameter $Q \simeq 1$ over cosmic time but can lie above or below this value within the uncertainties (Wisnioski et al., 2015). We focus on the case of axisymmetric instabilities that arise for $Q < Q_{crit} \simeq 0.7$, but are close to Q_{crit}. The parameter-space in close proximity of the marginally stable case has to be explored further, e.g. for higher temperatures or small scale turbulence, to proof the bottom-up scenario and exclude the direct formation of clumps as large as the observed ones.

- **Main cause for the different outcome between the runs:** In general, we find that the high resolution runs can reach very high densities before the APF sets in (for $MS:\ n_H \geq 5 \times 10^3$ cm^{-3} , for $SR:\ n_H \geq 2 \times 10^3$ cm^{-3}), which allows for further collapse and fragmentation into clumps on much smaller scales than the initial Toomre length. For the low resolution runs the APF already acts at very low densities preventing from further collapse (for $LR: n_H \geq 53$ cm^{-3}, for $ULR:\ n_H \geq 13$ cm^{-3}). Furthermore, all clumps exhibit a hot core which is lower for smaller and higher for more massive ones and ranges between $c_s \sim 30 - 250$ km s^{-1}. The APF sets in all runs the minimum thickness of the clumps. The APF has a different effect between the low and high resolution runs. The initial clumps for the main simulation MS show less influence by the APF and are rotationally supported, even more the higher mass mergers. Smaller clumps are still supported by rotation but tend to be more influenced by the APF and/or the lower

limit of $c_s \sim 10$ km s^{-1}. The initial clumps are three times larger than the minimum resolved Jeans length and the massive mergers 6 times. The initial clumps in the low resolution runs LR and ULR have a Jeans mass and an average density given by the APF and are only around 1.6 times larger than the minimum Jeans length. We conclude that these runs produce artificially given clumps that are in this case coincidental at mass scales similar to observed giant clumps at ~kpc spatial resolution. Rotation might also play a role for the more massive mergers, which show lesser influence by the APF.

- **General clump properties**: For the high-resolution runs the initial clumps merge within < 50 Myr to ~ 10^8 $M_\odot$ with a diameter of ~ 120 pc and are dominating the main clump mass. For all runs, typically 50 percent of the disc mass is within high densities and 30 percent in lower densities which directly surround the clumps. The definition of *high* and *low* densities is changing for the different runs. For the higher resolutions (MS, SR) the clumps are well defined above the densities $n_H \geq 100$ cm^{-3} and are shifted for run LR to $n_H \geq 10$ cm^{-3} and for ULR to $n_H \geq 1$ cm^{-3}. The simulations from high to lower resolution experience shifts for several clump properties. The main mass of many clumps is transferred to much less clumps with 10^9 $M_\odot$ and smaller clumps are suppressed in LR and ULR. E. g. the size of the 10^8 $M_\odot$ clumps is 3 times larger (diameter ~ 360 pc) in run LR and 6 times larger (diameter ~ 720 pc) in ULR compared to the high resolution simulation MS. Also here, the clumps are closely surrounded by even lower densities with 30 percent of the disc mass. The properties we find for the runs LR or ULR are consistent in mass and size with clumpy galaxy simulations from various studies with a similar resolution and pressure floor.

- **Hierarchical scales of clump clusters:** At higher resolution, the vast number of clumps build larger groups from bottom-up within relatively short times $\ll$ 50 Myr and over all the evolutionary time of 670 Myr. We identify clump clusters on several mass scales by spatially convolving the densities with a Gaussian between 100-2000 pc. The clusters appear in the mass distributions as single peaks with almost 1 dex difference for each beam smearing level if the bin sizes of the histograms are small enough. In our case, they describe the transition between the different cluster scales. Single clumps can only be identified with observations with spatial resolutions of at most 100 pc. This finding is equivalent to Tamburello et al. (2017) (from $H\alpha$ mocks). The smallest CCs appear in dense groups on scales with a diameter of $D_{FWHM} \simeq 450$ pc and a mass of $M_{FWHM} \simeq 4.5 \times 10^7$ $M_\odot$. Furthermore, we find dense groups on the scale, $D_{FWHM} \simeq 1.5$ kpc with a mass of $M_{FWHM} \simeq 3.2 \times 10^8$ $M_\odot$. On the next scale we identify more and more open clusters, which do not necessarily have a strong gravitational connection. They have on average $D_{FWHM} \simeq 2.5$ kpc and a mass of $M_{FWHM} \simeq 9 \times 10^8$ $M_\odot$. The strong relationship to the beam smearing can be described on average by $< M_{FWHM} >$ $(M_\odot) \simeq (4 \times 10^5) \times$ FWHM (pc). and $< D_{FWHM} >$ (pc) $\simeq (0.8 - 1) \times$ FWHM (pc) (resolution quadratically subtracted). The masses and sizes of the identified objects depend on the definition. Here, the convolution does not lead to perfect Gaussian profiles and the full mass for the FWHM is not captured. By increasing the measured sizes by 50 percent, we fully represent the total mass of the high density clumps (50 percent of the disc mass). In Fisher et al.

(2017) the clump sizes are larger than the kernel of the convolved beam. In our case the sizes are larger on average for small beam smearing and with increasing convolution kernel smaller (resolution quadratically subtracted). It is difficult to compare the exact measured properties with observations. E.g. the high densities we take into account are shielded in Hα observations. By considering a cut of the peak densities in the simulations leads to a larger FWHM of the clumps and consequently to a larger mass. Therefore, we refer here mainly to the similar trend of the clump clustering of the stars with observational resolution in the observations of Cava et al. (2018).
With larger BS more and more massive clumps appear at the center of the galaxy while the isolated clusters at larger radii disappear in the environment. The clusters at FWHM=500 pc show similarities in mass and size to the low resolution runs (LR, ULR), but are much more numerous for the high resolution. Therefore, high and low resolution simulations are also in this case not directly comparable.

- **Final remarks and outlook:** For the presented bottom-up scenario, simulations with different galaxy properties have to be performed to explore the relationship to the clump clusters better and the convergence of the clump properties with resolution needs to be explored further. Overall, it is very useful to provide the effective resolution, since it is the minimum Jeans length that is resolved in a simulation and gives already information about the smallest possible structures. The maximum resolution alone is not sufficient enough to quantify how well clumps are resolved.
  The ring formation is predicted by the Toomre instability theory for axisymmetric conditions. In a disc with initially more local variations (as e.g. expected in a galaxy that is fed from outside) in density or velocity the rings may not fully develop, but we think that this is not affecting the main results in this study, namely that the resolution and artificial pressure floor are relevant to reach higher densities and allow for many structures on the sub-Toomre scale. Moreover, it should be further explored if reducing the APF with the cost of artificial fragmentation is more helpful in certain circumstances than producing inflated clumps.
  The simulated model resembles galaxies, where the gas dominates the hydrodynamics and local gravity over the stars. Therefore, the lack of a stellar disc negligibly affects the fragmentation process we study if it is represented in the effective background potential as in our case. Nevertheless, the components of the galactic disc and a live dark matter halo can influence the dynamical friction and hence increase the migration of clumps to the centre where they can contribute to a stellar bulge component. The observed high-z galaxies typically have a bulge component, while bulge-less cases also exist. This causes a deeper potential well in the centre leading to additional rotation, which would have a stabilizing effect together with less fragmentation for the innermost fraction of the simulated galaxy and therefore, does not change the main findings. A follow-up paper will investigate the changes caused by star formation and stellar feedback. Interestingly, the isolated galaxy simulations in Ceverino et al. (2012) with an initial stellar disc component, stellar feedback and in Bournaud (2016) with added radiation pressure show visually similarities to our simulations.
  Furthermore, sophisticated comparisons with observations are necessary e.g. by using radiative transfer and by taking into account the sensitivity limit of the instruments (Cava et al., 2018; Fisher et al., 2017; Tamburello et al., 2017). The next generation of

large telescopes like the Extremely-Large-Telescope (ELT) will have better resolutions than 100 pc and will hence allow to identify individual clumps and to proof the concept of hierarchical clustering. A part of the hierarchy can be investigated already by a spatial resolution better than 1 kpc.

5.7 Acknowledgements

We thank the referee Frédéric Bournaud for helpful comments that improved the manuscript. We are grateful to Alessandro Ballone, Matias Blaña, Katharina Fierlinger, Guang-Xing Li, Go Ogiya, Michael Opitsch, for fruitful discussions. The computer simulations have been performed on the HPC system HYDRA at the Max Planck Computing & Data Facility (MPCDF) center in Garching. MS acknowledges support by the Deutsche Forschungsgemeinschaft through grant no. BU 842/25-1. This work was supported by a grant from the Max-Planck Institute for Extraterrestrial Physics, by the Excellence-Cluster Universe, and by the German-Israeli Foundation through grant no. GIF 1341-303./2016.

Chapter 6

Summary

In this thesis, we investigate the origin of the observed giant clumps and structure formation of irregular galaxies at high redshift. We study the gravitational disc instability in greater detail that can develop in gas-rich galaxies and lead to the creation of clumps and peculiar structure. Observations imply that the galaxies evolve with an average Toomre parameter $Q \simeq 1$ over cosmic time but can lie above or below within the uncertainties (Wisnioski et al., 2015). Locally, substantial deviations are expected for Q, with smaller values inside giant clumps and larger values in the intermediate regions. Therefore, we employ hydrodynamic high-resolution AMR simulations of an idealised galaxy model that is close to the critical value of the parameter for gravitational disc instability $Q \leq Q_{\rm crit}$ of the thick disc approximation. Hence, we primarily focus on axisymmetric instabilities, that arise on much shorter time scales than non-axisymmetric structures that develop at higher Q values and examine the problems arising in using lower resolution simulations. Finally, we compare the simulated clump properties with observations.

Currently, two approaches are applied to simulate the structure in high-redshift irregular galaxies in more detail. Cosmological zoom-in simulations are used, with the advantage to take the cosmological context into account, e.g. infalling gas from the cosmic web. We utilise a complementary approach and simulate a galaxy in an isolated box. The advantages are the significantly higher resolution that can be reached (initially and finally) and the well-defined conditions to reduce the complexity. Our simulations are one of a few with the highest resolved (2.9 pc) clumpy galaxies that currently exist. The Jeans length is resolved by unprecedented 19 cells that allow a higher initial resolution and, therefore, capture the effects of self-gravity and hydrodynamics for the structure formation robustly. The disc is initially already in hydrodynamic equilibrium, and a relaxation phase that could contaminate our results is not needed. The basis is an analytical solution that we derived, and that can be extended for more components like a stellar disc.

6.1 The Toomre-length for thick discs and the sub-Toomre-scale fragmentation

At first, we test the paradigm that a few kpc sized, and massive objects form in a galaxy directly due to gravitational disc instability. This hypothesis is based on a formation scenario that assumes a direct clump formation on the scales predicted by the linear perturbation theory. We emphasise that the linear stability analysis only describes the perturbation growth in the early stages. The non-linear growth that follows and the direct relation of the Toomre-scale to clump properties is an interpretation and not predicted by the analysis itself. Typically, the razor-thin

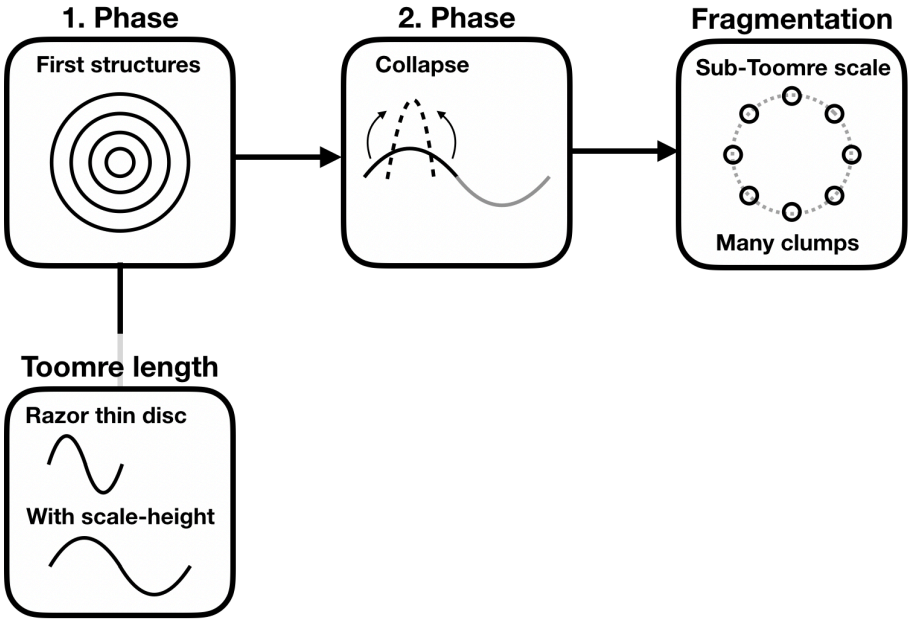

Figure 6.1: Illustration of the structure and clump formation by the Toomre instability. Only the first phase is related to local axisymmetric perturbations, which are for thick discs by a factor of ~ 2 times larger than in the classical razor-thin disc approximation. In a second phase the overdensities begin to collapse under their self-gravity and fragment into a vast number of clumps on much smaller scales (sub Toomre-scale).

disc approximation is applied to these calculations. Therefore, we revisit the axisymmetric perturbation theory and the resulting growth of structure by taking the realistic thickness of the disc into account **(Figure 6.1)**. From the linear stability analysis, we confirm the critical value $Q_{\rm crit} \sim 0.69$ for thick discs, found by several studies. Importantly, the fastest growing perturbation wavelength (often called the Toomre-length) is always a factor of ~ 2 times larger than in the classical razor-thin disk approximation for a typical vertical profile in hydrostatic equilibrium and an isotropic micro turbulence (sound speed). This result is independent of the adopted disc scale-height and by this independent of temperature and surface density. To test the analytical prediction of the ring formation, we compare it with a high-resolution hydrodynamic simulation of a massive gas disc with roughly $\sim 3 \times 10^{10}$ $M_\odot$. To fully develop the axisymmetric rings, we find that the disc scale-height has to be resolved initially by five cells. In the first phase rings form, with radial distances corresponding to their local fastest growing perturbation wavelength (several hundred to kpc lengths). *To our knowledge, this is the first proof of the fully developing axisymmetric instabilities in a disc simulation.* In the second phase, these rings contract, while at the same time accreting more gas from the inter-ring region. It is these collapsed and dense circular filaments that subsequently fragment into a large number of clumps. Contrary to what is typically assumed, the clump sizes are, therefore, not directly determined by the initially fastest growing wavelength (Toomre-length), but clumps form on a sub-Toomre length-scale!

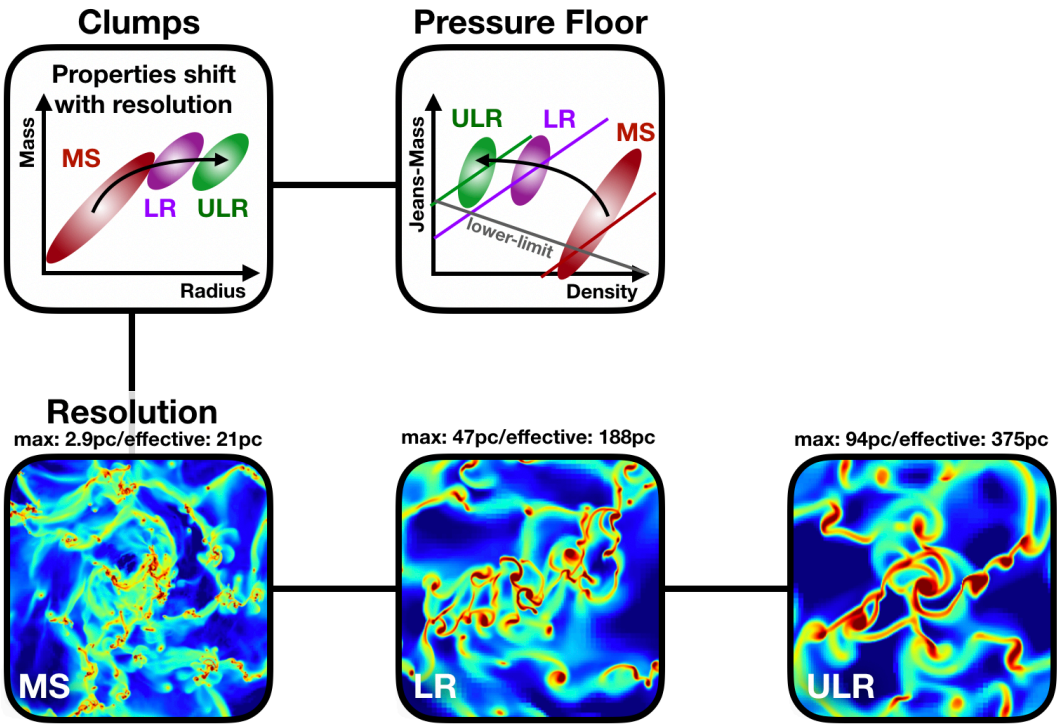

Figure 6.2: Illustration of the clump properties for the simulations that reach different maximum resolutions (top panel) and their surface density of the evolved discs (bottom panel). The clumps experience a significant shift in mass and size from high (MS) to low resolution (ULR) (1st plot). In the second plot, we compare their mass and average density with the expected Jeans mass given by the induced artificial pressure floor. It is evident that the initial clumps of the low-resolution runs (LR, ULR) are given by the APF. The initial clumps of run MS are influenced by the APF but are strongly rotationally supported. Only the low-mass clumps are mainly supported by the pressure given by the minimum temperature of the simulation (lower limit).

6.2 Properties of clumps in high-z galaxies: top-down vs. bottom-up

Studies using cosmological zoom-in simulations find mainly very massive and larger clumps (e.g. Ceverino, Dekel & Bournaud, 2010; Ceverino et al., 2012) than in the present thesis for a similar baryonic disc-mass. A common hypothesis is that the smaller clumps formed in high-resolution simulations are sub-fragments from a large scale giant clump and resemble the unresolved clumps of low-resolution simulations (see ***Figure 6.2*** *for an overview of the surface density for the evolved runs).* To prove the concept of sub-fragmentation of giant clumps, we simulate a massive gas disc with a mass of roughly $\sim 3 \times 10^{10}$ $M_{\odot}$, Toomre unstable (like in the previous study) at different initial and maximum resolutions ($\sim 3 - 90$pc). Importantly, all runs initially resolve the Toomre length by several resolution elements at all radii and therefore, can develop the same perturbations. However, a direct sub-fragmentation of the larger clumps from top-down (**Figure 6.3**) for an increased resolution is absent. The reason is the artificial pressure floor which we discuss in Section 6.3 in more detail. Instead of

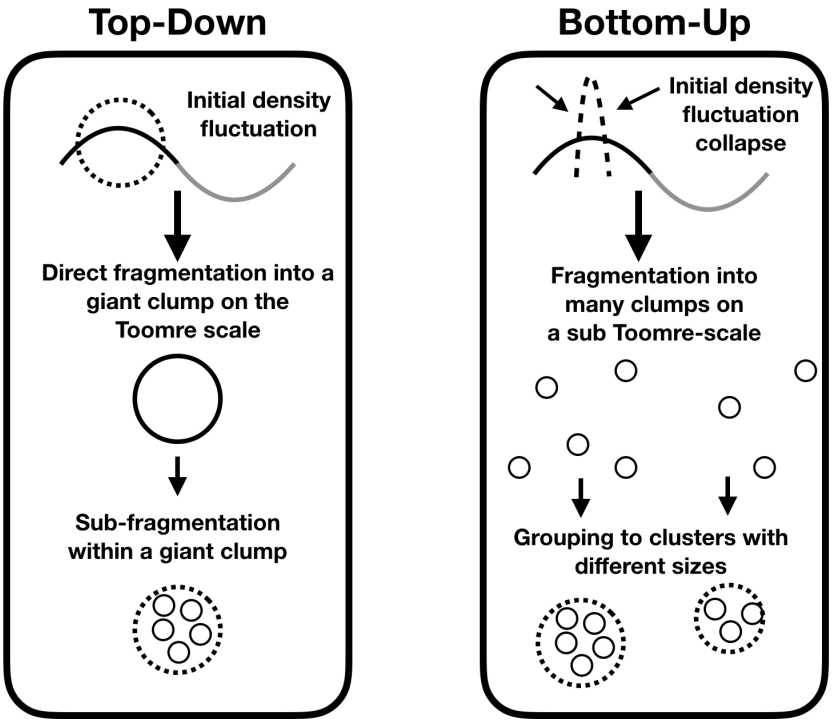

Figure 6.3: Illustration of two fragmentation scenarios. In the hypothetical top-down view the clumps form on the scales of the Toomre-length seeded by local perturbations and directly sub-fragment to gravitationally bound structures (local process), if the resolution in simulations allows. In the bottom-up scenario the initial perturbations collapse and the gas fragments to many clumps on the sub Toomre-scale, if the resolution or the APF in the simulations allows. The single clumps group to bound clusters (not local process), partly with different sizes and masses.

a top-down scenario, we find a transition from an immediate formation of a few large clumps in the low-resolution runs to fully developing rings for high-resolution. The rings can collapse further until they fragment to many clumps on much smaller scales than the initial Toomre length. For the high-resolution runs the initial clumps merge within < 50 Myr to ~ 10^8 $M_\odot$ clumps with a diameter of d_{MS} ~ 120 pc which dominate the total mass in clumps. For all runs, typically 50 per cent of the disc mass is within high densities ($n_H > 100 cm^{-3}$) and 30 per cent in lower densities, which directly surround the clumps and the rest is in the intermediate regions. The clumps in the lower resolution runs experience a strong shift towards lower densities (maximum and minimum) and the main mass resides in clumps with 10^9 $M_\odot$. E. g. the size of the 10^8 $M_\odot$ clumps is 3 times larger (d_{LR} ~ 360 pc) in run LR (minimum resolved Jeans-length $JL_{LR} \simeq 188$ pc) and 6 times larger (d_{ULR} ~ 720 pc) in ULR ($JL_{ULR} \simeq 375$ pc) compared to the high resolution simulation MS ($JL_{MS} \simeq 21$ pc).

6.3 The artificial pressure-floor and the impact on the clump properties

What is the main cause for different clump properties between the high- and low-resolution runs despite an initially resolved Toomre-length ***(Figure 6.2)****?* We find a strong relationship between the artificial pressure floor (APF) and the clump properties of the low-resolution simulations. Adding an APF is a numerical technique which is commonly used in clumpy galaxy simulations to prevent artificial fragmentation at the highest refinement level. The introduced pressure ensures a constant minimum Jeans length that is resolved by several resolution elements. In general, we find that the high-resolution runs can reach very high densities before the APF sets in (for $MS: n_{\rm H} \geq 4.4 \times 10^3$ cm^{-3}), which allows for further collapse and fragmentation into clumps on much smaller scales than the initial Toomre-length. For the low resolution runs the APF already acts at very low densities preventing from further collapse (for $LR: n_{\rm H} \geq 53$ cm^{-3}, for $ULR: \ n_{\rm H} \geq 13$ cm^{-3}). The initial clumps in the high-resolution simulations show less influence by the APF and are rotationally supported. The initial clumps are three times larger than the minimum resolved Jeans length and their merger products by six times. The initial clumps in the low resolution runs LR and ULR have a Jeans mass and an average density given by the APF leading to clump-sizes that are only around 1.6 times larger than the minimum Jeans length. Therefore, we conclude that these runs produce artificially given clumps that are in this case, coincidental at mass scales similar to observed giant clumps at ~kpc spatial resolution. Additionally, we think it is more advantageous to specify the minimum possible structures in the simulations due to the APF instead of specifying the maximum resolution. We call it the **effective resolution**! For run MS we have ~ 21 pc, run LR is limited to ~ 188 pc and run ULR to ~ 375 pc.

6.4 Clump Clusters formed due to the bottom-up scenario and their intrinsic properties

*The grouping to Clump clusters (CCs), the bottom-up scenario (****Figure 6.3****) and a comparison with intrinsic properties of observed giant clumps* ***(Figure 6.4)****.* In our high-resolution simulations, the vast number of clumps subsequently self-organize into larger groups within relatively short times $\ll 50$ Myr and are present over the whole simulation time. We call it the bottom-up scenario which is in contrast to the direct substructure formation within a giant clump (top-down view, discussed above). These CCs appear as single objects by considering observational limitations, since the imaging of distant galaxies is currently limited to a spatial resolution of ~1-2 kpc. Therefore, we apply a Gaussian convolution of FWHM = 1.6 kpc on our simulated gas disc MS and compare the clump properties with the observations of Genzel et al. (2011). We find that the small-scale substructure disappears and only a few giant clumps are visible with HWHM = 0.9-1.4 kpc and masses of $1.5 - 3 \times 10^9 {\rm M}_\odot$. They are organized in a ring with a radius of 4–7.7 kpc around the center of the galaxy which is often seen in observations. The model galaxy has around three times less baryonic mass than the observed galaxies in Genzel et al. (2011) which is reflected in three times less massive CCs. *When considering the beam-smearing effects on the kinematics, Genzel et al. (2011) concluded that these clumps are either pressure supported by high-velocity dispersion (see also*

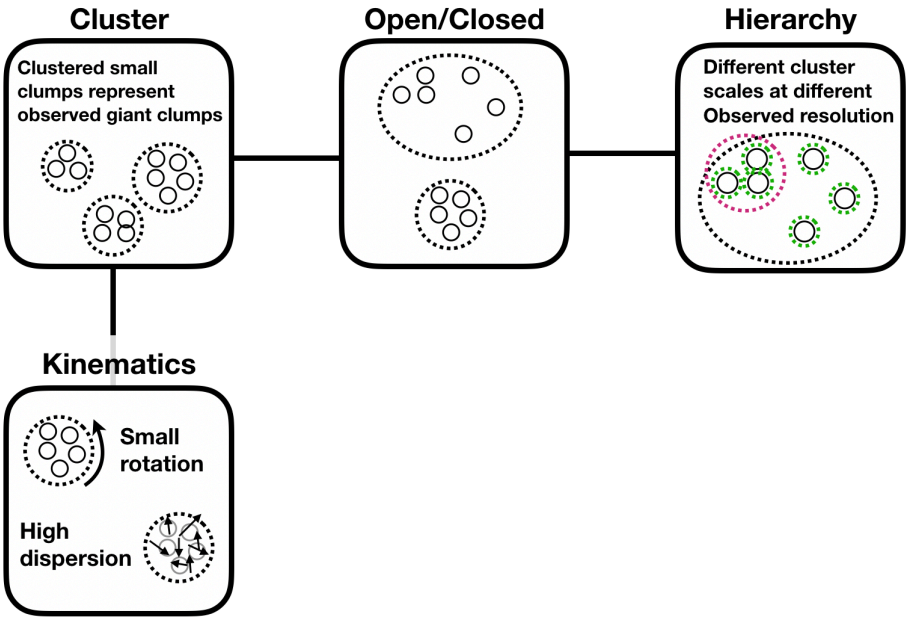

Figure 6.4: Illustration of the clump cluster properties deduced from our numerical experiments. Many smaller mass clumps group to clusters that appear as single kpc sized and massive objects for a large beam smearing (1.6kpc). The origin of the intrinsic velocity dispersion of the convolved giant clumps is given by the random motions of its sub-clumps (sub-structure). The small velocity gradient along the giant clumps is explained by the slow rotation of the CCs around its center. In the view of a single object the clump would appear as not in hydrostatic equilibrium and as still ongoing gravitational collapse. The clump clusters appear as groups on different mass and size scales (hierarchy). For smaller beam smearing (higher observational resolution) they are dense and possibly gravitational bound clusters. For a large beam smearing the objects are represented by gravitationally unbound open clusters or they are small and disappear in the image.

Dekel & Krumholz, 2013) or they are still undergoing collapse because of the small velocity gradients. We compare the internal kinematics of the CCs with the measurements obtained by the seminal work by Genzel et al. (2011). We take the line-of-sight (LOS) velocities of the clump regions and bin them into "channels" of width 34 km s^{-1} and spatially convolve each channel image. To obtain the intrinsic clump velocities, the beam-smeared LOS velocity of a rotating featureless exponential disk model is subtracted. The high intrinsic velocity dispersion $\sigma_{\mathrm{intrinsic}} = 65 - 105$ km s^{-1} of the CCs is caused by their subclump's high irregular motions. This is in contrast to previous assumptions that attributed the dispersion to turbulence generated by stellar feedback. We tested the effect of beam smearing on the inferred velocity dispersions and find no significant differences, indicating that these signatures can be used as realistic indicators of the CC kinematics. The observed high dispersion of massive clumps in gas-rich galaxies might, therefore, be indirect evidence for a cluster of weakly bound substructures and a characteristic property of CCs. This is also in agreement with the finding of (Genzel et al., 2011) that no significant correlation between their dispersion of $\sigma_{\mathrm{intrinsic}} = 53 - 95$ km s^{-1} and the star formation surface density exists. *Are the giant clumps rotationally supported?* From their high velocity dispersion and small velocity

gradients $V_{\rm grad}$ = 10 – 30 km s^{-1} (indication for rotation) the massive clumps, if considered as single objects, appear not in hydrostatic equilibrium indicating an ongoing gravitational collapse. In the CC picture this conclusion disappears and the small velocity gradients along the giant clumps is given by a rotation around their centers. The larger values correspond to faster rotating CCs and the smaller either to slowly spinning clusters or the substructure is "coincidently" close together to appear as a giant clump when beam-smeared.

6.5 The prediction of hierarchical scales of clump clusters

We identify clump clusters on several mass and size scales **(Figure 6.4)** by spatially convolving the surface density maps with a Gaussian with FWHM (full width at half maximum) between 100-2000 pc. Single clumps can be identified by an observational resolution better than 100 pc. The size of the beam is on average strongly related with the mass and the size of identified objects within the galaxy. With increasing beam smearing the clumps at larger radii begin to disappear due to a flat surface density and the center begins to dominate with a few or a single object. The smallest CCs appear in dense groups on scales with a diameter of $D_{\rm FWHM} \simeq 450$ pc and a mass of $M_{\rm FWHM} \simeq 4.5 \times 10^7$ M$_\odot$. Furthermore, we find dense groups on the scale, $D_{\rm FWHM} \simeq 1.5$ kpc with a mass of $M_{\rm FWHM} \simeq 3.2 \times 10^8$ M$_\odot$. On the next scale we identify more and more open clusters, which are not necessarily gravitationally bound. They have on average $D_{\rm FWHM} \simeq 2.5$ kpc and a mass of $M_{\rm FWHM} \simeq 9 \times 10^8$ M$_\odot$. The strong relationship to the beam smearing can be described on average by $< M_{\rm FWHM} >$ (M$_\odot$) $\simeq$ $(4 \times 10^5) \times$ FWHM (pc) and $< D_{\rm FWHM} >$ (pc) $\simeq (0.8 - 1) \times$ FWHM (pc) (resolution quadratically subtracted). The masses and sizes of the identified objects depend on the definition. Here, the convolution does not lead to perfect Gaussian profiles and the full mass for the FWHM is not captured. By increasing the measured sizes by 50 percent, we fully represent the total mass of the high density clumps (50 percent of the disc mass). In Fisher et al. (2017) the clump sizes are larger than the kernel of the convolved beam. In our case the sizes are larger on average for small beam smearing and with increasing convolution kernel smaller (resolution quadratically subtracted). It is difficult to compare the exact measured properties with observations. E.g. the high densities we take into account are shielded in Hα observations. By considering a cut of the peak densities in the simulations leads to a larger FWHM of the clumps and consequently to a larger mass. Therefore, we refer here mainly to the similar trend of the clump clustering of the stars with observational resolution in the observations of Cava et al. (2018).

We conclude that axisymmetric instabilities with a Toomre Q close to $Q \leq Q_{\rm crit}$ can reproduce the observed irregular high-redshift disc galaxies in many details, but differently than commonly expected. The high-resolution simulations show that structures can form on a sub-Toomre-scale. Importantly, the artificial pressure floor should only act at densities high enough to allow the gas to collapse. This leads to the fragmentation of many clumps (2nd phase), which group to clusters that appear as giant clumps when observed with limited spatial resolution and remarkably reproduce the observed internal kinematics. Furthermore, we predict a hierarchical scale of clump cluster properties that is related to observational beam smearing and can be revealed with the next generation of very large telescopes. Previous work has focused on a formation scenario where giant clumps directly form on the Toomre-scale and neglect the possibility of the 2nd phase. We also show that this view can be invoked by the artificial pressure floor that already acts at low densities, prevents further collapse and leads to artificially inflated clumps. Furthermore, we conclude that it is crucial to consider the disc thickness effects for the Toomre length (significantly larger), which is typically used to estimate clump properties in galaxies.

Chapter 7

Discussion and outlook

In this chapter, we shortly discuss key-findings and give an outlook into ongoing work that increases the complexity of our used models and generalises the results. At the end of the chapter, we give a solution that makes the handling of the enormous simulation data significantly more efficient in memory, storage usage and processing time.

7.1 Implications on the Toomre-length for the thick disc approximation and with anisotropic velocity dispersion

The local equations from the linear stability analysis of a razor-thin disc are typically adapted and related to a global disc property like its mass or kinematics. This approach is averaging the local conditions over the whole galaxy and can be seen as a representation of the initial conditions of a smooth disc. From these assumptions, clump properties have been predicted in the literature that can form under such conditions. However, we show in the thesis, the Toomre-length for discs with a typical vertical profile and an isotropic pressure support (sound speed) is with a constant factor of around ~ 2 times larger than in the thin disc approximation. Consequently, the mass estimation is four times larger when considering a circular clump patch. In the evolved galaxy simulation or observed galaxies, the radial σ_R and the vertical velocity dispersion σ_z are typically different. Since the scale-height is dependent on σ_z, it has an impact on the total potential in the mid-plane and therefore, can change the Toomre length (See Appendix A). For a larger radial dispersion, e.g. for $\sigma_R/\sigma_z = 1.25$ the Toomre length can be smaller by $\sim 15\%$ and for a dominating vertical dispersion $\sigma_R/\sigma_z = 0.75$ by $\sim 30\%$ larger. Accordingly, the observed anisotropic velocity dispersions also affects mass estimations.

7.2 Axisymmetric instabilities for different galaxy conditions

In the thesis, we study the fragmentation of a galaxy that has a minimum and initial sound-speed of ~ 10 km s^{-1} leading to a Toomre Q profile that allows to grow axisymmetric instabilities and to be close to the critical value for marginal stability $Q_{\rm crit} \simeq 0.7$. With the developed theoretical framework, the parameter space for axisymmetric instabilities can be extended (see Figure 7.1). For the following analysis, we keep fixed values for the Q profile, the scale-length of the gas disc and the dark matter profile. Only the densities are scaled, the isothermal sound-speed of the disc and the densities of the dark matter.

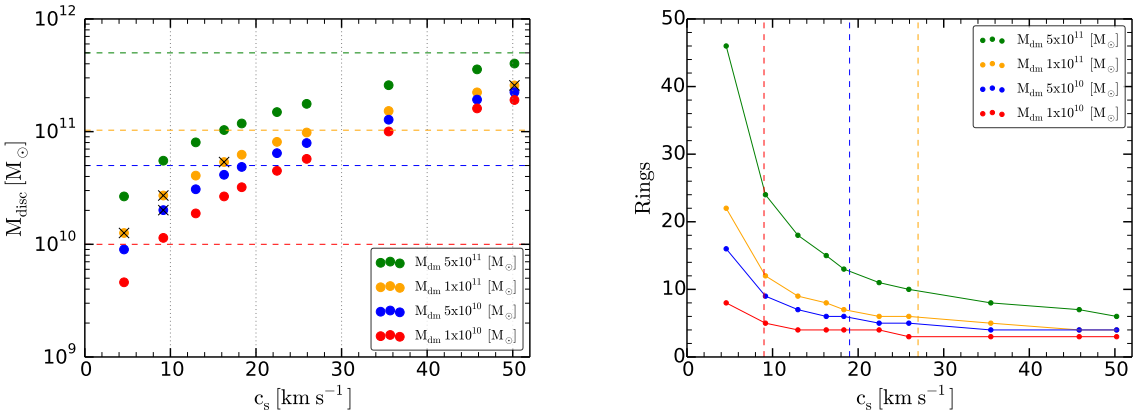

Figure 7.1: The parameter-space of growing axisymmetric instabilities for the thick disc approximation and a fixed Toomre Q profile. (a) The disc mass correlates with the dark matter mass (within the disc radius) and the gas-pressure, expressed by the sound speed. (b) The various initial conditions in Figure (a) lead to different growing perturbation sizes within a disc which is expressed by the number of growing rings. Above the horizontal or vertical dashed lines mark the point where the baryonic mass of the galaxy dominates over the corresponding dark matter within the disc radius.

The following general trends and conclusions can be drawn:
(a) An increasing disc mass correlates with a higher sound-speed and therefore, with larger perturbations that correspond to fewer rings in a smooth disc.
(b) A more massive dark matter halo is related to a larger baryonic mass at the same sound-speed but leads to smaller perturbation lengths. Therefore, the stronger the dark matter dominates the smaller the expected perturbations (more rings).
(c) Whenever the baryons dominate over the dark matter, we find similarly large perturbations, but with different disc masses and sound-speeds and therefore, different masses per ring/perturbation. These conditions are fascinating to investigate further since recent studies of the kinematics in high-z galaxies indicate cases where the dark matter fraction is low within the disc (Genzel et al., 2017).

The estimated parameter-space for the growing perturbations can be used to employ simulations to draw further conclusions on the clump number and mass per clump. Furthermore, the cases for discs around $Q = Q_{crit}$ and $Q > Q_{crit}$ for non-axisymmetric instabilities have to be explored further. From the discussions above a similar sequence is expected: the perturbations grow, but on much longer time scales, followed by a collapse phase and a sub fragmentation on smaller scales. The simulations and considerations so far start with a smooth disc configuration. The impact of initial turbulence on the structure formation is a future task.

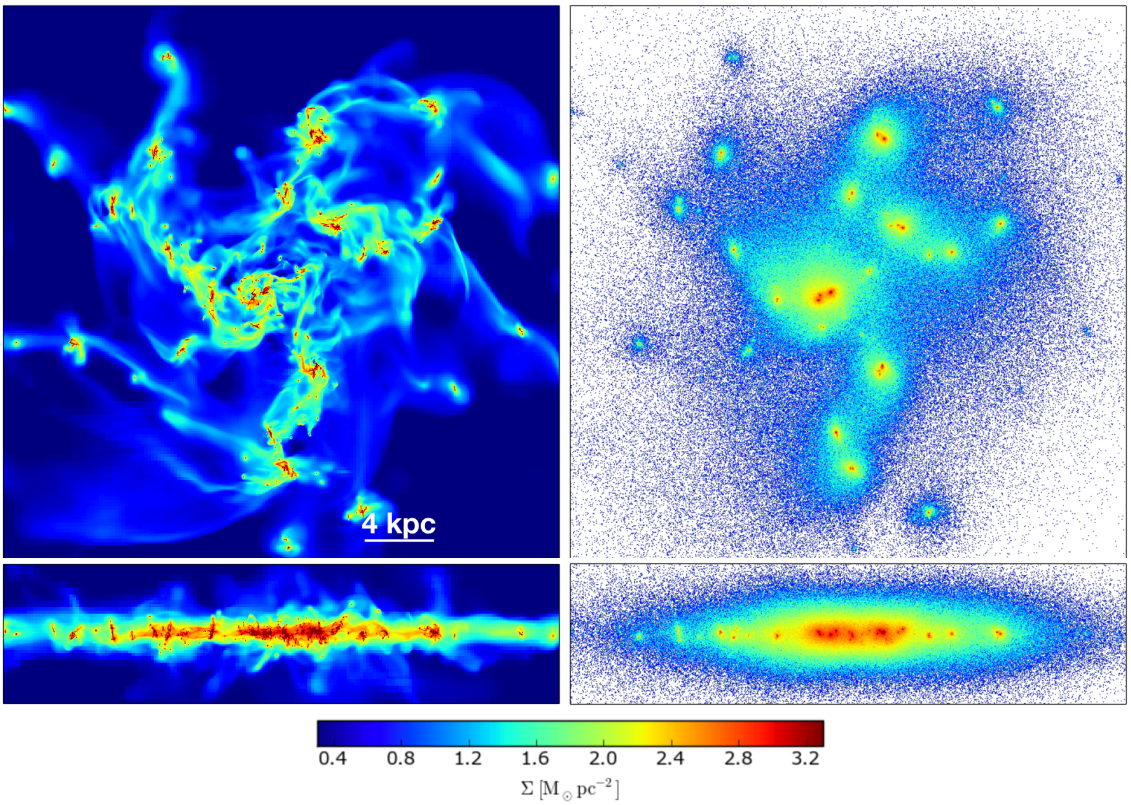

Figure 7.2: Surface density projections of the evolved galaxy simulation with star formation and supernova feedback (left panel: gas, right panel: stars). The upper row shows the disc in face-on view and the lower panel the edge-on view. In the gas component, many grouped clumps can be identified, and fountain-like outflows are leaving the disc on kpc-scales. In the stellar component, the more massive clumps are best visible, while the smaller ones are harder to see. The projections are realised with the MERA package (see Section 7.4).

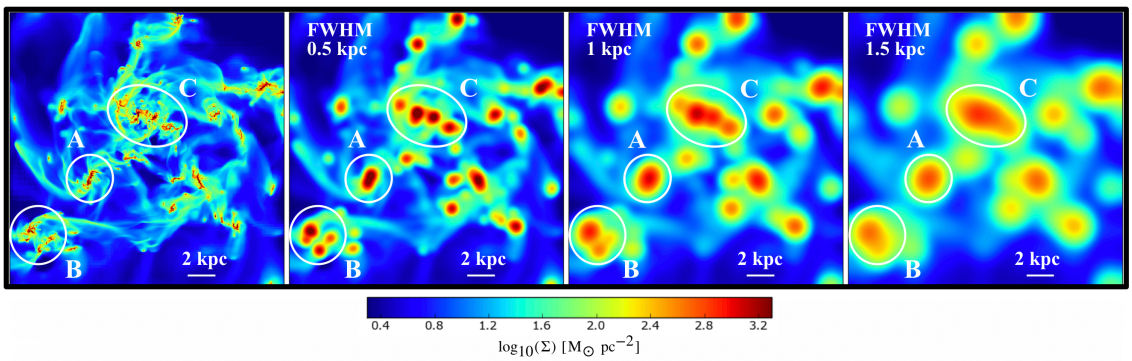

Figure 7.3: Face-on projection of the gas surface density seen in full resolution and for different beam smearings. Several characteristics can be identified for clump clusters when decreasing the observational resolution. The projections are realised with the MERA package (see Section 7.4).

7.3 Simulations with star formation and stellar feedback

Stars play a crucial role in galaxies. They form in dense molecular clouds and consume the dense gas component over time. Supernova feedback from massive stars give a part of the gas back and enrich the environment with higher elements. Furthermore, it heats the surrounding ISM and can affect the local environment kinematically, which can halt further star formation, effect clump life-times and lead to galactic outflows. Therefore, we extend the previous high-resolution simulation (~ 3pc) with star formation, supernova feedback, an adiabatic equation-of-state, and cooling above 10^4K. The details of the numerical prescriptions used in the code RAMSES are described in (Teyssier (2002); Schartmann et al. (2018)). We use the same initial Q profile at 10^4K with a slightly larger galaxy mass of $\sim 4 \times 10^{10}$ $M_\odot$. The stars form at densities $n_H > 100$ cm^{-3} which typically corresponds to molecular gas. At these densities, the gas is already collapsed and the sub-Toomre-scale fragmentation scenario is therefore, still present. New stars only form in clumps, are scattered out over time due to tidal stripping and are building-up a stellar disc which contains the older population. The evolved disc (Figure 7.2) represents a high-z star forming main sequence galaxy with a SFR ~ 24 $M_\odot$, f_{gas} ~ 75% and a depletion time ~ 700 Myr (for $n_H > 100$ cm^{-3}). The evolution goes along with strong fountain-like outflows reaching kpc-scales caused by supernova feedback (the fraction of gas reaching escape velocity is negligible). The more massive gas clumps are dense enough to stay long-lived, the impact on the surrounding ISM and the effect of additional stellar feedback including radiation pressure and photo-ionization has to be studied further. High-resolution simulations, including these recipes, show visually similarities to our models (Bournaud et al., 2014). Low-resolution simulations reach much smaller densities. Therefore, numerical star formation has to be applied at lower densities, and the stellar feedback models can have a different impact on clump formation, clump-life times and outflows. We find that smaller clumps group to clusters that can appear as single objects when observed with a lower spatial resolution (Figure 7.3), similarly to the simulations in the thesis including only a gas component. The details of the underlying clump statistics has to be elaborated. Depending on the underlying cluster arrangement we identify different characteristics, which we only partly describe in the thesis:
A: Dense groups that appear as a single object already with a small beam smearing (BS) and increase mainly their size more and more with decreasing resolution (studied in the thesis).
B: For an open cluster the number of clumps decrease with BS and the mass/size of its members increase (hierarchy of groups). Finally, they appear as a single object at larger FWHM (studied in the thesis).
C: Many clumps aligned in a line that appear as an elongated single object at larger FWHM.
More realistic mock observations are necessary for detailed comparisons, including the stellar light with stellar synthesis models, radiative transfer for the gas, dust, metallicity, cosmological dimming, and considering the sensitivity limit of current instruments.
The migration of clumps to contribute to a bulge component is in the literature debated. The effect on migration timescales due to dynamical friction caused by the underlying stellar disc, the gas component and a live dark matter halo needs to be investigated.

7.4 MERA, a tool to efficiently process and store huge simulation data-sets, written in the language Julia

In scientific computing, we are dealing with a steadily increasing amount of produced data, which requires the highest performance analysis tools. Therefore, most science-related libraries are written in low-level languages like C/C++ or Fortran with relatively long development times. In the following, we describe current approaches in reading and processing the RAMSES data. Existing Fortran post-processing tools interpolate the data onto a uniform grid and are controlled by the command-line. The reading and further calculations are fast, but it makes it impossible to load the full data set of simulation into the memory, and therefore, only smaller parts of the data cube can be accessed at once. The reduced data is often processed in a high-level language like Python (Van Rossum & Drake Jr, 1995) or R (R Core Team, 2013). Another way is to use Python for the high-level and interactive handling of the AMR data (no interpolation), but using, e.g. the C language in the background. This gives the user simple access, but it is more difficult to understand the backend program, and it is more time-consuming to extend the package. It is also possible to use Python only and existing external libraries like Numpy or Scipy that are written in low-level languages. Experience has shown us that the reading of the data with Python is slow. The performance of a function can be still limited by the implementation and by Python itself as the handler of all operations. With Mera[1], we develop a package for working with large 3D AMR and particle data sets to solve the addressed problems. It is entirely written in Julia (Bezanson et al., 2017) a powerful and relatively new language for numerical computing that aims at bridging the gap between ease-of-use and performance. An increasing number of scientists use it for their daily work, in lectures or for huge projects on HPC systems. The syntax is simple and great for math. The just-in-time compilation allows for interactive coding and to achieve an optimized machine code on the fly (in the background). Both enhance prototyping and code readability while maintaining high performance. Therefore, complex projects can be realized in relatively short development times.

Further features of Julia (see https://julialang.org):

- Package manager
- Runs on multiple platforms
- Multiple dispatch (Wikipedia, 2019c)
- Build-in parallelism
- Metaprogramming (Wikipedia, 2019b)

[1]The acronym Mera is originally deduced from a friends name. Recently, it turned out that the girlfriend of superhero Aquaman is called Mera (Wikipedia, 2019a). With her superpowers, she can control water, currently a unique skill among the Atlanteans. This is analogous to the superpowers of our code Mera in processing hydrodynamic data.

- Directly call C, FORTRAN, PYTHON (e.g. Matplotlib), R libraries
- ...

MERA Package features:

- Easy to install and update
- Fast and memory lightweight data reading/saving and handling
- The data is loaded and processed in a database framework (https://juliadb.org)
- Efficient workflow
- Many functionalities for advanced analysis
- Transparent operations of the functions
- Easy to extend
- Interactive and script functionality
- Many examples and tutorials

A showcase of the workflow with MERA to efficiently analyse and visualise RAMSES data and a performance test of an example is in the Appendix B.

Appendix A

The Toomre-length for anisotropic velocity dispersions

We extend the derivation of the isotropic Toomre-length for the thick disc approximation of (Paper 1) to a anisotropic version. Therefore, the sound-speed of the Toomre length (Equations B2, B3) is substituted with the radial velocity dispersion σ_R (Equation A.1, A.2) and for the scale height by the vertical velocity dispersion σ_z (Equation A.3).

The Toomre-length (fastest growing perturbation) for an exponential vertical profile is defined as

$$\lambda_{f_{\rm exp}} = \frac{2\sigma_{\rm R}^2}{3G\Sigma} + \frac{4\sigma_{\rm R}^2}{9G^2\Sigma^2}\frac{\left(\sigma_{\rm R}^2 + 6\pi G\Sigma z_0\right)}{T_{\rm A}} + T_A, \tag{A.1}$$

with the substitution

$$T_{\rm A} = \left(\sqrt{\frac{16\pi^4\sigma_{\rm R}^4 z_0^4}{G^2\Sigma^2} + \frac{64\pi^3\sigma_{\rm R}^6 z_0^3}{27G^3\Sigma^3}} + \frac{8\sigma_{\rm R}^6}{27G^3\Sigma^3} + \frac{8\pi\sigma_{\rm R}^4 z_0}{3G^2\Sigma^2} + \frac{4\pi^2\sigma_{\rm R}^2 z_0^2}{G\Sigma}\right)^{1/3} \tag{A.2}$$

and the scale hight

$$z_0 = \frac{\sigma_{\rm z}^2}{\pi G\Sigma}. \tag{A.3}$$

The fastest growing wavelength for the thin-disc approximation is

$$\lambda_{f_0} = \frac{2\sigma_{\rm R}^2}{G\Sigma}. \tag{A.4}$$

The Equation A.2 simplifies with the ratio of the velocity dispersion components $a = \sigma_R/\sigma_z$ and the Equations A.3 and A.4 to $\lambda_{f_{\rm exp}}(\Sigma, \sigma_{\rm R}, z_0(\sigma_z)) \rightarrow \lambda_{f_{\rm exp}}(\Sigma, \sigma_{\rm R}, \sigma_{\rm z}) \rightarrow \lambda_{f_{\rm exp}}\left(a, \lambda_{f_0}\right)$, and is

$$\lambda_{f_{\rm exp}} = \lambda_{f_0}\left(\frac{1}{3} + \frac{(1+\frac{6}{a^2})}{9T_{\rm B}} + T_{\rm B}\right), \tag{A.5}$$

with

$$T_{\rm B} = \frac{T_{\rm A}}{\lambda_{f_0}} = \left(\sqrt{\frac{3}{4a^8} + \frac{1}{27a^6}} + \frac{1}{27} + \frac{1}{3a^2} + \frac{1}{2a^4}\right)^{1/3}. \tag{A.6}$$

The isotropic case is represented by a = 1 with $\mathrm{A}_{\lambda_{\rm exp}} \sim 2.148$. The correction factor $\mathrm{A}_{\lambda_{\rm exp}}$ of the wavelengths is only dependent on the ratio $a = \sigma_R/\sigma_z$. For a dominating vertical dispersion σ_z, the wavelength is longer for a given Σ since the mid-plane potential is reduced, a dominating radial dispersion σ_R leads to a smaller perturbation. For smaller vertical dispersions $\mathrm{A}_{\lambda_{\rm exp}}$ is converging to the razor-thin disc case.

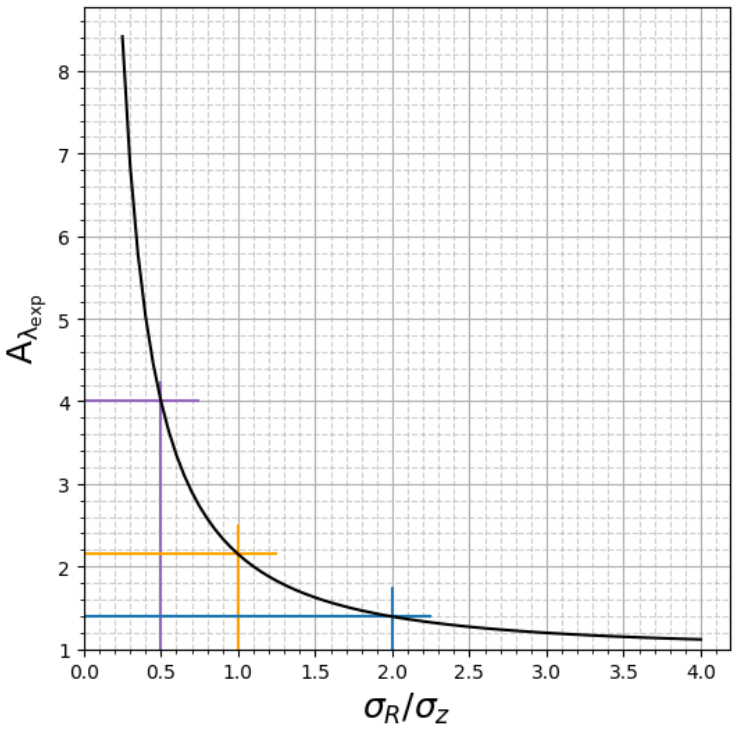

Figure A.1: Dependence of the correction factor for wavelengths of the thin disc approximation on the velocity dispersion ratios (black solid line). The colored solid lines mark some examples.

Appendix B

MERA by an example

MERA is a package to efficiently process, read and store large 3D AMR and particle data sets, written in the language JULIA (Bezanson et al., 2017). The following presentation is a small excerpt of MERA's capabilities and focuses on the gas data of a clumpy galaxy simulation with RAMSES (similar to the simulation in Section 7.3) and show some functions which typically have longer execution times in other packages. For each function and its features, a detailed documentation exists. We make use of multiple dispatch (Wikipedia, 2019c) to recognise the different provided input of data types: hydro, gravity, particles, clumps, etc... Therefore, the function names are the same for all data types, and only some keyword arguments vary. The following example is fully executed in Jupyter Lab with JULIA v1.1.1 on a MacBookPro with the following specifications: Processor: 2.4 GHz Intel Core i7; Memory: 16 GB 1867 MHz LPDDR3). The @time macro is used to profile the functions, printing the time it took to execute, the number of allocations and the total number of bytes its execution caused to be allocated, before returning the value of the expression.

Content:

- Simulation and Data Overview
- Efficient Reading and Storing of the Data
- Fast High-Resolution Projections
- Call PYPLOT (PYTHON)
- Create a Sub-Region
- 2D Histograms
- Data Masking

In [2]:
```
using Mera
```

Overview of the Simulation Output

The function "getinfo" prints an overview on the screen from simulation output 400 (here):

In [2]:
```
info = getinfo(400);
#info = getinfo(output=400, path="/different-path/", verbose=false
) # shows more options
```

```
[Mera]: 2019-07-07T11:32:36.628

Code: RAMSES
output [400] summary:
----------------------------------------------------------
simulation time: 594.98 [Myr]
boxlen: 48.0 [kpc]
ncpu: 2048
ndim: 3
level(s): 6 - 14 --> cellsize(s): 750.0 [pc] - 2.93 [pc]
hydro-variables:  7  --> (:rho, :vx, :vy, :vz, :p, :var6, :var7)
hydro-descriptor: (:density, :velocity_x, :velocity_y, :velocity_
z, :thermal_pressure, :passive_scalar_1, :passive_scalar_2)
gravity: true
particles: true
- Npart:    5.091500e+05
- Nstars:   5.066030e+05
- Ndm:      2.547000e+03
- Nsinks:   0.000000e+00
clumps: true
compilation-file: true
namelist-file: true
makefile: true
timer-file: false
----------------------------------------------------------
```

MERA uses predefined short variable names, but it is also possible to use the definitions in the descriptor files. Additionally, the descriptor-list can be customised by the user, which is recognised by the functions in **MERA**.

The created object "info" is of type: *InfoType* (composite type) and is recoginzed by the dedicated functions in **MERA**:

In [3]:
```
typeof(info)
```

Out[3]:
```
InfoType
```

Many simulation properties are assigned to the object "info" (here) and can be accessed from its fields (all values are stored in code units):

In [4]:
```
viewfields(info)
```

```
output  = 400
path    = /Users/mabe/Documents/Projects/JuliaLanguage/Mera/Mera/
tutorials/simulations/./
simcode = RAMSES
mtime   = 0.0
ctime   = 0.0
ncpu    = 2048
ndim    = 3
levelmin        = 6
levelmax        = 14
boxlen  = 48.0
time    = 39.9019537349027
aexp    = 1.0
H0      = 1.0
omega_m = 1.0
omega_l = 0.0
omega_k = 0.0
omega_b = 0.0
unit_l  = 3.085677581282e21
unit_d  = 6.76838218451376e-23
unit_m  = 1.9885499720830952e42
unit_v  = 6.557528732282063e6
unit_t  = 4.70554946422349e14
hydro   = true
nvarh   = 7
variable_list   = Symbol[:rho, :vx, :vy, :vz, :p, :var6, :var7]
hydro_descriptor        = Symbol[:density, :velocity_x, :velocity
_y, :velocity_z, :thermal_pressure, :passive_scalar_1, :passive_s
calar_2]
use_hydro_descriptor    = false
gravity = true
particles       = true
clumps  = true
Narraysize      = 0

scale ==> subfields: (:Mpc, :kpc, :pc, :mpc, :ly, :Au, :km, :m, :
cm, :mm, :μm, :Msol_pc3, :g_cm3, :Msol_pc2, :g_cm2, :Gyr, :Myr, :
yr, :s, :ms, :Msol, :Mearth, :Mjupiter, :g, :km_s, :m_s, :cm_s, :
nH, :erg, :g_cms2, :T_mu, :Ba)

grid_info ==> subfields: (:ngridmax, :nstep_coarse, :nx, :ny, :nz
, :nlevelmax, :nboundary, :ngrid_current, :bound_key, :cpu_read)
```

```
part_info ==> subfields: (:eta_sn, :age_sn, :f_w, :Npart, :Ndm, :
Nstars, :Nsinks)

compilation ==> subfields: (:compile_date, :patch_dir, :remote_re
po, :local_branch, :last_commit)

constants ==> subfields: (:Au, :Mpc, :kpc, :pc, :mpc, :ly, :Msol,
:Mearth, :Mjupiter, :Rsol, :me, :mp, :mn, :mH, :amu, :NA, :c, :G,
:kB, :Gyr, :Myr, :yr)
```

All calculations in **MERA** are realised in code units. The RAMSES scaling factors from code- to cgs-units are given for the length, density, mass, velocity and time assigned to the fields:

unitl, unitd, unitm, unitv, unit_t

To make life easier, we provide more predefined scaling factors, assigned to the sub-field *scale*:

In [5]:
```
viewfields(info.scale)
```

```
[Mera]: Fields to scale from user/code units directly to given un
its
================================================================
======
Mpc     = 0.0010000000000006482
kpc     = 1.0000000000006481
pc      = 1000.0000000006482
mpc     = 1.0000000000006482e6
ly      = 3261.5637769461323
Au      = 2.0626480623310105e23
km      = 3.0856775812820004e16
m       = 3.085677581282e19
cm      = 3.085677581282e21
mm      = 3.085677581282e22
µm      = 3.085677581282e25
Msol_pc3        = 0.9997234790001649
g_cm3   = 6.76838218451376e-23
Msol_pc2        = 999.7234790008131
g_cm2   = 0.20885045168302602
Gyr     = 0.014910986463557083
Myr     = 14.910986463557084
yr      = 1.4910986463557083e7
s       = 4.70554946422349e14
ms      = 4.70554946422349e17
Msol    = 9.99723479002109e8
Mearth  = 3.329677459032007e14
Mjupiter        = 1.0476363431814971e12
g       = 1.9885499720830952e42
km_s    = 65.57528732282063
m_s     = 65575.28732282063
cm_s    = 6.557528732282063e6
nH      = 30.987773856809987
erg     = 8.551000140274429e55
g_cms2  = 2.9104844143584656e-9
T_mu    = 517028.3199143136
Ba      = 2.910484414358466e-9
```

Load All Data of the Full Box

Only the data of the leaf-cells of the AMR grid are considered.

Further options are implemented:

Selection of the maximum level, variables, spatial ranges in domain-, physical-units or relative to a given centre etc..(see the commented line). Furthermore, the data is checked for negative densities or pressure.

In [6]:
```
gas = gethydro(info);
#gas = gethydro(info, lmax=10, [:rho, :vx, :p], xrange=[-10., 10.]
, yrange=[-10., 10.], zrange=[-2., 2.], center=[24.,24.,24.], rang
e_units=:kpc);
```

```
[Mera]: Get hydro data: 2019-07-06T23:35:15.753

Using var(s)=(1, 2, 3, 4, 5, 6, 7) = (:cpu, :rho, :vx, :vy, :vz,
:p, :var6, :var7)

domain:
xmin::xmax: 0.0 :: 1.0          ==> 0.0 [kpc] :: 48.0 [kpc]
ymin::ymax: 0.0 :: 1.0          ==> 0.0 [kpc] :: 48.0 [kpc]
zmin::zmax: 0.0 :: 1.0          ==> 0.0 [kpc] :: 48.0 [kpc]

Reading data...

100%|████████████████████████████████████████████████| Time: 0
:04:26

Memory used for data table :4.519803658127785 GB
------------------------------------------------------------
```

The progress bar (hour:minute:seconds) gives an excellent total time estimate for many functions in **MERA**.

The assigned object is now of composite-type: *HydroDataType*:

In [45]:
```
typeof(gas)
```

Out[45]:
```
HydroDataType
```

The data is stored in a JuliaDB table and the user selected hydro variables and parameters are assigned to fields:

In [46]:
```
viewfields(gas)
```

```
data ==> JuliaDB table: (:columns, :pkey, :perms, :cardinality, :
columns_buffer)

info ==> subfields: (:output, :path, :simcode, :mtime, :ctime, :n
cpu, :ndim, :levelmin, :levelmax, :boxlen, :time, :aexp, :H0, :om
ega_m, :omega_l, :omega_k, :omega_b, :unit_l, :unit_d, :unit_m, :
unit_v, :unit_t, :hydro, :nvarh, :variable_list, :hydro_descripto
r, :use_hydro_descriptor, :gravity, :particles, :clumps, :Narrays
ize, :scale, :grid_info, :part_info, :compilation, :constants)

lmin     = 6
lmax     = 14
boxlen   = 48.0
ranges   = [0.0, 1.0, 0.0, 1.0, 0.0, 1.0]
selected_hydrovars       = [1, 2, 3, 4, 5, 6, 7]
smallr   = 1.4774579400791327e-5
smallc   = 0.0

scale ==> subfields: (:Mpc, :kpc, :pc, :mpc, :ly, :Au, :km, :m, :
cm, :mm, :μm, :Msol_pc3, :g_cm3, :Msol_pc2, :g_cm2, :Gyr, :Myr, :
yr, :s, :ms, :Msol, :Mearth, :Mjupiter, :g, :km_s, :m_s, :cm_s, :
nH, :erg, :g_cms2, :T_mu, :Ba)
```

For convenience, all the fields from the info-object above are also accessible from the field "gas.info". In the data table, each row corresponds to a leaf cell and its properties to the columns. The positions cx,cy,cz are the cell-numbers that would correspond to a uniform 3D array for each level. This is used to reconstruct the grid in many functions of **MERA** and should not be modified.

In [47]:
```
gas.data
```

Out[47]:
```
Table with 50553133 rows, 12 columns:
Columns:
#   colname  type
──────────────────────
1   level    Int64
2   cpu      Int64
3   cx       Int64
4   cy       Int64
5   cz       Int64
6   rho      Float64
7   vx       Float64
8   vy       Float64
9   vz       Float64
10  p        Float64
11  var6     Float64
12  var7     Float64
```

If the column list is relatively long, the table is typically represented by an overview. To access certain columns, one can use the select function:

In [3]:
```
using JuliaDB
```

In [49]:
```
select(gas.data, (:level, :rho, :vx, :vy, :vz, :p))
```

Out[49]:
Table with 50553133 rows, 6 columns:

level	rho	vx	vy	vz	p
6	1.47746e-5	0.116339	0.116781	0.116751	2.85781e-7
6	1.47746e-5	0.126912	0.127382	0.168628	2.85781e-7
6	1.47746e-5	0.133826	0.134312	0.183555	2.85781e-7
6	1.47746e-5	0.13791	0.13841	0.186861	2.85781e-7
6	1.47746e-5	0.141117	0.141628	0.185921	2.85781e-7
6	1.47746e-5	0.144017	0.144541	0.183455	2.85781e-7
6	1.47746e-5	0.146723	0.147259	0.179809	2.85781e-7
6	1.47746e-5	0.149277	0.149824	0.175403	2.85781e-7
6	1.47746e-5	0.151709	0.152268	0.170531	2.85781e-7
6	1.47746e-5	0.15404	0.154609	0.16534	2.85781e-7
6	1.47746e-5	0.15638	0.156961	0.159946	2.85781e-7
6	1.47746e-5	0.158758	0.159351	0.15441	2.85781e-7
⋮					
14	1.41561	-0.24238	3.33088	0.176484	0.047303
14	1.29724	-0.220577	3.31409	0.153774	0.0436785
14	1.27011	-0.216775	3.31133	0.148499	0.0428342
14	1.89495	-0.237502	3.43133	0.274364	0.0530883
14	1.83967	-0.24	3.42444	0.270674	0.0515573
14	1.67429	-0.242795	3.38507	0.232914	0.0522781
14	1.59913	-0.244397	3.37508	0.225417	0.0500144
14	1.45658	-0.236722	3.34475	0.193656	0.0481347
14	1.41468	-0.235741	3.33892	0.18751	0.0465728
14	1.3037	-0.21582	3.31765	0.162586	0.043568
14	1.29413	-0.214441	3.31635	0.160881	0.0431636

Get some overview of the data associated with the object "gas". The calculated information can be accessed from the object *data_overview* (here) in code units for further calculations:

In [16]:
```
data_overview = dataoverview(gas)
```

```
Calculating...

100%|████████████████████████████████████████████████| Time: 0
:00:32
```

Out[16]:
Table with 9 rows, 16 columns:
Columns:

#	colname	type
1	level	Any
2	mass	Any
3	rho_min	Any
4	rho_max	Any
5	vx_min	Any
6	vx_max	Any
7	vy_min	Any
8	vy_max	Any
9	vz_min	Any
10	vz_max	Any
11	p_min	Any
12	p_max	Any
13	var6_min	Any
14	var6_max	Any
15	var7_min	Any
16	var7_max	Any

The mass column corresponds to the total mass of all cells for each level.

In [51]:
```
select(data_overview, (:level, :mass, :rho_min, :rho_max ) )
```

Out[51]:
Table with 9 rows, 4 columns:

level	mass	rho_min	rho_max
6	2.10536	1.47746e-5	0.000431662
7	0.506675	1.47746e-5	0.00206836
8	0.507118	1.47746e-5	0.009144
9	1.24512	1.47746e-5	0.0360798
10	2.39456	1.47746e-5	0.131398
11	2.60993	1.47746e-5	0.487535
12	2.2113	1.47746e-5	1.9644
13	1.84374	1.47746e-5	8.01279
14	17.8672	1.8429e-5	4.53175e5

Or simply convert the mass data in the table to Msol units by manipulating the column:

In [ ]:
```
data_overview = setcol(data_overview, :mass, :mass => value->value
* info.scale.Msol);
```

In [53]:
```
select(data_overview, (:level,:mass, :rho_min, :rho_max ) )
```

Out[53]:
```
Table with 9 rows, 4 columns:
level  mass        rho_min     rho_max
──────────────────────────────────────────
6      2.10477e9   1.47746e-5  0.000431662
7      5.06535e8   1.47746e-5  0.00206836
8      5.06977e8   1.47746e-5  0.009144
9      1.24478e9   1.47746e-5  0.0360798
10     2.3939e9    1.47746e-5  0.131398
11     2.60921e9   1.47746e-5  0.487535
12     2.21069e9   1.47746e-5  1.9644
13     1.84323e9   1.47746e-5  8.01279
14     1.78623e10  1.8429e-5   4.53175e5
```

Storing/Loading Into/From Compressed MERA Files

Remarks:

- The full data-object is stored in a HDF5 file (1.7 GB) and is more than a factor of 5 smaller in size than the original RAMSES output files (Hydro + AMR = 9.6 GB).
- Using the new data format, the full box can now be read within a short time, especially compared to simulations that use thousends of cores that are associated with thousends of files. All the data types from Julia, the JuliaDB data framework and composite types from **MERA** are reconstructed. In this case (2048 cores) the loading time of the data is reduced by at least a factor of 17 compared to the traditional data reading. This is especially useful for a time-sequence analysis.

Overview of the Used Disc Space

In [54]:
```
storageoverview(info);
```

```
Overview of the used disc storage for output: 400
-------------------------------------------------------
Folder:          14.1 GB         <1.41 MB>/file
AMR-Files:       2.75 GB         <1.38 MB>/file
Hydro-Files:     6.84 GB         <3.42 MB>/file
Gravity-Files:   4.47 GB         <2.24 MB>/file
Particle-Files: 39.24 MB         <19.62 KB>/file
Clump-Files:    602.47 KB        <301.23 Bytes>/file
```

Store the Hydro and AMR Data with a Comment into a Compressed MERA-File

In [10]:
```
comment_text = "Simulation box with self-gravity"
@time save_merafile(gas, filename="galaxy_400.mera", comment=comme
nt_text, fmode="w")
```

```
Create/overwrite mera file and add hydro data:

Directory: /Users/mabe/Documents/Projects/JuliaLanguage/Mera/Mera
/tutorials/simulations/./
mera_file_version: 1.0
Datatype: hydro
Data fields: (:level, :cpu, :cx, :cy, :cz, :rho, :vx, :vy, :vz, :
p, :var6, :var7)
Total fields: 176
Writing mode: w
Compression mode: blosc with: 3
Filesize: 2.038 GB
  9.400655 seconds (4.05 k allocations: 182.141 KiB)
```

Overview of the Stored Data Types in a MERA File:

The data occupies now less than a factor of 5 compared to the original RAMSES files (From 9.6GB to 1.7GB). The loaded and uncompressed data (leaf cells) needs 4.5 GB in the working memory:

In [12]:
```
@time view_merafile(filename="galaxy_400.mera")
```

```
Stored data:

hydro
-------
Directory: /Users/mabe/Documents/Projects/JuliaLanguage/Mera/Mera
/tutorials/simulations/./
Output: 400
mera_file_version: 1.0
Data fields: (:level, :cpu, :cx, :cy, :cz, :rho, :vx, :vy, :vz, :
p, :var6, :var7)
Uncompressed memory: 4.52 GB
Comment: Simulation box with self-gravity

Filesize: 2.038 GB
  0.003990 seconds (1.52 k allocations: 38.750 KiB)
```

Get the Simulation Overview of the Data in a MERA File:

(Comparable to the function: getinfo())

In [14]:
```
@time info = info_merafile(filename="galaxy_400.mera", datatype="h
ydro");
```

```
[Mera]: 2019-07-06T23:42:30.571

output [400] summary:
-------------------------------------------------------
simulation time: 594.98 [Myr]
boxlen: 48.0 [kpc]
ncpu: 2048
ndim: 3
level(s): 6 - 14 --> cellsize(s): 750.0 [pc] - 2.93 [pc]
hydro-variables: 7  --> (:rho, :vx, :vy, :vz, :p, :var6, :var7)
gravity: true
particles: true
- Npart:    5.091500e+05
- Nstars:   5.066030e+05
- Ndm:      2.547000e+03
- Nsinks:   0.000000e+00
clumps: true
-------------------------------------------------------

  0.023124 seconds (6.43 k allocations: 273.344 KiB)
```

Load the Data of a Selected Data Type:

In [3]:
```
@time gas = read_merafile(filename="galaxy_400.mera", datatype="hy
dro");
```

```
[Mera]: Get hydro data: 2019-07-07T11:21:10.348

mera_file_version: 1.0
Output: 400
simulation time: 594.98 [Myr]
boxlen: 48.0 [kpc]
ncpu: 2048
level(s): 6 - 14 --> cellsize(s): 750.0 [pc] - 2.93 [pc]
Read data fields: (:level, :cpu, :cx, :cy, :cz, :rho, :vx, :vy, :
vz, :p, :var6, :var7)

domain:
xmin::xmax: 0.0 :: 1.0          ==> 0.0 [kpc] :: 48.0 [kpc]
ymin::ymax: 0.0 :: 1.0          ==> 0.0 [kpc] :: 48.0 [kpc]
zmin::zmax: 0.0 :: 1.0          ==> 0.0 [kpc] :: 48.0 [kpc]

Memory used for data table :4.519803658127785 GB
-------------------------------------------------------

 15.972320 seconds (14.86 M allocations: 9.765 GiB, 7.24% gc time
)
```


AMR Overview

Get an overview of the AMR structure associated with the object gas (HydroDataType). The printed informations are stored in a JuliaDB table in code units associated with the object *oamr* (here) and can be used for further calculations:

In [17]:
```
println("Total cell number: ", length(gas.data))
oamr = amroverview(gas)
```

```
Total cell number: 50553133
Counting...

100%|████████████████████████████████████████████████| Time: 0
:00:20
```

Out[17]:

Table with 9 rows, 4 columns:

level	cells	cellsize	cpus
6	240956	0.75	52
7	106808	0.375	113
8	327464	0.1875	205
9	991134	0.09375	332
10	2463100	0.046875	562
11	4741974	0.0234375	1086
12	8116352	0.0117188	1832
13	13297129	0.00585938	2046
14	20268216	0.00292969	2024

The output of the cellsize is in code units and in this case corresponds to kpc. Each row (level) gives the total number of cells and related cpus.

Fast High Resolution Projections

...of the full box onto a (2^14)^2 grid. The commented line shows an example of a data-range selection relative to a given centre in physical units and two selected quantities in given units: surface density in Msol/pc^2, tangential-velocity in km/s (mass-weighted).

In [4]:
```
proj_z = projection(gas, :sd, unit=:Msol_pc2); # projection in z-direction, by default (face-on view of the galaxy)
#proj_z = projection(gas, [:sd, :vϕ], units=[:Msol_pc2, :km_s], xrange=[-10.,10.], yrange=[-10.,10.], zrange=[-2.,2.], center=[24.,24.,24.], range_units=:kpc);
```

```
[Mera]: 2019-07-07T11:21:59.542

domain:
xmin::xmax: 0.0 :: 1.0          ==> 0.0 [kpc] :: 48.0 [kpc]
ymin::ymax: 0.0 :: 1.0          ==> 0.0 [kpc] :: 48.0 [kpc]
zmin::zmax: 0.0 :: 1.0          ==> 0.0 [kpc] :: 48.0 [kpc]

Selected var(s)=(:sd,)


100%|████████████████████████████████████████████████████| Time: 0
:04:33
```

The maps and the unit information are stored into a dictionary:

In [19]:
```
proj_z.maps
```

Out[19]:
```
DataStructures.SortedDict{Any,Any,Base.Order.ForwardOrdering} wit
h 2 entries:
  :sd      => [0.708984 0.708984 … 0.708984 0.0; 0.708984 0.70898
4 … 0.708984 0…
  :sd_unit => :Msol_pc2
```

In [4]:
```
proj_x = projection(gas, :sd, unit=:Msol_pc2, direction=:x); # projection in x-direction (edge-on view of the galaxy)
```

```
[Mera]: 2019-07-07T11:34:03.823

domain:
xmin::xmax: 0.0 :: 1.0          ==> 0.0 [kpc] :: 48.0 [kpc]
ymin::ymax: 0.0 :: 1.0          ==> 0.0 [kpc] :: 48.0 [kpc]
zmin::zmax: 0.0 :: 1.0          ==> 0.0 [kpc] :: 48.0 [kpc]

Selected var(s)=(:sd,)


100%|████████████████████████████████████████████████████| Time: 0
:04:14
```

Use the Python Library: Pyplot

In [13]:
```
using PyPlot
```


In [22]:
```
# Using Python to plot with Matplotlib
figure(figsize=(16., 3.5))

subplot(1,3,1)
imshow( log10.( permutedims(proj_z.maps[:sd])), cmap="jet", origin="lower", extent=proj_z.cextent .* proj_z.scale.kpc, vmin=0, vmax=3)
xlabel("x [kpc]")
ylabel("y [kpc]")
colorbar(label=L"\mathrm{log10(\Sigma) \ [M_{\odot} pc^{-2}]}")

subplot(1,3,2)
imshow( log10.( permutedims(proj_x.maps[:sd])), cmap="jet", origin="lower", extent=proj_x.cextent .* proj_x.scale.kpc, vmin=0, vmax=4)
xlabel("y [kpc]")
ylabel("z [kpc]")
colorbar(label=L"\mathrm{log10(\Sigma) \ [M_{\odot} pc^{-2}]}" ) ;
```

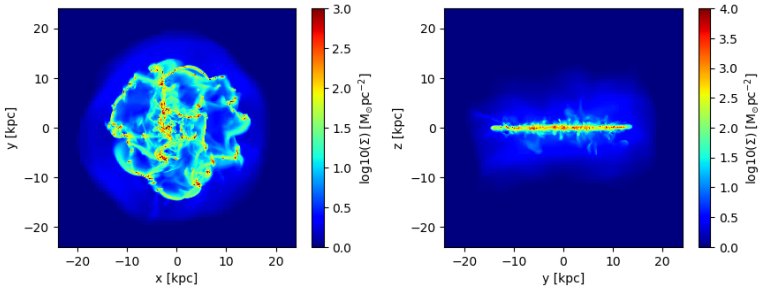

Cutout a Cylindrical Sub-Region

Fast high resolution projections of the disc region onto a (2^14)^2 grid.

In [7]:
```
@time gas_subregion = subregion_cylinder(gas, radius=10., height=2
., center=[24.,24.,24.], length_units=:kpc);
```

```
[Mera]: 2019-07-07T11:01:01.618

center: [0.5, 0.5, 0.5] ==> [24.0 [kpc] :: 24.0 [kpc] :: 24.0 [kp
c]]

domain:
xmin::xmax: 0.2916667 :: 0.7083333      ==> 14.0 [kpc] :: 34.0 [k
pc]
ymin::ymax: 0.2916667 :: 0.7083333      ==> 14.0 [kpc] :: 34.0 [k
pc]
zmin::zmax: 0.4583333 :: 0.5416667      ==> 22.0 [kpc] :: 26.0 [k
pc]

Radius: 10.0 [kpc]
Height: 2.0 [kpc]
Memory used for data table :2.7935050576925278 GB
------------------------------------------------------------

 16.428007 seconds (261.44 M allocations: 6.698 GiB, 4.49% gc tim
e)
```

In [11]:
```
proj_sub_z = projection(gas_subregion, :sd, unit=:Msol_pc2, direct
ion=:z);
```

```
[Mera]: 2019-07-07T11:03:20.617

domain:
xmin::xmax: 0.2916667 :: 0.7083333      ==> 14.0 [kpc] :: 34.0 [k
pc]
ymin::ymax: 0.2916667 :: 0.7083333      ==> 14.0 [kpc] :: 34.0 [k
pc]
zmin::zmax: 0.4583333 :: 0.5416667      ==> 22.0 [kpc] :: 26.0 [k
pc]

Selected var(s)=(:sd,)


100%|████████████████████████████████████████████████████| Time: 0
:00:45
```


In [9]:
```
proj_sub_x = projection(gas_subregion, :sd, unit=:Msol_pc2, direct
ion=:x);
```

```
[Mera]: 2019-07-07T11:02:23.537

domain:
xmin::xmax: 0.2916667 :: 0.7083333      ==> 14.0 [kpc] :: 34.0 [k
pc]
ymin::ymax: 0.2916667 :: 0.7083333      ==> 14.0 [kpc] :: 34.0 [k
pc]
zmin::zmax: 0.4583333 :: 0.5416667      ==> 22.0 [kpc] :: 26.0 [k
pc]

Selected var(s)=(:sd,)


100%|████████████████████████████████████████████████████| Time: 0
:00:23
```

In [10]:
```
proj_sub_y = projection(gas_subregion, :sd, unit=:Msol_pc2, direct
ion=:y);
```

```
[Mera]: 2019-07-07T11:02:47.619

domain:
xmin::xmax: 0.2916667 :: 0.7083333      ==> 14.0 [kpc] :: 34.0 [k
pc]
ymin::ymax: 0.2916667 :: 0.7083333      ==> 14.0 [kpc] :: 34.0 [k
pc]
zmin::zmax: 0.4583333 :: 0.5416667      ==> 22.0 [kpc] :: 26.0 [k
pc]

Selected var(s)=(:sd,)


100%|████████████████████████████████████████████████████| Time: 0
:00:24
```

In [14]:
```
# Using Python to plot with Matplotlib
unit_text = L"\mathrm{log10(\Sigma) \ [M_{\odot} pc^{-2}]}"
figure(figsize=(15.5, 3.5))

subplot(1,3,1)
imshow( log10.( permutedims(proj_sub_z.maps[:sd])), cmap="jet",  o
rigin="lower", extent=proj_sub_z.cextent .* proj_sub_z.scale.kpc,
vmin=0, vmax=3)
xlabel("x [kpc]")
ylabel("y [kpc]")
colorbar(label=unit_text)

subplot(1,3,2)
imshow( log10.( permutedims(proj_sub_y.maps[:sd]) ), cmap="jet",
origin="lower", extent=proj_sub_y.cextent .* proj_sub_y.scale.kpc,
vmin=0, vmax=4)
xlabel("x [kpc]")
ylabel("z [kpc]")
colorbar(orientation="horizontal", label=unit_text, pad=0.2)

subplot(1,3,3)
imshow( log10.( permutedims(proj_sub_x.maps[:sd]) ), cmap="jet",
origin="lower", extent=proj_sub_x.cextent .* proj_sub_x.scale.kpc,
vmin=0, vmax=4)
xlabel("y [kpc]")
ylabel("z [kpc]")
colorbar(orientation="horizontal",label=unit_text, pad=0.2) ;
```

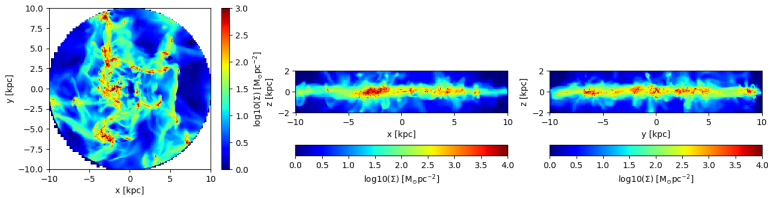

Create 2D Histograms and Masking

With the function *get_var()* the following quantities can be extracted from the data-base in given units to use it for further calculations:

In [3]:
```
get_var()
```

```
Predefined vars that can be calculated for each cell/particle:
------------------------------------------------------------------
==============================[gas]:==============================
       -all the non derived hydro vars-
:cpu, :level, :rho, :cx, :cy, :cz, :vx, :vy, :vz, :p, var6,...

              -derived hydro vars-
:x, :y, :z (in code units)
:mass, :cellsize, :freefall_time
(gamm needed)=> :cs, :mach, :jeanslength, :jeansnumber

============================[particles]:============================
        all the non derived  vars:
:cpu, :level, :id, :x, :y, :z, :vx, :vy, :vz, :mass, :age,....

============================[clumps]:============================
============================[sinks]:============================
====================[gas or particles]:=======================
:v, :ekin

related to a given center:
--------------------------
:r_cylinder, :r_sphere
:ϕ, :θ
:vr_cylinder, vr_sphere
:vϕ, :vθ
:l, :lx, :ly, :lz :lr, :lϕ, :lθ
------------------------------------------------------------------
```

Create a 2D histogram out of the two quantities in given units: disk-radius, vertical velocity (absolute value):

In [17]:
```
@time begin
    data = get_var(gas_subregion, [:r_cylinder, :vz], units=[:kpc,
:km_s], center=[24.,24.,24.], center_units=:kpc)
    hist2D = histogram_amr2D(gas_subregion, [data[:r_cylinder], ab
s.(data[:vz])], range1=[0., 10.], range2=[1., 1000.], nbins=[100,
100], weight=:mass)
end;
```

```
[Mera]: 2019-07-07T11:07:53.3
Range1: 0.0:0.1:10.0   ->bins=100
Range2: 1.0:9.99:1000.0   ->bins=100
Norm: none
 17.080384 seconds (497.08 M allocations: 12.529 GiB, 10.05% gc t
ime)
```

Create a 2D histogram by masking the high densities nH > 100 cm^-3:

(masking is a universal feature of the **MERA** functions)

In [19]:
```
@time begin
    mask = get_var(gas_subregion, :rho, unit=:nH) .< 100. # hydrog
en number density: particles/cm^3
    hist2Dmasked = histogram_amr2D(gas_subregion, mask=mask, [data
[:r_cylinder], abs.(data[:vz])], range1=[0., 10.],
                                range2=[1., 1000.], nbins=[100, 100],
weight=:mass)
end;
```

```
[Mera]: 2019-07-07T11:09:12.519
Range1: 0.0:0.1:10.0   ->bins=100
Range2: 1.0:9.99:1000.0   ->bins=100
Norm: none
 13.261180 seconds (269.41 M allocations: 7.976 GiB, 9.53% gc tim
e)
```

Create a 2D histogram by masking the high densities and considering only high sound-speeds Cs>100 km/s:

In [21]:
```
@time begin
    mask2 = mask .&  (get_var(gas_subregion, :cs, unit=:km_s, gamm
=1.4) .> 100.)
    hist2Dmasked2 = histogram_amr2D(gas_subregion, mask=mask2, [da
ta[:r_cylinder], abs.(data[:vz])], range1=[0., 10.],
                                range2=[1., 1000.], nbins=[100, 100],
weight=:mass)
end;
```

```
[Mera]: 2019-07-07T11:10:21.445
Range1: 0.0:0.1:10.0   ->bins=100
Range2: 1.0:9.99:1000.0   ->bins=100
Norm: none
  7.760740 seconds (131.42 M allocations: 5.920 GiB, 12.23% gc ti
me)
```


In [22]:
```
figure(figsize=(15, 3))
label_text = L"\mathrm{log10(Mass/bin) \ [M_{\odot}]}"

subplot(1, 3, 1)
imshow( log10.(permutedims(hist2D.xy) .* info.scale.Msol ), cmap="
jet", aspect=hist2D.ratio, extent=hist2D.extent, origin="lower", v
min=1.5, vmax=8.5)
xlabel(L"\mathrm{Radius \ [kpc]}")
ylabel(L" \mathrm{ |v_z| \ [km \ s^{-1} ]}")
colorbar(label=label_text)
title("All Densities")

subplot(1, 3, 2)
imshow( log10.(permutedims(hist2Dmasked.xy) .* info.scale.Msol ),
cmap="jet", aspect=hist2Dmasked.ratio, extent=hist2Dmasked.extent,
origin="lower", vmin=1.5, vmax=8.5)
xlabel(L"\mathrm{Radius \ [kpc]}")
ylabel(L" \mathrm{ |v_z| \ [km \ s^{-1} ]}")
colorbar(label=label_text)
title("Without High Densities")

subplot(1, 3, 3)
imshow( log10.(permutedims(hist2Dmasked2.xy) .* info.scale.Msol ),
cmap="jet", aspect=hist2Dmasked2.ratio, extent=hist2Dmasked2.exten
t, origin="lower", vmin=1.5, vmax=8.5)
xlabel(L"\mathrm{Radius \ [kpc]}")
ylabel(L" \mathrm{ |v_z| \ [km \ s^{-1} ]}")
colorbar(label=label_text)
title("High Sound-Speeds of Low Densities");
```

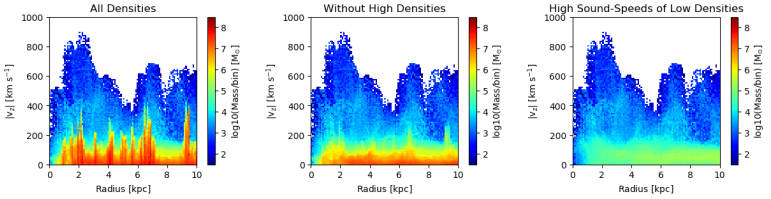

Calculate the total mass of the disc sub-region and with the different masks:

In [25]:
```
@time begin
    mass_disc   = msum(gas_subregion) * info.scale.Msol
    mass_mask   = msum(gas_subregion, mask=mask) * info.scale.Msol
    mass_mask2  = msum(gas_subregion, mask=mask2) * info.scale.Mso
l
end;
```

```
 16.368172 seconds (426.00 M allocations: 13.099 GiB, 11.68% gc t
ime)
```

In [24]:
```
println( "Gas-disc mass:            ", mass_disc, " Msol" )
println( "Gas-disc mass with mask1: ", mass_mask, " Msol" )
println( "Gas-disc mass with mask2: ", mass_mask2, " Msol" )
```

```
Gas-disc mass:            1.7960034391655632e10 Msol
Gas-disc mass with mask1: 5.92091794359765e9 Msol
Gas-disc mass with mask2: 1.3215892411888948e8 Msol
```

Bibliography

Agertz O., Lake G., Teyssier R., Moore B., Mayer L., Romeo A. B., 2009, Monthly Notices of the Royal Astronomical Society, 392, 294

Agertz O., Teyssier R., Moore B., 2009, Monthly Notices of the Royal Astronomical Society, 397, L64

Aumer M., Burkert A., Johansson P. H., Genzel R., 2010, The Astrophysical Journal, 719, 1230

Bassett R. et al., 2014, Monthly Notices of the Royal Astronomical Society, 442, 3206

Behrendt M., Burkert A., Schartmann M., 2015, Monthly Notices of the Royal Astronomical Society, 448, 1007

Behrendt M., Burkert A., Schartmann M., 2016, The Astrophysical Journal Letter, 819, L2

Behrendt M., Schartmann M., Burkert A., 2019, Monthly Notices of the Royal Astronomical Society, 488, 306

Benincasa S. M., Wadsley J. W., Couchman H. M. P., Pettitt A. R., Tasker E. J., 2019, Monthly Notices of the Royal Astronomical Society, 486, 5022

Bezanson J., Edelman A., Karpinski S., Shah V. B., 2017, SIAM review, 59, 65

Bigiel F., Leroy A., Walter F., Brinks E., de Blok W. J. G., Madore B., Thornley M. D., 2008, The Astronomical Journal, 136, 2846

Bigiel F. et al., 2011, The Astrophysical Journal, 730, L13

Binney J., Tremaine S., 2008a, Galactic Dynamics. Princeton Univ. Press, Princeton, NJ

Binney J., Tremaine S., 2008b, Galactic Dynamics: Second Edition. Princeton University Press

Bleuler A., Teyssier R., 2014, Monthly Notices of the Royal Astronomical Society, 445, 4015

Bleuler A., Teyssier R., Carassou S., Martizzi D., 2015, Computational Astrophysics and Cosmology, 2, 5

Bournaud F., 2016, Bulge Growth Through Disc Instabilities in High-Redshift Galaxies, Laurikainen E., Peletier R., Gadotti D., eds., Springer International Publishing, Cham, pp. 355–390

Bournaud F., 2016, in Astrophysics and Space Science Library, Vol. 418, Galactic Bulges, Laurikainen E., Peletier R., Gadotti D., eds., p. 355

Bournaud F., Elmegreen B. G., Elmegreen D. M., 2007, The Astrophysical Journal, 670, 237

Bournaud F., Elmegreen B. G., Martig M., 2009, The Astrophysical Journal Letter, 707, L1

Bournaud F., Elmegreen B. G., Teyssier R., Block D. L., Puerari I., 2010a, Monthly Notices of the Royal Astronomical Society, 409, 1088

Bournaud F., Elmegreen B. G., Teyssier R., Block D. L., Puerari I., 2010b, Monthly Notices of the Royal Astronomical Society, 409, 1088

Bournaud F. et al., 2014, The Astrophysical Journal, 780, 57

Bromm V., 2013, Reports on Progress in Physics, 76, 112901

Burkert A., 1995, The Astrophysical Journal Letter, 447, L25

Cappellari M., 2016, Annual Review of Astronomy and Astrophysics, 54, 597

Cappellari M. et al., 2011, Monthly Notices of the Royal Astronomical Society, 416, 1680

Carilli C. L., Walter F., 2013, Annual Review of Astronomy and Astrophysics, 51, 105

Carollo C. M., Scarlata C., Stiavelli M., Wyse R. F. G., Mayer L., 2007, The Astrophysical Journal, 658, 960

Cava A., Schaerer D., Richard J., Pérez-González P. G., Dessauges-Zavadsky M., Mayer L., Tamburello V., 2018, Nature Astronomy, 2, 76

Ceverino D., Dekel A., Bournaud F., 2010, Monthly Notices of the Royal Astronomical Society, 404, 2151

Ceverino D., Dekel A., Mandelker N., Bournaud F., Burkert A., Genzel R., Primack J., 2012, Monthly Notices of the Royal Astronomical Society, 420, 3490

Courant R., Friedrichs K., Lewy H., 1967, IBM J. Res. Dev., 11, 215

Daddi E. et al., 2010, The Astrophysical Journal, 713, 686

Daddi E., Dannerbauer H., Elbaz D., Dickinson M., Morrison G., Stern D., Ravindranath S., 2008, The Astrophysical Journal Letter, 673, L21

Darvish B., Scoville N. Z., Martin C., Mobasher B., Diaz-Santos T., Shen L., 2018, The Astrophysical Journal, 860, 111

Dekel A. et al., 2009, Nature Astronomy, 457, 451

Dekel A., Krumholz M. R., 2013, Monthly Notices of the Royal Astronomical Society, 432, 455

Dekel A., Sari R., Ceverino D., 2009a, The Astrophysical Journal, 703, 785

Dekel A., Sari R., Ceverino D., 2009b, The Astrophysical Journal, 703, 785

Delgado-Serrano R., Hammer F., Yang Y. B., Puech M., Flores H., Rodrigues M., 2010, Astronomy and Astrophysics, 509, A78

Dolag K., Gaensler B. M., Beck A. M., Beck M. C., 2015, Monthly Notices of the Royal Astronomical Society, 451, 4277

Elmegreen B. G., 1987, The Astrophysical Journal, 312, 626

Elmegreen B. G., 2011, The Astrophysical Journal, 737, 10

Elmegreen B. G., Bournaud F., Elmegreen D. M., 2008, The Astrophysical Journal, 688, 67

Elmegreen B. G., Elmegreen D. M., 1983, The Astrophysical Journal, 267, 31

Elmegreen B. G., Elmegreen D. M., 2005, The Astrophysical Journal, 627, 632

Elmegreen B. G., Elmegreen D. M., Fernandez M. X., Lemonias J. J., 2009, The Astrophysical Journal, 692, 12

Elmegreen B. G., Elmegreen D. M., Vollbach D. R., Foster E. R., Ferguson T. E., 2005a, The Astrophysical Journal, 634, 101

Elmegreen D. M., Elmegreen B. G., Hirst A. C., 2004, The Astrophysical Journal Letter, 604, L21

Elmegreen D. M., Elmegreen B. G., Ravindranath S., Coe D. A., 2007, The Astrophysical Journal, 658, 763

Elmegreen D. M., Elmegreen B. G., Rubin D. S., Schaffer M. A., 2005b, The Astrophysical Journal, 631, 85

Emsellem E. et al., 2007, Monthly Notices of the Royal Astronomical Society, 379, 401

Faucher-Giguère C.-A., 2018, Nature Astronomy, 2, 368

Fisher D. B., 2015, IAU General Assembly, 22, 2256258

Fisher D. B. et al., 2014, The Astrophysical Journal Letter, 790, L30

Fisher D. B. et al., 2017, Monthly Notices of the Royal Astronomical Society, 464, 491

Förster Schreiber N. M. et al., 2009, The Astrophysical Journal, 706, 1364

Förster Schreiber N. M. et al., 2006, The Astrophysical Journal, 645, 1062

Förster Schreiber N. M., Shapley A. E., Erb D. K., Genzel R., Steidel C. C., Bouché N., Cresci G., Davies R., 2011a, The Astrophysical Journal, 731, 65

Förster Schreiber N. M. et al., 2011b, The Astrophysical Journal, 739, 45

Frieman J. A., Turner M. S., Huterer D., 2008, Annual Review of Astronomy and Astrophysics, 46, 385

Fromang S., Hennebelle P., Teyssier R., 2006, Astronomy and Astrophysics, 457, 371

Gammie C. F., 2001, The Astrophysical Journal, 553, 174

Genzel R. et al., 2008, The Astrophysical Journal, 687, 59

Genzel R. et al., 2014, The Astrophysical Journal, 785, 75

Genzel R. et al., 2011, The Astrophysical Journal, 733, 101

Genzel R. et al., 2017, Nature Astronomy, 543, 397

Genzel R. et al., 2006, Nature Astronomy, 442, 786

Genzel R. et al., 2010, Monthly Notices of the Royal Astronomical Society, 407, 2091

Genzel R. et al., 2015, The Astrophysical Journal, 800, 20

Godunov S. K., 1959, Mat. Sb., Nov. Ser., 47, 271

Goldreich P., Lynden-Bell D., 1965, Monthly Notices of the Royal Astronomical Society, 130, 97

Green A. W. et al., 2010, Nature Astronomy, 467, 684

Griv E., Gedalin M., 2012, Monthly Notices of the Royal Astronomical Society, 422, 600

Grogin N. A. et al., 2011, The Astrophysical Journal Supplement Series, 197, 35

Guo Y. et al., 2015, The Astrophysical Journal, 800, 39

Guo Y. et al., 2018, The Astrophysical Journal, 853, 108

Harten A., Lax P. D., van Leer B., 1983, SIAM REVIEW, 25, 35

Hopkins P. F. et al., 2018, Monthly Notices of the Royal Astronomical Society, 480, 800

Hubbard M. E., 1999, Journal of Computational Physics, 155, 54

Huertas-Company M. et al., 2016, Monthly Notices of the Royal Astronomical Society, 462, 4495

Immeli A., Samland M., Gerhard O., Westera P., 2004a, Astronomy and Astrophysics, 413, 547

Immeli A., Samland M., Westera P., Gerhard O., 2004b, The Astrophysical Journal, 611, 20

Kennicutt, Robert C. J. et al., 2007, The Astrophysical Journal, 671, 333

Kennicutt R. C., Evans N. J., 2012, Annual Review of Astronomy and Astrophysics, 50, 531

Kennicutt, Jr. R. C., 1989, The Astrophysical Journal, 344, 685

Kereš D., Katz N., Weinberg D. H., Davé R., 2005, Monthly Notices of the Royal Astronomical Society, 363, 2

Kim C.-G., Kim W.-T., Ostriker E. C., 2006, The Astrophysical Journal Letter, 649, L13

Kim J.-h. et al., 2016, The Astrophysical Journal, 833, 202

Kim W.-T., Ostriker E. C., 2007, The Astrophysical Journal, 660, 1232

Kim W.-T., Ostriker E. C., Stone J. M., 2002, The Astrophysical Journal, 581, 1080

Koekemoer A. M. et al., 2011, The Astrophysical Journal Supplement Series, 197, 36

Lee N. et al., 2015, The Astrophysical Journal, 801, 80

Leroy A. K., Walter F., Brinks E., Bigiel F., de Blok W. J. G., Madore B., Thornley M. D., 2008, The Astronomical Journal, 136, 2782

Leroy A. K. et al., 2013, The Astronomical Journal, 146, 19

LeVeque R., 2013, Numerical Methods for Conservation Laws, Lectures in mathematics ETH Zürich. Birkhäuser Basel

Lin C. C., Shu F. H., 1964, The Astrophysical Journal, 140, 646

Madau P., Dickinson M., 2014, Annual Review of Astronomy and Astrophysics, 52, 415

Magneticum, 2019, A set of hydrodynamical simulations of different cosmological volume. http://www.magneticum.org, [Online; accessed 18-July-2019]

Mandelker N., Dekel A., Ceverino D., Tweed D., Moody C. E., Primack J., 2014, Monthly Notices of the Royal Astronomical Society, 443, 3675

Mo H., van den Bosch F., White S., 2010, Galaxy Formation and Evolution. Cambridge University Press

Naab T., Ostriker J. P., 2017, Annual Review of Astronomy and Astrophysics, 55, 59

Noguchi M., 1999, The Astrophysical Journal, 514, 77

Nü, 2006, Octree Illustration — Wikipedia, the free encyclopedia. https://commons.wikimedia.org/w/index.php?curid=2986260, [Online; accessed 09-April-2019]

Oklopčić A., Hopkins P. F., Feldmann R., Kereš D., Faucher-Giguère C.-A., Murray N., 2017, Monthly Notices of the Royal Astronomical Society, 465, 952

Planck Collaboration et al., 2018a, arXiv e-prints, arXiv:1807.06209

Planck Collaboration et al., 2018b, arXiv e-prints, arXiv:1807.06205

Planck Collaboration et al., 2018c, arXiv e-prints, arXiv:1807.06211

Popesso P. et al., 2019, Monthly Notices of the Royal Astronomical Society, 483, 3213

Press W. H., Schechter P., 1974, The Astrophysical Journal, 187, 425

R Core Team, 2013, R: A Language and Environment for Statistical Computing. R Foundation for Statistical Computing, Vienna, Austria

Robertson B. E., Kravtsov A. V., 2008, The Astrophysical Journal, 680, 1083

Roe P. L., 1986, Annual Review of Fluid Mechanics, 18, 337

Romeo A. B., Agertz O., 2014, Monthly Notices of the Royal Astronomical Society, 442, 1230

Santini P. et al., 2014, Astronomy and Astrophysics, 562, A30

Schartmann M., Mould J., Wada K., Burkert A., Durré M., Behrendt M., Davies R. I., Burtscher L., 2018, Monthly Notices of the Royal Astronomical Society, 473, 953

Schiminovich D. et al., 2010, Monthly Notices of the Royal Astronomical Society, 408, 919

Schneider P., 2015, Extragalactic Astronomy and Cosmology: An Introduction. Springer-Verlag Berlin Heidelberg

Schruba A. et al., 2011, The Astronomical Journal, 142, 37

Schulze F., Remus R.-S., Dolag K., Burkert A., Emsellem E., van de Ven G., 2018, Monthly Notices of the Royal Astronomical Society, 480, 4636

Scoville N. et al., 2014, The Astrophysical Journal, 783, 84

Scoville N. et al., 2016, The Astrophysical Journal, 820, 83

Shetty R., Ostriker E. C., 2006, The Astrophysical Journal, 647, 997

Silk J., Mamon G. A., 2012, Research in Astronomy and Astrophysics, 12, 917

Spergel D. N., 2015, Science, 347, 1100

Spitzer, Jr. L., 1942, The Astrophysical Journal, 95, 329

Springel V. et al., 2005, Nature Astronomy, 435, 629

Swinbank A. M., Smail I., Sobral D., Theuns T., Best P. N., Geach J. E., 2012, The Astrophysical Journal, 760, 130

Tacconi L. J. et al., 2010, Nature Astronomy, 463, 781

Tacconi L. J. et al., 2018, The Astrophysical Journal, 853, 179

Tacconi L. J. et al., 2008, The Astrophysical Journal, 680, 246

Tacconi L. J. et al., 2013, The Astrophysical Journal, 768, 74

Tadaki K. et al., 2018, Nature Astronomy, 560, 613

Tamburello V., Mayer L., Shen S., Wadsley J., 2015, Monthly Notices of the Royal Astronomical Society, 453, 2490

Tamburello V., Rahmati A., Mayer L., Cava A., Dessauges-Zavadsky M., Schaerer D., 2017, Monthly Notices of the Royal Astronomical Society, 468, 4792

Teklu A. F., Remus R.-S., Dolag K., Beck A. M., Burkert A., Schmidt A. S., Schulze F., Steinborn L. K., 2015, The Astrophysical Journal, 812, 29

Teyssier R., 2002, Astronomy and Astrophysics, 385, 337

Teyssier R., 2015, Annual Review of Astronomy and Astrophysics, 53, 325

Teyssier R., Chapon D., Bournaud F., 2010, The Astrophysical Journal Letter, 720, L149

Toomre A., 1964, The Astrophysical Journal, 139, 1217

Truelove J. K., Klein R. I., McKee C. F., Holliman, II J. H., Howell L. H., Greenough J. A., 1997, The Astrophysical Journal Letter, 489, L179

Übler H. D. N. et al., 2019, arXiv e-prints, arXiv:1906.02737

van den Bergh S., 1976, The Astrophysical Journal, 206, 883

van der Walt S. et al., 2014, PeerJ, 2, e453

van der Wel A. et al., 2014, The Astrophysical Journal, 788, 28

van Dokkum P. G. et al., 2015, The Astrophysical Journal, 813, 23

van Leer B., 1976, in Computing in Plasma Physics and Astrophysics, ed. D Biskamp, p. 1. Amsterdam: North-Holland

Van Rossum G., Drake Jr F. L., 1995, Python tutorial. Centrum voor Wiskunde en Informatica Amsterdam, The Netherlands

Wang H.-H., Klessen R. S., Dullemond C. P., van den Bosch F. C., Fuchs B., 2010, Monthly Notices of the Royal Astronomical Society, 407, 705

Waskom M. et al., 2017, mwaskom/seaborn: v0.8.1 (september 2017)

Wikipedia, 2019a, Mera (comics) — Wikipedia, the free encyclopedia. http://en.wikipedia.org/w/index.php?title=Mera%20(comics)&oldid=905860828, [Online; accessed 18-July-2019]

Wikipedia, 2019b, Metaprogramming — Wikipedia, the free encyclopedia. http://en.wikipedia.org/w/index.php?title=Metaprogramming&oldid=905604637, [Online; accessed 10-July-2019]

Wikipedia, 2019c, Multiple dispatch — Wikipedia, the free encyclopedia. http://en.wikipedia.org/w/index.php?title=Multiple%20dispatch&oldid=900845761, [Online; accessed 10-July-2019]

Wisnioski E. et al., 2015, The Astrophysical Journal, 799, 209

Wisnioski E., Glazebrook K., Blake C., Poole G. B., Green A. W., Wyder T., Martin C., 2012, Monthly Notices of the Royal Astronomical Society, 422, 3339

Wuyts S. et al., 2012, The Astrophysical Journal, 753, 114

Wuyts S. et al., 2013, The Astrophysical Journal, 779, 135

Wuyts S. et al., 2011, The Astrophysical Journal, 742, 96

Zanella A. et al., 2015, Nature Astronomy, 521, 54

Zanella A. et al., 2019, Monthly Notices of the Royal Astronomical Society, 489, 2792